



HAL
open science

Synthèse et caractérisation de nanocomposites à base de nitrure de silicium et de bore comme support catalytique mesoporeux pour applications énergétiques

Abhijeet Lale

► To cite this version:

Abhijeet Lale. Synthèse et caractérisation de nanocomposites à base de nitrure de silicium et de bore comme support catalytique mesoporeux pour applications énergétiques. Material chemistry. Université Montpellier, 2017. English. NNT : 2017MONTT203 . tel-01871719

HAL Id: tel-01871719

<https://theses.hal.science/tel-01871719>

Submitted on 11 Sep 2018

HAL is a multi-disciplinary open access archive for the deposit and dissemination of scientific research documents, whether they are published or not. The documents may come from teaching and research institutions in France or abroad, or from public or private research centers.

L'archive ouverte pluridisciplinaire **HAL**, est destinée au dépôt et à la diffusion de documents scientifiques de niveau recherche, publiés ou non, émanant des établissements d'enseignement et de recherche français ou étrangers, des laboratoires publics ou privés.

**THÈSE POUR OBTENIR LE GRADE DE DOCTEUR
DE L'UNIVERSITÉ DE MONTPELLIER**

En Chimie et Physico-Chimie des Matériaux

École doctorale Sciences Chimie Balard

Unité de recherche UMR 5635

**SYNTHESIS AND CHARACTERIZATION OF SILICON AND
BORON -BASED NITRIDE NANOCOMPOSITES AS
CATALYTIC MESOPOROUS SUPPORTS FOR ENERGY
APPLICATIONS**

Présentée par Abhijeet LALE

Le 04 Octobre 2017

**Sous la direction de Samuel BERNARD
et Umit DEMIRCI**

Devant le jury composé de

Saim ÖZKAR, Professeur, Middle East Technical University, Ankara (Turkey)

Emanuel IONESCU, HDR, Technical University of Darmstadt (Germany)

Fabrice ROSSIGNOL, Directeur de Recherche CNRS, Limoges (France)

Sylvain DEVILLE, Directeur de Recherche CNRS, Cavillon (France)

Samuel BERNARD, Directeur de Recherche CNRS, Montpellier (France)

Umit B DEMIRCI, Professeur, Université de Montpellier (France)

Rapporteur

Rapporteur

Examineur

Examineur

Directeur de thèse

Co-Directeur de thèse



**UNIVERSITÉ
DE MONTPELLIER**

Table des matières**CHAPTER 1 LITERATURE REVIEW**

1. Introduction.....	20
2. Energy Context.....	21
2.1 Electrochemical Power Sources.....	21
2.1.1. Batteries.....	22
2.1.2. Fuel Cells.....	23
2.1.3. Supercapacitors.....	25
2.2 Hydrogen storage materials.....	26
2.2.1. Physical-based storage.....	27
2.2.2. Material-based storage.....	27
2.3. (Electro)catalyst supports and electrode materials.....	31
2.3.1. Catalyst supports for the hydrolysis of NaBH ₄	31
2.3.2. Electrocatalyst supports and electrode materials.....	35
3. The Polymer-Derived Ceramics (PDCs)	41
3.1. Principle of PDC route.....	41
3.2. The PDC route toward Si-based ceramics.....	44
3.2.1. Silicon carbide (SiC).....	45
3.2.2. Silicon nitride (Si ₃ N ₄) and silicon carbonitride (Si-C-N).....	48
3.2. The PDC route toward Boron Nitride (BN).....	51
4. The PDC route towards the design of nanocomposites	53
4.1. Definition of nanocomposites.....	53
4.2. PDC-based strategies to design ceramic nanocomposites.....	56
4.2.1. Addition of fillers to preceramic polymers.....	56
4.2.2. Mixed precursors and polymers.....	58
4.2.3. Single-source precursors.....	59
4.3. Transition metal-containing PDC nanocomposites.....	60
4.3.1. Si-based nanocomposites through modification of organosilicon precursors with transition metals.....	60

4.3.2. B-based nanocomposites through modification of borazine, polyborazylene and ammonia borane with transition metals:	69
5. The PDC route towards the design of mesoporous components.....	71
5.1. Sacrificial fillers	71
5.2. Soft templating	72
5.3. Hard templating	73
6. Conclusion	75
References.....	76
<u>CHAPTER 2 MATERIALS AND METHODS</u>	
1. Introduction.....	104
2. Molecular precursors and preceramic polymers	104
2.1 Presentation of the commercially-available organosilicon polymers.....	104
2.2 BN precursors.....	107
2.3 Synthesis of metal-modified organosilicon polymers and BN precursors.....	109
2.3.1 Tetrakis(dialkyl)aminometallics:	110
2.3.2 Synthesis of metal-modified organosilicon polymers.....	110
3. Pyrolysis of preceramic polymers as powders	114
4. Preparation of mesoporous monoliths via nanocasting using template.....	114
4.1 Nanocasting using template	114
4.2 Mesoporous SiC and Si-C-N monoliths	115
4.3 Mesoporous Si ₃ N ₄ , Si-M-N and B-M-N monoliths.....	116
4.3.1 Mesoporous PHPS derived Si ₃ N ₄ monolith	116
4.3.2 Polymetallosilazane/borane derived mesoporous monoliths.....	117
4.4 Deposition of Platinum Nanoparticles (np-Pt) on the ceramic monoliths.....	118
5. Preparation of MXene/SiCN composite.....	118
6. Synthesis of Pt/Si-C-N nanocatalysts.....	119
7. Characterization Techniques.....	120
7.1 Physico-Chemical Characterizations	120
7.2 Electronic Microscopy.....	122
References:.....	124
<u>CHAPTER 3 BORON-BASED NON-OXIDE CERAMICS</u>	
1. Introduction:.....	128

2. Results and Discussion:	130
2.1. Preparation and characterization of BN from AB and PB:	130
2.1.1 BN from ammonia borane:	130
2.1.2 BN from polyborazylene:	134
2.2. Preparation and characterization of B-M-N ceramics (M = Ti, Zr, Hf)	139
2.2.1 Preparation and characterization of B-Ti-N ceramics	139
2.2.2 Preparation and characterization of B-Zr-N and B-Hf-N ceramics.....	154
2.3. Preparation and characterization of highly crystallized BN.....	158
2.3.1 Synthesis in solution	159
2.3.1.2 <i>High temperature behavior</i>	164
2.3.2 Reactive ball-milling	166
4. Conclusion	169
References	171
<u>CHAPTER 4 SILICON-BASED NON-OXIDE CERAMICS</u>	
1. Introduction	176
2. Preparation of polysilazane-derived Si₃N₄	177
2.1 Perhydropolysilazane (PHPS)-derived Si ₃ N ₄	177
2.2 Poly(vinylmethyl-co-methyl)silazane (HTT1800)-derived Si ₃ N ₄	181
2.3 Conclusion	184
3. Preparation of Si-Ti-N ceramics	185
3.1. Polytitanosilazane synthesis	186
3.2. Polytitanosilazane-to-amorphous ceramic conversion	193
3.3. Crystallization behavior:	198
3.4 Microstructural characterization using Transmission Electron Microscopy	204
4 Preparation of Si-Zr-N and Si-Hf-N ceramics	208
4.1 Si-Zr-N ceramics	208
4.1.1 Synthesis and characterization of Zr modified polysilazanes	208
4.1.2 Polymer to ceramic conversion	210
4.1.3 Microstructural evolution and high temperature behavior	211
4.1.4 Microstructure analysis using TEM	215
4.2 Si-Hf-N ceramics.....	218
4.2.1 Synthesis and characterization of Hf modified polysilazanes.....	218

4.2.2 Polymer to ceramic conversion analysis with TGA	220
4.2.3 High Temperature microstructural analysis.....	222
4.2.4 Microstructural analysis through TEM.....	227
4. Conclusion	228
References.....	229

CHAPTER 5 SHAPING AND APPLICATIONS

1. Introduction.....	233
2. Design of mesoporous components	235
2.1. Preparation of mesoporous SiC, Si-C-N and Si ₃ N ₄ monoliths	236
2.1.1 Mesoporous SiC and Si-C-N monoliths:	239
2.1.2 Mesoporous Si ₃ N ₄ monoliths	245
2.2. Preparation of mesoporous BN monoliths	248
2.2.1 Synthesis strategy	248
2.2.2 Characterization.....	249
2.3. Preparation of mesoporous Si-Ti-N monoliths	253
2.3.1. Synthesis strategy:	253
2.3.2. Characterization:.....	253
2.3. Preparation of mesoporous B-Ti-N monoliths.....	257
2.3.1. Synthesis strategy	257
3. Design of Pt-supported mesoporous Components-Catalytic application.....	259
3.1. Catalytic activity of Pt-supported SiC, Si-C-N and Si ₃ N ₄ samples	260
3.1.1. Pt impregnation	260
3.1.2. Hydrolysis of NaBH ₄	262
3.2. Catalytic activity of Pt-supported Si-Ti-N samples.....	265
3.2.1. Pt impregnation	266
3.2.2. Hydrolysis of NaBH ₄	267
4. Conclusions:.....	274
References:.....	275

Abstract (English):

The thesis has been funded by a collaborative research partnership between Indian (Dr. Ravi Kumar, Department of Metallurgical and Materials Engineering, Indian Institute of Technology-Madras (IIT Madras), Chennai) and French institutes (Dr. Samuel Bernard, European Membrane Institute, CNRS, Montpellier), IFCPRA/CEFIPRA. It is focused on the synthesis, and characterization of binary (silicon nitride and boron nitride) and ternary (Si-M-N, B-M-N (M = Ti, Zr, Hf)) ceramics which are prepared through a precursor approach based on the Polymer-Derived Ceramics (PDCs) route. The idea behind the preparation of the ternary systems is to form nanocomposite structures in which metal nitrides (M = Ti, Zr, Hf) nanocrystals grow during the synthesis of silicon nitride and boron nitride. A complete characterization from the polymer to the final material is done. Then, these materials have been prepared as mesoporous monoliths coupling the PDCs route with a nanocasting approach to be applied as supports of platinum nanoparticles for the hydrolysis of liquid hydrogen carriers such as sodium borohydride. The performance as catalyst supports has been evaluated in terms of volume of hydrogen released and reproducibility. We showed that the very high specific surface area TiN/Si₃N₄ nanocomposites displayed the best performance because of the catalytic activity of amorphous Si₃N₄, the presence of nanoscaled TiN and the synergetic effect between Pt nanoparticles, nanoscaled TiN and amorphous Si₃N₄. Interesting, these materials are multi-functional as demonstrated as a proof of concept: they can be applied as electrocatalyst supports, electrode materials for fuel cells and supercapacitors, in particular those containing 2D layered materials and free carbon.

Résumé:

La présente thèse s'inscrit dans un projet collaboratif de type CEFIPRA entre l'Inde (Dr. Ravi Kumar, Department of Metallurgical and Materials Engineering, Indian Institute of Technology-Madras (IIT Madras), Chennai) et la France (Dr. Samuel Bernard, Institut Européen des Membranes, CNRS, Montpellier). Les travaux de thèses se sont consacrés à la synthèse de céramiques de type non-oxyde autour de systèmes binaires (nitrure de silicium et nitrure de bore) et ternaires (Si-M-N, B-M-N (M=Ti, Zr, Hf)) à partir de précurseurs moléculaires et polymères, i.e., la voie polymères précéramiques ou PDCs. L'idée principale de ce travail est de former des structures nanocomposites à partir des systèmes ternaires dans lesquelles des nanocristaux de nitrures métalliques (M=Ti, Zr, Hf) se développent pendant la synthèse du nitrure de silicium et du nitrure de bore. Une caractérisation complète allant des polymères aux matériaux finaux a été conduite. Ces matériaux ont ensuite été préparés sous forme de composés mésoporeux (monolithes) en couplant la voie des polymères précéramiques à une approche de nanomoulage. Ces monolithes à haute surface spécifique et mésoporosité interconnectée ont alors été appliqués comme support de nanoparticules de platine pour l'hydrolyse du borohydrure de sodium pour générer de l'hydrogène. Les performances en tant que support de catalyseur ont été évaluées en termes de volume d'hydrogène libéré et de reproductibilité. Nous avons montré que les nanocomposites TiN/Si₃N₄ de surface spécifique très élevée présentent les meilleures performances grâce à l'activité catalytique du Si₃N₄ amorphe, de la présence de TiN nanométrique et de l'effet synergétique entre les nanoparticules Pt, le TiN nanostructuré et le Si₃N₄ amorphe. En preuve de concept, nous avons montré que ces structures nanocomposites étaient multifonctionnelles: elles peuvent être appliquées en tant que supports d'électro-catalyseurs et matériaux d'électrodes dans les piles à combustibles et les super-condensateurs, en particulier pour ceux contenant des matériaux lamellaires 2D et du carbone libre.

Acknowledgements:

I wish to express my sincere gratitude to those who supported me and contributed directly or indirectly to my PhD work.

First and foremost I want to thank my PhD advisor, Dr. Samuel Bernard, for allowing me to work on this interesting subject and giving me the chance to be a part of his research group in the “IEM”. He has showed me how good science can be. His constant support and faith in my abilities is something I will always remember. His contagious zeal for scientific rigor and positive outlook is something I would like to imbibe in my professional life. I will always cherish the personal bond I formed with him over the course of these three years.

I am very thankful for my co-supervisor Prof. Umit B. Demirci, for the all insights and help with my work and thesis. He is an excellent example of a successful supervisor and researcher with his professionalism and devotion. I learnt a lot about time management and research organization from him.

I wish to recognize in particular Prof. Christel Gervais for her valuable help she provided with Solid State NMR data acquisitions and analysis, Dr Johan Alauzun for helping me with ICP test for my samples, Dr Gurpreet Singh and Dr. Benoit Guenot for helping with electrochemical characterizations

I also wish to thank Dr. rer. Nat. N. V. Ravikumar without whose help I would not have got this great opportunity to work in France. I would also like to thank his student and my good friend Awin Wasan for all his help with the acquisition of TEM images.

I am especially grateful for past and present colleagues in the lab I had the pleasure to work with but also chat and build funny memories: Vanessa, Anthony, Salem, Sergii, Emmanuelle, Charlotte, David, Maxime, Maria-Jo, Shota, Ikuya, Shotaro, Lucie, Mona, Thomas, Istvan, Joel and others.

I would like to specially thank three people: Dr. Antoine Viard (Mr H), Diane Foblan and Marion Schmidt (Dumb-Dumb), for bearing with me for the past three years and trying to teach me to speak French. I cannot thank them enough for their presence, help, friendship and their faith in me. I will never forget the joy and value they added to these 3 years.

Especially Dumb-Dumb for being the clocharde and a constant source of entertainment during the long evenings I spent in the lab.

I am in debt for the all the team in the “IEM” from researchers (Philippe, Sophie, Stéphanie, Claude, Sebastien, Yves Marie, Mihail...), to administration team (Florence, Jean Pierre, Cathy, Dominique, Fabienne and Christelle) to the technical service (Patrice, Jean Pierre, Daniel), to the computer service (Henri, Jean Michel, Yoann) and to all the characterization platform personnel (Eddy, Nathalie, Didier, Valérie, Arie, and Mans).

I need to thank also the CEFIPRA/IFCPAR project for the financial support and for giving me the chance to meet and discuss with great researchers. Also I would like to thank CAMPUS FRANCE for all their help with the administrative part of my contract.

I would also like to thank my flatmates: Harshesh, Ankush and Saurabh for their constant support and throughout the three years.

It is time to thank the most important people in my life, my FAMILY. I would like to thank my mother for unwavering support and faith in me. She always stood like a rock by me through all my ups and downs. Without her support I would never have been able to reach where I am now. I would like to thank my father for being their every time I needed him and my elder brother for motivating me whenever I felt down. I would also like to thank my sister-in-law and niece for their constant support and love. I would also like to thank my friends and teachers back in India, especially Dr Ashutosh Gandhi, who taught me to how to do effective research and helped me develop an scientific aptitude. This acknowledgement will be incomplete without thanking my Girlfriend, Sanjot, who was there with me through every thick and thin even though we were seven seas apart.

I would like to dedicate this thesis to my late maternal grandfather Mr. Sharad Tilloo who was a philosophical guiding light in my life. His words of wisdom and faith in me have brought me to where I am today.

GENERAL INTRODUCTION



At the turn of the 21st century the world population stood at a staggering 7 billion. In the past one century human population has exploded by 3 fold to what it was in the early 1900's. The figure 1 (NETL, National Energy Technology Laboratory, US DOE) below compares the growth of population to the energy consumption during the same period.

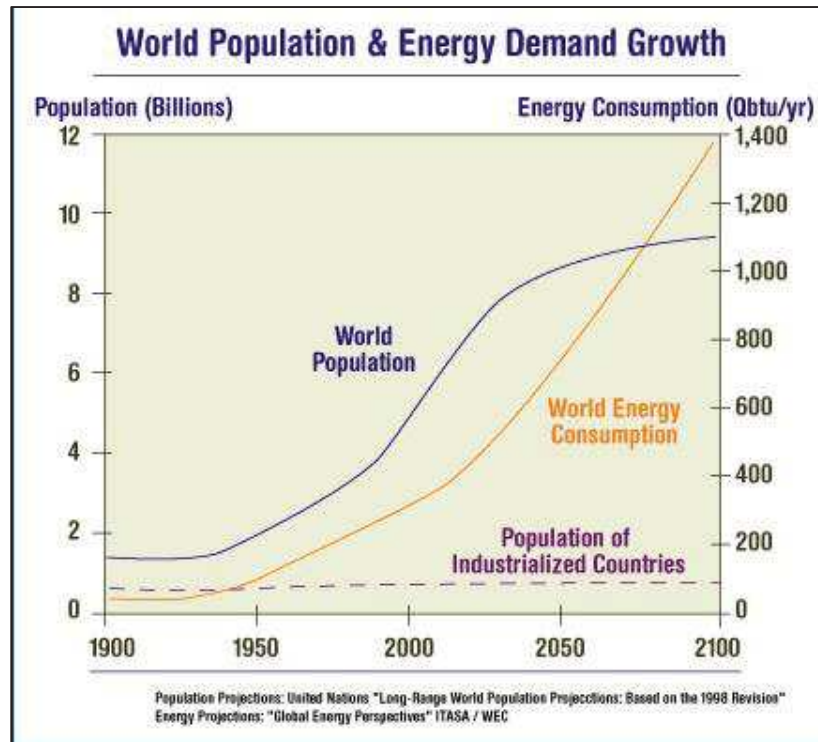


Figure 1 World population and Energy Requirement plotted versus time

The demand for energy increases with increasing population and is expected to increase even further as we cross new frontiers of science. Thus finding new sources of energy has been one of the fundamental pursuits in science and technology. For the past few centuries fossil fuels like coal and wood have been the main stay of energy industry in powering the world. There was shift from coal to crude oil in the second half of the 20th century. The attractive properties of crude oil and its relative abundance lead to it's over use and over exploitation in early years. The industrial revolution in the early 19th century and mass production methods in the mid 20th century pumped a lot of CO and CO₂ along with other harmful gases like (NO)_x in the atmosphere which have now lead to change in climate and global warming. This exploitation of the nature led to environmental problems like deforestation, pollution of water bodies and air. Thus energy and environment are two sides of the same coin.

To protect the environment and allow human race to grow at the same pace a solution is required which takes into account sustainability and renewability. There are various sources of energy in nature which follow these two principles. The most common example is our closest star '*The Sun*'. But we need to remember that these renewable sources have their own inherent problems like cost and operational limitations. These systems need to be coupled with each other to make efficient and sustainable use. One such technology which can be used in the coupling process is hydrogen economy. Nevertheless, the development of a **hydrogen economy** is hampered by three main issues that can be problematic: i) **production**, ii) **storage** and iii) **purification**. In this thesis we focus on the first problem and up till a certain extent on energy storage in general.

Hydrogen has the **highest gravimetric energy density** and can be produced from a variety of feedstock including fossil resources as well as renewable resources. It is mainly produced from natural gas at high temperature involving a severe evolution of carbon dioxide which requires separation methods to purify hydrogen. A simpler way to produce hydrogen is found in **liquid-phase carriers** which can be used in combination with fuel cells to produce electrical energy (for automobiles, stationary applications such as power generators and portable electronics) with zero emission except water. Based on the important opportunities offered by this new-born technology, we have been interested in the **hydrogen generation** through such processes. Chemical compounds like boranes, hydrides and organic acids are abundant sources of hydrogen which can be easily adapted for existing infrastructure used for liquid fuels. These sources generally require presence of catalyst to make the process of generation feasible. As a main focus of this thesis we **develop materials which can be used for these catalytic processes as catalyst or as catalyst supports**.

Common oxide ceramics such as silica and alumina have largely dominated the ceramic field, and the understanding of their chemistry, processing and properties has been well documented. In contrast, non-oxide ceramics have been significantly less investigated most probably because their strong and predominantly covalent atomic bonds impose high temperature solid-state sintering, thereby increasing their cost in comparison to oxides. However, ceramic processing techniques based on molecular engineering and polymer chemistry may significantly reduce the processing temperature and costs of these high-tech ceramics, while offering much more versatility in terms of shaping, structure and texture.

Within this context, we firstly focused our work on the design of **precursor (molecular and polymeric)**-derived binary nitrides such as **boron nitride and silicon nitride** to be explored as catalyst supports. Because the addition of other elements to these nitrides may extend and improve their performance, we focused secondly on the molecular design of multi-element boron- and silicon-based non oxide ceramics in the **B-M-N and Si-M-N-C systems** with M = Ti, Zr, Hf as catalyst supports.

The thesis has been funded by a **collaborative research partnership** between Indian (Dr. Ravi Kumar, Department of Metallurgical and Materials Engineering, Indian Institute of Technology-Madras (IIT Madras), Chennai) and French institutes (Dr. Samuel Bernard, European Membrane Institute, CNRS, Montpellier), IFCPRA/CEFIPRA.

The present manuscript is divided into **five chapters**.

The **first chapter** deals with the **state of art** in the field of energy conversion, energy storage and ceramic synthesis from polymer route.

The **second chapter** deals with the **experimental techniques** involved in synthesizing the material systems and the **characterization tools**.

The **third chapter** discussed on the synthesis and characterization of **precursor-derived boron nitride (BN) and its nanocomposite derivatives** by introducing transition metal such as Ti, Zr and Hf at molecular scale in BN precursors. We describe in the first part of the chapter the preparation of BN from ammonia borane and polyborazylene, then we report in the second part the chemical modification of BN precursors with transition metal-based precursors and the complete structural characterization of the resulting metal-modified BN materials. A last part is focused on the control of the crystallinity of BN

In the **fourth chapter**, we applied the concept and structure used in chapter 3 by changing the matrix from BN to **silicon nitride (Si₃N₄)**. The role of the chemistry of the precursors behind the elaboration process of **Si-M-N ceramics** is highlighted.

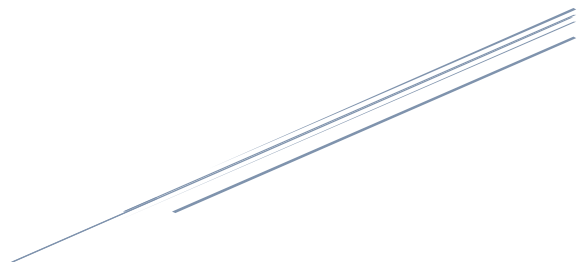
In the **fifth chapter**, we explore the potential of the materials prepared in chapters 3 and 4 as **mesoporous components** to be used as **catalyst supports** of platinum nanoparticles for the **hydrolysis of a liquid-based carrier, sodium borohydride**.

The manuscript ends with a **conclusion** in which we summarize the results and discussions proposed in each chapter, and underlines its prospective future by evaluating some **perspectives**.

CHAPTER 1

LITERATURE

SURVEY



1. Introduction

With the growing world population and impending climate change we face the challenge of meeting the increased energy requirements with cleaner and greener sources of energy and ways to keep our environment clean. The most promising technologies of clean energy being already used and being optimized for the future are electrochemical power sources including batteries, fuel cells and supercapacitors. Material science is the key to make these technologies commercially available for everyone. Within this context, the first part of the present chapter deals with the description of these technologies. We particularly focused on the **fuel cell and supercapacitor systems** and on the issues that still limit the commercialization of these technologies: the **hydrogen source** for fuel cells and the **(electro)catalyst supports and electrode materials** for both systems. Then, we described the state-of-the-art processes to produce hydrogen from solid hydrogen storage materials with a particular focus on the **hydrolysis reaction of sodium borohydride** and the ideal catalytic supports. This part is followed by the state-of-the-art electrocatalyst supports and electrode materials that are investigated in the context of fuel cells and supercapacitors. We briefly propose our objectives in terms of alternative materials in this first part to transition toward the second part of this chapter. In the second part, we particularly discuss on the **polymer derived ceramic (PDC) route** to prepare Si- and B-based ceramics with a particular focus on **nanocomposites** and **porous materials** to be used as catalyst support for the hydrolysis of sodium borohydride and electrocatalyst supports/electrode materials for fuel cells and supercapacitors.

2. Energy Context

Electrochemical power sources represent one of the next generation energy sources which can facilitate the transition from fossil fuels to renewable energy sources. The scientific and technological challenges of electrochemical power sources are mainly related to the emergence of new, advanced knowledge and fundamental understanding of materials. Below, we provide a state-of-the-art of three types of electrochemical power source-based technologies and the current key materials that are applied in such technologies. We discuss on their advantages/disadvantages and propose alternative materials that will be developed in the present manuscript.

2.1 Electrochemical Power Sources

Electrochemical cells and systems are important in a wide range of industrial sectors. These form the base of upcoming technologies like renewable energy, energy management conservation, and storage, pollution control/monitoring, and greenhouse gas reduction. A large number of electrochemical technologies have been developed in the past and these systems continue to evolve in terms of life cycle, performance and cost. Existing technologies are being retrofitted with emerging technologies like fuel-cells, large format lithium-ion batteries, electrochemical reactors, ion transport membranes and supercapacitors. This growing demand (multi billion dollars) for electrochemical energy systems along with the increasing maturity of a number of technologies is having a significant effect on the global research and development effort which is increasing in both in size and depth.

Although the energy storage and conversion mechanisms are different in batteries, fuel cell and supercapacitors; there are still some similarities in the three systems which are more detailed below; especially fuel cells and supercapacitors.

2.1.1. Batteries

Batteries are self-contained units that store chemical energy that on demand can directly convert it into electrical energy to power a variety of equipment. Batteries can be classified into three types: primary batteries that are discharged once and discarded; secondary rechargeable batteries that can be discharged and then restore to the original condition by reversing the current flow through the cell; and lastly specialty batteries that are designed to fulfil a specific purpose. These are closed systems, with the anode and cathode being the charge-transfer medium and taking an active role in the redox reaction (Figure 1.1) as “active masses”, *i.e.*, energy storage and conversion occur in the same compartment (Table 1.1).

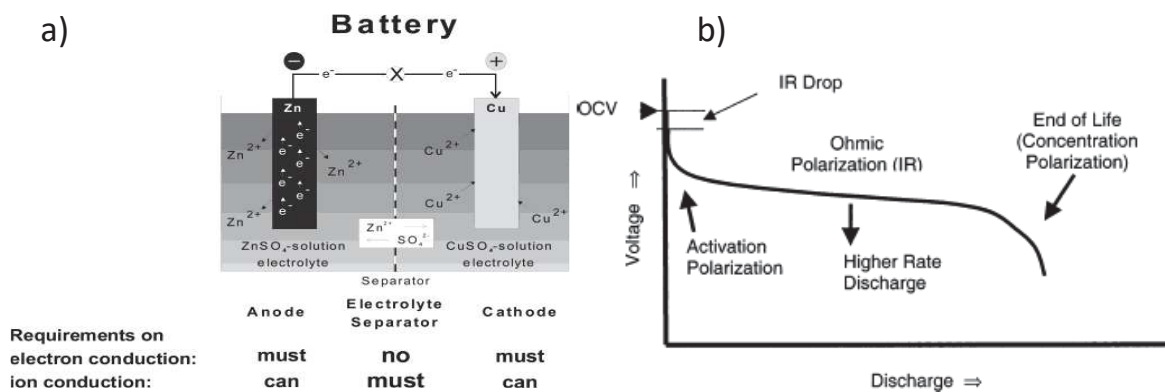


Figure 1.1 a) Schematic of a Daniel cell; b) Typical I-V graph for a battery

Table 1.1 Major advantages and disadvantages of batteries

Advantages	Disadvantages
operate over a wide temperature range	low energy content compared to other fuels
choice of chemical system and voltage	expensive compared to coal and gasolin
variable in size /commonality of cell sizes	no single general purpose system
can deliver high current pulses	
operate in any orientation	
can choose best battery for a specific purpose	

2.1.2. Fuel Cells

Fuel cells, like batteries, convert chemical energy residing in a liquid and gaseous fuel into electrical energy on demand. Earliest reference to the term “Fuel Cell” was made by German physical chemist Wilhelm Ostwald in 1894¹. He ideated the use of a device which utilized electrochemical mechanism instead of combustion (chemical oxidation) of natural fuels, such as those in power plants. He suggested that as in this case the reaction will bypass the intermediate stage of heat generation, this would be a “cold combustion”, and hence will not be subject to limitations placed by the Carnot cycle.

Ostwald, in his work had only considered the thermodynamic aspect of the fuel cell but had entirely left out the kinetic aspects of such reactions using natural fuels. The first experiments after the publication of his paper showed that it was very difficult to build such devices using electrochemical oxidation of natural fuels.

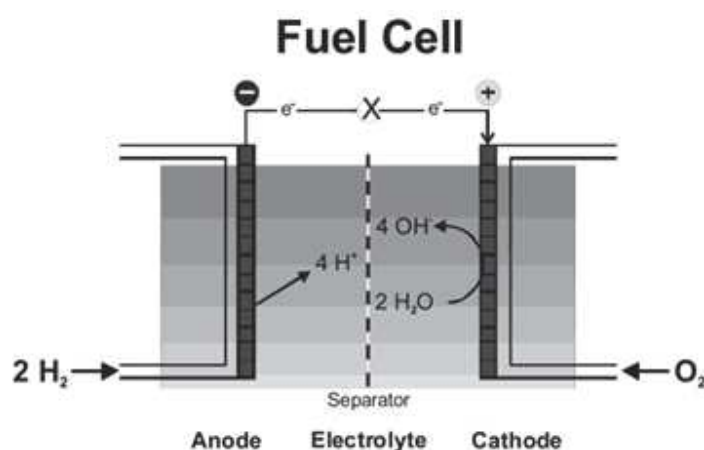


Figure 1.2 Basic illustration of a common fuel cell

Around the mid- 1980s, another application (apart from Ostwald's idea of powerful plants) of fuel cells which came up was its use as an autonomous power source of intermediate or small capacity. These were intended for use in areas where the grid was inaccessible, such as in means of transport, in portable devices and in remote areas. This new application changed the meaning of the term “Fuel Cell” from a power source with current producing reaction involving natural fuels to an electrochemical power source which works as long as the reactants are provided and products are removed (Figure 1.2). The most widely used example of a fuel cell with gaseous reactants is hydrogen–oxygen (air) fuel cells. An example of a fuel cell with at least one liquid reactant is the methanol–oxygen (air) fuel cell in which methanol is supplied as an aqueous solution.

In modern fuel cells, electrical energy is generated by conversion of chemical energy via redox reactions. These reactions occur at the anode and cathode. As reactions at the anode usually take place at lower electrode potentials than at the cathode, the terms negative and positive electrode (indicated as minus and plus poles) are used. The more negative electrode is designated the anode, whereas the cathode is the more positive one. Thus according to the modern definition these are open systems where the cathode and anode are charge-transfer media and the active masses undergoing the redox reaction are delivered from outside the cell, either from the environment, for example, oxygen from air, or from a tank, for example, fuels such as hydrogen and hydrocarbons. This also is one of the main differences between a battery and a fuel cell.

Fuel cells are placed under the subheading of energy conversion technologies in the regime of electrochemical devices. They have a wide variety and their output can range from a few watts to a Megawatts range. There has a lot of study on their operating regimes and widely varying performance characteristics²⁻⁴. They can be categorized depending on the type of electrolyte used, the fuel used and fuel usage can be further divided on the operating temperature range (Figure 1.3).

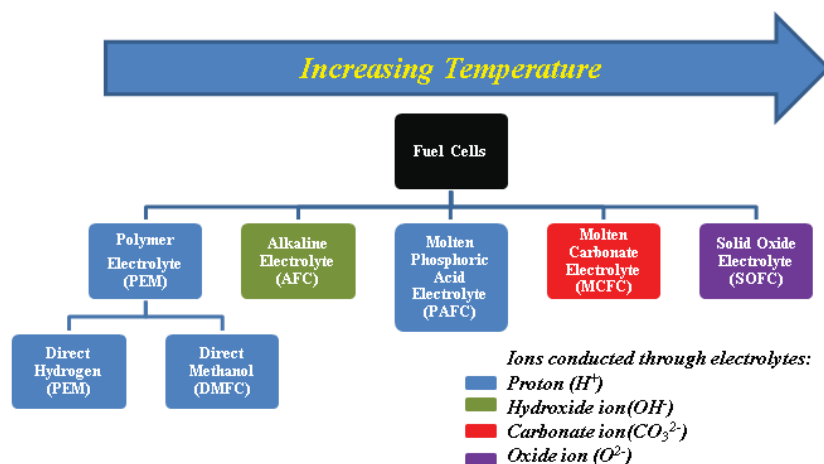


Figure 1.3 Different fuel cells depending on operating temperature

One of the most common fuel cells in use today is the Proton-Exchange Membrane Fuel Cell (PEMFC). These operate at relatively low temperatures ranging from 60°C to 90°C, hence are well suited for both domestic as well as commercial applications. These were first developed by Grubb and Niedrach at General Electric in the 1960s for use as power source in the Gemini spacecrafts^{1,5,6}. The polymeric proton exchange membrane serves as a solid electrolyte and the conductivity is due to the presence of water. The membrane swells leading

to dissociation of the acidic functional groups and formation of protons free to move about throughout the membrane. The following reactions occur in the PEMFC:

At hydrogen anode: $2H_2 + 4nH_2O \rightarrow 4H^+ \cdot nH_2O + 4e^-$

At oxygen cathode: $O_2 + 4H^+ \cdot nH_2O + 4e^- \rightarrow (n + 2)H_2O$

The membrane being currently used in most commercial PEMFC is called Nafion® and it is manufactured by Du Pont.

Due to their light weight and relatively mild operating conditions these are being looked at for use in commercial applications like cars and household uses. The current systems have a specific power of current of 600-800 mW.cm⁻².

2.1.3. Supercapacitors

These are electrochemical devices that use charge separation for storing energy. Generally these have same electrodes on both sides with the difference being the active material loading in each case⁷. Figure 1.4³³⁵ shows a schematic form of this symmetrical supercapacitor.

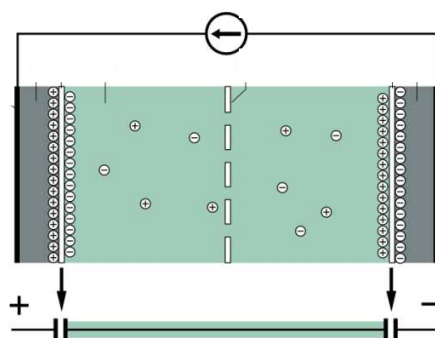


Figure 1.4 Basic illustration of a common supercapacitor

They typically store 10 to 100 times more energy per unit volume or mass than electrolytic capacitors, can accept and deliver charge much faster than batteries, and tolerate many more charge and discharge cycles than rechargeable batteries. When the electrodes are polarized by an applied voltage, ions in the electrolyte form electric double layers of opposite polarity to the electrode's polarity. For example, positively polarized electrodes will have a layer of negative ions at the electrode/electrolyte interface along with a charge-balancing layer of positive ions adsorbing onto the negative layer. The opposite is true for the negatively polarized electrode.

In our work, we are more focused on fuel cells and supercapacitors and in particular on the two major issues that limit the commercialization of fuel cells and supercapacitors: the hydrogen source for fuel cells and the electrode materials in fuel cells and supercapacitors. Our objectives are to propose alternative hydrogen sources like **sodium borohydride as liquid hydrogen carriers** for fuel cells and materials like catalyst supports for the hydrolysis of NaBH_4 and **electrocatalyst supports/electrode materials** for both fuel cells and supercapacitors.

2.2 Hydrogen storage materials

Around 50% of the hydrogen produced in the world is made *via* steam-methane reforming; a mature production process in which high-temperature steam (700–1000 °C) is used to produce hydrogen from a methane source, such as natural gas. In steam-methane reforming, methane reacts with steam under 3–25 bar pressure (1 bar = 14.5 psi) in the presence of a catalyst to produce hydrogen, carbon monoxide, and a relatively small amount of carbon dioxide. Subsequently, in what is called the "water-gas shift reaction," the carbon monoxide and steam are reacted using a catalyst to produce carbon dioxide and more hydrogen. In a final process step called "pressure-swing adsorption," carbon dioxide and other impurities are removed from the gas stream, leaving essentially pure hydrogen. Steam reforming can also be used to produce hydrogen from other fuels, such as ethanol, propane, or even gasoline. However, this is a complex energy-consuming process and methane is also a major contributor to rising CO_2 levels and thus climate change.

The search for hydrogen storage materials capable of efficiently storing hydrogen in a compact and lightweight package and delivering hydrogen on demand is one of the most difficult challenges for the upcoming hydrogen economy. Hydrogen storage is a key enabling technology for the advancement of hydrogen and fuel cell technologies in applications including stationary power, portable power, and transportation. Hydrogen has the highest energy per mass of any fuel; however, its low ambient temperature density results in a low energy per unit volume, therefore requiring the development of advanced storage methods that have potential for higher energy density.

There are mainly **two ways to store hydrogen**, namely, **physical storage** and **material based storage**. Figure 1.5³³⁶ gives a brief overview of the storage options.

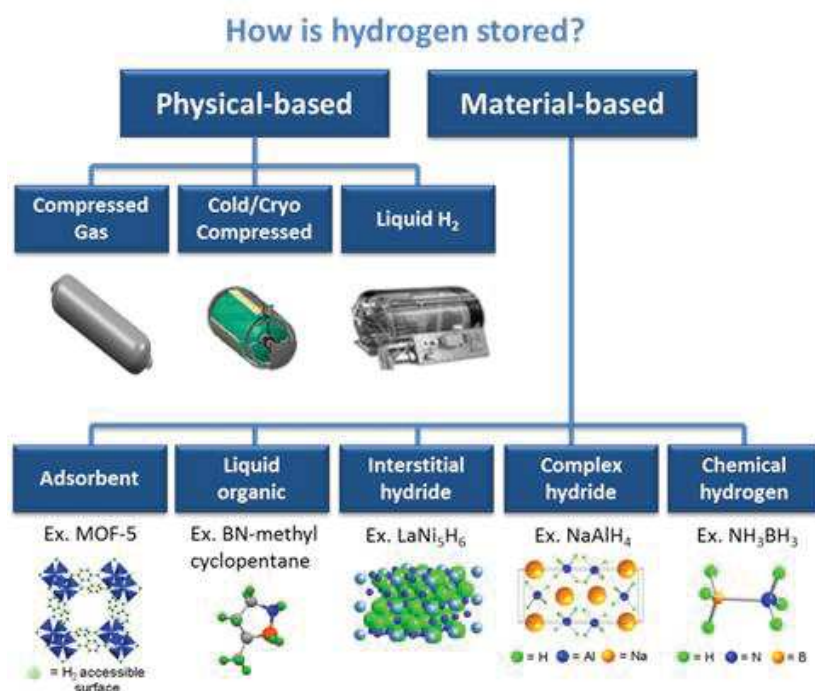


Figure 1.5 Different types of hydrogen storage systems

2.2.1. Physical-based storage

Hydrogen can be stored physically as either a gas or a liquid. Storage of hydrogen as a gas typically requires high-pressure tanks (350–700 bar [5,000–10,000 psi] tank pressure). Storage of hydrogen as a liquid requires cryogenic temperatures because the boiling point of hydrogen at **one atmosphere pressure is -252.8°C** . Although physical storage is the most mature hydrogen storage technology as of now, storing it physically for onboard operation can be risky owing to the highly flammable nature of hydrogen.

2.2.2. Material-based storage

To avoid the risks related to physical storage of hydrogen it is imperative to develop materials which can store hydrogen via adsorption or as chemical units within themselves. Chemical hydrogen storage materials with high gravimetric and volumetric hydrogen densities have the potential to overcome the challenges associated with hydrogen storage. Moreover, the liquid-phase nature of these hydrogen storage systems provides significant advantages of easy recharging, and the availability of the current liquid fuel infrastructure for recharging.

The chemical hydrides can be divided into two types: organic hydrogen carriers and inorganic hydrogen carriers. The following flowchart (Figure 1.6) lists the major compounds in this series.

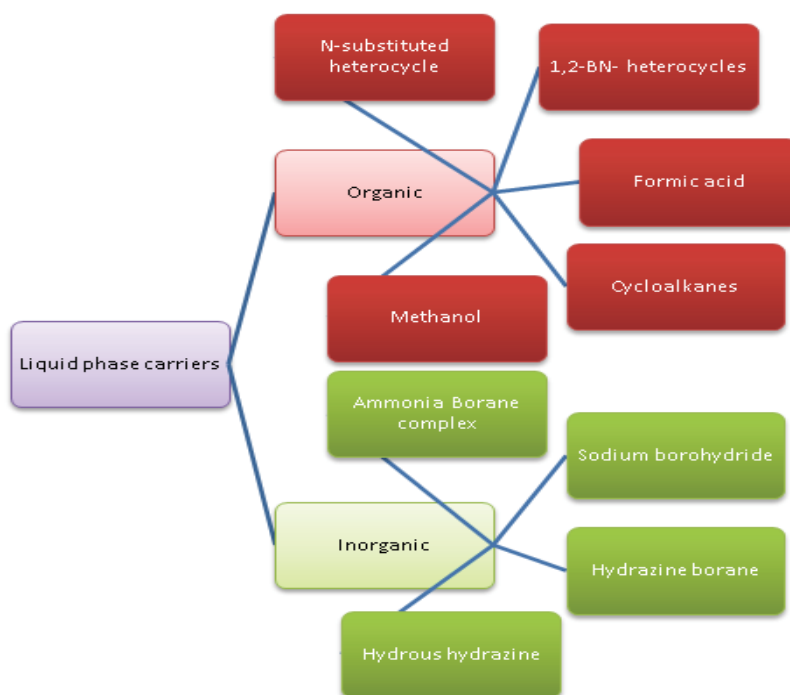
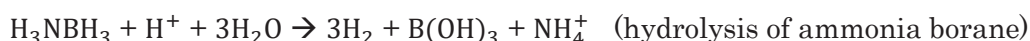


Figure 1. 6 Different types of liquid phase hydrogen storage systems

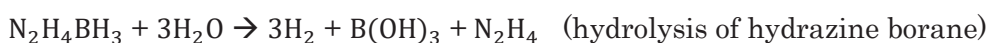
Hydrogen release through suitable dehydrogenation reactions has been particularly described for a variety of compounds, such as cycloalkanes, N-heterocycles, 1,2-BN-heterocycles, methanol, formic acid, hydrous hydrazine and ammonia borane (AB)⁸⁻¹¹.

In these categories, we focused on boron-based compounds. As a reference in the category of boron-based compounds Ammonia Borane (AB) is a stable solid at room temperature which is easily dissolvable in polar solvents like water and tetrahydrofuran (THF). Due to its high theoretical volumetric (146 g. L^{-1}) and gravimetric (19.6 wt%) hydrogen capacities it is promising candidate for meeting the standards set by U.S. DOE^{10,12,13}. Its thermolysis under nitrogen generates H_2 but also toxic gases like ammonia, diborane and borazine¹⁴⁻²⁶. Hence an aqueous catalytic hydrolysis of AB is the preferred option²⁷. There have been extensive studies on this system as seen by the number of review articles on AB^{8,28-33}. Different types of catalyst ranging from noble metals to first row transition elements have been tested for making this system usable for practical application^{27,34-40} but the system is far from practical usability mainly due to the high cost involved in its synthesis and regeneration cycle. Also it generates meta-borates as byproducts which, if not dissolved, acts as a poison for the catalyst. The irreversibility and the low solubility of the AB/by-product are major hurdles for the implementation of AB hydrolysis-based hydrogen storage system. Moreover, there may be

some NH_3 release due to the generation of NH_4^+ during the AB hydrolysis (as shown in equation below), which is highly detrimental for fuel cells. The most attractive aspects of AB hydrolysis are its high stability in water ($\text{pH} > 7$) without catalysts and its fast kinetics of hydrogen generation over catalysts at room temperature, which is unattainable in most other hydrogen storage material-based systems. Thus, such a hydrogen storage system would likely find a niche in special applications for hydrogen availability where the benefits outweigh the high cost of AB.

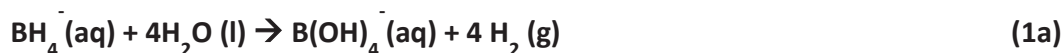


As an alternative for AB, hydrazine borane (HB) has been proposed as a new hydrogen storage material^{29,41}. HB is of interest only if the hydrogen can be recovered by hydrolysis of the BH_3 group and selective decomposition of the N_2H_4 . Thus, the current research devoted to the catalytic decomposition of hydrous hydrazine could be particularly helpful. The complete dehydrogenation of $\text{HB}-3\text{H}_2\text{O}$ leads to a high material-based GHSC of 10.0 wt%, which is much higher than that of the AB hydrolysis system. However, HB apparently suffers from the same issues as AB and hydrazine: (1) since HB is prepared by reacting NaBH_4 with hydrazine salts, the recycling processes of the spent fuel of HB are cost- and energy-ineffective; (2) the low solubility of HB (6 g HB per 100 g of H_2O at 25 °C)⁴² requires a large amount of excess water to realize the liquid-phase hydrogen storage, thus greatly decreasing its material-based excess GHSC; (3) the spontaneous and catalytic hydrolysis of the BH_3 group of HB in aqueous solution results in the occurrence of free N_2H_4 , and therefore there are safety issues related to the dehydrogenation of hydrous hydrazine. Consequently, these significant barriers of the HB dehydrogenation severely hinder its application in liquid-phase hydrogen storage. Moreover, owing to its high theoretical GHSC when HB is used as a solid, some special applications could be expected.



Sodium borohydride (SB) is one the most studied inorganic compounds as a source of hydrogen due to its high theoretical hydrogen capacity of 10.8 wt%⁴³, easy control of the hydrogen generation rate, friendly operation conditions and environmentally benign hydrolysis product ($\text{NaB}(\text{OH})_4$ at room temperature and NaBO_2 above 120°C)⁴³⁻⁴⁵. The hydrogen can be released either by thermolysis^{46,47} or by hydrolysis⁴⁸⁻⁵². However, hydrolysis is more practical approach to generate hydrogen as one half of hydrogen comes from water

resulting in high hydrogen storage capacity. Also the hydrogen produced is free from impurities and humidified and hence be directly used in a fuel cell. NaBH_4 undergoes hydrolysis at room temperature and liberates a theoretical hydrogen content of 10.8 wt% via the following reaction^{45,48}. Ideally, one mole of SB reacts with 4 moles of water to liberate 4 moles of hydrogen.



Interestingly, H_2 is pure and the by-product, sodium tetrahydroxyborate, can be recycled into SB^{50,53–55}. However, NaBH_4 provides the harshest conditions faced by any system facilitating hydrolysis. Figure 1.7 illustrates this concept.

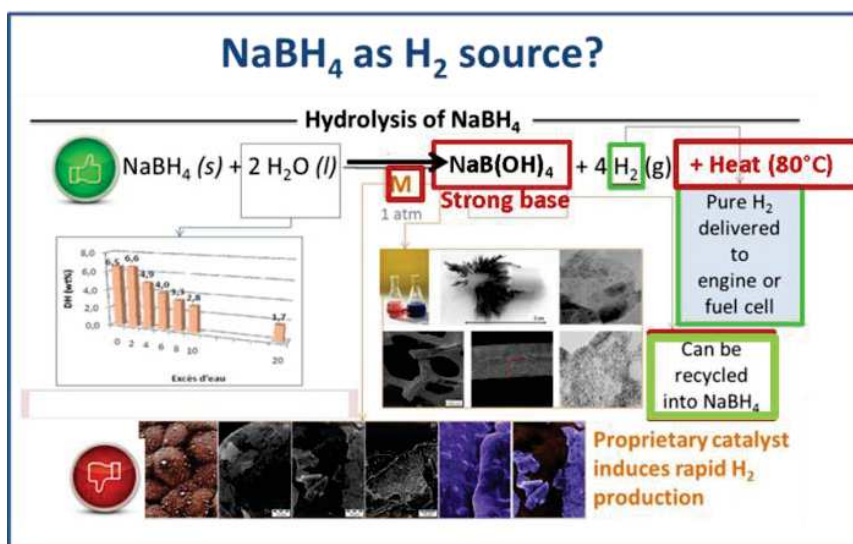
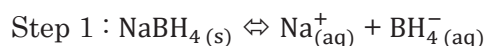


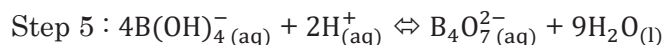
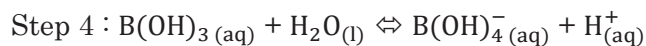
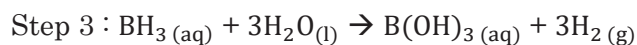
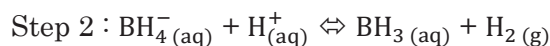
Figure 1.7 Reason to choose NaBH_4 as hydrogen source

So NaBH_4 upon hydrolysis

- generates sodium tetrahydroxyborate which makes the reaction medium highly basic (pH~14),
- is exothermic and the reaction temperature quickly reaches 80°C in certain conditions
- Needs a catalyst such as platinum (Pt) preferentially as nanoparticles distributed on a support to avoid agglomeration and improve the catalytic activity, the support being suitably selected to optimize the Pt activity.

NaBH_4 also suffers from self hydrolysis⁵⁶ (as shown in the equations below) in the presence of water. This creates a problem in storing it as an aqueous solution.





To avoid this problem, Step 2 is disfavored by increasing the pH of the system by addition of a base like NaOH. It was observed by Bartkus *et al.*⁵⁷ that the self-hydrolysis rate becomes negligible above pH=13. In addition, to increase the rate of hydrolysis after the addition of a base, a catalyst is needed. This can either be done by homogeneous catalysis, in which an acid is added to the system, or by heterogeneous catalysis, in which a metal/support system catalyzes the reaction by lowering the activation energy. We focus our attention on heterogeneous catalysis as it provides an “on-off” control for catalyzing the reaction⁵⁶.

Most of the currently used and state of the art systems for hydrolysis are oxide based (Al_2O_3 or SiO_2) or carbon based which in our experience undergo massive structural degradation due to harsh conditions like those mentioned above. **The oxide based systems start collapsing with increase in pH due to self hydrolysis and the carbon based systems swell due to adsorption of water.** The noble metal or transition metal catalyst deposited on these system starts leaching out due to inefficient immobilization and grain growth. As mentioned above NaBH_4 offers the harshest conditions upon hydrolysis and any potential system which can withstand these will be able to work with other fuels without degradation. As a consequence we decided to investigate the hydrolysis of NaBH_4 and in particular the design of suitable catalytic supports for the hydrolysis of NaBH_4 . Besides this, we focused on development of electrocatalytic supports and electrode materials for fuel cells and supercapacitors, respectively. Such (electro)catalysts supports including catalysts, electrocatalyst and electrode materials are the topic of the next section.

2.3. (Electro)catalyst supports and electrode materials

2.3.1. Catalyst supports for the hydrolysis of NaBH_4

Selection of supports generally depends on the surface area, the pore volume, the arrangement and type of the porosity as well as the Lewis and/or Bronsted acidity of materials. Apart from these few properties which are important but generally overlooked are thermal conductivity, mechanical stability and chemical resistance towards reaction

medium. Alumina, silica, zeolites and MOFs are generally used as catalyst supports for various catalytic reactions. As an illustration, silica has been used as a support for the catalytic hydrolysis of ammonia borane. However, the application of silica, zeolites, metal oxides or MOFs in catalytic hydrolysis is somehow limited because their hydrothermal stability may turn to be poor in the severe conditions we have imposed in our study, leading in general to the collapse of the porous structure.

Brack *et al.*⁴¹ compiled a list of all supported heterogeneous catalyst used for hydrolysis of NaBH_4 which are given in Tables 1.2 and 1.3.

Table 1.2 List of noble metal catalyst on supports

Catalyst	Form	Activity($\text{mLH}_2 \cdot \text{min}^{-1} (\text{g.catalyst}^{-1})$)	NaBH_4 conc./wt%	NaOH conc./wt%	Temp/ $^\circ\text{C}$
Ru	Supported on IRA 400 resin	189	20	10	25
Pt/Ru-LiCoO₂	Catalyst dispersed on a nickel mesh	2400	5	5	25
Pt/Pd-CNT	Supported on CNT paper	126	0.1	0.4	29
Ru₆₀Co₂₀Fe₂₀ alloy	Supported on activated carbon fibers	5030	10	4	25
Pt/Ru-LiCoO₂	Catalyst bed	3000	10	5	25
Ru	Supported on ion exchange resin beads	132	5	1	25
Ru	Supported on polymer beads	216	1	1	Not stated
Ru on graphite	Supported on graphite	969	10	5	30
Rh/TiO₂	Immobilized onto titanium dioxide support to form a catalyst bed	210	15	5	23
Alumina carrier Ru composite	Supported on alumina	68.2	12.5	1	25

Table 1.3 List of non-noble metal and alloy catalyst on supports

Catalyst	Form	Activity (mL H ₂ min ⁻¹ (g catalyst ⁻¹))	NaBH ₄ conc. (wt%)	NaOH conc. (wt%)	T/°C
Co-B/Ni foam	Dip coated	7200	25	3	20
Co-B	Thin film prepared by pulsed laser deposition	3300	0.1	Not stated	25
Co-B	Supported on carbon black	2073	0.75	8	25
Co-P	Electroplated on copper	954	10	1	30
Co-W-B/Ni foam	Electrolessly plated	15	20	5	30
Co-B/Ni foam	Electrolessly plated	11	20	10	30
Co-B	Thin film prepared by pulsed laser deposition	5016	0.1	4	25
Co/PPX-Cl	Metallized films	4250	2.5	10	25
Ni(O) nanoclusters	Stabilized on PVP	4250	0.57	0	25
Co-B/Pd	Dry dip coated	2875	20	4	30
Co on activated C	Powder	3600	5	1	30
Co-B	Carbon supported	166	1	5	25
Co-Ni-P	Electrodeposited	2479	10	10	30
Co-B	Electrolessly plated	1640	10	5	25
Ni-Ru	Electrolessly plated	400	10	5	35
Fe-Co-B/Ni foam	Electrolessly plated	22	15	5	30
Co-P-B	Thin film prepared by pulsed laser deposition	4320	0.95	1	25

Co-P/Ni foam	Electrolessly plated	3584	10	1	30
Co-P on Cu sheet	Electrolessly plated	1846	5	1	25
Co-B	Supported on attapulgite clay	3350	5	10	25
Co-alumina on Cu plates	Electrodeposited	383	3	1	80
Co-B	CoCl ₂ solution added to a solid powder mixture of NaOH and NaBH ₄	23,333	50	5	Unregulated
Co NPs embedded on a B thin film	Pulsed laser deposition	3375	0.095	0	25
Co-B NPS	Supported on hydrogels	120	0.19	5	30
Co-Ni-P/Pd-TiO₂	Electrolessly plated	460	1.13	10	25
Co-B NPs	Supported on TiO ₂	12,5	1	3.75	30
Co-B NPs	Supported on Al ₂ O ₃	11,65	1	3.75	30
Co-B NPs	Supported on CeO ₂	10,39	1	3.75	30
Co	Supported on colloidal carbon spheres	1911	1	10	20
Co-B	Impregnation onto carbon supports	1358	1	8	27
Co-W-P on Cu substrates	Electrolessly plated	5000	10	10	30
Co-B	Solution plasma process	4380	2	7	25
Co-ZIF-9	Solvothermal	182	0.5	5	30
Co-P	Electrodeposition	5965	10	10	30
Co-Ni-P	Electrolessly plated	3636	10	10	30
Zr/Co	Impregnation onto carbon supports	1708	5	2	Not stated

Co-B	Supported on carbon black	8034	10	5	25
Ni-Co-P	Supported on alumina	6600	2	4	55
PAN/CoCl ₂ -CNT nanofibers	Electrospun	1255	1	0	25
Co-B/Ni foam	Electrolessly plated	24,4	15	5	30
Co/Ni foam	Magnetron sputtered	2650	3.8	4.5	23
Co ₃ O ₄	Solution combustion synthesized powder	1240	0.6	0	20
Co NPs	Supported on a polyacrylamide hydrogel network	537	3.8	5	30

We looked at Pt support systems which can withstand the harsh conditions mentioned in the previous section without degradation of both the catalyst and the support. B-based non-oxide ceramics such as BN and its nanocomposite as well as Si based ceramic systems like SiC, Si-C-N and Si₃N₄ warrant attention due to their excellent mechanical properties, good stability in harsh chemical conditions and high thermal conductivity. As a catalyst non-porous (SSA < 60 m².gm⁻¹) Si₃N₄ has been tested as powdered support for metals like Ag, Pd and Pt⁵⁸⁻⁶¹. The major problem with powders is the recovery of these systems from the reaction medium, thus making them expensive one time use system. To overcome these difficulties we propose the use of **mesoporous BN, SiC, Si-C-N and Si₃N₄ monoliths and their nanocomposite derivatives through the polymer derived ceramic (PDC) route** which will be discussed later in section 3 to 5.

2.3.2. Electrocatalyst supports and electrode materials

Conventional electrode materials can be divided into three different groups depending on the charge storage mechanism. Figure 1.8³³⁷ illustrates the taxonomy of the supercapacitor electrode materials.

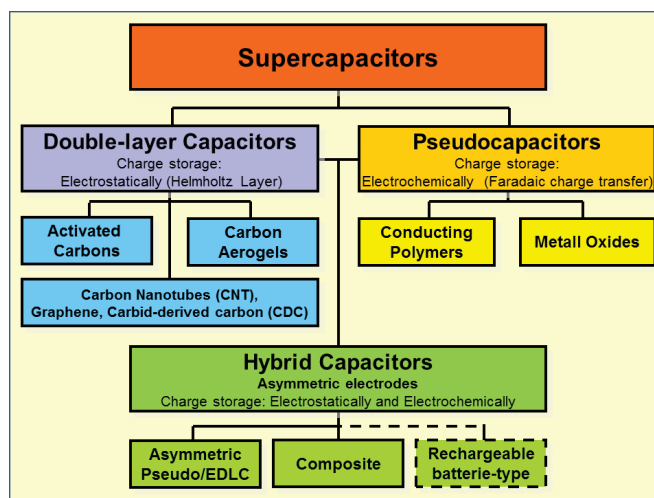


Figure 1.8 Taxonomy of supercapacitor on basis of charge storage mechanism

The electrocatalyst supports and electrode materials play a significant role in the performance of the energy storage and conversion devices. Carbon, metal compounds and conducting polymers are the three main types used as electrode materials for energy storage devices. In particular, carbon based electrodes (activated carbon⁶², carbon nanotubes^{63–65}, graphene^{66–69}, etc.) with high conductivity and stability usually have excellent recycling stability and high power density as supercapacitor electrodes, battery anodes and as support for fuel cells. Furthermore, they are usually cheap and easy to prepare.

In fuel cells, especially in polymer electrolyte membrane (PEM), the carbon black supported platinum (Pt) nanoparticles remains the state-of-the-art electrocatalyst and Vulcan XC-72 carbon black (SSA: 218 m².gm⁻¹ and V_{Porosity}: 0.41 cm³.gm⁻¹)⁷⁰ is the most popular catalyst support currently used in the Pt/C electrocatalysts. However, it has been demonstrated that carbon undergoes corrosion under the oxidizing conditions of a fuel cell, thereby degrading the electrocatalyst and significantly reducing the durability of a PEM fuel cell system⁷¹. Carbon is known to undergo electrochemical oxidation to form surface oxides and CO/CO₂ under these conditions⁷² and potential cycling can further increase the rate of carbon support corrosion⁷³. Significant oxidation of carbon support can be expected to decrease the performance of a fuel cell, due to the loss and/or agglomeration of Pt particles caused by the mass loss of carbon supports. Surface C/O groups can also decrease the conductivity of catalysts and weaken its interaction with the support resulting in an accelerated Pt sintering⁷⁴; thus drastically affecting the performance of a PEM fuel cell. These results indicate the vulnerability of carbon support under fuel cell operating conditions.

An ideal catalyst support material should have corrosion resistance properties under strongly oxidizing conditions of PEM fuel cell: high water content, low pH (<1), high temperature (50–90°C), high potentials (> 0.9 V) and high oxygen concentration. Besides this, some basic requirements should be met including good conductivity (at least 0.1 S.cm⁻¹) and high surface area (>500 m².gm⁻¹).

A material which has been extensively investigated as electrode/electrocatalyst support material is titanium nitride (TiN) due to its excellent thermal and chemical stability as well as electrical conductivity^{75–82}. Its performance as an electrocatalyst support for Pt nanoparticles in direct methanol fuel cell is better than that of traditionally used Pt/Vulcan XC-72 catalyst⁸³. It has also been tested as supercapacitor electrode material with sufficiently high performance⁸⁴. Sampath and Thotiyil^{85,86} explored the synergetic effect between the Pt and PtRu metallic catalyst deposited on TiN support. They suggested that the TiN scavenges CO during electrochemical oxidation of methanol thereby protecting the Pt nanoparticles from poisoning which is not the case with Pt/vulcan XC-72 system. They also suggested certain electronic synergy between Pt/TiN which leads to enhanced performance and can reduce the amount of Pt required thereby bringing down the cost of the system.

Even with high chemical stability, the TiN support becomes susceptible to corrosion at high current values when the passivating film is broken down this lead to degradation of the support as demonstrated by Avasarala and Halder^{73,87}. It is also known that the activity of TiN decreases with increasing size of its crystals (aging) which is exactly what happens when it is exposed to high currents in a harsh electrolytic environment. The same can happen when the Pt nanoparticles are not efficiently immobilized on supports thereby decreasing their activity as well. To overcome this problem, we have proposed the use of mesoporous Ti(C)N/SiCN (silicon carbonitride) nanocomposite monoliths through the PDC route as discussed in sections 4-5. The TiN nanoparticles are enclosed within an amorphous SiCN matrix which prevents the nanoparticle growth (ageing) and protects it from corrosion because of the high stability and robustness of the matrix.

In supercapacitor, the high internal resistivity of carbon-based electrodes, due to contact resistance between carbon particles decreases the supercapacitor performance⁸⁸. In addition, the surface area inaccessible to electrolyte ions⁸⁹ also impedes the capacitance performance of carbon materials, resulting in limited capacitance values of only 40–160 F.g⁻¹ for both activated carbon and carbon aerogels⁹⁰ and 10–35 F.g⁻¹ for CNTs⁹¹. Furthermore, activated

carbon, the most commonly used carbon based electrode faces a major problem of ageing and corrosion related issues due to harsh operating conditions in terms of a humid oxidative atmosphere⁹². A potential electrode material for supercapacitors should have the following properties⁹³:

- High specific surface areas, in the order of $1000 \text{ m}^2.\text{gm}^{-1}$
- Good intraparticle and interparticle conductivity in porous matrices
- Good electrolyte accessibility to intrapore space of carbon materials

Any new material should confer with these properties apart from being low cost, non-toxic, and chemically stable and should have big range of operating temperature. Recently Gogotsi *et al.* started working with new types of 2D supercapacitor electrode material called MXenes^{94–97}.

MXenes are derived from the family of hexagonal MAX phases (ternary nitrides and carbides), where M represents early transition metals (Ti, V, Cr, Nb), A stands for an A-group element (Al, Si, Sn, In etc) and X represents C and/or N (Figure 1.9)³³⁸.

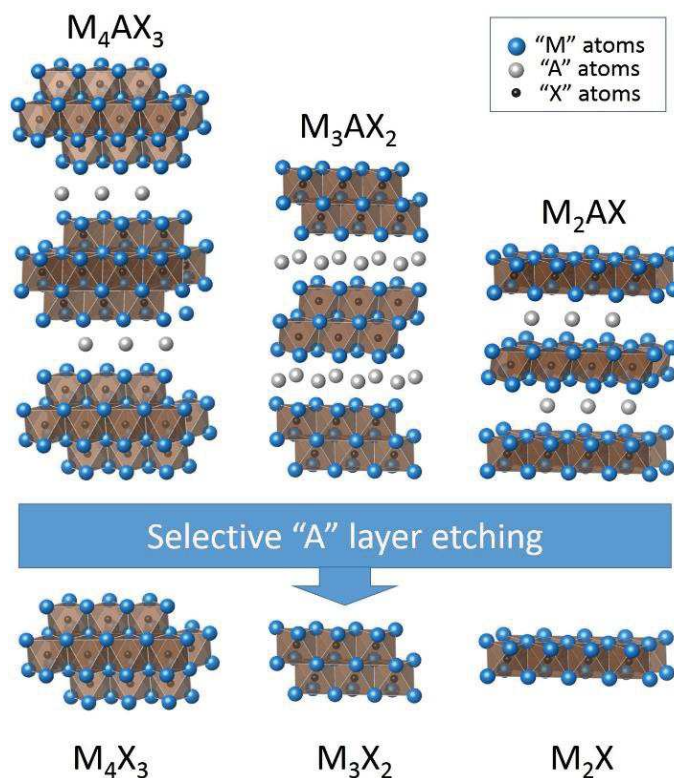


Figure 1.9 Structure of MAX phase and MXene formed after selective etching

They display the following formula $M_{n+1}AX_n$, where $n = 1$ to 3. MXenes are derived from MAX phases by selective removal of A from the system generally by chemical leaching. Theoretically a lot of MXenes are possible but experimentally only 11 have been synthesized till date^{98,99}. The MXene surface can be modified by surface termination which leads to interesting properties in terms of band gap and conductivity. MXenes are hydrophilic and are majorly hydroxyl terminated. Furthermore, the highly layered 2D structure provides enough surface area for electrolyte to interact and the surface modification provides it with high conductivity. Cation intercalation (Mg^{2+} , K^+ , Na^+ , Al^{3+} , NH_4^+ , Ba^{2+} , Ca^{2+} , Cs^+ , Li^+) can lead to high capacitance (over 300 F.cm^{-3}). The cation intercalation rates are unusually high in MXene and the process is referred to as intercalation pseudocapacitance¹⁰⁰. These reasons have led to recent interest in the use of MXene as electrode material. A binder free $Ti_3C_2T_x$ MXene (T: Al, Mn) with a surface area of $98 \text{ m}^2.\text{gm}^{-1}$ was obtained by delamination and tested for electrode use. It showed high flexibility and a high volumetric capacitance of 350 F.cm^{-3} with a NaOH electrolyte^{94,96}. Although the shape of the cyclic voltammetry curves slightly differs depending on the cation^{94,101}, there are no pronounced peaks and the cyclic voltammetry profiles look ‘capacitor-like’ (Figure 1.10). However, due to continuous exposure to the electrolyte the MXene electrode undergoes aging (crystal growth).

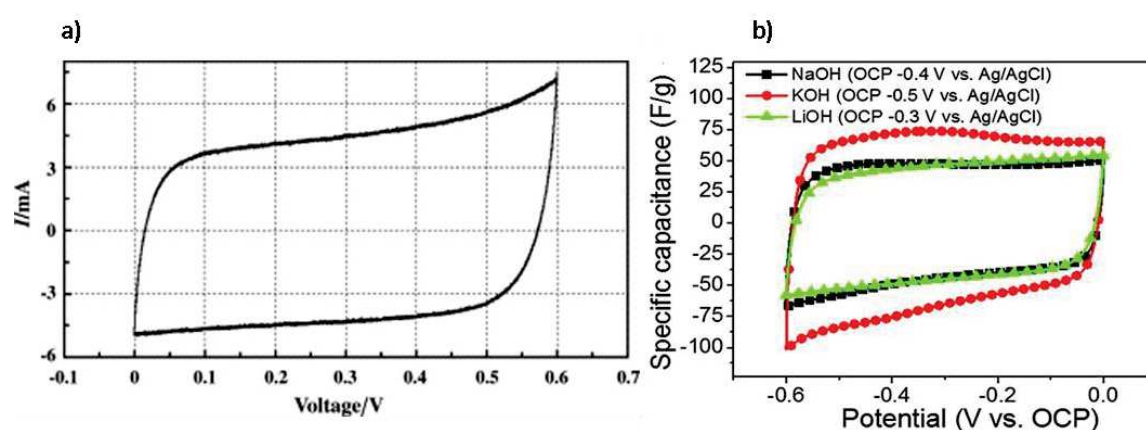


Figure 1.10 a) Ideal ‘capacitor-like’ cyclic voltammetry curve¹⁰²; b) Electrochemical performance of $Ti_3C_2T_x$ -based supercapacitors in various aqueous electrolytes⁹⁴

To avoid MXenes aging, we propose to prepare **MXene-based ceramic composites** through the **PDC route** which will be discussed later in section 3. Such composite can provide enhanced electrochemical and mechanical performance while avoiding corrosion of MXenes because of the presence of the ceramic matrix. The later will also protect the MXene structure from

effects of leaching and they will provide structural strength without harming its conductive properties. The PDC route is investigated in the following section.

3. The Polymer-Derived Ceramics (PDCs)

Preceramic polymers have been proposed over 50 years ago as precursors for ceramics. More than 10000 research papers have been published regarding precursor¹⁰³ ceramics but less than 1% of those use the term precursor/polymer derived ceramics (PDC). The route can be used to prepare Si-based ceramics¹⁰³, which have formed the core of this field, and also B-based¹⁰⁴ and Al-based ceramics in various systems including carbides, carbonitrides, nitrides, borides and silicides¹⁰⁵.

3.1. Principle of PDC route

In order to produce ceramic components with near net precision and controlled chemical composition, it appeared obvious to chemists that improved control of compositional homogeneity and purity as well as processability in ceramic synthesis should be achieved by use of single-source precursors, preceramic polymers and solution techniques. With this viewpoint focused on, the PDC emerged over the last decades.

The PDC route provides a facile method to synthesize complex shapes of ceramics such as fibers, coating and porous materials, in a way not known with more conventional approaches. In principle, conventional polymer processing techniques like polymer infiltration pyrolysis, injection molding, coating using solvents, extrusion or resin transfer molding can be used to shape the preceramic polymer which can then be converted in to final ceramic component by heating to a temperature high enough to consolidate all the elements in the polymeric structure to the ceramic. Figure 1.11 gives a general overview of the PDC route¹⁰⁶.

The molecular structure of the monomer unit has a huge influence not only on the chemical/elemental composition of the final ceramic but also on the number of phases present in the ceramic, their distribution and the microstructure. Hence, we not only control the microscopic properties of the final ceramic but also the macroscopic properties just by tweaking the preceramic polymer used. Apart from having the desired elemental composition, we can summarize the properties^{103,107}: the polymer should have sufficiently high molecular mass in order to avoid volatilization of low-molecular components; it should display rheological properties which are suited for processability, and latent reactivity for curing and crosslinking step to provide ceramics with high yield. However, gathering all these requirements in only one molecule is very challenging.

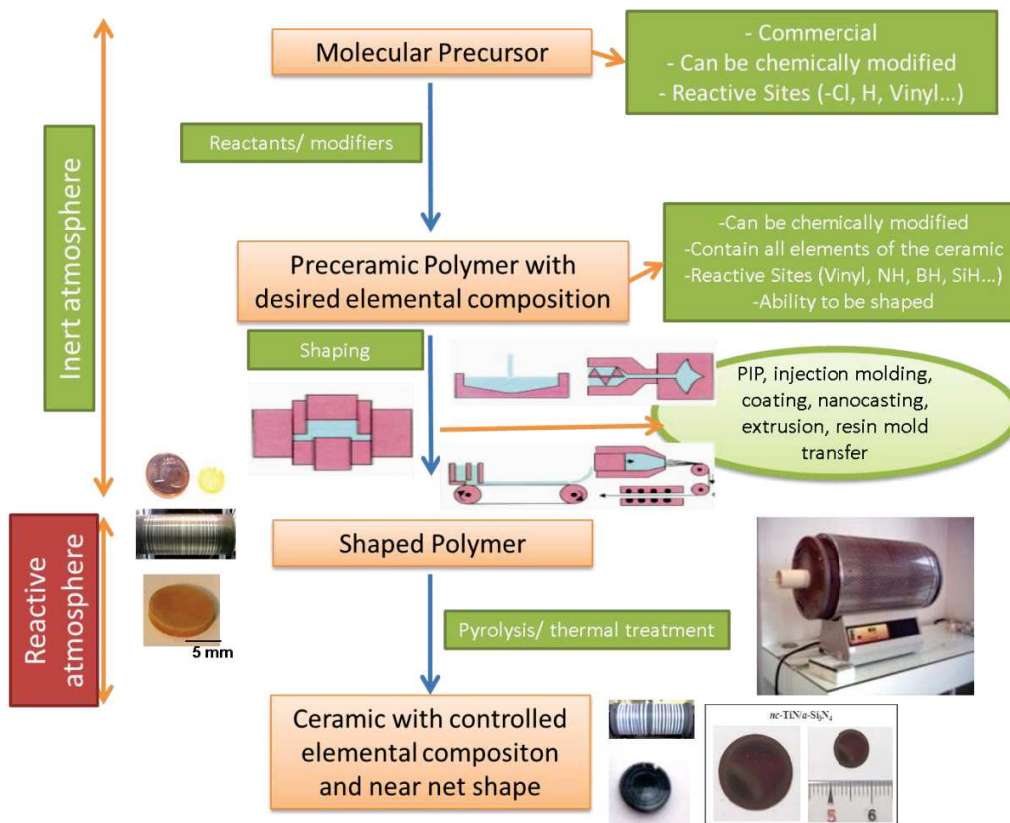


Figure 1.11 General overview of the polymer derived ceramic route

Once the preceramic polymer is selected, the next step in the processing/shaping the polymer to obtain the desired net/green body. Since the preceramic polymers are still polymeric in nature at the temperature at which the shaping/processing is carried out, there are varied and unique ways to shape the polymer as compared to ceramic powders or pastes. One of the main advantages of using preceramic polymers is to avoid problems related to brittle fracture while machining and wear of tool to shape the ceramics since these are shaped before ceramization¹⁰⁸ at significantly lower processing temperatures. Since rheological properties of the preceramic polymer can be easily manipulated, it allows its easy use in plastic forming techniques (resin transfer molding (RTM), extrusion, warm pressing, fiber drawing, injection molding). Table 1.4 compiled by Colombo *et al.*¹⁰³ shows various shaping techniques used in processing of PDC.

As the preceramic polymer needs to transform into a thermoset to retain the shape, a precursor needs to be a cross-linkable compounds. The incorporation of functional group which can take part in with the crosslinking and/or the addition of catalyst, the cross-linking temperature can be brought down, also, the lower cross-linking temperature helps in

reducing the evaporation of oligomers with formation of bubbles and increases the ceramic yield^{109,110}.

Table 1.4 Shaping techniques used in PDC processing

Shaping technique used	References
Casting/freeze casting	Melcher and colleagues ^{111–114}
Impregnation/infiltration	Satoa and colleagues ^{115–117}
Tape casting	Cromme <i>et al.</i> ¹¹⁸
Coating (spraying, dip- or spin-coating, chemical vapor deposition)	Goerke and colleagues ^{119–121}
Pressing (cold/warm—uniaxial, cold— isostatic)	Haug and colleagues ^{122–124}
Injection molding	Zhang and colleagues ^{125,126}
Extrusion	Mutsuddy and colleagues ^{127–129}
Fiber drawing	Bunsell and colleagues ^{130,131}
Blowing/foaming	Zeschky and colleagues ^{132–134}
Machining	da Rocha <i>et al.</i> ¹⁰⁸
Joining	Colombo and colleagues ^{135–137}
Rapid prototyping	Friedel <i>et al.</i> ¹³⁸
Ink jetting	Mott and colleagues ^{139,140}
Electro-hydrodynamic-spraying/spinning	Nangrejo and colleagues ^{141–145}
Aerosol spraying	Xiao and colleagues ^{146,147}
Self-assembly	Garcia and colleagues ^{148–150}
Microcomponent processing (UV/X-ray lithography, nano-/microcasting, replication, microextrusion, embossing/forging)	Hanemann and colleagues ^{151–161}
Microfluidics processing	Ye <i>et al.</i> ¹⁶²
Emulsion processing	Bakumov <i>et al.</i> ¹⁶³
Formation of nanostructures (tubes, fibers, wires, cables, belts, coils), directly by pyrolysis	Otoishi and colleagues ^{114,164–171}

The thermal decomposition of the preceramic polymer leads to the formation of the intended ceramic. It is divided broadly into two parts: cross-linking (<500°C) and ceramization (600 -

1400°C). The cross-linking step can involve a lot of reactions depending on the composition of the preceramic polymer. It usually allows thermosetting the polymer. Crosslinking is in general done by thermolysis but for low dimensional components, e-beams and γ radiation can be applied^{172–174}. UV curing can also be used for microcomponents and fibers if photosensitive functional groups are grafted on the backbone of the polymer^{157,175,176}. Crosslinking is followed by ceramization which starts from 600°C and may well exceed to 1400°C in some cases. This step involves the release of all organic groups still attached to the backbone chain and leads to an amorphous ceramic network. Crystallization therefore occurs at higher temperature. The PDC route is an attractive method to prepare 1) crystalline structures, 2) amorphous structures constituted of a combination of elements homogeneously distributed at atomic scale for which the binding energies are derived from predominantly local covalent bonds and 3) composites or nanocomposites composed of 2 or 3 phases. The main family of PDC that has been investigated during the last decades concerns the Si-based non-oxide ceramics. They mainly display an amorphous structure as used. These have been discussed in the following section.

3.2. The PDC route toward Si-based ceramics

Most of the structural and functional ceramics being used are Si-based ceramics including silicon carbide (SiC) and silicon nitride (Si₃N₄). A third element can be added to these binary systems to form the silicon oxycarbide (Si-O-C) or oxinitrides (Si-O-N) and silicon carbonitride (Si-C-N). These systems are produced from organosilicon polymers as depicted in the Figure 1.12.

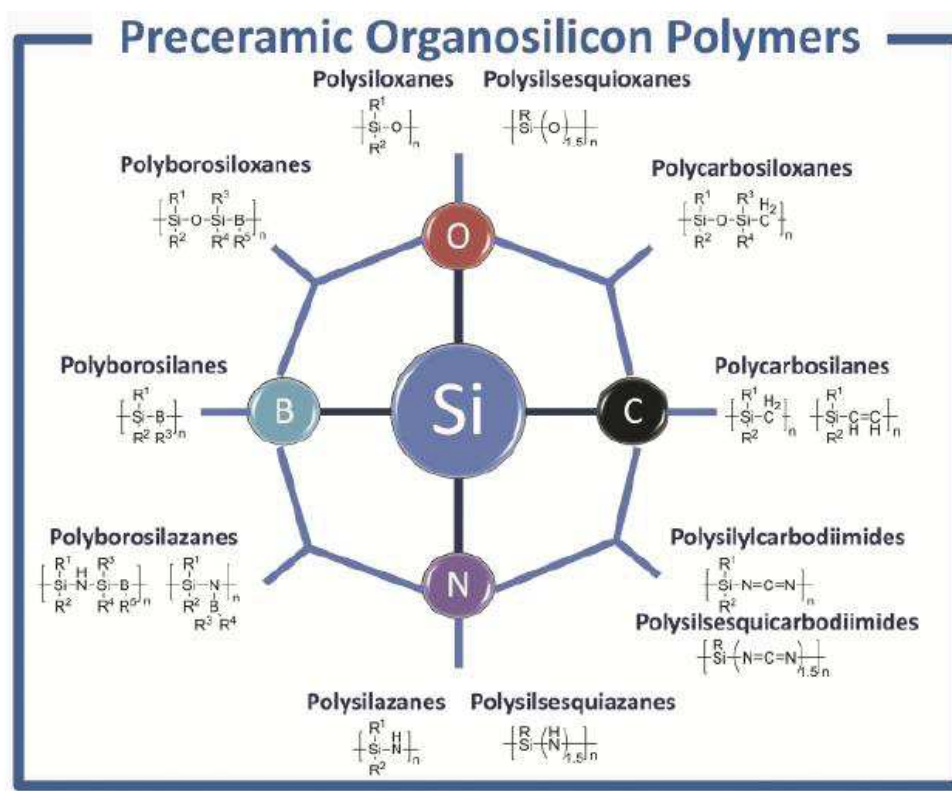


Figure 1.12 Different polymeric precursors to form ceramic systems¹⁰³

Figure 1.12 also shows that metals and metalloids such as titanium (Ti) and boron (B) can be added at molecular scale in these polymers to tune the properties of both the polymers and ceramics. In the next part, we discuss on the preparation of SiC, Si₃N₄ and Si-C-N ceramics which have been investigated in the present PhD thesis.

3.2.1. Silicon carbide (SiC)

As ceramic fibers of silicon carbide (SiC) was done in the middle of the seventies^{177,178,179}.

There are two types of commercially-available organosilicon polymers to prepare SiC. They display the structural configuration [-Si-C-]_n. Yajima *et al.* reported in 1975 the preparation of β-SiC through pyrolysis of methyl-substituted polysilanes, namely PCS. PCS, a solid, fusible and soluble preceramic polymer, has been investigated as a precursor for SiC fibers for over 30 years. The first synthesis was reported by Kumada *et. al.* via thermal reorganisation of polymethylsilane (Figure 1.13)¹⁸⁰. This reaction is better known as the Kumada rearrangement.

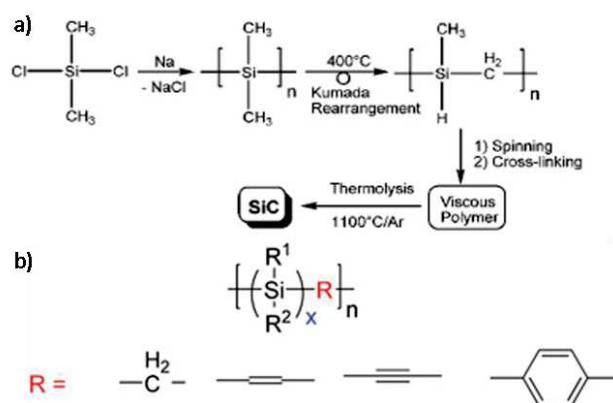


Figure 1.13 a) Synthesis of SiC from dichlorosilane involving Kumada rearrangement- Yajima process; b) Basic structural formula for SiC precursors¹⁰³

Apart from Yajima's process, other route like polycondensation of chlorosilanes, hydrosilylation reactions or polymerization by ring-opening mechanism can lead to designing of new polymers which form SiC¹⁸¹. Pyrolysis of PCS under argon lead to formation of SiC but with considerable amount of free carbon while that of polymethylsilane leads to excess Si as discussed before¹⁸². The presence of excess Si and C degrades the thermomechanical properties of this ceramic at high temperature by making it more prone to thermal oxidation. Furthermore, the preparation of geometries other than fibers is procedurally difficult because of the low ceramic yield of PCS and the dimensional changes which occur during the pyrolytic conversion into SiC.

To avoid this, Interrante *et al.* developed hyperbranched polycarbosilanes, hydridopolycarbosilanes (HPCS) (Figure 1.14) which produced a stoichiometric ceramic Si:C as 1:1¹⁸³. Interrante *et al.*¹⁸³ observed a highly branched structure with a chemical formula corresponding to $[\text{SiH}_x\text{CH}_2]_n$ (where $x=0-3$). By using IR spectroscopy, they observed peaks for SiH, SiH₂ and SiH₃. The ¹³C NMR spectra confirmed the presence of SiCH₂CH₃, SiCH₂Si and Si(CH₂)₃ type groups. So the overall structure of HPCS was highly branched.

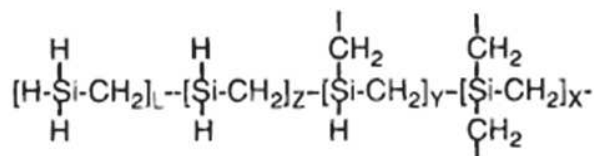


Figure 1.14 Structure of HPCS as described by Interrante *et al.*¹⁸⁴

HPCS was later modified to allylhydridopolysilane (AHPCS)¹⁸⁵, in which 10% H on Si is replaced by allyl group in order to provide better processability, in particular to produce ceramic matrix composites¹⁸⁴. AHPCS has a nominal structure of $[\text{Si}(\text{CH}_2\text{CH}=\text{CH}_2)\text{CH}_2]_{0.1}[\text{SiH}_2\text{CH}_2]_{0.9}$ (manufactured by Starfire Systems, Inc., 877 25th St., Watervliet, NY, 12189)¹⁸⁶. The presence of allyl groups in its structure results in a precursor with improved thermal cure characteristics, as well as enhanced ceramic yield after pyrolysis.

At an intermediate stage of HPCS preparation the chloropolycarbosilane is substituted with a small amount of olefinic functionality like allyl leading to formation of allylhydridopolycarbosilane. This is done to modify the viscosity vs temperature and cross-linking characteristics. Upon pyrolysis under argon Interrante *et al.*¹⁸⁷ observed that the polymer thermoset via thermally induced hydrosilation process between 150-400°C which is a hard clear glass with no weight loss. This crosslinked polymer converted to SiC with a yield of nearly 80-90% upon pyrolysis to 1000°C with a little amount of excess carbon. They further explored the use of AHPCS as liquid polymer for preparation of SiC/SiC_f composite using vacuum polymer impregnation and pyrolysis process (PIP). AHPCS is used in different shaping process to generate dense pieces as Ionescu *et al.*¹⁸⁶ demonstrated, membranes as our group did recently and as macroporous supports¹⁸⁸. AHPCS can also be mixed with other elements like titanium to form nanocomposites as our group recently investigated. To avoid formation of cracks they prepared the green body by pressing at room temperature and then cross-linking the pellet at 300°C with a mass loss of 6 wt%. This green body was then pyrolyzed at 1050°C under an argon atmosphere. The prepared pellet was crack free but still had high porosities. To tackle this, PIP process was employed and the pyrolyzed pellet was immersed in AHPCS for 24 hours and then pyrolyzed again. This process was repeated multiple times and a dense piece with <0.5% porosity was obtained after 6 cycles. Although the pellets contained excess free carbon and oxygen, they were removed upon annealing till 1700°C. This led to increase in porosity but the pellet was still crack-free. They concluded that the PIP process could be employed a multiple number of times to generate a dense piece with a density of 2.5 to 2.6 gm.cm⁻³. However, this is still lower than SiC made from conventional routes.

In the present work, we have investigated the conversion of AHPCS into SiC (chapter 5).

3.2.2. Silicon nitride (Si_3N_4) and silicon carbonitride (Si-C-N)

Polysilazanes are well known as Si_3N_4 and Si-C-N ceramic precursors. There exists a large variety of compounds that allows to tailor the chemistry and structure of final materials¹⁸⁹. Polysilazanes composed of only Si, N and H such as hydridopolysilazane (HPZ) later called perhydropolysilazane PHPS ($[\text{H}_2\text{SiNH}]_n$) or those composed of Si, N, C and H and pyrolyzed under ammonia can lead to formation of Si_3N_4 or amorphous SiN_x ceramics with low or no carbon contamination as shown in the Table 1.5. A lot of work has been done on the synthesis of Si_3N_4 from the beginning of this century^{190,191}.

Table 1.5 Synthesis of silicon nitride from different precursors and the effect of pyrolysis atmosphere and temperature

Silazanes/Pyrolysis atmosphere/Temperature	Ceramics
$(\text{H}_2\text{SiNH})_x/\text{N}_2/1150^\circ\text{C}$ ¹⁹²	Si_3N_4 powders (free Si)
$(\text{H}_2\text{SiN}(\text{CH}_3))_x/\text{N}_2/850\text{--}1600^\circ\text{C}$	Si_3N_4 powders
$(\text{H}_2\text{SiNH})_x/\text{N}_2$ or $\text{NH}_3/1100\text{--}1300^\circ\text{C}$	Si_3N_4 powders & fibres (free Si)
$(\text{RSi}(\text{NH})_{1.5})_x/\text{NH}_3/400\text{--}1200^\circ\text{C}$	$\alpha\text{-Si}_3\text{N}_4$ powders
$(\text{H}_2\text{SiNH})_x/\text{NH}_3/400\text{--}1000^\circ\text{C}$	$\alpha\text{-Si}_3\text{N}_4$ powders
$((\text{CH}_3)\text{HSiNH})_x/\text{NH}_3/600\text{--}800^\circ\text{C}$	$\alpha\text{-Si}/\text{N}/(\text{H})$ films (CVD)
$(\text{CH}_3\text{CH}_2\text{SiNH})_x/\text{NH}_3$ or $\text{H}_2/600\text{--}800^\circ\text{C}$	$\alpha\text{-Si}/(\text{C})/\text{N}/\text{H}$ films (CVD)
$((\text{CH}_3)_2\text{SiNH})_4/\text{NH}_3/900\text{--}1500^\circ\text{C}$	$\text{Si}_2\text{N}_2(\text{NH})$ & Si_3N_4 powders

Silicon diimide $[\text{Si}(\text{NH}_2)_n]$ has been used for synthesis of pure Si_3N_4 (alpha form) at 1250°C ^{193,194}. However, the high viscosity and insoluble nature of the precursor restricted its widespread use for processability in solution. By ammonolysis of various carbon containing polysilazanes, monolithic Si_3N_4 was synthesized¹⁹⁵. SiC and C free $\alpha\text{-Si}_3\text{N}_4$ was formed by pyrolysis of polymethylsilazane (PMSZ), $-(\text{SiH}_2\text{NMe})-$, under NH_3 although the ceramic yield was considerably low, 38 wt%¹⁹⁶. A vinyl-containing silazane was also pyrolyzed under ammonia and crystalline Si_3N_4 with 2 wt.% of carbon was obtained. In this case, the nitridation temperatures were much lower, they were found to be between 300°C and 650°C . In addition, Si_3N_4 was also synthesized using a carbon-containing ethylsilazane-precursor and ammonia in CVD process¹⁹⁷. Pyrolysis of perhydropolysilazane $(\text{H}_2\text{SiNH})_x$ at 1150°C under Ar and N_2 leads to the formation of Si_3N_4 (along with free silicon) with a ceramic yield

of 70-85 wt% whereas the polymer under ammonia leads to formation of pure near stoichiometric Si_3N_4 with a ceramic yield of 60-75 wt%^{192,198-200}.

PHPS is a highly reactive preceramic polymer containing two Si-H and N-H functions in its structure^{192,200-203}. Through pyrolysis under nitrogen, PHPS leads to a composite material composed of a majority of Si_3N_4 and around 13 wt% of silicium (Si)²⁰². As PHPS is commercially available in solution (to avoid its further polymerization) and is highly reactive even at room temperature, the precise measurement of its ceramic yield is difficult because cross-linking inherently occurs at low temperature. As an illustration, the measured weight loss at 1000°C varies from 16.0 %²⁰² to 24.7%²⁰³ in the literature; therefore the ceramic yield is calculated to vary from 75.3 % to 84 %. Such values, even though they are different, are sufficiently high to keep the maximum of product in the porosity of templates through the nanocasting process meaning that PHPS seems to be an ideal precursor for preparing materials with tailored mesoporosity. Within this context, we have investigated the ceramic conversion of PHPS into Si_3N_4 in chapter 4 and we focused in chapter 5 on the designing of mesoporous Si_3N_4 monoliths from PHPS.

Polysilazanes consisting of Si, N and C backbone elements are ideal precursors for formation of ternary Si-C-N ceramics. A lot of work was devoted to the fabrication of ternary Si-C-N systems by using different kinds of polysilazane precursors. Chemistry of the backbone structure, functionality and degree of cross-linking are factors that control the ceramic yield of polysilazanes. It was observed that with cross-linked polysilazanes like $(\text{RSiHNH})_n$ and $(\text{R}_2\text{SiNH})_m$ R= -H, -CH₃, -CH=CH₂, phenyl etc) gave high ceramic yield of 80-85% upon pyrolysis at 1400°C under argon^{204,205}. Besides the pyrolysis temperature and precursor chemistry, ceramic yield is affected by heating rate and pyrolysis atmosphere. It was observed by Bahloul *et al.*²⁰⁶ that ceramic residue of vinylsilazane increased from 15 to 30% with increase in heating rate from 1 to 60°C/min. Table 1.6 shows different precursors that can be used for preparing Si-C-N system with their ceramic yield under different atmospheres. Cross-linking of various polysilazanes was studied by Vioux *et al.*²⁰⁷. They cross-linked various models containing vinyl, NCH₃, SiCH₃ groups Si-H and/or N-H bonds and identified the mechanisms that governed the crosslinking as well as the kinetic rate. They observed that by efficient cross-linking they avoided the early distillation of oligomers during pyrolysis thereby increasing the ceramic yield. They identified that the occurrence of hydrosilylation reaction at around 120°C allows more cross-linking. This led to formation of

Si-C-Si and Si-C-C-Si bonds which are immune to depolymerization reaction (transamination and exchange of Si-N bonds) hence leading to higher yields. These carbosilane bridges led to higher carbon content in the final ceramics. Hence the use of co-organosilazanes with a balance between vinyl and Si-H will lead to ceramics with higher yields and lower carbon content in the final ceramics. Such polymers display the highest ceramic yield to produce Si-C-N ceramics. HTT1800® called later Durazane is a co-organosilazane which has been explored in this thesis.

Another study by Vioux *et al.* explored the mechanism of the polymer-to-ceramic conversion for various cross-linked polysilazanes under atmospheres of argon and ammonia using TGA-MS²⁰⁸. They observed that under inert atmosphere, mineralization involves various free radical reaction and large amounts of excess carbon were obtained when the precursor had unsaturated carbon groups like vinyl or benzene rings. While for ammonia, the mechanism was heavily dependent on the nature of group attached to Si atoms. But generally, amination was complete in the range of 300°C to 750°C by nucleophilic substitution in case of Si-H bonds and hemolytic cleavage of Si-C in case of carbon based substituent groups. Amination and carbon removal coincide in the same temperature range for polysilazanes containing methyl and phenyl groups as they are removed by hydrogen abstraction from ammonia as methane and benzene while for vinyl groups the carbon is removed only after decomposition of ammonia at 750°C as HCN.

Table 1.6 Ceramic yield of preceramic polymers under various atmospheres

Silazanes	Ceramic yield (wt.%)	Pyrolysis conditions
PHMS (Poly(hydridomethylsilazane)) ²⁰⁴	80–85	1000°C, Ar, 10°C/min
PHMS (NCP 200) ²⁰⁹	60–70	1000°C, Ar
PUMVS (Ceraset) ²¹⁰	70–80	1000–1100°C, Ar
PVS (Poly(vinylsilazane)) ²¹¹	85	1150°C, Ar, 10°C/min
PVS (VT 50) ²⁰⁹	70–80	1000°C, Ar
Poly(carbosilazane) (PCS) ²¹²	50–80	1000°C, Ar
Poly(phenylsilazane) (PPS) ²¹³	50–70	800°C, N ₂ , 0.5°C/min
Poly(hexylsilazane) (PHS) ²¹³	25–40	800°C, N ₂ , 0.5°C/min
Poly(silacyclobutasilazane) ²¹⁴	66–73	1200°C, Ar
Poly(ureidosilazanes) ²¹⁵	61–73	1000–1400°C (Ar, NH ₃)

Pyrolysis of polysilazane under an inert atmosphere in the temperature of 800°C to 1200°C generally yields an amorphous Si-C-N ceramic. Table 1.7 shows the chemical composition of Si-C-N ceramics derived from various polysilazanes under inert gas.

Table 1.7 Difference in chemical composition of ceramics depending on pyrolysis conditions

Polysilazane	Chemical composition of the derived ceramics	Pyrolysis conditions
Polyhydridomethylsilazane, PHMSZ (NCP 200) ²¹⁶	SiC _{0.58} N _{0.90}	1000°C, Ar
Polyvinylsilazane (PVSZ) ²¹¹	SiC _{1.47} N _{0.98} O _{0.06} H _{0.06}	1400°C, N ₂
Polyureavinylmethylsilazane, PUMVSZ (Ceraset) ²¹⁰	SiC _{0.86} N _{0.82} O _{0.02}	1000°C, Ar
Polymethylvinylsilazane (PMVSZ) ²⁰⁶	SiC _{1.08} N _{0.78} O _{0.16} H _{0.66}	850°C, N ₂
Polymethylvinylsilazane (PMVSZ) ²⁰⁶	SiC _{0.06} N _{0.01} O _{2.08} H _{0.18}	800°C, O ₂
Polycarbosilazane (PCSZ) ²¹²	SiC _{0.78} N _{0.48} O _{0.05} H _{0.18}	1100°C, Ar

Si-C-N phase diagram can be used to determine the composition and phases of polysilazane derived ceramics. Above 1440°C (without presence of any additives), amorphous Si-C-N will transform into Si₃N₄ and SiC and probably above 1600°C will likely convert completely into SiC with loss of N₂ due to reaction between free carbon and Si₃N₄. The final crystalline phases are mainly determined by the composition of the amorphous Si-C-N materials obtained at lower temperatures. Analysis of the ternary Si-C-N phase diagrams provides a very useful way to evaluate the composition of an amorphous Si-C-N ceramics or to predict the final crystalline phases.

In the present study, we used commercially available HTT1800 polysilazane to investigate its conversion into Si₃N₄ and Si-C-N to prepare mesoporous monoliths.

As an alternative to Si-based non-oxide ceramics, B-based non-oxide ceramics such as boron nitride (BN) display interesting chemical and thermal stability for the applications we targeted. The preparation of precursor-derived BN is discussed below.

3.2. The PDC route toward Boron Nitride (BN)

In contrast to Si-based ceramics, precursor-derived BN are not stable as amorphous structure. Therefore, BN should be prepared in its thermodynamic stable phase, i.e.,

hexagonal. With a preformed ring like structure, the correct boron to nitrogen ratio and only hydrogen as the extra element, **borazine** $H_3B_3N_3H_3$ appears to be an ideal molecular precursor of boron nitride. It is easy and economical to produce by a simple reaction between ammonium sulfate and sodium borohydride in tetraglyme at a low temperature of 120–140°C²¹⁷. Molecular hydrogen and ammonia are only by-products of conversion of borazine to BN by pyrolysis till 1450°C. But borazine is a highly volatile compound and is therefore first self-condensed at low temperature in an autoclave to generate **polyborazylene**, a preceramic polymer, with a controlled molecular weight, physical state and composition. A large number of studies were focused on the self-condensation of borazine to polyborazylene, most of which suggested the generation of naphthalenic (a) and biphenylic (b) type structures^{218–229} as shown in Figure 1.15.

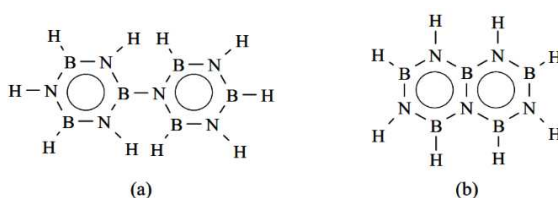


Figure 1.15 (a) Biphenylic, (b) naphthalenic structures for polyborazylene after self condensation of borazine

Sneddon *et al.*^{221–223} were the first authors to isolate a solid polyborazylene through the self-condensation of borazine under vacuum at 70°C for approximately 48 hours. Even though it had a highly branched or partially crosslinked structure it was soluble and hence proved to be an excellent precursor to prepare fiber coatings²²¹. Polyborazylene delivered BN by pyrolysis under argon or ammonia in the temperature range 900–1450°C in excellent chemical (89%–99%) and ceramic yield (84%–93%). Through the study of the self-condensation of borazine at low temperature (45–60°C) under argon in an autoclave, the possibility to control the physical state of polyborazylene from liquid (45–55°C) state (with viscosity increasing with the increase of the synthesis temperature) to solid state ($\geq 60^\circ\text{C}$) by adjusting the temperature of thermolysis^{227,229} was demonstrated. Since polyborazylens varied in their physical state from liquids to solids, they appeared suitable for various processing and shaping techniques. Table 1.8 shows the physical state, chemical composition and ceramic yield of polyborazylens isolated at different temperatures.

Table 1.8 Effect of thermolysis temperature on polyborazylene synthesis

Samples	T _{Thermolysis} (°C)	Physical state	Shaping process type	Empirical formulae (1)	Weight loss (%) (2)
PB45	45	Liquid (extremely volatile)	Solution-based shaping	[B _{3.0} N _{3.0} H _{4.8}] _n	70
PB50	50	Liquid (volatile)	Solution-based shaping	[B _{3.0} N _{3.8} H _{4.0}] _n	53.2
PB60	60	Solid	Plastic-forming technique	[B _{3.0} N _{3.5} H _{4.5}] _n	8.8

(1) Referenced to B_{3.0}; Oxygen values < 2 wt%; (2) Weight loss measured by TGA performed in a nitrogen atmosphere up to 1000 °C (5 °C·min⁻¹).

Moreover polyborazylene is complex to prepare and not commercially available. Alternatively, we focus on the use of ammonia borane NH₃BH₃ (AB) as a preceramic precursor which is commercially available. Suib et al studied the polymer to ceramic conversion of AB to h-BN under nitrogen. They found the conversion to be divided into 3 different steps. The first weight loss occurred around 120°C suggesting the formation of polyaminoborane. It was immediately converted to polyiminothane in some cases leading to formation of borazine ring structure at 210°C, the second weight loss regime. The next and final weight loss occurred around 1150°C due to loss of H₂ and indicating the completion of ceramization of process. These precursors have been utilized in chapter 3, and then used to prepare mesoporous monoliths in chapter 5.

In the following section we discuss on the preparation of nanocomposites from the precursors we discussed previously. In particular we focus on nanocomposites with SiC, Si₃N₄, Si-C-N and BN matrix.

4. The PDC route towards the design of nanocomposites

4.1. Definition of nanocomposites

“A nanocomposite may be defined as a material system containing at least two Gibbsian phases one of which is nanoscaled.”

Or

“Nanocomposite is a multiphase solid material where one of the phases has one, two or three dimensions less than 100 nanometers or structures having nano-scale repeat distances between the different phases that make up the material.”

The term “nanocomposites” was first used in the 1980’s to describe heterogeneity in systems prepared by sol-gel synthesis by Roy and Komarneni²³⁰. The term was extended by Niihara in the 1990’s to cover the domain of ceramic composite nanostructures²³¹. Nanocomposites are essentially different from conventional composite materials in the sense that there is an exceptionally high surface to volume ratio for the reinforcing phase and/or a very high aspect ratio. The secondary phase (Figure 1.16) can be made up of nanoparticles (e.g. minerals), nanosheets (e.g. exfoliated clay stacks) or nanofibers (e.g. carbon nanotubes or electrospun fibers). The area of interface between matrix and secondary phase is greater than conventional composite materials by an order of magnitude.

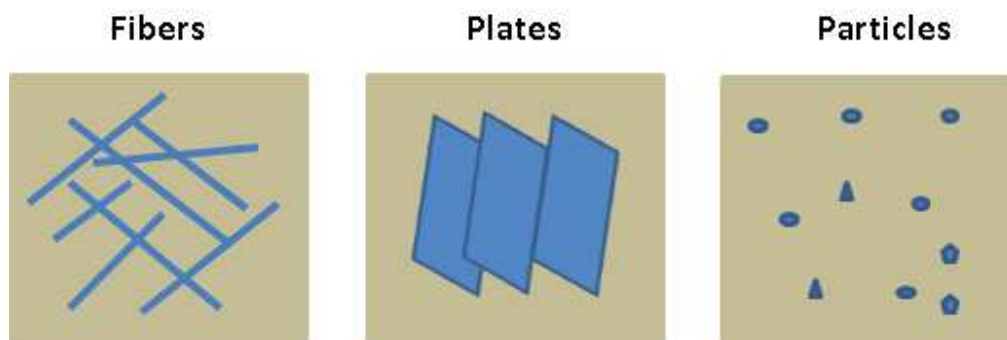


Figure 1.16 Different types of secondary phase materials

Depending on the composition of the secondary phase the nanomaterials can be classified into three types (Figure 1.17):

1. **Metal Matrix Nanocomposite:** A nanoscale composite with at least one part as metal (matrix) and other may be a metal, ceramic or organic compound.
2. **Polymer Matrix Nanocomposite:** Polymer nanocomposites (PNC) consist of a polymer or copolymer having nanoparticles or nanofillers dispersed in the polymer matrix.
3. **Ceramic Matrix Nanocomposite:** Type of nanocomposite with matrix as a chemical compound from the group of oxides, nitrides, borides, silicides etc. and second phase, metal or a ceramic, generally being dispersed homogeneously.

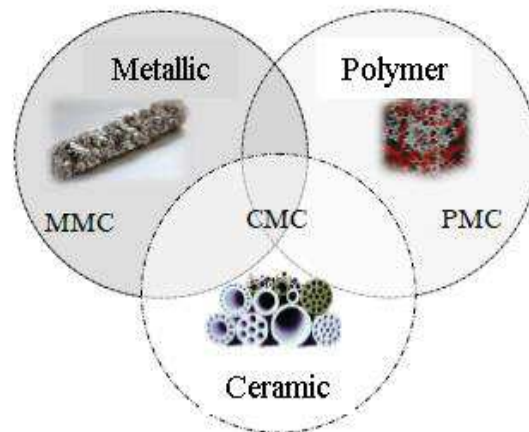


Figure 1.17 General Schematic of type of Nanocomposites

The ceramic matrix nanocomposite can be further divided into five different types depending on the dispersion of second phase, crystallinity of the matrix and size of the secondary phase particles. Based on the previously mentioned parameters Niihara further divided the ceramic matrix nanocomposite into the first four following parts as shown in Figure 1.18²³¹.

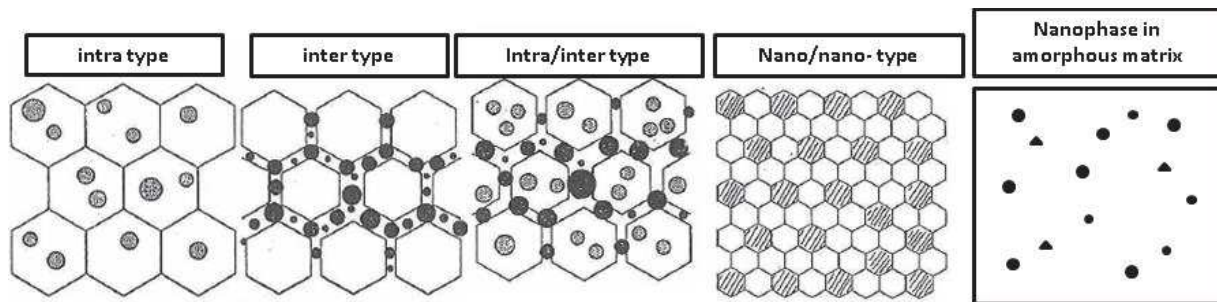


Figure 1.18 Classification of Ceramic nanocomposites according to Niihara

The fifth part was added by Veprek and Reiprick²³² when then developed super hard coatings using precipitated nanocrystalline TiN in an amorphous Si₃N₄ matrix, which is the type of nanocomposite of particular interest to us. This type of ceramic matrix nanocomposite shows extremely high values of strength which is a requisite for catalyst supports working in harsh environments, as those we target. The mechanical strength of brittle and ductile materials depends on the formation and propagation of dislocations and cracks^{233,234}. Elastic modulus of the material controls the stress needed to form and propagate both the dislocations and cracks²³³. Although there are other factors like the type and shape of dislocations and cracks which also influence the stress required, in general we can say that the strength of material increases with increasing modulus. The hall petch model gives a mathematical formulation of the strength of materials. It suggests that smaller grain sizes are preferred for higher

strengths. Strength of a material also increases due to precipitation hardening where a dislocation is pinned when it encounters a hard precipitates. A simple analysis yields the Hall-Petch relationship between the strength in terms of the critical stress σ_c and grain size^{233,235,236}.

$$\sigma_c = \sigma_0 + k l^{-1/2}$$

The hall petch relationship is valid only for sufficiently large grains (>100 nm)^{237–239} which can accommodate dislocation source hence it can be used to explain the exceptionally large strength values for these nanocomposites with nanocrystalline precipitates in amorphous matrix. Koehler²⁴⁰ suggested that two epitaxial heterostructures, one with high elastic modulus and other with lower elastic modulus, can lead to enhancement in strength. This was based on the argument that frank-read source multiplication of dislocation cannot operate in thin layers and the dislocation formed in the layer with lower elastic modulus will stay trapped in the same layer as it will be opposed by its mirror image when it tries to cross the interface between the two layers. Koehler extended his argument and that this mechanism will work even if one of the layers is amorphous. The amorphous material has further advantage that it can easily accommodate any strain due to lattice mismatch due to randomly oriented crystalline material in an isotropic composite.

4.2. PDC-based strategies to design ceramic nanocomposites

PDC nanocomposites can be made from different route. Interrante *et al.*²⁴¹ suggested two routes, firstly from direct reaction between two preceramic polymers and secondly from a single source preceramic precursor. Paine *et al.*²⁴² in their review extended this by adding a work of Seyferth *et al.*²⁰⁴, regarding synthesis of nanocomposites by adding various active or passive fillers to preceramic polymers. In this section we discuss these various synthesis techniques briefly.

4.2.1. Addition of fillers to preceramic polymers

The polymer-to-ceramic conversion is inevitably accompanied by the release of gaseous by-products, which causes a more or less important weight loss (generally not lower than 15%) and an overall volume shrinkage of the component (can reach 70%). The addition of filler as a secondary phase within the polymer can offset this shrinkage and thereby prevent a catastrophic failure of the component. There are two types of fillers. Passive fillers remain

totally inert during the whole polymer-to-ceramic conversion. They do not undergo any transformation or evolution during the heat treatment and do not react with the ceramic residue of the preceramic polymer, or with the gaseous by-products released during pyrolysis or the treatment atmosphere. Their only function is to diminish the percentage of the whole volume that evolves during the pyrolysis step, thus reducing the total weight loss, shrinkage and generation of cracks, as well as to favor the escape of gaseous species by the creation of an easier means of escape. Figure 1.19 shows a schematic representation of the passive filler in a preceramic polymer.

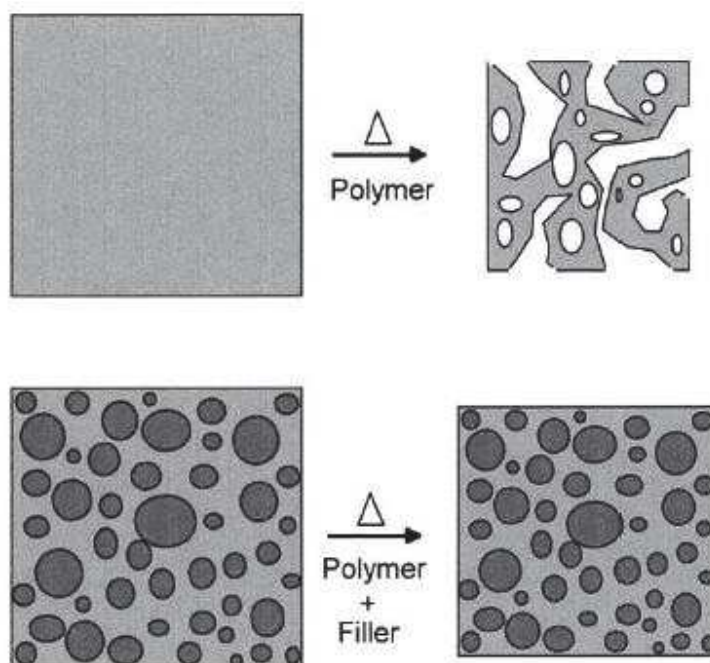


Figure 1.19 Schematic representation of controlling shrinkage using passive filler

Typical examples of passive fillers for preceramic polymers can be micro or nanopowders of SiC or Si₃N₄²⁴³. Katsuda *et al.* suggested use of nano-sized fillers like multi-walled carbon nanotubes for increasing the fracture toughness of polymer derived ceramics²⁴⁴.

The CTE (coefficient of thermal expansion) of the filler phase is also of fundamental importance, since it determines the global CTE of the final composite. A tailorable CTE could be useful in applications such as coatings (e.g. on metals), but it should be noted that a high CTE mismatch between the ceramic residue and the filler(s) could cause the formation of micro-cracks that could have detrimental effects on the final mechanical properties.

The concept of active or reactive fillers was introduced in the early 90's by the work of Greil *et al.* and Seyferth *et al.*^{245,246}. It was carried on further by Paine *et al.*. These fillers permit the obtainment of a near-net-shape conversion of preceramic polymers into bulk components with extremely limited (or even absent) global shrinkage. Active fillers can increase their volume during pyrolysis by reacting with gaseous species released from the polymer decomposition, or by reacting with the atmosphere of the furnace, thus effectively compensate the polymer shrinkage. In some cases as shown by Seyferth *et al.*, the choice of temperature and atmosphere along with reactive filler can lead to formation of different phases. As in case of tungsten (W) powder in a polysilazane (W:Si = 5:3) leads to formation of WC and W₅Si₃ at 1500°C under Ar but the same system under NH₃ till 800°C and then under Ar till 1500°C resulted in the formation of only W₅Si₃. Another important aspect of this study was complete absence of Si₃N₄ in the presence of W which is otherwise the primary reaction product from the used polysilazane under NH₃. Even in Si rich ratios formation of Si₃N₄ was completely suppressed by presence of W. Thus it was shown that presence of various metallic active fillers can lead to various effects on the phases formed. Apart from these nanosized filler can also be used as active fillers in oxynitrides and silicates as shown by Bernardo *et al.*²⁴⁷.

4.2.2. Mixed precursors and polymers

This method involves mixing precursors of two different ceramics homogeneously as a neat liquid as suggested by Interrante *et al.*²⁴¹ followed by pyrolysis. They suggested a “hot drop”^{248,249} approach which involves a rapid pyrolysis of the mixture of preceramic polymers by dropping it onto a preheated surface. For mixture compositions where the phase separation may not an issue lower heating rates could be employed. Interrante *et al.* used this procedure for synthesis of AlN/SiC composite using [Et₂AlNH₂]₃ and SiC forming precursors like vinylic polysilane (VPS), methylhydridopolysilane (MPCS) or hydridopolysilane (HPCS)²⁴¹. Nanocrystalline composites of 2H AlN and β-SiC and 2H solid solutions of SiC/AlN can be obtained as products of the pyrolysis, depending on the specific pyrolysis procedure (hot drop vs. direct pyrolysis) and precursor combination employed. In any case, following annealing of the ceramic powders at 1600 °C, the crystallite sizes were less than 500 nm and typically on the order of 10-50 nm. They have also blended VPS with [Et₂AlNH₂]₃ and pyrolyzed the mixture under NH₃²⁴¹. This results in formation of Si₃N₄/AlN composites with grain sizes of 40-80 nm. The crystallinity and phase of the grains varied greatly with processing and annealing conditions. Similarly, mixtures of VPS with

polyborazinyamine (PBZA)²⁵⁰ gave a precursor that, upon pyrolysis, gave Si₃N₄/BN composites²⁵¹. Sneddon *et al.* blended liquid borazine with hydridopolysilazane (HPZ), and pyrolysis of the resulting polymer gave boron containing β-Si₃N₄/β-SiC composites in which the crystallization is again suppressed by BN²⁵².

The main issue using this method is separation of phases if the pyrolysis rates are not high enough, which generally is the case of component/ shaped ceramic processing. Ceramic composites prepared using this method require conventional powder processing routes for component production which can cause grain growth during high temperature processing leading to inferior properties.

4.2.3. Single-source precursors

Due to the need to avoid phase separation and easy processability, Interrante *et al.* suggested to form single source molecular compounds that contain all the necessary elements of the desired composite in requisite proportions. This process involves deliberate construction of very distinct molecular moieties which contain the compositional elements in specific stoichiometric combination or reactions of preformed polymers or molecular species. By controlling the pyrolysis temperature, atmosphere and heating rate we can control the phase distribution and crystallite size of the composite formed. Apart from providing a homogeneous distribution of elements this process allows us to obtain an easily processable precursor which could be used for developing coatings, fibers or monolithic structures.

Using the single-source precursor route, Interrante *et al.*²⁴¹ synthesized SiC/AlN composite in effort to have improved homogeneity over mixed precursor route. They reacted cyclotrisilazane with triethylaluminium and formed a polyaluminosilazane (PAS). These single-source precursors are generally formed by condensation reactions between the most reactive groups of the reactants. In this case N-H of the polysilazane reacts with the organoaluminum compound forming a new Al-N bond which forms a part of the backbone of the single source precursor as well as the ceramic. Different properties like rheology of the polymer and yield of the ceramic can be controlled by adjusting the ratio between the two reactants. Heating PAS-derived composites to 1600-1800°C produced 2H-SiC/AlN following pyrolysis in N₂ or α-, β-Si₃N₄ /AlN if pyrolysis was done in NH₃. Nanocrystallites (5-500 nm) were typically observed in samples that were poorly crystalline by XRD powder patterns. They also prepared other nanocomposite systems like AlN/BN, TiN/BN, TiN/AlN and

Si₃N₄/BN and investigated the effects of various parameters. Hence this method offers great control over the synthesis of the final ceramic and allows tailoring properties at the molecular level. The focus of this thesis is using the single source precursor strategy to develop silicon and boron-based nanocomposites through modification of the Si₃N₄, Si-C-N and BN precursors described previously with transition metals such as titanium (Ti), zirconium (Zr) and hafnium (Hf).

4.3. Transition metal-containing PDC nanocomposites

4.3.1. Si-based nanocomposites through modification of organosilicon precursors with transition metals

Three systems are considered here: the Si-M-C, Si-M-C-N and Si-M-N systems.

- The Si-M-C system

The term polymetallo(carbo)silane²⁵³ refers to a class of polymers composed of Si, C, H and sometimes O as well as a metal M (Ti, Zr, Hf). They can be synthesized by reacting transition metal-based molecular precursors like metallocenes (dichlorometallocenes) and/or metal tetrachlorides with SiC precursors like polycarbosilane (HPCS, AHPCS, etc.). Table 1.9 shows an overview²⁵⁴⁻²⁶⁴.

Table 1.9 Different ceramic systems obtained depending on metal precursor

Polymer	Precursor	Products
Polycarbosilanes	(C ₅ H ₅) ₂ MCl ₂ MCl ₄ / MOCl ₂	MC/SiC
	M(CH ₂ C ₆ H ₅) ₄	Si _x C _y M _z
	M(X) ₄ X=OCH ₂ CH ₂ CH ₂ CH ₃ /CH ₃ COCHCOCH ₃	SiC/MC/C/MSi

The reaction mechanism depends on the nature of the metal precursor. In the first case there is a direct reaction between the two precursors, the metallic precursor reacts directly with polycarbosilane via the chlorinated groups of the metal precursor and the Si-H bonds of the polycarbosilane thereby by removing the chloride with hydrogen. This reaction was evidenced by Amoros *et al.*²⁵⁹ when they showed the reaction via three dichlorides of metallocene and

polycarbosilane according to the following reaction. The heat treatment under an argon atmosphere resulted in the formation of nanocomposite MC/SiC.

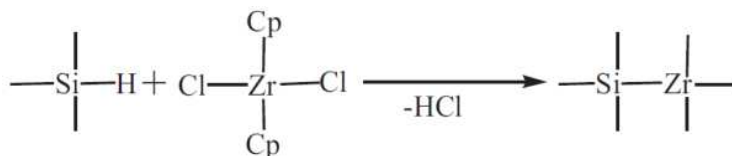


Figure 1.20 Removal of excess chlorine to synthesize non-oxide polymers

Zhaoju *et al.*^{260,261} used the same reaction with dichloride of titanocene to generate a TiC/SiC type nanocomposite from the AHPCS (Figure 1.21). However, some chlorinated residues can be found in the polymer thereby altering the properties of the final ceramic nanocomposites. Recent studies have allowed the synthesis of precursor non-oxide polymers containing zirconium and silicon by using organolithiols by metathesis, in order to eliminate the residual chlorine, reaction represented by Figure 1.20.

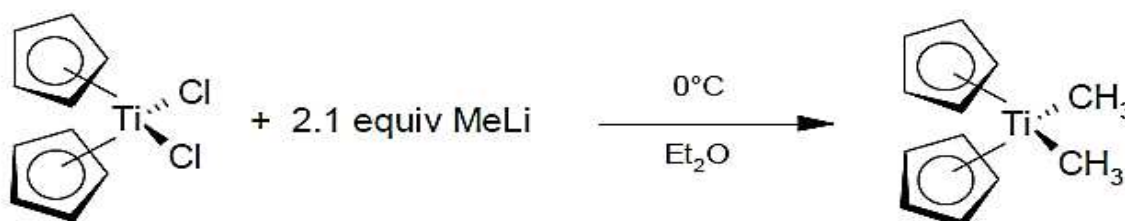


Figure 1.21 Synthesis of Cp₂TiMe₂

The Cp₂TiMe₂ was synthesized for the first time in 1956 by Clauss and Bestian, starting from a titanocene and 2.1 equivalents of methyllithium in diethyl ether. This reaction represents the synthesis of Petasis reagent by metathesis of a methyllithium and a titanocene dichloride. Grignard reagents are also used for the synthesis of Petasis reagents²⁶⁵. Here the primary use of Petasis reagents based on Ti or Zr and the use of the Grignard reagents of type RMgCl or RMgBr, the objective is twofold: substitute the chlorinated groups of the metallocene dichlorides by the groups of reagents like alkene, vinyl, allyl type, etc. in order to react them with the functional groups of the polycarbosilane and eliminate the residual chlorine by forming solid by-products of type MgCl₂ or MgBr₂ easily separable from the final product. Other parameters are important in the development of such nanocomposites like the ratio molar ratio between the precursor and the preceramic polymer as well as the temperature and the pyrolysis atmosphere. The crystalline phases obtained will therefore be influenced

by the molar ratio chosen; an example is given in Figure 1.22. In the case of Ti-Si-C ternary system which has different phase compositions at two temperatures of 1100 and 1300°C.

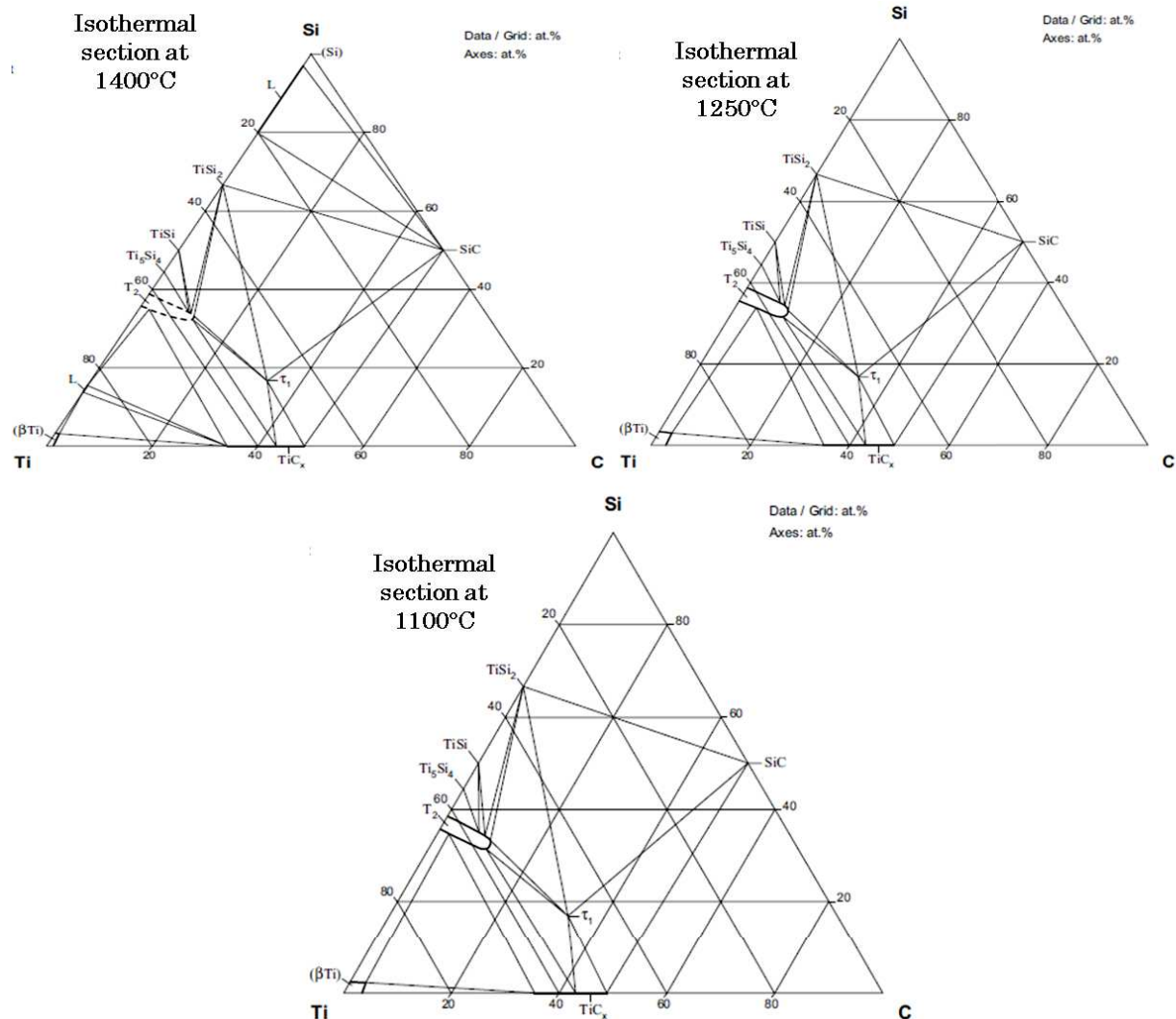


Figure 1.22 Equilibrium phases of Si-Ti-C systems²⁶⁶

- The Si-M-C-N system

The characteristic features of the Si-based non-oxide ceramics include their resistance to crystallization and the high thermal and chemical stabilities. Wide ranging applications are observed for these materials including high performance coatings, sensors, nanocomposites and fibers. The potential of these materials, for instance in energy technologies, can be extended by the incorporation of metallic or intermetallic nanoparticles/phases. Late transition metals form metallic particles or phases during pyrolysis due to the reductive conditions in combination with their noble character, and they are highly relevant for

catalytic applications. This system includes both MCN/SiC type nanocomposite and npM/SiCN (metal nanoparticle in SiCN matrix) nanocomposite. In the first type we have a SiC matrix with metal carbonitride nanoparticles inside it, like the works of Ionescu *et al.*²⁶⁷ on high temperature ceramic nanocomposites $\text{HfC}_x\text{N}_{1-x}/\text{SiC}$, while second type includes systems which have a SiCN matrix with metal nanoparticles embedded in the matrix like Pt/SiCN²⁶⁸ system studied by Zaheer *et al.* and Fe/SiCN^{269,270} system studied by Francis *et al.* and Li *et al.*

For the first type, Wen *et al.*²⁶⁷ designed a one pot synthesis technique to generate $\text{HfC}_x\text{N}_{1-x}/\text{SiC}$ nanocomposites as ultra high temperature ceramic. The purpose of preparing this nanocomposite was to exploit its high hardness, high elastic modulus, chemical stability, and electrical conductivity and relatively high thermal conductivity even under extremely harsh environments^{271–274}. It is known that the preparation of HfC using conventional route faces problems in densification due to low self diffusion, grain growth at high temperature and low stability in oxidative environments^{275–283}. Encapsulation of this in an amorphous matrix of SiC overcomes these problems but such a system can only be prepared using precursor routes. The nanocomposite was prepared by reaction between AHPCS and tetrakis(dimethylamino)Hafnium(IV) (TDMAH) precursor. The polymer to ceramic conversion was carried out under argon atmosphere at 1100°C. The ceramic nanocomposite powder was then further converted into a monolith using Spark Plasma Sintering. Based on solid state ¹³C and ²⁹Si NMR studies, Wen *et al.* established that the reaction pathway between AHPCS and TDMAH involved two types of reactions: the allyl and Si–H groups of SMP10 are involved in hydrosilylation, which leads to an increased crosslinking degree of the precursor; additionally, TDMAH reacts with the Si–H groups of AHPCS to form Si–N–Hf linkages and gaseous CH₄. This is depicted in the Figure 1.23²⁶⁷.

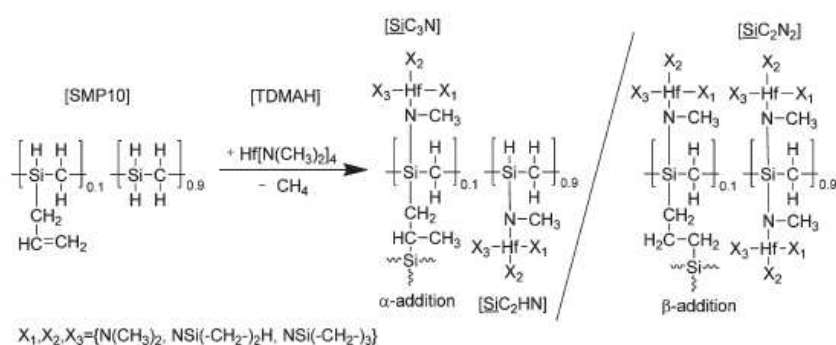


Figure 1.23 Two possible reaction pathways for reaction b/w AHPCS and TDMAHf

The high temperature behavior of these samples was found to be very interesting. At 1400°C the $\text{HfC}_x\text{N}_{1-x}$ was found encapsulated in a 2-4 nm thick layer of turbostratic carbon. These second phase nanoparticles were uniformly distributed throughout the matrix with a particle size of 8 nm at 1400°C to 37 nm at 1700°C. The very low increase in grain size was attributed to the surrounding carbon layer which is known to act as a diffusion barrier^{284,285}. The SPS sintered nanocomposite monolith was found to have a higher electrical conductivity of 136 S cm^{-1} over a Hf free SiC monolith due to the presence of nano $\text{HfC}_x\text{N}_{1-x}$ and carbon which provide it metallic properties.

Additionally further work was done to increase the high temperature oxidation behavior of this nanocomposite system by addition of B to the system. The work done by Yuan *et al.* involved use of commercially available HTT1800 polymer to produce the matrix instead of AHPCS and the dimethyl boron sulfide was added to the reaction mixture as the boron source²⁸⁶. Figure 1.24 shows the reaction pathways that could have occurred.

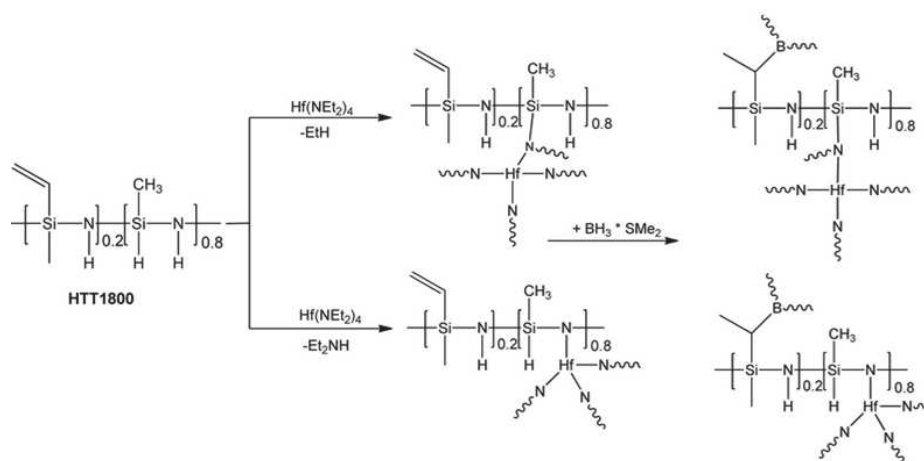


Figure 1.24 Reaction pathway for reaction b/w HTT1800 and TDMAHF²⁸⁶

Different ratios were synthesized and the polymer to ceramic conversion was carried out under two different gases, Ar and N_2 , to compare the prepared ceramics. It was observed that at 1700°C there was an amorphous matrix of SiBCN with HfC(N) nanoparticles distributed across the matrix. In both argon and nitrogen atmospheres, high temperature annealing of SiHfBCN leads to ceramic nanocomposites with interesting phase compositions (i.e., HfC(N)/HfB₂/SiC in argon and HfNC/Si₃N₄/SiBCN in nitrogen), which are expected to be promising candidates for applications at (ultra)high temperatures and under extreme environmental conditions.

The second system npM/SiCN (metal nanoparticle in a SiCN matrix), were prepared by reacting a coordination compound (metal complex) of late transition metals with a polymeric preceramic precursor²⁸⁷. The metal transfer from the complex to the polymer chain leads to formation of a metal modified precursor which upon pyrolysis converts to metal containing PDCs. For this purpose polysilazanes containing vinyl and Si-H bonds were chosen so that the presence of all these reactive sites allows better incorporation of metal atom in the polymer chain. The formation of a covalent bond between the metal atom and polymer chain is important to avoid loss of metal atom via sublimation during pyrolysis. This technique also allows broad dispersion of metal atom, wide applicability (easy availability of various metal coordination complexes) and use of commercially available polymers. One of the earliest nanocomposite prepared using this was Fe@SiCN system by reaction of FeCl₃ and polysilazane followed by pyrolysis under ammonia, nitrogen and argon^{269,270}. Along with low ceramic yields, contamination from left over FeCl₃ posed a problem. Francis *et al.* milled Fe powder along with Ceraset™ cross-linked at 280°C and the milled mixture was warm pressed before being pyrolyzed to a ceramic. XRD of the samples showed formation of crystalline phases are Fe₃Si, Fe₅Si₃, and SiC. The crystallization of SiC was assumed to occur from the liquid Fe–Si–C alloy being formed during the molten state of silicides at 1300°C. Further work was carried out by Riedel *et al.* when then used HTT1800 as the polysilazane and modified it using a Ni(II) complex. This resulted in formation of nanoporous silicon oxycarbonitride ceramic modified by Ni nanoparticle²⁸⁸. Furthermore Kempe *et al.* developed a aminopyridinato²⁸⁹ metal complex using metals from late transition series like Pt²⁶⁸, Ir²⁹⁰, Ru₂Pd²⁹⁰, Cu²⁹¹, Pd²⁹² etc. The copper aminopyridinato complex [Cu₂Ap₂^{TMS}] coordination compound undergoes a metal transfer reaction with the PSZ, here HTT1800, with the release of Ap^{TMS}H. After cross-linking with dicumylperoxide (DCP) at 120°C the preceramic green body is formed (Figure 1.25). Pyrolysis results in an amorphous SiCN ceramic enhanced by Cu nanoparticles (Cu@SiCN).

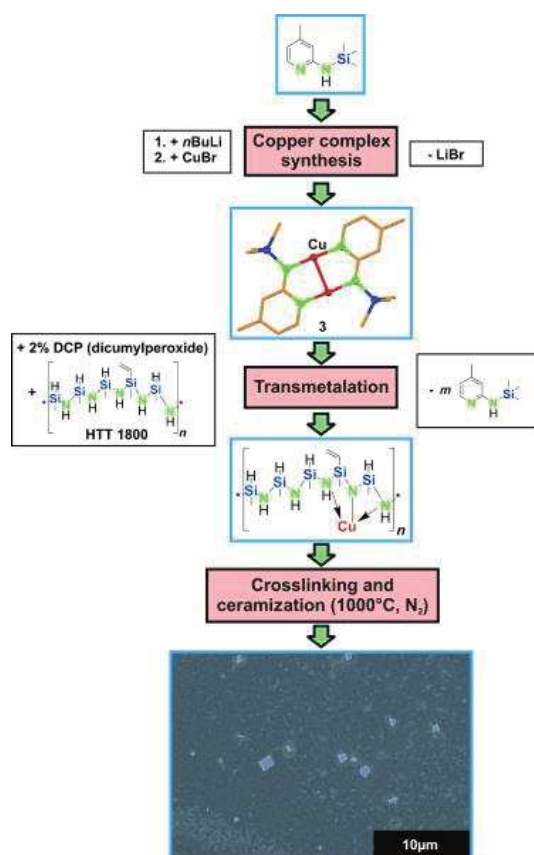


Figure 1.25 Synthesis of Cu nanoparticles doped SiCN²⁹¹

Sachu *et al.*²⁶⁸ prepared a hierarchically mesoporous Pt@SiCN system using a similar technique but also added a sacrificial filler in the synthesis which would generate mesoporosity. It was observed that the size of metal nanoparticle increases with increase in the content of the metal aminopyridinato complex. Wiesner *et al.*²⁹³ developed a highly innovative bottom-up approach to fabricate porous SiCN ceramics with integrated platinum nanoparticles. The material was structured through a combination of micromolding and multicomponent colloidal self-assembly. The coordination compound $[(\text{cod})\text{PtMe}_2]$ (COD = 1,5 cyclooctadiene) was used as a platinum precursor. Heat treatment (1000°C under inert atmosphere) resulted in hierarchically structured porous ceramic material functionalized with Pt nanoparticles. The nanostructuring of these metals in the metal enhanced SiCN nanocomposite leads to development of properties like superparamagnetism and ferromagnetism in these materials. Kempe *et al.* extensively used these nanocomposites in heterogeneous catalysis application. As a proof of concept we did performed a preliminary investigation on Pt/SiCN nanocomposites as catalyst in the hydrolysis of NaBH_4 to generate H_2 . This will be discussed in perspectives.

- The Si-M-N system:

Most of the early work done on ternary system like Si-M-N system was mainly focused on these systems developed by techniques like CVD and rarely used single source precursor route. Ternary Si-M-N materials exhibit outstanding high-temperature stability as well as good mechanical and interesting electrical properties^{294,295}. Thus, Si-M-N ceramics such as Si-Ta-N, Si-Mo-N, Si-Ti-N and Si-Hf-N exhibit effective work function values in the range of 4.16 to 4.8 eV²⁹⁶ and high dielectric constants ($\epsilon = 5-15$, dielectric constant values changed with the variation of metal and silicon content)^{297,298} making them attractive candidates for e.g. nano/micro electro mechanical systems (NEMS/MEMS). The single source precursor route leading to MN/Si₃N₄ nanocomposites was first investigated by Iwamoto *et al.* This was offered a much better homogeneity in composition and properties over the work of Wang *et al.*²⁹⁹ where they used Si₃N₄ powder and Ti(OBu)₄ as in situ source of Ti. Ziegler *et al.*³⁰⁰ explored the use of polytitanosilazanes for synthesis of a hybrid nanoscale composite system of SiC/Si₃N₄-TiC/TiN. The polymer to ceramic conversion was carried out under N₂ at 1000°C. They used 3 different types of polysilazanes to study their effect on the state (liquid or solid) of the polymer. They observed that for all three polysilazanes the polymer was liquid for smaller (<4) Si/Ti ratio, solid for intermediate ratios (4<Si/Ti<15) and again liquid for all higher ratios. They extensively studied the reaction occurring between the TDMAT and the polysilazanes. They concluded that below the Si/Ti atomic ratio of 2 the reaction would not be complete as the high number of adjacent [Ti(N(CH₃)₂)₂] attached to the polysilazane backbone result in steric hindrance. While as they increased the Si/Ti atomic ratio above 13 the reaction mixture was less and less polytitanosilazane and primarily unreacted polysilazane. Thus they concluded that only between 3 to 8 Si/Ti atomic ratios was it possible to obtain the hybrid nanoscale composite system.

Using PHPS as matrix precursor and tetrakisdimethylaminotitanium (TDMAT) as nanophase precursor, Iwamoto and Sato both proposed a highly cross-linked structure for polytitanosilazane with N-Ti-N bridges as shown in Figure 1.26.

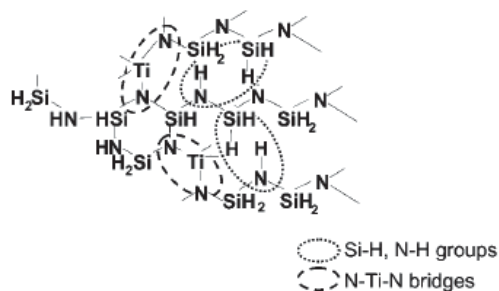


Figure 1.26 Cross-linked structures for polytitanosilazane

The ratio between Ti/Si in these systems has a lot of effect on the microstructural composition of the ceramic. Iwamoto *et al.*³⁰¹ observed that for Ti/Si ratios greater than 0.1 lead to a stable amorphous Si_3N_4 matrix till 1400°C which is not the case with ratios smaller than this and in absence of Ti from the system. The same was observed by Sato *et al.*³⁰² when they studied the low temperature crystallization of this system. Ionescu³⁰³ changed the metal in the ternary system from Ti to Hf and performed pyrolysis of these polymers with different ratios to generate Si_3N_4 -HfN system. Figure 1.27 gives the illustration with reaction between PHPS and (tetrakis(dimethyl)amino)Hafnium. The reaction can occur at the either the N-H bond or the Si-H bond. Although the spectroscopy study by Ionescu *et al.*³⁰³ suggests that the reaction is generally faster at the N-H bond (a) given its more reactive nature.

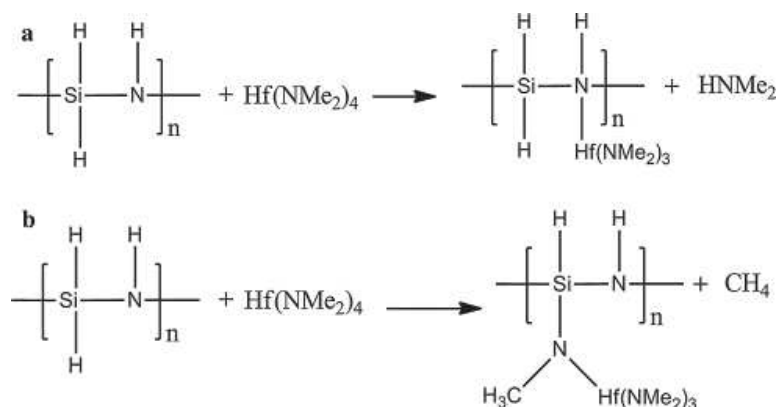


Figure 1.27 Possible parallel pathways of the reaction between TDMAH and PHPS

The crystallization of Si_3N_4 matrix was pushed from 1300°C to 1600°C as the content of Hf in the system increases. Figure 1.28 shows the effect of increasing Hf content in the Si-Hf-N system on the microstructural composition. The mass ratio of Hf:Si ratio was increased from 2:98 (SiHfN-1), 30:70 (SiHfN-3).

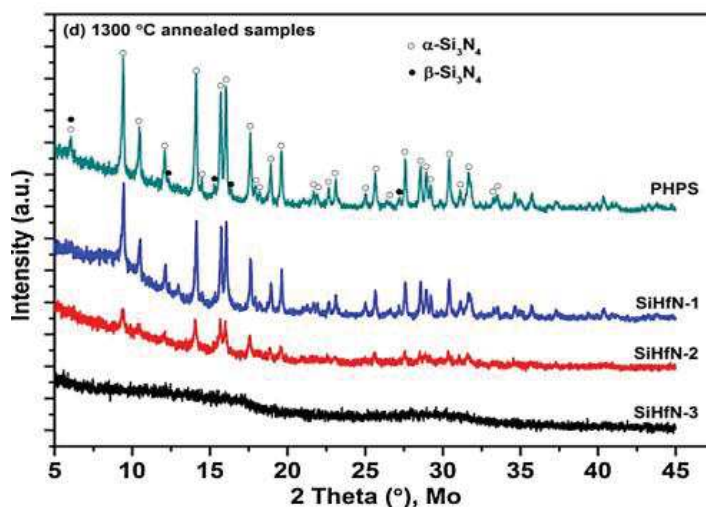


Figure 1.28 Effect of Si/Hf ratio on microstructure of nanocomposite³⁰³

Another interesting observation made by Ionescu *et al.*³⁰³, Sato *et al.*³⁰², and Iwamoto *et al.*³⁰¹ was the crystallization of only α - Si_3N_4 when using PHPS as the matrix forming polymer.

Since the PhD thesis of Mirna Chaker Bechelany, our group has explored these materials for different applications. We firstly demonstrated the high potential of preceramic polymers to generate dense structures made of TiN nanocrystals homogeneously dispersed in an amorphous structure of Si_3N_4 to propose very high hardness and Young's modulus³⁰⁴. Here, we have investigated the chemistry behind the preparation of Si-M-N ceramics (with M as Ti, Zr, Hf) (Chapter 4) as well as their use as supports for platinum nanoparticles to be used in the hydrolysis of NaBH_4 (Chapter 5)

4.3.2. B-based nanocomposites through modification of borazine, polyborazylene and ammonia borane with transition metals:

Polymer derived nanocomposite ceramics based on boron nitride and transition metal nitrides have not been discussed much in the literature although a lot of work has been done on nanocomposite systems like BN/ Si_3N_4 , BN/SiC, BN/Carbon based 2D materials etc. These have been extensively used as structural materials due to the high strength and high temperature stability provided by BN to the matrix or has been used to remove organic/inorganic pollutants in the case of BN/Carbon based 2D materials.

Very recently some attention has been focused on preparing a nanocomposite with BN and transition metal nitride, more specifically Tantalum Nitride (Ta_3N_5)³⁰⁵. Tantalum nitride (Ta_3N_5), with Ta^{5+} in the preferable d0 electronic configuration, has attracted tremendous

attentions due to its suitable band gap position for overall water splitting and visible light absorption³⁰⁶⁻³⁰⁸. However, Ta₃N₅ photo-catalyst usually suffers from recombination of photo-generated electron-hole pairs and poor stability due to self-oxidation by photo-generated holes^{305,309}. Liu *et al.*³¹⁰ noted that the presence of a low light responsive and optically inert support like SiO₂ lead to suppressed aggregation of Ta₃N₅ nanoparticles during high temperature nitridation process, improved photocatalytic activity and improved dispersion of photo-catalyst in the solution. In the same way, hexagonal BN (hBN) with its optical inertness and chemical durability and more importantly its negatively charged surface lead to efficient charge carrier separation in other nanocomposite photo-catalysts systems like BN powders/TiO₂³¹¹, BN fibers/TiO_{2-x}N_x³¹², BN nanosheets/BiOBr³¹³ and BN nanosheets/In₂S₃³¹⁴ etc. These systems have also shown superior photocatalytic activity on dye degradation. Wang *et al.* predicted that porous hBN fibers are assumed to be an efficient support of the adsorption-enhanced heterocatalysts, which cannot only promote the transfer of holes and subsequently suppress the oxidative deactivation of Ta₃N₅, but can also adsorb the reactants in the liquid phase to the surface of photocatalysts. It is predictable that the heterostructure photocatalysts based on porous BN fibers labeled BN_f should exhibit good photocatalytic performance. They were able to prepare Ta₃N₅/BN_f nanocomposite with Ta₃N₅ having spherical morphology and a diameter of 10 nm. The specific surface area of Ta₃N₅/BN_f composites was much higher than that of pure Ta₃N₅ nanoparticles. The absorbance of Ta₃N₅/BN_f composites to visible light gradually decreased with increasing the content of BN_f in the composites. By comparison with pure Ta₃N₅ powders, both the photocatalytic activity and stability of Ta₃N₅/BN_f composite were significantly enhanced. The negatively charged BN_f support can not only effectively enhance the separation of photogenerated electrons and holes, but also acts as the efficient adsorbent to dye molecules. Even with such good performance these materials face the economic challenge of being too costly due to the use of Ta. We propose the use of early transition element based nitrides like TiN³¹⁵, which has both electronic and photocatalytic activities similar to Ta₃N₅ while ZrN³¹⁵ has electronic properties similar to Ta₃N₅ and can be easily synthesized in a nanocomposite with BN matrix using single source precursors.

We have investigated the chemistry behind the preparation of B-M-N (M: Ti, Zr, Hf) ceramics in chapter 3 before their preparation as mesoporous monoliths in chapter 5. Because a large

part of the thesis has been focused on the design of mesoporous components, the next section describes the strategy to design mesoporosity in PDCs.

5. The PDC route towards the design of mesoporous components

In general, the specific surface area, the pore volume, the arrangement and type of the porosity as well as the Lewis and/or Brønsted acidity of materials are primarily considered when selecting a support for catalysts or electrocatalysts as well as an electrode material. The mechanical strength and especially the chemical resistance towards the reaction medium are not always viewed as the most important properties.

A lot of work has been done with regard to developing polymer-derived porous ceramics. The applications of porous ceramics are not only dependent on the chemical composition of porous scaffold but also on the pore size distribution (PSD), tortuosity, specific surface area (SSA), closed/open (3D interconnectivity), etc., which all are determined by the selected manufacturing process. For example, while high surface area (provided by micro- (<2 nm) and meso- (2–50 nm) pores) gives the functionality to the component, macroporosity (50 nm to several mm) improves heat and mass transfer. For the envisioned applications, we targeted mesoporous materials. There are three methods to develop the mesoporosity of polymer-derived ceramics.

5.1. Sacrificial fillers

Highly porous ceramics can be obtained by homogeneous dispersion of a solid sacrificial filler (in form of a micro or nanosized beads/particles generally made of organics or natural salts) throughout the preceramic polymer by stirring or ball milling^{316, 317}. Upon heat treatment these fillers are generally decomposed and leave behind microstructure with pores. Depending on the filler loading the porosity can vary anywhere from 20 to 90% and can also be percolating network of interconnected porosities. Template removal always produces dense and thick struts, resulting in, generally speaking, enhanced mechanical properties with respect to those of components obtained via the replica technique, in some cases compressive strengths of up to 30 MPa were reported depending on the amount of porosity³¹⁶. Figure 1.29 shows a schematic of the process.

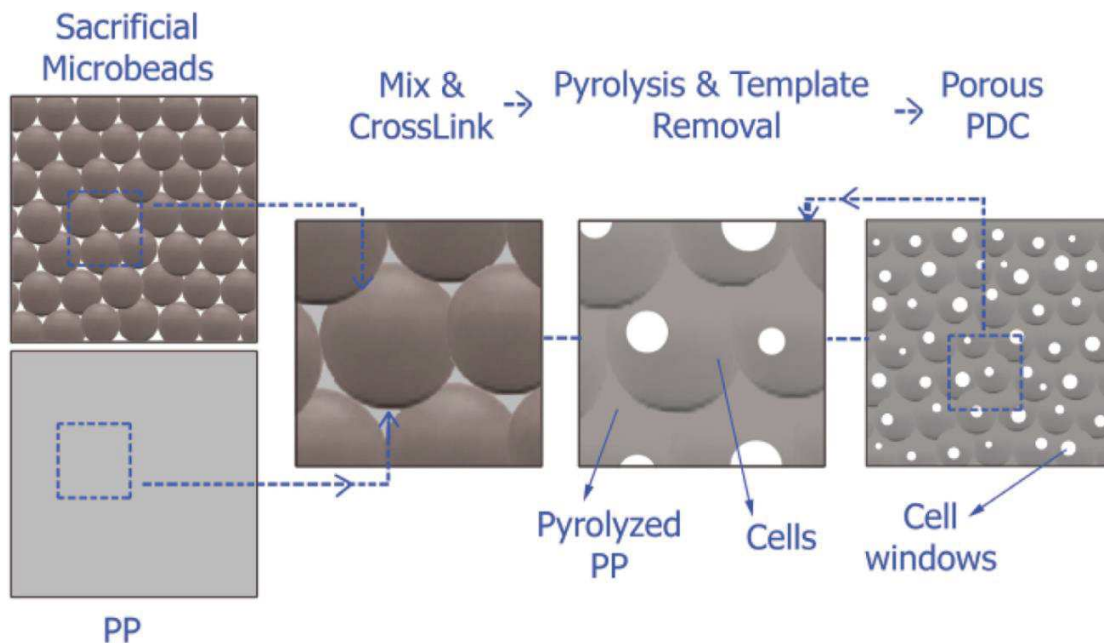


Figure 1.29 Creating porous structure using sacrificial fillers³¹⁷

5.2. Soft templating

A lot of pioneering work has been done with respect to using soft templating approach to generate porous ceramics with PDC route by use of wood, coral, polymeric foams, etc.^{318–320}. This route is suitable with preceramic polymers to generate macroporous cellular solids due to enhanced wetting and partial melting of cross-linked polymer during heat treatment. The final formed macroporous ceramic has a homogeneous crack free structure. As defined by Greil *et al.*³²¹, his approach is identified by the fact that the template is removed in the same step as the conversion of preceramic polymer to ceramic. Figure 1.30 shows the schematic of the process.

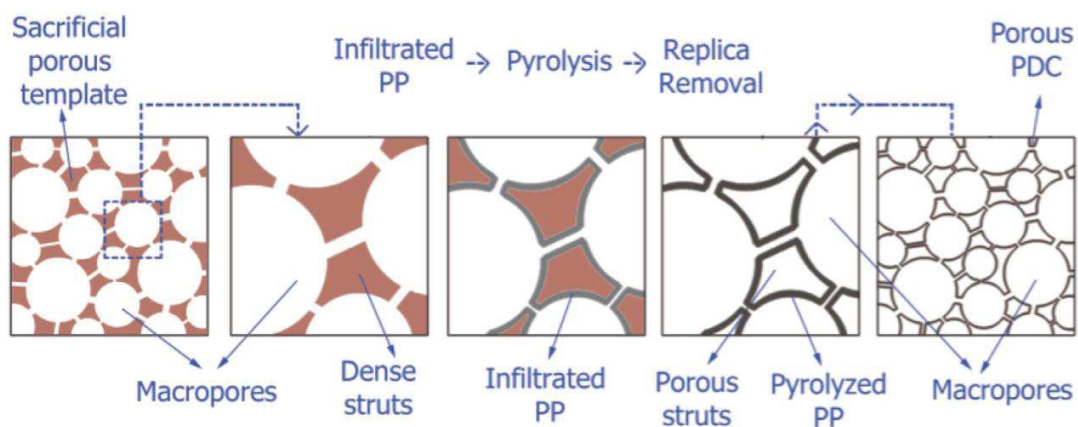


Figure 1.30 Schematic of Soft Templating approach

Polyurethane (PU) template has been used to generate SiOC foam with hierarchical macropore size ranging from 300 micrometer for infiltrating foam to 2500 micrometer for matrix foam³¹⁹. Similar SiOC foams with SiC nanowires were produced using PU template. Infiltration of the foam with a silicone resin and pyrolysis at 1400°C led to the formation of SiC NWs inside the pores, due to carbothermal reactions. The resulting foams had porosity and cell size in the 77–85 vol% and 400–600 nm range, respectively³²⁰. The shape and size of these porosities and the porous structure depend completely on the shape and surface structure of the template and the extent of infiltration of preceramic polymer in the template. Polysilazane was infiltrated into a porous polyethylene (PE) monolith, prepared from a polymeric bicontinuous microemulsion. The PSZ/PE composite was crosslinked and pyrolyzed (1000°C) to obtain nanoporous SiCN, with a pore diameter in the range of 60–100 nm and SSA of 24 m².gm⁻¹ ³²². Soft template can also be considered as the mixture of preceramic polymer and block copolymers as proposed by Wiesner³²³ in 2004. The idea behind the process is that a part of the block is soluble into the preceramic polymer and the other is not. Therefore, micelles are formed and this leads to mesoporous materials (usually ordered) after pyrolysis.

5.3. Hard templating

Hard templating approach is different from the previous method by the fact that an extra step is required to remove the template after the polymer to ceramic conversion to generate a porous structure. This step is either a pyrolysis under reactive atmosphere or leaching using an acid. This method is generally used to prepare highly ordered or disordered mesoporous ceramic. It is also known as nanocasting. Templates like SBA-15 and CMK-3 have been used to synthesize ordered mesoporous (OM) SiOC using polysiloxane³²⁴, OM-SiC using polycarbosilane³²⁵ with SSA (PSD) of 616 m².gm⁻¹ (3.3 nm) and 460-720 m².g⁻¹ (2 - 3.7 nm) respectively. In the first case the silica template of SBA-15 is removed by HF etching after conversion to ceramic and in the second case the CMK-3 is removed by using a reactive atmosphere of NH₃ at 400°C. Two or more templates can be used to form ceramics with extremely high SSA and very narrow pore size distribution. OM-SiC with SSA of 942 m².gm⁻¹ was synthesized by addition of triblock copolymer as binder to preceramic polymer with hard template of silica like KIT-6^{326–328}. Mesoporous SiBCN was prepared by direct nanocasting of a boron-modified PCSZ into OM-silica, followed by crosslinking, pyrolysis (1000°C/ 2h/ N₂) and HF etching^{329–331}. An open, continuous and highly ordered 2D hexagonal

SiBCN framework was produced. The SSA, pore volume and pore diameter were reported as $337 \text{ m}^2.\text{gm}^{-1}$, $0.55 \text{ cm}^3.\text{gm}^{-1}$, and 4.6 nm , respectively. Our group³³² used an integrated chemical route to synthesize micro/mesoporous BN monoliths. We initially prepared silica foams using sol–gel process, lyotropic mesophases and bilyquid foams as dual soft templates. These foams served as hard template to synthesize carbonaceous templates by impregnating them a carbon precursor followed by carbonization under an inert atmosphere. The silica template was then removed using HF and the carbonaceous template was then impregnated with BN precursor like polyborazylene and then converted in to ceramic under N_2 . The template was then removed under NH_3 in the subsequent step at high temperature. Bernard and co-workers³³³ used a similar process to generate micro/mesoporous BN, but instead of silica template they used fau type zeolite. This zeolite was impregnated and fixed with carbon at high temperature using a CVD process. The zeolite was then removed with HF and the carbonaceous template impregnated with polyborazylene. This was then converted to BN under N_2 followed by carbon template removal under NH_3 . Figure 1.31 shows a schematic representation of hard templating process.

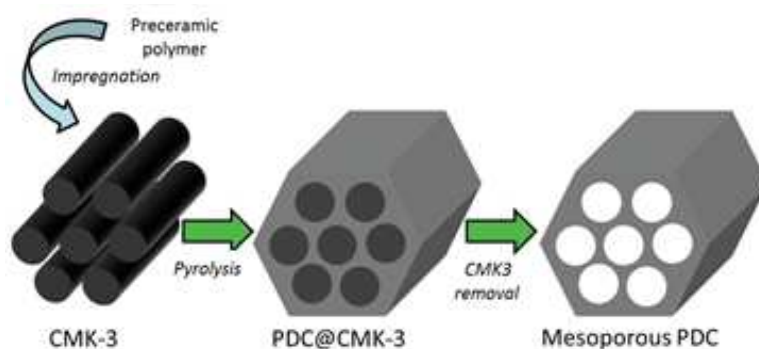


Figure 1.31 Schematic of Hard Templating approach

This approach has been majorly used to generate ordered or disordered mesoporous ceramics with interconnected porosities from preceramic polymers. We employed this approach using activated carbon monoliths to prepare 3D mesoporous BN, SiC, Si_3N_4 and Si-C-N ceramic monoliths and their nanocomposite to be used as supports in catalytic hydrolysis of NaBH_4 and as proof of concept, as electrocatalyst supports and electrode materials.

6. Conclusion

This chapter dealt with providing a literature survey of the electrochemical power sources and in particular are the two major issues that still limit their commercialization as fuel cells and supercapacitors, i.e., the hydrogen source, electrocatalyst support and electrode materials. With this context, we prepared non-oxide ceramics with high potential as supports for Pt for the hydrolysis of sodium borohydride to generate hydrogen on demand to fuel cells and as electrocatalyst supports and electrode materials in fuel cells and supercapacitors respectively. We provided a state of the art on synthesis of Si and B based carbide, carbonitride, nitride and their nanocomposites using the polymer derived ceramic (PDC) route. We focused our attention on the PDC route in this thesis due to its advantages to control the ceramic composition precisely, its ability to synthesize complex shapes and the relatively low processing temperature. The approach involves use of “single source” precursors to generate BN, SiC, Si-C-N, Si₃N₄ ceramics and their derived nanocomposite ceramics with in-situ growth of MN (M= Ti, Zr, Hf) nanocrystals in the matrix of before mentioned ceramics. This approach involves reacting two precursors, one being the precursor of the nanophase and the other that of the matrix. The synthesis is directed so that there is phase separation during crystallization where the nanophase emerges out of the amorphous or crystallized matrix. These materials are prepared as mesoporous components. Template impregnation has been discussed as the preferred process to design the mesoporosity in PDCs. These systems have potential applications technologies like fuel and supercapacitors and are discussed in thesis under the same purview.

References

1. S. Bagotsky, V., M. Skundin, A. & M. Volfkovich, Y. *Electrochemical Power Sources*. (John Wiley & Sons, Inc., 2014). doi:10.1002/9781118942857
2. Devanathan, R. Recent developments in proton exchange membranes for fuel cells. *Energy Environ. Sci.* **1**, 101 (2008).
3. Giddey, S., Badwal, S. P. S., Kulkarni, A. & Munnings, C. A comprehensive review of direct carbon fuel cell technology. *Progress in Energy and Combustion Science* **38**, 360–399 (2012).
4. Kulkarni, A. & Giddey, S. Materials issues and recent developments in molten carbonate fuel cells. *Journal of Solid State Electrochemistry* **16**, 3123–3146 (2012).
5. Grubb, W. T. & Niedrach, L. W. Batteries with Solid Ion-Exchange Membrane Electrolytes. *J. Electrochem. Soc.* **107**, 131–135 (1960).
6. Perry, M. L. & Fuller, T. F. A Historical Perspective of Fuel Cell Technology in the 20th Century. *J. Electrochem. Soc.* **149**, S59 (2002).
7. Zhang, L. L. & Zhao, X. S. Carbon-based materials as supercapacitor electrodes. *Chem. Soc. Rev.* **38**, 2520 (2009).
8. Hamilton, C. W., Baker, R. T., Staubitz, A. & Manners, I. B–N compounds for chemical hydrogen storage. *Chem. Soc. Rev.* **38**, 279–293 (2009).
9. Wang, P. Solid-state thermolysis of ammonia borane and related materials for high-capacity hydrogen storage. *Dalt. Trans.* **41**, 4296 (2012).
10. Huang, Z. & Autrey, T. Boron–nitrogen–hydrogen (BNH) compounds: recent developments in hydrogen storage, applications in hydrogenation and catalysis, and new syntheses. *Energy Environ. Sci.* **5**, 9257 (2012).
11. Moussa, G., Moury, R., Demirci, U. B., Şener, T. & Miele, P. Boron-based hydrides for chemical hydrogen storage. *Int. J. Energy Res.* **37**, 825–842 (2013).
12. Stephens, F. H., Pons, V. & Tom Baker, R. Ammonia–borane: the hydrogen source par excellence? *Dalt. Trans.* **100**, 2613–2626 (2007).
13. Peng, B. & Chen, J. Ammonia borane as an efficient and lightweight hydrogen storage medium. *Energy Environ. Sci.* **33**, 608 (2008).
14. Diyabalanage, H. V. K. *et al.* Calcium Aminotrihydroborate: A Hydrogen Storage Material. *Angew. Chemie Int. Ed.* **46**, 8995–8997 (2007).
15. Shrestha, R. P., Diyabalanage, H. V. K., Semelsberger, T. A., Ott, K. C. & Burrell, A.

- K. Catalytic dehydrogenation of ammonia borane in non-aqueous medium. *Int. J. Hydrogen Energy* **34**, 2616–2621 (2009).
16. Kim, S.-K. *et al.* Tetraglyme-mediated synthesis of Pd nanoparticles for dehydrogenation of ammonia borane. *Chem. Commun.* **48**, 2021 (2012).
 17. Jaska, C. A., Temple, K., Lough, A. J. & Manners, I. Transition Metal-Catalyzed Formation of Boron–Nitrogen Bonds: Catalytic Dehydrocoupling of Amine-Borane Adducts to Form Aminoboranes and Borazines. *J. Am. Chem. Soc.* **125**, 9424–9434 (2003).
 18. Chen, X. *et al.* Nitrogen-containing carbon nanostructures: A promising carrier for catalysis of ammonia borane dehydrogenation. *Carbon N. Y.* **68**, 462–472 (2014).
 19. Li, Z., Zhu, G., Lu, G., Qiu, S. & Yao, X. Ammonia Borane Confined by a Metal–Organic Framework for Chemical Hydrogen Storage: Enhancing Kinetics and Eliminating Ammonia. *J. Am. Chem. Soc.* **132**, 1490–1491 (2010).
 20. Tang, Z., Chen, X., Chen, H., Wu, L. & Yu, X. Metal-Free Catalysis of Ammonia-Borane Dehydrogenation/Regeneration for a Highly Efficient and Facilely Recyclable Hydrogen-Storage Material. *Angew. Chemie Int. Ed.* **52**, 5832–5835 (2013).
 21. Gutowska, A. *et al.* Nanoscaffold Mediates Hydrogen Release and the Reactivity of Ammonia Borane. *Angew. Chemie Int. Ed.* **44**, 3578–3582 (2005).
 22. de Jongh, P. E. & Adelhelm, P. Nanosizing and Nanoconfinement: New Strategies Towards Meeting Hydrogen Storage Goals. *ChemSusChem* **3**, 1332–1348 (2010).
 23. Li, L. *et al.* Lithium-Catalyzed Dehydrogenation of Ammonia Borane within Mesoporous Carbon Framework for Chemical Hydrogen Storage. *Adv. Funct. Mater.* **19**, 265–271 (2009).
 24. Kim, S.-K. *et al.* Palladium Catalysts for Dehydrogenation of Ammonia Borane with Preferential B–H Activation. *J. Am. Chem. Soc.* **132**, 9954–9955 (2010).
 25. Bluhm, M. E., Bradley, M. G., Butterick III, R., Kusari, U. & Sneddon, L. G. Amineborane-Based Chemical Hydrogen Storage: Enhanced Ammonia Borane Dehydrogenation in Ionic Liquids. *J. Am. Chem. Soc.* **128**, 7748–7749 (2006).
 26. Xiong, Z. *et al.* High-capacity hydrogen storage in lithium and sodium aminoboranes. *Nat. Mater.* **7**, 138–141 (2008).
 27. Xu, Q. & Chandra, M. Catalytic activities of non-noble metals for hydrogen generation from aqueous ammonia-borane at room temperature. *J. Power Sources* (2006). doi:10.1016/j.jpowsour.2006.09.043

28. Jiang, H. L., Singh, S. K., Yan, J. M., Zhang, X. B. & Xu, Q. Liquid-Phase chemical hydrogen storage: Catalytic hydrogen generation under ambient conditions. *ChemSusChem* **3**, 541–549 (2010).
29. Yadav, M. & Xu, Q. Liquid-phase chemical hydrogen storage materials. *Energy Environ. Sci.* **5**, 9698 (2012).
30. Jiang, H.-L. & Xu, Q. Catalytic hydrolysis of ammonia borane for chemical hydrogen storage. *Catal. Today* **170**, 56–63 (2011).
31. Xu, Q. & Chandra, M. A portable hydrogen generation system: Catalytic hydrolysis of ammonia–borane. *J. Alloys Compd.* **446–447**, 729–732 (2007).
32. Sanyal, U., Demirci, U. B., Jagirdar, B. R. & Miele, P. Hydrolysis of Ammonia Borane as a Hydrogen Source: Fundamental Issues and Potential Solutions Towards Implementation. *ChemSusChem* **4**, 1731–1739 (2011).
33. Umegaki, T. *et al.* Boron- and nitrogen-based chemical hydrogen storage materials. *Int. J. Hydrogen Energy* **34**, 2303–2311 (2009).
34. Chandra, M. & Xu, Q. Room temperature hydrogen generation from aqueous ammonia-borane using noble metal nano-clusters as highly active catalysts. *J. Power Sources* **168**, 135–142 (2007).
35. Dai, H.-B., Kang, X.-D. & Wang, P. Ruthenium nanoparticles immobilized in montmorillonite used as catalyst for methanolysis of ammonia borane. *Int. J. Hydrogen Energy* **35**, 10317–10323 (2010).
36. Durap, F., Zahmakıran, M. & Özkar, S. Water soluble laurate-stabilized ruthenium(0) nanoclusters catalyst for hydrogen generation from the hydrolysis of ammonia-borane: High activity and long lifetime. *Int. J. Hydrogen Energy* **34**, 7223–7230 (2009).
37. Zahmakıran, M. & Özkar, S. Zeolite framework stabilized rhodium(0) nanoclusters catalyst for the hydrolysis of ammonia-borane in air: Outstanding catalytic activity, reusability and lifetime. *Appl. Catal. B Environ.* **89**, 104–110 (2009).
38. Metin, Ö., Şahin, Ş. & Özkar, S. Water-soluble poly(4-styrenesulfonic acid-co-maleic acid) stabilized ruthenium(0) and palladium(0) nanoclusters as highly active catalysts in hydrogen generation from the hydrolysis of ammonia–borane. *Int. J. Hydrogen Energy* **34**, 6304–6313 (2009).
39. Chen, W. *et al.* Unique reactivity in Pt/CNT catalyzed hydrolytic dehydrogenation of ammonia borane. *Chem. Commun.* **50**, 2142 (2014).

40. Aijaz, A. *et al.* Immobilizing Highly Catalytically Active Pt Nanoparticles inside the Pores of Metal–Organic Framework: A Double Solvents Approach. *J. Am. Chem. Soc.* **134**, 13926–13929 (2012).
41. Brack, P., Dann, S. E. & Wijayantha, K. G. U. Heterogeneous and homogenous catalysts for hydrogen generation by hydrolysis of aqueous sodium borohydride (NaBH_4) solutions. *Energy Sci. Eng.* **3**, 174–188 (2015).
42. Hannauer, J. *et al.* High-extent dehydrogenation of hydrazine borane $\text{N}_2\text{H}_4\text{BH}_3$ by hydrolysis of BH_3 and decomposition of N_2H_4 . *Energy Environ. Sci.* **4**, 3355 (2011).
43. Marrero-Alfonso, E. Y., Beaird, A. M., Davis, T. A. & Matthews, M. A. Hydrogen Generation from Chemical Hydrides. *Ind. Eng. Chem. Res.* **48**, 3703–3712 (2009).
44. Liu, B. H. & Li, Z. P. A review: Hydrogen generation from borohydride hydrolysis reaction. *Journal of Power Sources* **187**, 527–534 (2009).
45. Schlesinger, H. I. *et al.* Sodium Borohydride, Its Hydrolysis and its Use as a Reducing Agent and in the Generation of Hydrogen ¹. *J. Am. Chem. Soc.* **75**, 215–219 (1953).
46. Demirci, U. B. & Miele, P. Sodium tetrahydroborate as energy/hydrogen carrier, its history. *Comptes Rendus Chim.* **12**, 943–950 (2009).
47. Nakamori, Y. *et al.* Development of metal borohydrides for hydrogen storage. *J. Phys. Chem. Solids* **69**, 2292–2296 (2008).
48. Amendola, S. C. *et al.* A Safe, portable, hydrogen gas generator using aqueous borohydride solution and Ru catalyst. *Int. J. Hydrogen Energy* (2000). doi:10.1016/S0360-3199(00)00021-5
49. Amendola, S. C. *et al.* An ultrasafe hydrogen generator: Aqueous, alkaline borohydride solutions and Ru catalyst. *ACS Div. Fuel Chem. Prepr.* **44**, 864–866 (1999).
50. Shang, Y. & Chen, R. Hydrogen storage via the hydrolysis of NaBH_4 basic solution: Optimization of NaBH_4 concentration. *Energy and Fuels* **20**, 2142–2148 (2006).
51. Wee, J.-H., Lee, K.-Y. & Kim, S. H. Sodium borohydride as the hydrogen supplier for proton exchange membrane fuel cell systems. *Fuel Process. Technol.* **87**, 811–819 (2006).
52. Fakioglu, E., Yurum, Y. & Veziroglu, T. N. A review of hydrogen storage systems based on boron and its compounds. *Int. J. Hydrogen Energy* **29**, 1371–1376 (2004).
53. Retnamma, R., Rangel, C. M., Novais, A. Q. & Matthews, M. A. Kinetics of Sodium

- Borohydride Hydrolysis in Aqueous-Basic Solutions. in *IV Iberian Symposium on Hydrogen, Fuel Cells and Advanced Batteries. Estoril, Portugal, June 26-28 2013* 26–29 (2013).
54. Davis, R. Boron Hydrides. III. Hydrolysis of Sodium Borohydride in Aqueous Solution. *J. Am. Chem. Soc.* **84**, 885–892 (1962).
 55. Liu, B. H. & Li, Z. P. A review: Hydrogen generation from borohydride hydrolysis reaction. *J. Power Sources* **187**, 527–534 (2009).
 56. Retnamma, R., Novais, A. Q. & Rangel, C. M. Kinetics of hydrolysis of sodium borohydride for hydrogen production in fuel cell applications: A review. *Int. J. Hydrogen Energy* **36**, 9772–9790 (2011).
 57. Bartkus, T. P., T'ien, J. S. & Sung, C.-J. A semi-global reaction rate model based on experimental data for the self-hydrolysis kinetics of aqueous sodium borohydride. *Int. J. Hydrogen Energy* **38**, 4024–4033 (2013).
 58. Santos Aires, F. J. C. & Bertolini, J. C. On the use of silicon nitride in catalysis. *Top. Catal.* (2009). doi:10.1007/s11244-009-9296-z
 59. Aires, F. J. C. S., Kurzina, I., Cervantes, G. G. & Bertolini, J. C. Pd catalysts supported on silicon nitride for the combustion of methane: Influence of the crystalline and amorphous phases of the support and of the preparation method on the catalytic performances. *Catal. Today* (2006). doi:10.1016/j.cattod.2006.06.012
 60. Monnet, F., Schuurman, Y., Cadete Santos Aires, F., Bertolini, J. . & Mirodatos, C. Silicon nitride supported platinum catalysts for the partial oxidation of methane at high temperatures. *Catal. Today* **64**, 51–58 (2001).
 61. Kurzina, I. A., Cadete Santos Aires, F. J. & Bertolini, J. C. Deep Oxidation of Methane on a Pt/Si₃N₄ Catalyst. *Theor. Exp. Chem.* **40**, 241–245 (2004).
 62. Syarif, N., Ivandini, T. A. & Wibowoa, W. Direct Synthesis Carbon/Metal Oxide Composites for Electrochemical Capacitors Electrode. *Int. Trans. J. Eng. Manag. Appl. Sci. Technol.* **3**, 21–34 (2012).
 63. Cheng, Q. *et al.*. Graphene and carbon nanotube composite electrodes for supercapacitors with ultra-high energy density. *Phys. Chem. Chem. Phys.* **13**, 17615 (2011).
 64. Mishra, A. K. & Ramaprabhu, S. Functionalized Graphene-Based Nanocomposites for Supercapacitor Application. *J. Phys. Chem. C* **115**, 14006–14013 (2011).
 65. Du, C. & Pan, N. Carbon Nanotube-Based Supercapacitors. *Nanotechnol. Law Bus.*

- 569–576 (2007).
66. Marcano, D. C. *et al.* Improved Synthesis of Graphene Oxide. *ACS Nano* **4**, 4806–4814 (2010).
 67. Liu, C., Yu, Z., Neff, D., Zhamu, A. & Jang, B. Z. Graphene-Based Supercapacitor with an Ultrahigh Energy Density. *Nano Lett.* **10**, 4863–4868 (2010).
 68. Cheng, H. M. Development of graphene-based materials for energy storage. in *2010 8th International Vacuum Electron Sources Conference and Nanocarbon* 49–49 (IEEE, 2010). doi:10.1109/IVESC.2010.5644354
 69. Wang, H., Hao, Q., Yang, X., Lu, L. & Wang, X. Graphene oxide doped polyaniline for supercapacitors. *Electrochem. commun.* **11**, 1158–1161 (2009).
 70. Lázaro, M. J. *et al.* *Carbon black : production, properties, and uses.* (Nova Science Publishers, 2011).
 71. Shao, Y., Yin, G. & Gao, Y. Understanding and approaches for the durability issues of Pt-based catalysts for PEM fuel cell. *J. Power Sources* **171**, 558–566 (2007).
 72. Kangasniemi, K. H., Condit, D. A. & Jarvi, T. D. Characterization of Vulcan Electrochemically Oxidized under Simulated PEM Fuel Cell Conditions. *J. Electrochem. Soc.* **151**, E125 (2004).
 73. Avasarala, B. & Haldar, P. Electrochemical oxidation behavior of titanium nitride based electrocatalysts under {PEM} fuel cell conditions. *Electrochim. Acta* **55**, 9024–9034 (2010).
 74. Knights, S. D., Colbow, K. M., St-Pierre, J. & Wilkinson, D. P. Aging mechanisms and lifetime of PEFC and DMFC. *J. Power Sources* **127**, 127–134 (2004).
 75. Jin, X., Gao, L., Li, J. & Zheng, S. Influence of Microstructure Evolution on the Electroconducting Behavior of Intragranular TiN/ZTM Nanocomposites. *J. Am. Ceram. Soc.* **87**, 162–165 (2004).
 76. Musil, J. Hard and superhard nanocomposite coatings. *Surf. Coatings Technol.* **125**, 322–330 (2000).
 77. Qiu, Y. & Gao, L. Novel Polyaniline/Titanium Nitride Nanocomposite: Controllable Structures and Electrical/Electrochemical Properties. *J. Phys. Chem. B* **109**, 19732–19740 (2005).
 78. Kaskel, S., Schlichte, K. & Kratzke, T. Catalytic properties of high surface area titanium nitride materials. *J. Mol. Catal. A Chem.* **208**, 291–298 (2004).
 79. Lee, Y. J. Low-impurity, highly conformal atomic layer deposition of titanium nitride

- using NH₃-Ar-H₂ plasma treatment for capacitor electrodes. *Mater. Lett.* **59**, 615–617 (2005).
80. Kaskel, S., Schlichte, K., Chaplais, G. & Khanna, M. Synthesis and characterisation of titanium nitride based nanoparticles. *J. Mater. Chem.* **13**, 1496 (2003).
81. Centeno, M. Á., Carrizosa, I. & Odriozola, J. A. Deposition–precipitation method to obtain supported gold catalysts: dependence of the acid–base properties of the support exemplified in the system TiO₂–TiO_xN_y–TiN. *Appl. Catal. A Gen.* **246**, 365–372 (2003).
82. Zhai, H., Li, J., Zhang, S., Chen, Y. & Zhang, B. Preparation of tetragonal zirconia containing titanium nitride powder by in-situ selective nitridation. *J. Mater. Chem.* **11**, 1092–1095 (2001).
83. Lee, J.-M. *et al.* Methanol electrooxidation of Pt catalyst on titanium nitride nanostructured support. *Appl. Catal. A Gen.* **375**, 149–155 (2010).
84. Choi, D. & Kumta, P. N. Nanocrystalline TiN Derived by a Two-Step Halide Approach for Electrochemical Capacitors. *J. Electrochem. Soc.* **153**, A2298 (2006).
85. Musthafa, O. T. M. & Sampath, S. High performance platinized titanium nitride catalyst for methanol oxidation. *Chem. Commun. (Camb)*. 67–69 (2008).
doi:10.1039/b715859a
86. Thotiyl, M. M. O. & Sampath, S. Electrochemical oxidation of ethanol in acid media on titanium nitride supported fuel cell catalysts. *Electrochim. Acta* **56**, 3549–3554 (2011).
87. Avasarala, B. & Haldar, P. On the stability of TiN-based electrocatalysts for fuel cell applications. *Int. J. Hydrogen Energy* **36**, 3965–3974 (2011).
88. Zhang, Y. *et al.* Progress of electrochemical capacitor electrode materials: A review. *Int. J. Hydrogen Energy* **34**, 4889–4899 (2009).
89. Qu, D. Studies of the activated carbons used in double-layer supercapacitors. *J. Power Sources* **109**, 403–411 (2002).
90. Yu, G.-Y. *et al.* Synthesis of Ru/carbon nanocomposites by polyol process for electrochemical supercapacitor electrodes. *Mater. Lett.* **60**, 2453–2456 (2006).
91. Arabale, G. *et al.* Enhanced supercapacitance of multiwalled carbon nanotubes functionalized with ruthenium oxide. *Chem. Phys. Lett.* **376**, 207–213 (2003).
92. Wang, G., Zhang, L. & Zhang, J. A review of electrode materials for electrochemical supercapacitors. *Chem. Soc. Rev.* **41**, 797–828 (2012).

93. Conway, B. E. *Electrochemical Supercapacitors*. (Springer US, 1999).
doi:10.1007/978-1-4757-3058-6
94. Lukatskaya, M. R. *et al.* Cation Intercalation and High Volumetric Capacitance of Two-Dimensional Titanium Carbide. *Science (80-.)*. **341**, 1502 LP-1505 (2013).
95. Levi, M. D. *et al.* Solving the Capacitive Paradox of 2D MXene using Electrochemical Quartz-Crystal Admittance and In Situ Electronic Conductance Measurements. *Adv. Energy Mater.* **5**, 1400815 (2015).
96. Naguib, M. *et al.* Two-Dimensional Nanocrystals Produced by Exfoliation of Ti₃AlC₂. *Adv. Mater.* **23**, 4248–4253 (2011).
97. Naguib, M., Mochalin, V. N., Barsoum, M. W. & Gogotsi, Y. 25th anniversary article: MXenes: A new family of two-dimensional materials. *Adv. Mater.* (2014).
doi:10.1002/adma.201304138
98. Kurtoglu, M., Naguib, M., Gogotsi, Y. & Barsoum, M. W. First principles study of two-dimensional early transition metal carbides. *MRS Commun.* **2**, 133–137 (2012).
99. Khazaei, M. *et al.* Novel Electronic and Magnetic Properties of Two-Dimensional Transition Metal Carbides and Nitrides. *Adv. Funct. Mater.* **23**, 2185–2192 (2013).
100. Augustyn, V. *et al.* High-rate electrochemical energy storage through Li⁺ intercalation pseudocapacitance. *Nat. Mater.* **12**, 518–522 (2013).
101. Come, J. *et al.* Controlling the actuation properties of MXene paper electrodes upon cation intercalation. *Nano Energy* **17**, 27–35 (2015).
102. Khomenko, V., Frackowiak, E. & Béguin, F. Determination of the specific capacitance of conducting polymer/nanotubes composite electrodes using different cell configurations. *Electrochim. Acta* **50**, 2499–2506 (2005).
103. Colombo, P., Mera, G., Riedel, R. & Sorarù, G. D. Polymer-Derived Ceramics: 40 Years of Research and Innovation in Advanced Ceramics. *J. Am. Ceram. Soc.* no-no (2010). doi:10.1111/j.1551-2916.2010.03876.x
104. Bernard, S., Fiaty, K., Cornu, D., Miele, P. & Laurent, P. Kinetic modeling of the polymer-derived ceramics route: Investigation of the thermal decomposition kinetics of poly[B-(methylamino)borazine] precursors into boron nitride. *J. Phys. Chem. B* **110**, 9048–9060 (2006).
105. Mera, G., Tamayo, A., Nguyen, H., Sen, S. & Riedel, R. Nanodomain Structure of Carbon-Rich Silicon Carbonitride Polymer-Derived Ceramics. *J. Am. Ceram. Soc.* **93**, 1169–1175 (2010).

106. Bernard, S. *Design, processing, and properties of ceramic materials from preceramic precursors*. (Nova Science Publishers, 2012).
107. Wynne, K. J. & Rice, R. W. Ceramics Via Polymer Pyrolysisdagger. *Annu. Rev. Mater. Sci.* **14**, 297–334 (1984).
108. Rocha, R. M. da, Greil, P., Bressiani, J. C. & Bressiani, A. H. de A. Complex-shaped ceramic composites obtained by machining compact polymer-filler mixtures. *Mater. Res.* **8**, 191–196 (2005).
109. Harshe, R., Balan, C. & Riedel, R. Amorphous Si(Al)OC ceramic from polysiloxanes: bulk ceramic processing, crystallization behavior and applications. *J. Eur. Ceram. Soc.* **24**, 3471–3482 (2004).
110. Janakiraman, N. & Aldinger, F. Fabrication and characterization of fully dense Si–C–N ceramics from a poly(ureamethylvinyl)silazane precursor. *J. Eur. Ceram. Soc.* **29**, 163–173 (2009).
111. Melcher, R., Cromme, P., Scheffler, M. & Greil, P. Centrifugal Casting of Thin-Walled Ceramic Tubes from Preceramic Polymers. *J. Am. Ceram. Soc.* **86**, 1211–1213 (2003).
112. Liu, X., Li, Y.-L. & Hou, F. Fabrication of SiOC Ceramic Microparts and Patterned Structures from Polysiloxanes via Liquid Cast and Pyrolysis. *J. Am. Ceram. Soc.* **92**, 49–53 (2009).
113. Yoon, B.-H., Park, C.-S., Kim, H.-E. & Koh, Y.-H. In Situ Synthesis of Porous Silicon Carbide (SiC) Ceramics Decorated with SiC Nanowires. *J. Am. Ceram. Soc.* **908**, 3759–3766 (2007).
114. Yoon, B.-H., Lee, E.-J., Kim, H.-E. & Koh, Y.-H. Highly Aligned Porous Silicon Carbide Ceramics by Freezing Polycarbosilane/Camphene Solution. *J. Am. Ceram. Soc.* **90**, 1753–1759 (2007).
115. Sato, K. *et al.* Fabrication and pressure testing of a gas-turbine component manufactured by a preceramic-polymer-impregnation method. *Compos. Sci. Technol.* **59**, 853–859 (1999).
116. Erdal, M., Guceri, S. I. & Danforth, S. C. Impregnation Molding of Particle-Filled Preceramic Polymers: Process Modeling. *J. Am. Ceram. Soc.* **82**, 2017–2028 (1999).
117. Sung, I.-K., Yoon, S.-B., Yu, J.-S. & Kim, D.-P. Fabrication of macroporous SiC from templated preceramic polymers. *Chem. Commun. (Camb)*. **50**, 1480–1481 (2002).
118. Cromme, P., Scheffler, M. & Greil, P. Ceramic tapes from preceramic polymers. *Adv. Eng. Mater.* **4**, 873–876 (2002).

119. Goerke, O., Feike, E., Heine, T., Trampert, A. & Schubert, H. Ceramic coatings processed by spraying of siloxane precursors (polymer-spraying). *J. Eur. Ceram. Soc.* **24**, 2141–2147 (2004).
120. Colombo, P., Paulson, T. E. & Pantano, C. G. Synthesis of Silicon Carbide Thin Films with Polycarbosilane (PCS). *J. Am. Ceram. Soc.* **40**, 2333–2340 (2005).
121. Smirnova, T. P. *et al.* SiCN alloys obtained by remote plasma chemical vapour deposition from novel precursors. *Thin Solid Films* **429**, 144–151 (2003).
122. Haug, R., Weinmann, M., Bill, J. & Aldinger, F. Plastic forming of preceramic polymers. *J. Eur. Ceram. Soc.* **19**, 1–6 (1999).
123. Galusek, D., Sedláček, J. & Riedel, R. Al₂O₃–SiC composites prepared by warm pressing and sintering of an organosilicon polymer-coated alumina powder. *J. Eur. Ceram. Soc.* **27**, 2385–2392 (2007).
124. Kumar, R., Cai, Y., Gerstel, P., Rixecker, G. & Aldinger, F. Processing, crystallization and characterization of polymer derived nano-crystalline Si–B–C–N ceramics. *J. Mater. Sci.* **41**, 7088–7095 (2006).
125. Walter, S., Suttor, D., Erny, T., Hahn, B. & Greil, P. Injection moulding of polysiloxane/filler mixtures for oxycarbide ceramic composites. *J. Eur. Ceram. Soc.* **16**, 387–393 (1996).
126. Zhang, T., Evans, J. R. G. & Woodthorpe, J. Injection moulding of silicon carbide using an organic vehicle based on a preceramic polymer. *J. Eur. Ceram. Soc.* **15**, 729–734 (1995).
127. Mutsuddy, B. C. Use of organometallic polymer for making ceramic parts by plastic forming techniques. *Ceram. Int.* **13**, 41–53 (1987).
128. Perale, G. *et al.* A novel process for the manufacture of ceramic microelectrodes for biomedical applications. *Int. J. Appl. Ceram. Technol.* **5**, 37–43 (2008).
129. Kim, Y.-W., Eom, J.-H., Wang, C. & Park, C. B. Processing of Porous Silicon Carbide Ceramics from Carbon-Filled Polysiloxane by Extrusion and Carbothermal Reduction. *J. Am. Ceram. Soc.* **91**, 1361–1364 (2008).
130. OKAMURA, K., SHIMOO, T., SUZUYA, K. & SUZUKI, K. SiC-Based Ceramic Fibers Prepared via Organic-to-Inorganic Conversion Process-A Review. *J. Ceram. Soc. Japan* **114**, 445–454 (2006).
131. Bunsell, A. R. & Piant, A. A review of the development of three generations of small diameter silicon carbide fibres. *J. Mater. Sci.* **41**, 823–839 (2006).

132. Zeschky, J. *et al.* Polysilsesquioxane derived ceramic foams with gradient porosity. *Acta Mater.* **53**, 927–937 (2005).
133. Colombo, P. Engineering porosity in polymer-derived ceramics. *J. Eur. Ceram. Soc.* (2008). doi:10.1016/j.jeurceramsoc.2007.12.002
134. Kim, Y.-W. & Park, C. B. Processing of microcellular preceramics using carbon dioxide. *Compos. Sci. Technol.* **63**, 2371–2377 (2003).
135. Lewinsohn, C. A. & Elangovan, S. in *27th Annual Cocoa Beach Conference on Advanced Ceramics and Composites: A: Ceramic Engineering and Science Proceedings, Volume 24, Issue 3* 317–322 (John Wiley & Sons, Inc.). doi:10.1002/9780470294802.ch48
136. Lewinsohn, C. A., Colombo, P., Reimanis, I. & Ünal, Ö. Stresses Occurring during Joining of Ceramics Using Preceramic Polymers. *J. Am. Ceram. Soc.* **84**, 2240–2244 (2004).
137. Colombo, P., Sglavo, V. & Pippel, E. Joining of reaction-bonded silicon carbide using a preceramic polymer. *J. Mater. Sci.* **33**, 2405–2412 (1998).
138. Friedel, T., Travitzky, N., Niebling, F., Scheffler, M. & Greil, P. Fabrication of polymer derived ceramic parts by selective laser curing. *J. Eur. Ceram. Soc.* **25**, 193–197 (2005).
139. Scheffler, M., Bordia, R., Travitzky, N. & Greil, P. Development of a rapid crosslinking preceramic polymer system. *J. Eur. Ceram. Soc.* **25**, 175–180 (2005).
140. Mott, M. & Evans, J. R. G. Solid Freeforming of Silicon Carbide by Inkjet Printing Using a Polymeric Precursor. *J. Am. Ceram. Soc.* **84**, 307–13 (2004).
141. Eick, B. M. & Youngblood, J. P. SiC nanofibers by pyrolysis of electrospun preceramic polymers. *J. Mater. Sci.* **44**, 160–165 (2009).
142. Shin, D. G., Riu, D. H. & Kim, H. E. Web-type silicon carbide fibers prepared by the electrospinning of polycarbosilanes. *J. Ceram. Process. Res.* **9**, 209–214 (2008).
143. Welna, D. T., Bender, J. D., Wei, X., Sneddon, L. G. & Allcock, H. R. Preparation of Boron-Carbide/Carbon Nanofibers from a Poly(norbornenyldodecaborane) Single-Source Precursor via Electrostatic Spinning. *Adv. Mater.* **17**, 859–862 (2005).
144. Sarkar, S., Chunder, A., Fei, W., An, L. & Zhai, L. Superhydrophobic Mats of Polymer-Derived Ceramic Fibers. *J. Am. Ceram. Soc.* **91**, 2751–2755 (2008).
145. Nangrejo, M. *et al.* Electrohydrodynamic forming of porous ceramic capsules from a preceramic polymer. *Mater. Lett.* **63**, 483–485 (2009).

146. Bahloul-Hourlier, D., Doucey, B., Laborde, E. & Goursat, P. Investigations on thermal reactivity of Si/C/N nanopowders produced by laser aerosol or gas interactions. *J. Mater. Chem.* **11**, 2028–2034 (2001).
147. Xiao, T. D., Gonsalves, K. E., Strutt, P. R. & Klemens, P. G. Synthesis of Si(N,C) nanostructured powders from an organometallic aerosol using a hot-wall reactor. *J. Mater. Sci.* **28**, 1334–1340 (1993).
148. Malenfant, P. R. L., Wan, J., Taylor, S. T. & Manoharan, M. Self-assembly of an organic–inorganic block copolymer for nano-ordered ceramics. *Nat. Nanotechnol.* **2**, 43–46 (2007).
149. Garcia, C. B. W. *et al.* Synthesis and characterization of block copolymer/ceramic precursor nanocomposites based on a polysilazane. *J. Polym. Sci. Part B Polym. Phys.* **41**, 3346–3350 (2003).
150. Wan, J., Malenfant, P. R. L., Taylor, S. T., Loureiro, S. M. & Manoharan, M. Microstructure of block copolymer/precursor assembly for Si–C–N based nano-ordered ceramics. *Mater. Sci. Eng. A* **463**, 78–88 (2007).
151. Hanemann, T. *et al.* Microstructuring of Pre-ceramic Polymers. *Adv. Eng. Mater.* **4**, 869–873 (2002).
152. Schulz, M., Börner, M., Haußelt, J. & Heldele, R. Polymer derived ceramic microparts from X-ray lithography—cross-linking behavior and process optimization. *J. Eur. Ceram. Soc.* **25**, 199–204 (2005).
153. Lee, H.-J., Yoon, T.-H. & Kim, D.-P. Fabrication of microfluidic channels derived from a UV/thermally cured pre-ceramic polymer via a soft lithographic technique. *Microelectron. Eng.* **84**, 2892–2895 (2007).
154. Freimuth, H. *et al.* Formation of Complex Ceramic Miniaturized Structures by Pyrolysis of Poly(vinylsilazane). *J. Am. Ceram. Soc.* **79**, 1457–1465 (1996).
155. Yang, H., Deschatelets, P., Brittain, S. T. & Whitesides, G. M. Fabrication of High Performance Ceramic Microstructures from a Polymeric Precursor Using Soft Lithography. *Adv. Mater.* **13**, 54–58 (2001).
156. Liu, Y. *et al.* Application of microforging to SiCN MEMS fabrication. *Sensors Actuators A Phys.* **95**, 143–151 (2002).
157. Liew, L.-A. *et al.* Fabrication of SiCN MEMS by photopolymerization of pre-ceramic polymer. *Sensors Actuators A Phys.* **95**, 120–134 (2002).
158. Pender, M. J., Forsthoefel, K. M. & Sneddon, L. G. Molecular and polymeric

- precursors to boron carbide nanofibers, nanocylinders, and nanoporous ceramics. *Pure Appl. Chem.* **75**, 1287–1294 (2003).
159. Cheng, Q.-M., Interrante, L. V., Lienhard, M., Shen, Q. & Wu, Z. Methylene-bridged carbosilanes and polycarbosilanes as precursors to silicon carbide—from ceramic composites to SiC nanomaterials. *J. Eur. Ceram. Soc.* **25**, 233–241 (2005).
160. Termoss, H. *et al.* Shaping potentialities of aluminum nitride polymeric precursors. *J. Eur. Ceram. Soc.* **29**, 857–861 (2009).
161. Yoon, T., Lee, H., Yan, J. & Kim, D. Fabrication of SiC-Based Ceramic Microstructures from Pre-ceramic Polymers with Sacrificial Templates and Lithographic Techniques—A Review. *J. Ceram. Soc. Japan* **114**, 473–479 (2006).
162. Ye, C., Chen, A., Colombo, P. & Martinez, C. Ceramic microparticles and capsules via microfluidic processing of a pre-ceramic polymer. *J. R. Soc. Interface* **7 Suppl 4**, S461–73 (2010).
163. Bakumov, V., Schwarz, M. & Kroke, E. Emulsion processing of polymer-derived porous SiC/(O) ceramic bodies. *J. Eur. Ceram. Soc.* **29**, 2857–2865 (2009).
164. Otoishi, S. & Tange, Y. Growth rate and morphology of silicon carbide whiskers from polycarbosilane. *J. Cryst. Growth* **200**, 467–471 (1999).
165. Zheng, J., Kramer, M. J. & Akinc, M. *In situ* Growth of SiC Whisker in Pyrolyzed Monolithic Mixture of AHPCS and SiC. *J. Am. Ceram. Soc.* **83**, 2961–2966 (2000).
166. Berger, A. *et al.* Nanoprocesses in polymer-derived Si-O-C ceramics: Electronmicroscopic observations and reaction kinetics. *Phys. status solidi* **202**, 2277–2286 (2005).
167. Yang, W. *et al.* Ultra-Long Single-Crystalline alpha-Si₃N₄ Nanowires: Derived from a Polymeric Precursor. *J. Am. Ceram. Soc.* **88**, 1647–1650 (2005).
168. Yang, W. *et al.* Synthesis of Ceramic Nanocomposite Powders with in situ Formation of Nanowires/Nanobelts. *J. Am. Ceram. Soc.* **91**, 1312–1315 (2008).
169. Haberecht, J., Krumeich, F., Stalder, M. & Nesper, R. Carbon nanostructures on high-temperature ceramics – a novel composite material and its functionalization. *Catal. Today* **102–103**, 40–44 (2005).
170. Gao, F., Yang, W., Fan, Y. & An, L. Mass production of very thin single-crystal silicon nitride nanobelts. *J. Solid State Chem.* **181**, 211–215 (2008).
171. Cai, K. F., Huang, L. Y., Zhang, A. X., Yin, J. L. & Liu, H. Ultra Long SiCN Nanowires and SiCN/SiO₂Nanocables: Synthesis, Characterization, and Electrical

- Property. *J. Nanosci. Nanotechnol.* **8**, 6338–6343 (2008).
172. Narisawa, M., Idesaki, A., Kitano, S. & Okamura, K. Use of Blended Precursors of Poly (vinylsilane) in Polycarbosilane for Silicon Carbide Fiber Synthesis with Radiation Curing. *J. Am. Cera.Soc* **51**, 1045–1051 (1999).
173. Idesaki, A. *et al.*. Synthesis of a minute SiC product from polyvinylsilane with radiation curing: Part I radiation curing of polyvinylsilane. *J. Mater. Sci.* **39**, 5689–5694 (2004).
174. Idesaki, A. *et al.*. Application of electron beam curing for silicon carbide fiber synthesis from blend polymer of polycarbosilane and polyvinylsilane. in *Radiation Physics and Chemistry* **60**, 483–487 (2001).
175. Pham, T. A., Kim, P., Kwak, M., Suh, K. Y. & Kim, D.-P. Inorganic polymer photoresist for direct ceramic patterning by photolithography. *Chem. Commun. (Camb)*. **14**, 4021–4023 (2007).
176. Schulz, M. *et al.*. Cross linking behavior of preceramic polymers effected by UV- And synchrotron radiation. *Adv. Eng. Mater.* **6**, 676–680 (2004).
177. YAJIMA, S., HAYASHI, J., OMORI, M. & OKAMURA, K. Development of a silicon carbide fibre with high tensile strength. *Nature* **261**, 683–685 (1976).
178. Yajima, S., Hayashi, J. & Omori, M. CONTINUOUS SILICON CARBIDE FIBER OF HIGH TENSILE STRENGTH. *Chem. Lett.* **4**, 931–934 (1975).
179. Lipowitz, J., Rabe, J. A., Zangvil, A. & Xu, Y. in *Proceedings of the 21st Annual Conference on Composites, Advanced Ceramics, Materials, and Structures: A: Ceramic Engineering and Science Proceedings* 147–157 (John Wiley & Sons, Inc., 1997). doi:10.1002/9780470294437.ch16
180. KUMADA, M., NAKAJIMA, J.-I., ISHIKAWA, M. & YAMAMOTO, Y. Synthesis and Intramolecular Rearrangements of Chloromethylpenta-methyldisilane and 1-Chloromethyl-2-chlorotetramethyldisilane. *J. Org. Chem.* **23**, 292–295 (1958).
181. Birot, M., Pillot, J.-P. & Dunogues, J. Comprehensive Chemistry of Polycarbosilanes, Polysilazanes, and Polycarbosilazanes as Precursors of Ceramics. *Chem. Rev.* **95**, 1443–1477 (1995).
182. HEMIDA, A. T., BIROT, M., PILLOT, J. P., DUNOGUES, J. & PAILLER, R. Synthesis and characterization of new precursors to nearly stoichiometric SiC ceramics: Part 1 The copolymer route. *J. Mater. Sci.* **32**, 3475–3483 (1997).
183. Whitmarsh, C. K. & Interrante, L. V. Synthesis and Structure of a Highly Branched

- Polycarbosilane Derived from (Chloromethyl) trichlorosilane. *Organochemicals* **10**, 1336–1344 (1991).
184. Sreeja, R., Swaminathan, B., Painuly, A., Sebastian, T. V. & Packirisamy, S. Allylhydridopolycarbosilane (AHPCS) as matrix resin for C/SiC ceramic matrix composites. *Mater. Sci. Eng. B Solid-State Mater. Adv. Technol.* **168**, 204–207 (2010).
 185. I. L. Rushkin, Q. Shen, S. E. Lehman & Interrante, L. V. Modification of a Hyperbranched Hydridopolycarbosilane as a Route to New Polycarbosilanes. *Macromolecules* **30**, 3141–3146 (1997).
 186. Kaur, S., Riedel, R. & Ionescu, E. Pressureless fabrication of dense monolithic SiC ceramics from a polycarbosilane. *J. Eur. Ceram. Soc.* **34**, 3571–3578 (2014).
 187. Interrante, L. V. *et al.* High yield polycarbosilane precursors to stoichiometric SiC. Synthesis, pyrolysis and application. *Mater. Res. Soc. Symp. - Proc.* **346**, 593–603 (1994).
 188. Konegger, T., Tsai, C.-C., Peterlik, H., Creager, S. E. & Bordia, R. K. Asymmetric polysilazane-derived ceramic structures with multiscalar porosity for membrane applications. *Microporous Mesoporous Mater.* **232**, 196–204 (2016).
 189. Kroke, E. *et al.* Silazane derived ceramics and related materials. *Mater. Sci. Eng. R Reports* **26**, 97–199 (2000).
 190. Persoz, M. No Title. *Ann. Chim. Phys.* **44**, 315 (1839).
 191. Schutzenberger, P. & Colson, H. No Title. *C. R. Acad. Sci.* **92**, 1508 (1885).
 192. Seyferth, D., Wiseman, G. H. & Prud'homme, C. A Liquid Silazane Precursor To Silicon Nitride. *J. Am. Ceram. Soc.* **66**, C-13-C-14 (1983).
 193. Schumb, W. C. & Towle, L. H. THE PARTIAL AMMONOLYSIS OF SILICON TETRACHLORIDE. *J. Am. Chem. Soc.* **75**, 6085–6086 (1953).
 194. Niedenzu, K., Fritz, P. & Dawson, J. W. Boron-Nitrogen Compounds. XVI. Some New Boron-Nitrogen Heterocycles. *Inorg. Chem.* **3**, 1077–1079 (1964).
 195. Burns, G. T. & Chandra, G. Pyrolysis of Preceramic Polymers in Ammonia: Preparation of Silicon Nitride Powders. *J. Am. Ceram. Soc.* **72**, 333–337 (1989).
 196. Seyferth, D. & Wiseman, G. H. Preceramic organosilazane polymers. (1984).
 197. Bae, Y. W., Du, H., Gallois, B., Gonsalves, K. E. & Wilkens, B. J. Structure and Chemistry of Silicon Nitride and Silicon Carbonitride Thin Films Deposited from Ethylsilazane in Ammonia or Hydrogen. *Chem. Mater.* **4**, 478–483 (1992).
 198. Isoda, T. *et al.* Perhydropolysilazane precursors to silicon nitride ceramics. *J. Inorg.*

- Organomet. Polym.* **2**, 151–160 (1992).
199. Kamo, A., Isoda, T., Resezfrch, C. & Corporation, T. Into Silicon Nitride-Based Ceramics. **29**, 4883–4888 (1994).
200. Blanchard, C. R. & Schwab, S. T. X-ray Diffraction Analysis of the Pyrolytic Conversion of Perhydropolysilazane into Silicon Nitride. *J. Am. Ceram. Soc.* **77**, 1729–1739 (1994).
201. Iwamoto, Y. *et al.* Crystallization Behavior of Amorphous Silicon Carbonitride Ceramics Derived from Organometallic Precursors. *J. Am. Ceram. Soc.* **84**, 2170–2178 (2004).
202. Günthner, M. *et al.* Advanced coatings on the basis of Si(C)N precursors for protection of steel against oxidation. *J. Eur. Ceram. Soc.* **29**, 2061–2068 (2009).
203. MORI, Y., UEDA, T., KITAOKA, S. & SUGAHARA, Y. Preparation of Si-Al-N-C Ceramic Composites by Pyrolysis of Blended Precursors. *J. Ceram. Soc. Japan* **114**, 497–501 (2006).
204. Seyferth, D. & Wiseman, G. High-Yield Synthesis of Si₃N₄/SiC Ceramic Materials by Pyrolysis of a Novel Poly organosilazane. *Communiactions Am. Ceram. Soc.* **67**, 132–133 (1984).
205. Seyferth, D., Strohmamm, C., Tracy, H. J. & Robison, J. L. Synthesis and Useful Reactions of Organosilicon Polymeric Precursors for Ceramics. *MRS Proc.* **249**, (1991).
206. Bahloul, D., Pereira, M., Goursat, P., Yive, N. S. C. K. & Corriu, R. J. P. Preparation of Silicon Carbonitrides from an Organosilicon Polymer: I, Thermal Decomposition of the Cross-linked Polysilazane. *J. Am. Ceram. Soc.* **76**, 1156–1162 (1993).
207. Choong Kwet Yive, N. S., Corriu, R. J. P., Leclercq, D., Mutin, P. H. & Vioux, A. Silicon carbonitride from polymeric precursors: thermal cross-linking and pyrolysis of oligosilazane model compounds. *Chem. Mater.* **4**, 141–146 (1992).
208. Choong Kwet Yive, N. S., Corriu, R. J. P., Leclercq, D., Mutin, P. H. & Vioux, A. Thermogravimetric analysis/mass spectrometry investigation of the thermal conversion of organosilicon precursors into ceramics under argon and ammonia. 2. Poly(silazanes). *Chem. Mater.* **4**, 1263–1271 (1992).
209. Frieß, M. No Title. (MPI für Metallforschung Stuttgart, 1994).
210. Li, Y.-L. *et al.* Thermal cross-linking and pyrolytic conversion of

- poly(ureamethylvinyl)silazanes to silicon-based ceramics. *Appl. Organomet. Chem.* **15**, 820–832 (2001).
211. Lavedrine, A. *et al.* Pyrolysis of polyvinylsilazane precursors to silicon carbonitride. *J. Eur. Ceram. Soc.* **8**, 221–227 (1991).
212. Mocaer, D. *et al.* Si-C-N ceramics with a high microstructural stability elaborated from the pyrolysis of new polycarbosilazane precursors. *J. Mater. Sci.* **28**, 2615–2631 (1993).
213. Blum, Y. D., Schwartz, K. B. & Laine, R. M. Preceramic polymer pyrolysis. *J. Mater. Sci.* **24**, 1707–1718 (1989).
214. Burns, G. T., Saha, C. K., Zank, G. A. & Freeman, H. A. Polysilacyclobutasilazanes: pre-ceramic polymers for the preparation of sintered silicon carbide monoliths. *J. Mater. Sci.* **27**, 2131–2140 (1992).
215. Seyferth, D., Strohmman, C., Dando, N. R. & Perrotta, A. J. Poly(ureidosilazanes): Preceramic Polymeric Precursors for Silicon Carbonitride and Silicon Nitride. Synthesis, Characterization, and Pyrolytic Conversion to Si₃N₄/SiC Ceramics. *Chem. Mater.* **7**, 2058–2066 (1995).
216. Riedel, R., Passing, G., Schonfelder, H. & Brook, R. J. Synthesis of dense silicon-based ceramics at low temperatures. *Nature* **355**, 714–717 (1992).
217. Wideman, T. & Sneddon, L. G. Convenient Procedures for the Laboratory Preparation of Borazine. *Inorg. Chem.* **34**, 1002–1003 (1995).
218. Gervais, C. *et al.* Chemically derived BN ceramics: Extensive ¹¹B and ¹⁵N solid-state NMR study of a preceramic polyborazilene. *Chem. Mater.* **13**, 1700–1707 (2001).
219. Kim, D. & Economy, J. Occurrence of Liquid Crystallinity in a Borazine Polymer. *Chem. Mater.* **6**, 395–400 (1994).
220. Kim, D. P. & Economy, J. Fabrication of oxidation-resistant carbon fiber/boron nitride matrix composites. *Chem. Mater.* **5**, 1216–1220 (1993).
221. Fazen, P. J. *et al.* Synthesis, Properties, and Ceramic Conversion Reactions of Polyborazylene. A High-Yield Polymeric Precursor to Boron Nitride. *Chem. Mater.* **7**, 1942–1956 (1995).
222. Sneddon, L. G. *et al.* Polymeric precursors to boron based ceramics. *Pure Appl. Chem.* **63**, 407–410 (1991).
223. Fazen, P. J., Beck, J. S., Lynch, A. T., Remsen, E. E. & Sneddon, L. G. Thermally induced borazine dehydropolymerization reactions. Synthesis and ceramic conversion

- reactions of a new high-yield polymeric precursor to boron nitride. *Chem. Mater.* **2**, 96–97 (1990).
224. Thomas, J., Weston, N. E. & O'Connor, T. E. **Turbostratic ¹ Boron Nitride, Thermal Transformation to Ordered-layer-lattice Boron Nitride**. *J. Am. Chem. Soc.* **84**, 4619–4622 (1962).
225. Laubengayer, A. W., Moews, P. C. & Porter, R. F. The Condensation of Borazine to Polycyclic Boron-Nitrogen Frameworks by Pyrolytic Dehydrogenation ¹. *J. Am. Chem. Soc.* **83**, 1337–1342 (1961).
226. Mamantov, G. & Margrave, J. L. Decomposition of liquid borazine. *J. Inorg. Nucl. Chem.* **20**, 348–351 (1961).
227. Li, J., Bernard, S., Salles, V., Gervais, C. & Miele, P. Preparation of Polyborazylene-Derived Bulk Boron Nitride with Tunable Properties by Warm-Pressing and Pressureless Pyrolysis. *Chem. Mater.* **22**, 2010–2019 (2010).
228. Bechelany, M. *et al.* Synthesis of boron nitride nanotubes by a template-assisted polymer thermolysis process. *J. Phys. Chem. C* **111**, 13378–13384 (2007).
229. Termoss, H. *et al.* Preparation of boron nitride-based coatings on metallic substrates via infrared irradiation of dip-coated polyborazylene. *J. Mater. Chem.* **19**, 2671 (2009).
230. Roy, R., Komarneni, S. & Roy, D. M. Multi-Phasic Ceramic Composites made by Sol-Gel Technique. *MRS Proc.* **32**, 347 (1984).
231. Niihara, K. New Design Concept of Structural Ceramics. *J. Ceram. Soc. Japan* **99**, 974–982 (1991).
232. Vepřek, S. & Reiprich, S. A concept for the design of novel superhard coatings. *Thin Solid Films* **268**, 64–71 (1995).
233. Honeycombe, R. W. K. (Robert W. K. *The plastic deformation of metals*. (E. Arnold, 1984).
234. Kelly, A. (Anthony) & Macmillan, N. H. (Norman H. *Strong solids*. (Clarendon Press, 1986).
235. Hall, E. O. The Deformation and Ageing of Mild Steel: III Discussion of Results. *Proc. Phys. Soc. Sect. B* **64**, 747–753 (1951).
236. Petch, N. J. The Cleavage Strength of Polycrystals. *J. Iron Steel Inst.* **174**, 25–28 (1953).
237. Laboratories, S. MetallTrans_1973_4_1599. *Metall. Trans.* **4**, 1599 (1973).

-
238. Lehoczky, S. L. Retardation of dislocation generation and motion in thin-layered metal laminates. *Phys. Rev. Lett.* **41**, 1814–1818 (1978).
239. Lehoczky, S. L. Strength enhancement in thin-layered Al-Cu laminates. *J. Appl. Phys.* **49**, 5479–5485 (1978).
240. Koehler, J. S. Attempt to design a strong solid. *Phys. Rev. B* **2**, 547–551 (1970).
241. Interrante, L. V, Schmidt, W. R., Marchetti, P. S. & Maciel, G. E. Pyrolysis of Organometallic Precursors As A Route to Novel Ceramic Materials. *MRS Proc.* **249**, (1991).
242. Paine, R. T., Janik, J. F. & Fan, M. Some recent developments in precursor routes to ceramic nanocomposites. *Polyhedron* (1994). doi:10.1016/S0277-5387(00)80256-9
243. Greil, P. Polymer Derived Engineering Ceramics. *Adv. Eng. Mater.* **2**, 339–348 (2000).
244. Katsuda, Y., Gerstel, P., Narayanan, J., Bill, J. & Aldinger, F. Reinforcement of precursor-derived Si-C-N ceramics with carbon nanotubes. *J. Eur. Ceram. Soc.* **26**, 3399–3405 (2006).
245. Greil, P. Active-Filler-Controlled Pyrolysis of Pre-ceramic Polymers. *Journal of the American Ceramic Society* **78**, 835–848 (1995).
246. Seyferth, D. & Plenio, H. Borasilazane Polymeric Precursors for Borosilicon Nitride. *J. Am. Ceram. Soc.* **73**, 2131–2133 (1990).
247. Bernardo, E., Fiocco, L., Parciannello, G., Storti, E. & Colombo, P. Advanced Ceramics from Pre-ceramic Polymers Modified at the Nano-Scale: A Review. *Materials (Basel)*. **7**, 1927–1956 (2014).
248. Interrante, L. V *et al.* An Investigation Into the Preparation, Properties, and Processing of SiC/AlN and Si₃N₄/AlN Solid Solutions from Organometallic Precursors. *MRS Proc.* **121**, 465 (1988).
249. Czekaj, C. L. *et al.* Preparation of Silicon Carbide/Aluminum Nitride Ceramics Using Organometallic Precursors. *J. Am. Ceram. Soc.* **73**, 352–357 (1990).
250. Narula, C. K., Schaeffer, R., Paine, R. T., Datsy, A. & Hammett, W. F. Synthesis of boron nitride ceramics from poly(borazinylamine) precursors. *J. Am. Chem. Soc.* **109**, 5556–5557 (1987).
251. Schmidt, W. R., Hurley, W. J., Sukumar, V., Doremus, R. H. & Interrante, L. V. Polymer-Derived Si₃N₄/BN Composites. *MRS Proc.* **171**, (1989).
252. Su, K., Remsen, E. E., Zank, G. A. & Sneddon, L. G. Synthesis, characterization, and

- ceramic conversion reactions of borazine-modified hydridopolysilazanes: new polymeric precursors to silicon nitride carbide boride (SiNCB) ceramic composites. *Chem. Mater.* **5**, 547–556 (1993).
253. Ashby, M. *Materials selection in mechanical design*. (Butterworth-Heinemann, 1999).
254. Tsirlin, A. M. *et al.* Nano-structured metal-containing polymer precursors for high temperature non-oxide ceramics and ceramic fibers—syntheses, pyrolyses and properties. *J. Eur. Ceram. Soc.* **22**, 2577–2585 (2002).
255. Tao, X., Qiu, W., Li, H. & Zhao, T. Synthesis of nanosized zirconium carbide from preceramic polymers by the facile one-pot reaction. *Polym. Adv. Technol.* **21**, n/a-n/a (2010).
256. Li, Y., Han, W., Li, H., Zhao, J. & Zhao, T. Synthesis of nano-crystalline ZrB₂/ZrC/SiC ceramics by liquid precursors. *Mater. Lett.* **68**, 101–103 (2012).
257. ISHIKAWA, T., KOHTOKU, Y. & KUMAGAWA, K. Production mechanism of polyzirconocarbo- silane using zirconium(IV)acetylacetonate and its conversion of the polymer into inorganic materials. *J. Mater. Sci.* **33**, 161–166 (1998).
258. Inzenhofer, K., Schmalz, T., Wrackmeyer, B. & Motz, G. The preparation of HfC/C ceramics via molecular design. *Dalt. Trans.* **40**, 4741 (2011).
259. Amoròs, P., Beltràn, D., Guillem, C. & Latorre, J. Synthesis and characterization of SiC/MC/C ceramics (M = Ti, Zr, Hf) starting from totally non-oxidic precursors. *Chem. Mater.* **14**, 1585–1590 (2002).
260. Yu, Z. *et al.* Preparation, cross-linking and ceramization of AHPCS/Cp₂ZrCl₂ hybrid precursors for SiC/ZrC/C composites. *J. Eur. Ceram. Soc.* **32**, 1291–1298 (2012).
261. Yu, Z., Min, H., Zhan, J. & Yang, L. Preparation and dielectric properties of polymer-derived SiCTi ceramics. *Ceram. Int.* **39**, 3999–4007 (2013).
262. Alt, H. G., Föttinger, K. & Milius, W. Synthesis, characterization and polymerization potential of ansa-metallocene dichloride complexes of titanium, zirconium and hafnium containing a Si–N–Si bridging unit. *J. Organomet. Chem.* **564**, 109–114 (1998).
263. Yu, Z. *et al.* Synthesis and Characterization of SiC(Ti) Ceramics Derived from a Hybrid Precursor of Titanium-Containing Polycarbosilane. *J. Inorg. Organomet. Polym. Mater.* **21**, 412–420 (2011).
264. Cai, T. *et al.* Synthesis of soluble poly-yne polymers containing zirconium and silicon and corresponding conversion to nanosized ZrC/SiC composite ceramics. *Dalt. Trans.*

- 42, 4285 (2013).
265. Petasis, N. A. & Bzowej, E. I. Titanium-mediated carbonyl olefinations. 1. Methylenations of carbonyl compounds with dimethyltitanocene. *J. Am. Chem. Soc.* **112**, 6392–6394 (1990).
266. Du, Y. *et al.* in *Light Metal Systems. Part 4* (eds. Effenberg, G. & Ilyenko, S.) 1–10 (Springer-Verlag, 2006). doi:10.1007/b97924
267. Wen, Q. *et al.* Single-source-precursor synthesis of dense SiC/HfC_xN_{1-x}-based ultrahigh-temperature ceramic nanocomposites. *Nanoscale* **6**, 13678–13689 (2014).
268. Sachau, S. M. *et al.* Micro-/Mesoporous Platinum??SiCN Nanocomposite Catalysts (Pt@SiCN): From Design to Catalytic Applications. *Chem. - A Eur. J.* **22**, 15508–15512 (2016).
269. Francis, A., Ionescu, E., Fasel, C. & Riedel, R. Crystallization Behavior and Controlling Mechanism of Iron-Containing Si–C–N Ceramics. *Inorg. Chem.* **48**, 10078–10083 (2009).
270. Li, Y. *et al.* Preparation of Si-C-N-Fe magnetic ceramics from iron-containing polysilazane. *Appl. Organomet. Chem.* **17**, 120–126 (2003).
271. Savino, R., De Stefano Fumo, M., Paterna, D., Di Maso, A. & Monteverde, F. Arc-jet testing of ultra-high-temperature-ceramics. *Aerosp. Sci. Technol.* **14**, 178–187 (2010).
272. Pierson, H. O. *Handbook of refractory carbides and nitrides : properties, characteristics, processing, and applications.* (Noyes Publications, 1996).
273. Fahrenholtz, W. G., Hilmas, G. E., Talmy, I. G. & Zaykoski, J. A. Refractory Diborides of Zirconium and Hafnium. *J. Am. Ceram. Soc.* **90**, 1347–1364 (2007).
274. Wuchina, E., Opila, E., Opeka, M., Fahrenholtz, W. & Talmy, I. UHTCs: Ultra-High Temperature Ceramic Materials for Extreme Environment Applications. *Electrochem. Soc. Interface* 30–36 (2007).
275. Sarin, P. *et al.* In situ studies of oxidation of ZrB₂ and ZrB₂–SiC composites at high temperatures. *J. Eur. Ceram. Soc.* **30**, 2375–2386 (2010).
276. Shimada, S., Inagaki, M. & Matsui, K. Oxidation Kinetics of Hafnium Carbide in the Temperature Range of 480o to 600oC. *J. Am. Ceram. Soc.* **75**, 2671–2678 (1992).
277. Sciti, D., Guicciardi, S. & Nygren, M. Densification and Mechanical Behavior of HfC and HfB₂ Fabricated by Spark Plasma Sintering. *J. Am. Ceram. Soc.* **91**, 1433–1440 (2008).
278. Sun, S.-K. *et al.* Reactive spark plasma sintering of ZrC and HfC ceramics with fine

- microstructures. *Scr. Mater.* **69**, 139–142 (2013).
279. Opeka, M. M., Talmy, I. G., Wuchina, E. J., Zaykoski, J. A. & Causey, S. J. Mechanical, Thermal, and Oxidation Properties of Refractory Hafnium and zirconium Compounds. *J. Eur. Ceram. Soc.* **19**, 2405–2414 (1999).
280. KNUDSEN, F. P. Dependence of Mechanical Strength of Brittle Polycrystalline Specimens on Porosity and Grain Size. *J. Am. Ceram. Soc.* **42**, 376–387 (1959).
281. Silvestroni, L., Sciti, D., Kling, J., Lauterbach, S. & Kleebe, H.-J. Sintering Mechanisms of Zirconium and Hafnium Carbides Doped with MoSi₂. *J. Am. Ceram. Soc.* **92**, 1574–1579 (2009).
282. Savino, R., De Stefano Fumo, M., Silvestroni, L. & Sciti, D. Arc-jet testing on HfB₂ and HfC-based ultra-high temperature ceramic materials. *J. Eur. Ceram. Soc.* **28**, 1899–1907 (2008).
283. Rice, R. W., Wu, C. C. & Boichelt, F. Hardness-Grain-Size Relations in Ceramics. *J. Am. Ceram. Soc.* **77**, 2539–2553 (1994).
284. Lu, Y., Zhu, Z. & Liu, Z. Carbon-encapsulated Fe nanoparticles from detonation-induced pyrolysis of ferrocene. *Carbon N. Y.* **43**, 369–374 (2005).
285. Gim, J. *et al.* Pyro-Synthesis of Functional Nanocrystals. *Sci. Rep.* **2**, 127 (2012).
286. Yuan, J. *et al.* Single-Source-Precursor Synthesis of Hafnium-Containing Ultrahigh-Temperature Ceramic Nanocomposites (UHTC-NCs). *Inorg. Chem.* **53**, 10443–10455 (2014).
287. Ionescu, E., Kleebe, H.-J. & Riedel, R. Silicon-containing polymer-derived ceramic nanocomposites (PDC-NCs): preparative approaches and properties. *Chem. Soc. Rev.* **41**, 5032–52 (2012).
288. Seifollahi Bazarjani, M. *et al.* Nanoporous silicon oxycarbonitride ceramics derived from polysilazanes in situ modified with nickel nanoparticles. *Chem. Mater.* **23**, 4112–4123 (2011).
289. Kempe, R. The Strained η²-NAmino-NPyridine Coordination of Aminopyridinato Ligands. *Eur. J. Inorg. Chem.* **2003**, 791–803 (2003).
290. Forberg, D. *et al.* Single-catalyst high-weight% hydrogen storage in an N-heterocycle synthesized from lignin hydrogenolysis products and ammonia. *Nat. Commun.* **7**, 13201 (2016).
291. Glatz, G. *et al.* Copper-containing SiCN precursor ceramics (Cu@SiCN) as selective hydrocarbon oxidation catalysts using air as an oxidant. *Chemistry* **16**, 4231–8

- (2010).
292. Zaheer, M., Motz, G. & Kempe, R. The generation of palladium silicide nanoalloy particles in a SiCN matrix and their catalytic applications. *J. Mater. Chem.* **21**, 18825 (2011).
 293. Kamperman, M. *et al.* Integrating Structure Control over Multiple Length Scales in Porous High Temperature Ceramics with Functional Platinum Nanoparticles. *Nano Lett.* **9**, 2756–2762 (2009).
 294. Reid, J. S., Kolawa, E., Ruiz, R. P. & Nicolet, M.-A. Evaluation of amorphous (Mo, Ta, W)–Si–N diffusion barriers for $\langle \text{Si} \rangle$ –Cu metallizations. *Thin Solid Films* **236**, 319–324 (1993).
 295. Kim, K. H., Choi, S. & Yoon, S. Superhard Ti–Si–N coatings by a hybrid system of arc ion plating and sputtering techniques. *Surf. Coatings Technol.* **161**, 243–248 (2002).
 296. Wen, H. C. *et al.* Systematic investigation of amorphous transition-metal-silicon-nitride electrodes for metal gate CMOS applications. *Dig. Tech. Pap. 2005 Symp. on, VLSI Technol.* (2005).
 297. Pant, G., Panchaipetch, P., Kim, M. J., Wallace, R. M. & Gnade, B. E. Low temperature UV/ozone oxidation formation of HfSiON gate dielectric. *Thin Solid Films* **460**, 242–246 (2004).
 298. Miotti, L. *et al.* Thermal stability of nitrated high-k dielectrics. *Phys. status solidi* **201**, 870–880 (2004).
 299. Wang, C. M. Microstructure development of Si₃N₄-TiN composite prepared by in situ compositing. *J. Mater. Sci.* **30**, 3222–3230 (1995).
 300. Hapke, J. & Ziegler, G. Synthesis and pyrolysis of liquid organometallic precursors for advanced Si-Ti-C-N composites. *Adv. Mater.* **7**, 380–384 (1995).
 301. IWAMOTO, Y., KIKUTA, K. & HIRANO, S. Synthesis of Poly-Titanosilazanes and Conversion into Si₃N₄-TiN Ceramics. *J. Ceram. Soc. Japan* **108**, 350–356 (2000).
 302. Sato, K., Saitoh, T., Nagano, T. & Iwamoto, Y. Low Temperature Crystallization Behavior of α -Si₃N₄ from Ti-doped Amorphous Silicon Nitride Derived from Polytitanasilazanes. *J. Ceram. Soc. Japan* **114**, 502–506 (2006).
 303. Zhou, C. *et al.* Synthesis and high-temperature evolution of single-phase amorphous Si-Hf-N ceramics. *J. Eur. Ceram. Soc.* **35**, 2007–2015 (2015).
 304. Bechelany, M. C. *et al.* In situ controlled growth of titanium nitride in amorphous

- silicon nitride: A general route toward bulk nitride nanocomposites with very high hardness. *Adv. Mater.* **26**, 6548–6553 (2014).
305. Zhang, P., Zhang, J. & Gong, J. Tantalum-based semiconductors for solar water splitting. *Chem. Soc. Rev.* **43**, 4395 (2014).
306. Osterloh, F. E. Inorganic nanostructures for photoelectrochemical and photocatalytic water splitting. *Chem. Soc. Rev.* **42**, 2294–2320 (2013).
307. Maeda, K. & Domen, K. New non-oxide photocatalysts designed for overall water splitting under visible light. *J. Phys. Chem. C* **111**, 7851–7861 (2007).
308. Moriya, Y., Takata, T. & Domen, K. Recent progress in the development of (oxy)nitride photocatalysts for water splitting under visible-light irradiation. *Coord. Chem. Rev.* **257**, 1957–1969 (2013).
309. Morbec, J. M., Narkeviciute, I., Jaramillo, T. F. & Galli, G. Optoelectronic properties of Ta₃N₅: A joint theoretical and experimental study. *Phys. Rev. B* **90**, 155204 (2014).
310. Liu, X., Zhao, L., Domen, K. & Takanabe, K. Photocatalytic hydrogen production using visible-light-responsive Ta₃N₅ photocatalyst supported on monodisperse spherical SiO₂ particulates. *Mater. Res. Bull.* **49**, 58–65 (2014).
311. Fu, X., Hu, Y., Yang, Y., Liu, W. & Chen, S. Ball milled h-BN: An efficient holes transfer promoter to enhance the photocatalytic performance of TiO₂. *J. Hazard. Mater.* **244–245**, 102–110 (2013).
312. Liu, D. *et al.* A novel TiO₂-xNx/BN composite photocatalyst: Synthesis, characterization and enhanced photocatalytic activity for Rhodamine B degradation under visible light. *Catal. Commun.* **57**, 9–13 (2014).
313. Di, J. *et al.* Advanced photocatalytic performance of graphene-like BN modified BiOBr flower-like materials for the removal of pollutants and mechanism insight. *Appl. Catal. B Environ.* **183**, 254–262 (2016).
314. Meng, S. *et al.* Selective oxidation of aromatic alcohols to aromatic aldehydes by BN/metal sulfide with enhanced photocatalytic activity. *Appl. Catal. B Environ.* **182**, 356–368 (2016).
315. Alexander A. Gromov, L. N. C. *Nitride Ceramics: Combustion, Synthesis, Properties and Applications*. (Wiley, 2014).
316. Colombo, P. Conventional and novel processing methods for cellular ceramics. *Philos. Trans. A. Math. Phys. Eng. Sci.* **364**, 109–24 (2006).

317. Ewert, J.-K. *et al.* Enhanced capacitance of nitrogen-doped hierarchically porous carbide-derived carbon in matched ionic liquids. *J. Mater. Chem. A* **3**, 18906–18912 (2015).
318. Skinner, D. P., Newnham, R. E. & Cross, L. E. Flexible composite transducers. *Mater. Res. Bull.* **13**, 599–607 (1978).
319. Ceron-Nicolat, B., Fey, T. & Greil, P. Processing of Ceramic Foams with Hierarchical Cell Structure. *Adv. Eng. Mater.* **12**, 884–892 (2010).
320. Pan, J. *et al.* Preparation of SiC nanowires-filled cellular SiCO ceramics from polymeric precursor. *Ceram. Int.* **38**, 6823–6829 (2012).
321. Zeschky, J. *et al.* Preceramic polymer derived cellular ceramics. *Compos. Sci. Technol.* (2003). doi:10.1016/S0266-3538(03)00269-0
322. Jones, B. H. & Lodge, T. P. High-Temperature Nanoporous Ceramic Monolith Prepared from a Polymeric Bicontinuous Microemulsion Template. *J. Am. Chem. Soc.* **131**, 1676–1677 (2009).
323. Kamperman, M., Garcia, C. B. W., Du, P., Ow, H. & Wiesner, U. Ordered mesoporous ceramics stable up to 1500 °C from diblock copolymer mesophases. *J. Am. Chem. Soc.* **126**, 14708–14709 (2004).
324. Yuan, X. *et al.* Synthesis of ordered mesoporous silicon oxycarbide monoliths via preceramic polymer nanocasting. *Microporous Mesoporous Mater.* **147**, 252–258 (2012).
325. Vakifahmetoglu, C., Zeydanli, D. & Colombo, P. Porous polymer derived ceramics. *Materials Science and Engineering R: Reports* (2016). doi:10.1016/j.mser.2016.05.001
326. Yuan, X., Lü, J., Yan, X., Hu, L. & Xue, Q. Preparation of ordered mesoporous silicon carbide monoliths via preceramic polymer nanocasting. *Microporous Mesoporous Mater.* **142**, 754–758 (2011).
327. Wang, J. *et al.* Preparation of cubic ordered mesoporous silicon carbide monoliths by pressure assisted preceramic polymer nanocasting. *Microporous Mesoporous Mater.* **168**, 142–147 (2013).
328. Krawiec, P. *et al.* Ordered mesoporous carbide derived carbons: Novel materials for catalysis and adsorption. *J. Phys. Chem. C* **113**, 7755–7761 (2009).
329. Bernard, S., Majoulet, O., Sandra, F., Malchere, A. & Miele, P. Direct Synthesis of Periodic Mesoporous SilicoBoron CarboNitride Frameworks via the Nanocasting from Ordered Mesoporous Silica with Boron-Modified Polycarbosilazane. *Adv. Eng. Mater.*

- 15, 134–140 (2013).
330. Bernard, S. & Miele, P. Ordered mesoporous polymer-derived ceramics and their processing into hierarchically porous boron nitride and silicoboron carbonitride monoliths. *New J. Chem.* **38**, 1923 (2014).
331. Majoulet, O. *et al.*. Silicon–boron–carbon–nitrogen monoliths with high, interconnected and hierarchical porosity. *J. Mater. Chem. A* **1**, 10991 (2013).
332. Alauzun, J. G. *et al.*. Novel monolith-type boron nitride hierarchical foams obtained through integrative chemistry. *J. Mater. Chem.* **21**, 14025 (2011).
333. Schlienger, S. *et al.*. Micro-, Mesoporous Boron Nitride-Based Materials Templated from Zeolites. *Chem. Mater.* **24**, 88–96 (2012).
334. Bernard, S. & Miele, P. Nanostructured and architected boron nitride from boron, nitrogen and hydrogen-containing molecular and polymeric precursors. *Materials Today* **17**, 443–450 (2014).
335. By Tosaka - Own work, CC BY 3.0,
<https://commons.wikimedia.org/w/index.php?curid=4484785>
336. <https://energy.gov/eere/fuelcells/hydrogen-storage>
337. By Elcap - Own work, CC0,
<https://commons.wikimedia.org/w/index.php?curid=25527749>
338. By Prussianblue1403 - Using VESTA software Previously published: NO, CC BY-SA 3.0, <https://en.wikipedia.org/w/index.php?curid=45091060>

CHAPTER 2

MATERIALS AND

METHODS



1. Introduction

The various ceramic systems were synthesized keeping in mind the properties required in their intended final application. This chapter represents the experimental part of this manuscript. We firstly discuss on the use of commercial polymers and synthesis of the home-made preceramic polymers for preparing non-oxide ceramics like Silicon Carbide (SiC), Silicon Nitride (Si_3N_4), Silicon Carbonitride (Si-C-N) and BN, as well as (nano)composite systems like Metal Nitride (Ti, Zr, Hf)/Silicon (Carbo) Nitride and Metal Nitride (Ti, Zr, Hf)/Boron Nitride as presented in chapters 3 and 4. Secondly, we describe the process to prepare mesoporous monoliths made from the above mentioned compositions to be used in various applications like hydrogen generation from chemical hydrides from aqueous media as discussed in chapter 5. Thirdly, the synthesis of MXene/SiCN composites is detailed. They are prepared for electrocatalysis tests as reported in chapter 5. Finally the chapter ends with the detail of the various tools used for the characterization of the materials at each step of their preparation.

2. Molecular precursors and preceramic polymers

All chemical products are handled in an argon-filled glove box (MBraun MB200B; O_2 and H_2O concentrations kept at < 0.1 ppm). The preceramic polymers were synthesized under argon atmosphere due to their sensitivity to air and moisture. Argon ($> 99.995\%$) is purified by passing through successive columns of phosphorus pentoxide, siccapentTM, and BTS catalysts. Schlenk flasks are dried at 120°C overnight before pumping under vacuum and filling them with argon for synthesis.

2.1 Presentation of the commercially-available organosilicon polymers

The following organosilicon polymers were briefly discussed in the first chapter. Here we detail the physical properties and the nature of these polymers. Table 2.1 details the list of commercial polymers and solvents used.

Table 2. 1 List of various chemicals used along with their manufacturer details and commercial name

Product	Manufacturer	Commercial Name
AHPCS (allylhydridopolycarbosilane)	Starfire Systems	AHPCS SMP10
HTT1800 (polycarbolsilazane)	Clariant Advanced Chemicals	HTT1800
PHPS (perhydropolysilazane)	Mitsuya Boeki Ltd.	Aquamica NN-120
Ammonia Borane	Sigma-Aldrich	Borane-ammonia complex 97%
Toluene	Acros Organics	99.85 %, Extra Dry over Molecular Sieve, AcroSeal(R)
Tetrahydrofuran	Sigma-Aldrich	Tetrahydrofuran anhydrous, $\geq 99.9\%$, inhibitor-free

1) Perhydropolysilazne (PHPS)

This is polysilazane free of any carbon atom. It has Si, N and H as its constituent elements and is the precursor used to prepare Si_3N_4 (figure 2.1). It can be synthesized by different route like ammonolysis of dichlorosilane (H_2SiCl_2) in benzene as solvent¹.

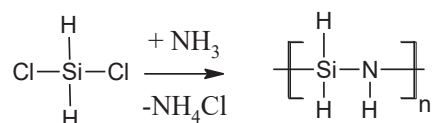


Figure 2.1 Synthesis of perhydropolysilazane from dichlorosilane

Due to the highly reactive nature of dichlorosilane to air and moisture and its hazardous nature, it is complex to synthesize it in academic laboratory.

As a consequence, we obtain PHPS from Aquamica (Japan) under brand name NN110-20. It is 20 vol% solutions in xylene. It is a transparent liquid with a density of $1.1\text{g}\cdot\text{cm}^{-3}$ ($0.92\text{g}\cdot\text{cm}^{-3}$ with solvent) and viscosity of 30-50 mPa.s at 25°C . It can have a ceramic yield up to 80% depending on the pyrolysis atmosphere. It is heavily used in the electronic industry to synthesize SiO_2 films and make dielectrics. Now Merck manufactures PHPS through a subsidiary DurXtreme®. The polymer is investigated in chapter 4 and chapter 5.

2) Poly(methylvinyl)-co-(methyl)silazane HTT1800®:

HTT1800 is a polycarbolsilazane commercially known as KiON-HTT1800® and sold by Clariant Technologies (Germany). It is a co-polymer composed of various reactive

sites such as vinyl, Si-H and N-H groups (Figure 2.2). Upon pyrolysis at 1000°C under N₂ it gives Si-C-N ceramic while under NH₃ it gives Si₃N₄, although the yield is lower. Due to the presence of methyl and vinyl groups it can have free carbon in the ceramics.

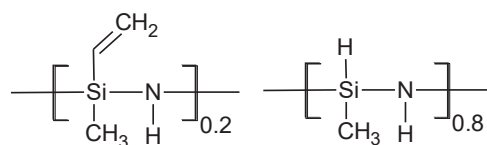


Figure 2.2 Chemical formula HTT1800

Table 2.2 Physical properties of HTT1800

Properties	HTT 1800
Viscosity	20-50 mPa.s
Density	1.0 g.cm ⁻³
Fire point	16.25°C
Shelf Life	24 months from date of manufacture at 20°C
Solubility	Hexane/Toluene/Insoluble in water
Crosslinking temperature	175-200°C
Appearance	Pale yellow liquid

This liquid polycarbosilazane is most often used in infiltration processes and as a coating due to its low viscosity and good adhesion. It is now sold by Merck with the commercial name Durazane. The polymer is investigated in chapter 4 and 5.

3) Allylhydridopolycarbosilane (AHPCS):

AHPCS is commercially sold as SMP-10 by Starfire Systems®, USA. It is a preceramic polymer to synthesize Silicon Carbide (SiC). It is a yellow colored viscous liquid.

Table 2.3 Physical properties of AHPCS

Properties	AHPCS SMP-10
Viscosity	0.1 Pa.s

Density	0.998 g.cm ⁻³
Fire Point	89°C
Surface Tension	30 dynes.cm ⁻²
Solubility	Hexane/Toluene/Insoluble in water
Cross-linking Temperature	121-124°C

It is a hyper-branched polycarbosilane (figure 2.3). Whitmarsh and Interrante² were the first to synthesize hydridopolycarbosilane (HPCS), a predecessor of AHPCS, by reaction between a Grignard reagent and (chloromethyl)trichlorosilane followed by reduction with lithium tetrahydroaluminate (LiAlH₄). It is a precursor comprising silicon-bonded hydrogen atoms and leading to the stoichiometric SiC 1:1, i.e., free of any free-carbon. Substitution of 5-10 % of the Si-X groups (X= H, Cl) in HPCS with Si-allyl groups before reduction with LiAlH₄ lead to the formation of AHPCS which had better cross-linking properties and a higher ceramic yield as compared to HPCS.

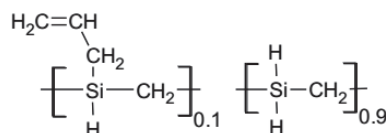


Figure 2.3 Chemical formula AHPCS

2.2 BN precursors

1) Ammonia Borane: Ammonia borane (>98%) is supplied by Sigma Aldrich as a part of their hydrogen generation kit. It is a white crystalline solid first synthesized by Shore and Parry in 1955. It is also used as one of the monomeric BN generators. Upon pyrolysis it undergoes crosslinking to first form diborane which further converts to borazine and polyborazine at high temperature and finally gets converted to boron nitride as shown in the following figure 2.4³. Ammonia borane is investigated in chapter 3.

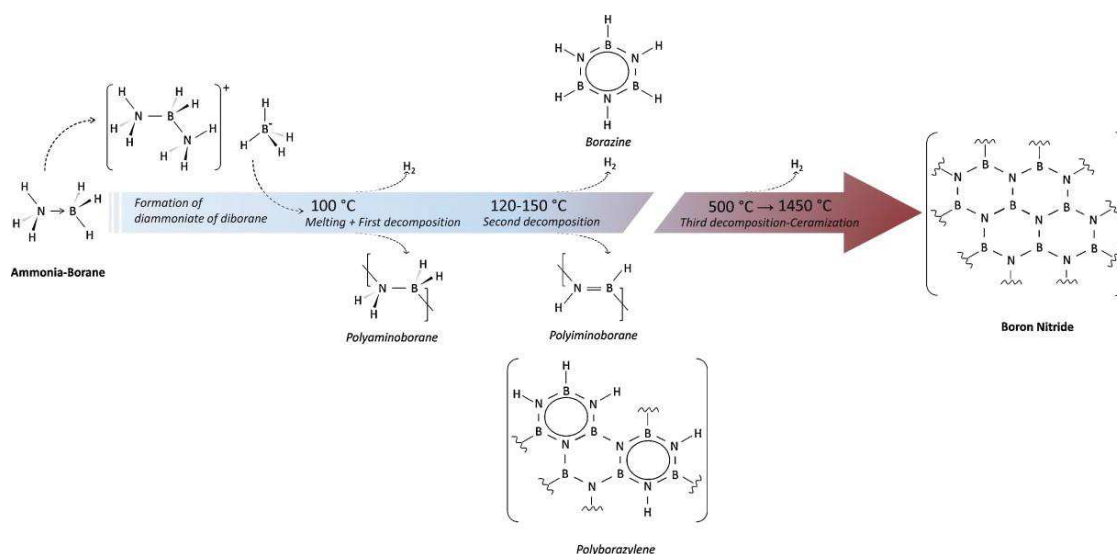


Figure 2.4 Thermal conversion of Ammonia-borane into BN along with intermediate products

2) Borazine and polyborazylene: Any potential polymeric precursor for BN should have good ratio of B:N and should (Figure 2.5) have H as the only other element apart from B and N. Borazine (BZ) ($\text{H}_3\text{B}_3\text{N}_3\text{H}_3$), a preformed six-membered hexagonal planar ring, has the correct elemental composition for forming BN. It was first discovered by Stock in 1926 but it was only in 1995 that Sneddon *et al.* synthesized it economically by reaction between $(\text{NH}_4)_2\text{SO}_4$ and NaBH_4 in tetraglyme in a low temperature range (120°C to 140°C)⁴.

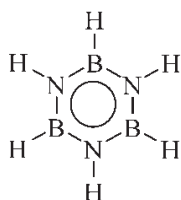


Figure 2.5 Simple structure of borazine

We used the same reaction to synthesize borazine and the initial reactants were supplied by Sigma Aldrich. Due to its high volatility sometimes it is used as its polymeric form polyborazylene (PBZ) (Figure 2.6). BZ is polymerized to PBZ by dehydrocoupling between B-H and N-H during thermolysis in an autoclave. The autoclave is sealed with BZ at 0°C under an argon atmosphere and heated to 45°C to 60°C temperature range to produce different types of PBZ. These change viscosity and state as we move from 45°C to 60°C . The PBZ obtained at 60°C labelled as **PB60**, is

solid and used for further experiments. Figure shows the general structure of PBZ, it is either a biphenylic or naphthalenic type structure.

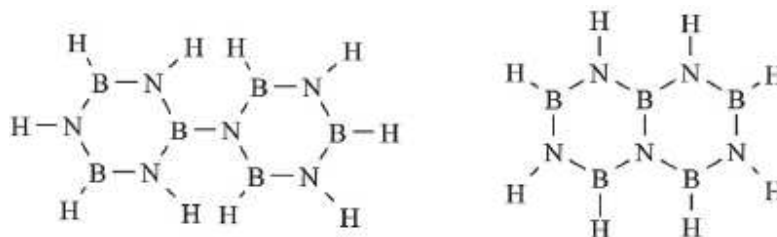


Figure 2.6 Biphenylic and naphthalenic structures of polyborazylene

3. Li modified BN precursor: The presence of first group light elements like Li, Na is known to improve the crystallization of BN produced by powder metallurgy. For this purpose we synthesized a Li modified BNH precursor which will give BN upon pyrolysis. The reaction was carried in two ways: solution synthesis and reactive ball milling. Solution synthesis is carried out in an inert atmosphere in an ice bath at 0°C as the reactivity of LiNH₂ is very high. LiNH₂ is added to a solution of ammonia borane in THF drop by drop using an addition ampule with B:Li molar ratio of 1:1. Once the entire Li precursor was added the reaction temperature was increased to 40°C and allowed to continue for 24 hours. After this solvent was removed under reduced pressure using a recovery Schlenk Distillation Bridge and a liquid nitrogen trap. A white insoluble powder was obtained after drying which was named ABLi1. While for reactive ball milling, the powders were added to the reactor in a glove box in 1:1 ratio by mole (1:5 weight ratio of powder and balls) and then ball milled at 200 rpm for 4 hours with 10 min intervals. The retrieved powder was labelled **ABLi1-BM**.

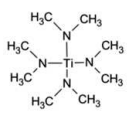
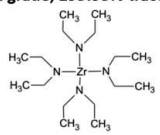
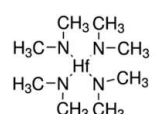
2.3 Synthesis of metal-modified organosilicon polymers and BN precursors

The modification of organosilicon polymers including PHPS and HTT1800 and BNH precursors including AB, BZ and PBZ occurs by their reaction with tetrakisdiethylaminometallics. The characterization and behavior of metal modified organosilicon polymers and BNH precursors are discussed in chapter 3 and 4. In chapter 5 these are used to prepare mesoporous monoliths.

2.3.1 Tetrakis(dialkylamido)metallics:

Tetrakis(dialkylamido)metallics of Titanium (Ti), Zirconium (Zr) and Hafnium (Hf) were used as sources for metal nitrides in this study. These are commercially available at Sigma Aldrich with a purity of 99.999%. These amines are pungent smelling corrosive liquids in case of Ti and Zr and solid in case of Hf at room temperature. They are highly volatile precursors, sensitive to air and moisture and hence were always handled under inert atmosphere. Table 2.4 below shows the structure of the precursors and some basic properties.

Table 2.2 Different types of metallic amino precursors with physical characteristics

Metal Precursor	Molecular weight (g .mol ⁻¹)	Density at 25°C (g .ml ⁻¹)	Boiling point (°C)
Tetrakis(dimethylamido)titanium(IV) (TDMATi) 99.999% trace metals basis 	224.17	0.947 (orange liquid)	50
Tetrakis(diethylamido)zirconium(IV) (TDEAZr) electronic grade, ≥99.99% trace metals basis 	379.74	1.026 (yellow liquid)	128
Tetrakis(dimethylamido)hafnium(IV) (TDMAHf) ≥99.99% 	354.79	1.098 (white solid)	26-29 (melting point)

2.3.2 Synthesis of metal-modified organosilicon polymers

The synthesis of polymetallosilazane and poly(metallo)carbosilazane is done by a simple reaction between the silazane like PHPS or HTT1800 and the metallic precursors TDMAT, TDEAZr or TDMAHf with a fixed ratio. To illustrate the process, we explain synthesis of NCPTi2.5-RT, made from reacting PHPS and TDMAT with a Si/Ti molar ratio of 2.5. Other polymers can be synthesized in the same manner just by changing the polysilazane, metal precursor and the Si/M ratio.

The Si/Ti molar ratio is set to be 2.5. To achieve this, the following equation is followed:

$$\frac{n(\text{PHPS})}{n(\text{TDMATi})} = 2.5$$

A specific quantity of TDMAT (17.84 mmol) is added dropwise to a 10 g solution of PHPS in xylene (20 vol%) dissolved in 150 ml of toluene at ambient temperature under an inert atmosphere. The system is prepared as shown in Figure 2.7 and the reaction is connected to a bubbler for the gaseous byproduct to escape the system. The mixture is stirred for 3 hours and the solution changes color from yellow or orange to black or dark. At the end of three hours the system is heated to 115°C (reflux temperature of toluene) for three days to allow the reaction to approach completion.

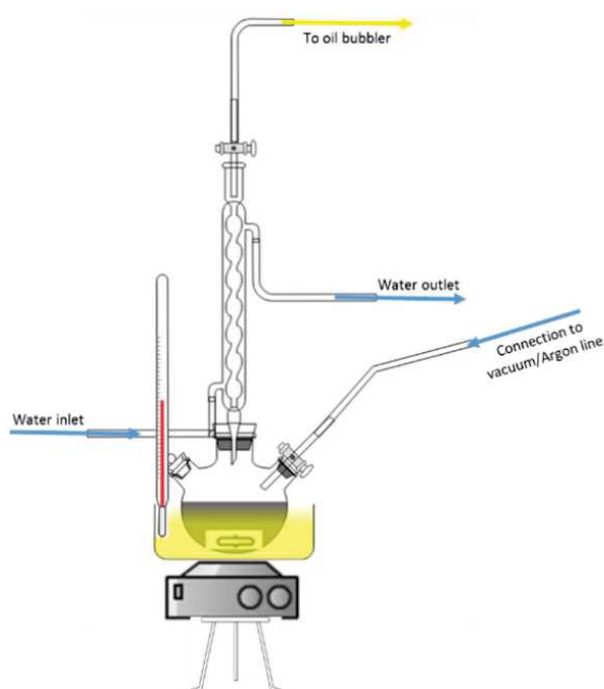


Figure 2. 7 Polymetallosilazane reaction setup

After three days the reaction mixture is cooled down to ambient temperature and the solvent is removed under reduced pressure at room temperature using a distillation bridge, recovery Schlenk and a liquid nitrogen trap as shown in the Figure 2.8.

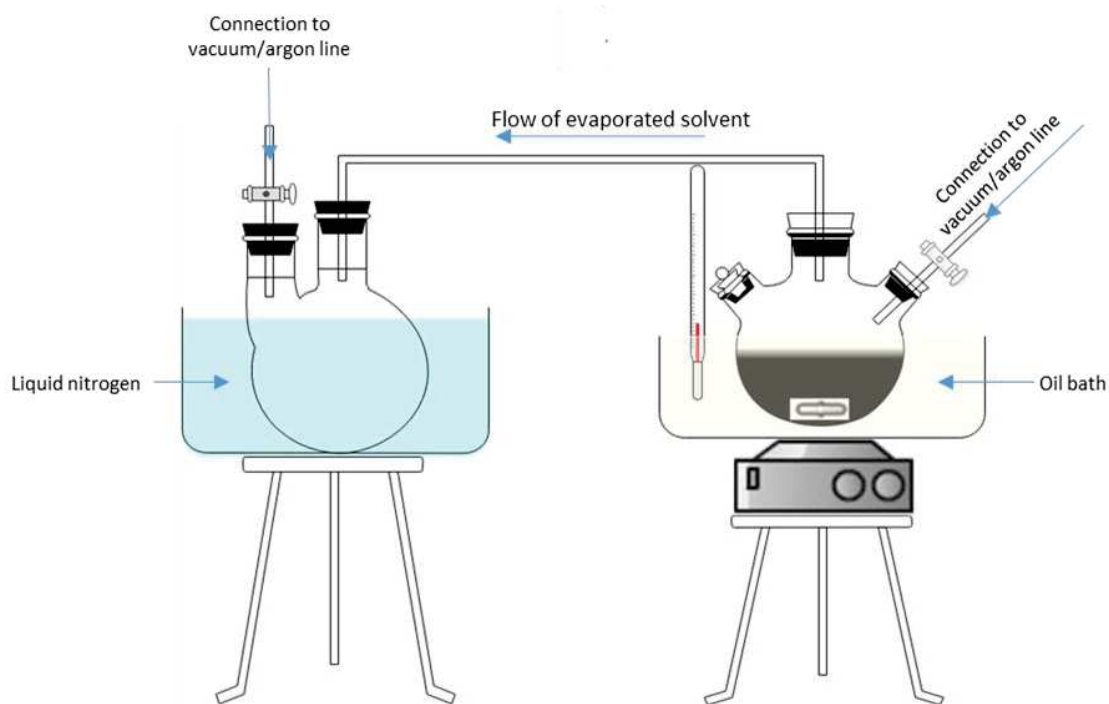


Figure 2.8 Solvent extraction setup from polymetallosilazane

A dried black metallic looking powder was obtained in the Schlenk. It was heated till 60°C for 1 hour under reduce pressure to remove any traces of solvent.

Depending on the metal precursor, polysilazane and the Si/M molar ratio, the final product can range from a dark black liquid to a bright yellow powder. Various polymetallosilazanes were synthesized namely, *NCPMX* (X=Si/Ti = 1, 2.5, 5) (M=Ti, Zr, Hf) (PHPS-M precursor) and *NCHMX* (X=Si/Ti = 1, 2.5) (M= Ti, Zr, Hf) (HTT1800-M precursor). The physical state of these polymer ranges from viscous liquids to solid powders.

2.3.3 Synthesis of metal-modified BNH precursors

The synthesis of transition metal modified BNH precursors is very similar to the previously described process of polymetallosilazane. A reaction between BNH precursors and metallic precursors leads to formation of polymetalloborane. The following equation is used to fix the molar ratio between B/M.

$$\frac{n(\text{Ammonia borane})}{n(\text{TDMATi})} = 3$$

To illustrate the process, we describe the synthesis of **ABTi3** sample from ammonia borane and TDMAT with a B/Ti molar ratio of 3. Other polymers can be synthesized in the same

manner but we should take care that the B content in ammonia borane, PZ and PBZ are different. A fixed quantity of TDMAT (17.84 mmol) is added dropwise to a 1.65 g of Ammonia borane solution in 120 ml of THF at ambient temperature under inert atmosphere using a setup similar to shown in Figure 2.9. The system is prepared as shown in the figure and the reaction is connected to a bubbler for the gaseous byproduct to escape the system. The mixture is stirred for 3 hours and the solution changes color from yellow or orange to black or dark. At the end of three hours the system is heated to 75°C (reflux temperature of THF) for three days to allow the reaction to approach completion. After three days the reaction mixture is cooled down to ambient temperature and the solvent is removed under reduced pressure at room temperature using a distillation bridge, recovery Schlenk and a liquid nitrogen trap as shown in Figure 2.8. A dried black metallic looking powder was obtained in the Schlenk. It was heated till 60°C for 1 hour under reduce pressure to remove any traces of solvent. The black powder obtained is a polytitanoborane.

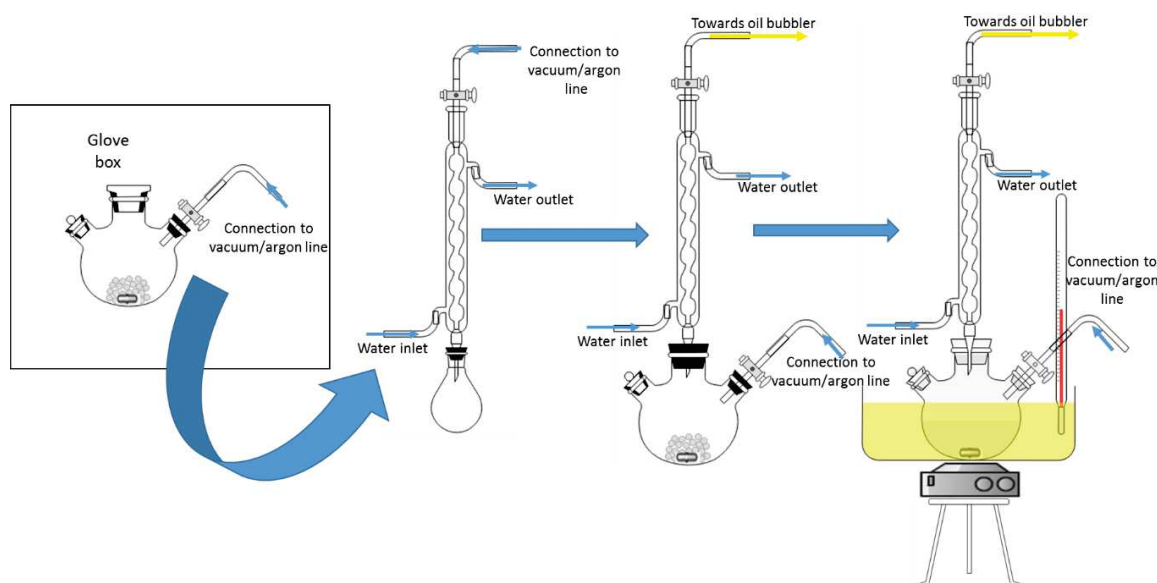


Figure 2. 9 Step by Step schematic of polymetalloborane synthesis

Depending on the B precursor used we can obtain different precursors like polymetalloborazine, borazine or polyborazylene is used. The powder changes color (light to dark) as the B/M ratio decreases. The following table shows all the polymetalloboranes and polymetalloborazines synthesized. The ammonia borane based nanocomposites were denoted by **ABMX** (X=B/M=1, 3, 5) (M=Ti, Zr, Hf).

Table 2.3 Different types of polymetallobranes/borazines synthesized

Sample Name	BN precurosr	Metal precursor	B/M ratio
ABTi3	Ammonia borane	TDMAT	3
ABTi1	Ammonia borane	TDMAT	1
ABTi5	Ammonia borane	TDMAT	5
ABZr3	Ammonia borane	TDEAZr	3
ABHf3	Ammonia borane	TDMAHf	3
PB60Ti3	Polyborazylene	TDMAT	3

3. Pyrolysis of preceramic polymers as powders

The powder was transferred into a silica tube inserted in a horizontal tube furnace (Thermoconcept® OS50/450/12) under an argon flow. The tube was pumped under vacuum for 30 min and then refilled with argon, nitrogen or ammonia depending on the chemistry of polymers. For AHPCS, pyrolysis was done under Argon. For PHPS and PHPS derived polymetallosilazane it was done under ammonia and for HTT1800 and its derived polymetallosilazane the pyrolysis was performed both under nitrogen and ammonia. For BNH precursors and their derived polymetalloboranes pyrolysis was performed under ammonia. The powder was heated till 1000°C for 2 hours under ammonia with a heating and cooling rate of 5°C/min. These samples underwent heat-treatment at higher temperature using a graphitic furnace (Gero Model HTK 8). The furnace is pumped out for 30 min then refilled with nitrogen (200 mL/min) before undergoing a cycle consisting of ramping at 5°C/min to the final temperature, remaining there for 2 hours and then cooling down to RT at 2°C/min.

4. Preparation of mesoporous monoliths via nanocasting using template

Preceramic polymers were used to prepare 3-D mesoporous monoliths by nano-casting technique in chapter 5.

4.1 Nanocasting using template

Nanocasting refers to replicating the structure of template material on to an intended material by impregnating the template with the precursor and then removing the template while converting the precursor into a solid using either heat or light (figure 2.10)

Activated carbon monolith has been used as a template. It is labelled as *ACM*. Before using as template it is passivated, i.e., removal of any residual oxygen, moisture or dangling groups (-OH, -COOH), under vacuum (5×10^{-1} mbar) at 600°C for 10 hours in a tubular furnace without any structural modifications. The activated carbon used for templating has the following structural and textural properties: monolith/rod type; specific surface area of 953 m² g⁻¹ and 5.2 nm of pore size. The treated monoliths were transferred in to the glove box to be stored under inert atmosphere. A specific amount of *ACMs* are weighed and taken in a Schlenk flask. The Schlenk is put under dynamic vacuum for 30 mins to remove any inert gas from the porosities.

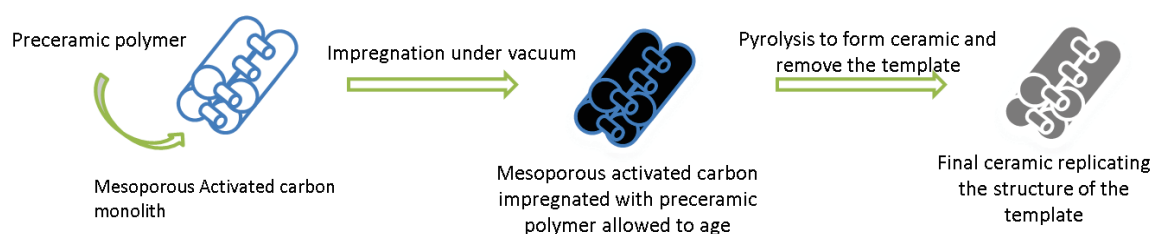


Figure 2.10 Schematic of nanocasting route

4.2 Mesoporous SiC and Si-C-N monoliths

The preceramic polymers, stored in Schlenks, are infiltrated into the *ACM* under reduced pressure conditions to allow better impregnation in to the porosities of the template. The amount of preceramic polymer infiltrated is calculated using an optimum mass ratio between the polymer and the monolith. The system was sonicated for 24 hours while the being under static vacuum. This was followed by washing off excess polymer from the monoliths by toluene under inert gas flow. The system was again put under dynamic vacuum for one hour to allow the monoliths to dry. This generated the impregnated monoliths labelled *AHPCS/ACM* and *HTT1800/ACM*.

The Schlenk was taken to the glove box to store the monoliths in an inert atmosphere before being transferred into a tubular furnace for pyrolysis. The samples are transferred into a silica tube inserted in a horizontal tube furnace (Thermoconcept® OS50/450/12) under an argon flow. The tube is pumped under vacuum for 30 min and refilled with argon (*AHPCS/ACM*) and nitrogen (*HTT1800/ACM*) (120 mL min^{-1}) to be subjected to a cycle of ramping at 1°C min^{-1} to 1000°C, dwelling there for 2 h. Then cooling to RT is carried out at 2°C min^{-1} to produce samples *SiC/ACM* (obtained from *AHPCS/ACM*) and *Si-C-N/ACM*

(obtained from *HTT1800/ACM*). We apply higher temperatures using a graphitic furnace (Gero Model HTK 8) to follow the evolution of their porosity as a function of the pyrolysis temperature. The furnace is pumped out for 30 min then refilled with argon (*SiC/ACM*) or nitrogen (*Si-C-N/ACM*) (200 mL min⁻¹) before undergoing a cycle consisting of ramping at 5°C min⁻¹ to the final temperature, remaining there for 2 h and then cooling down to RT at 2°C min⁻¹. Then, as-received samples undergo heat-treatment under air (to remove the *ACM*) in a muffle furnace (Thermoconcept® KLS03/10) through a cycle of ramping of 1°C min⁻¹ to 600°C, dwelling there for 5 h, and then cooling to RT at 1°C min⁻¹. Samples are labelled **mSiCX** and **mSi-C-NX** (X being the two first numbers of the final temperature, *e.g.*, 12 for 1200).

4.3 Mesoporous Si₃N₄, Si-M-N and B-M-N monoliths

The synthesis of mesoporous silicon nitride, Si-based metal nitride nanocomposite and B-based metal nitride nanocomposite are done using the same nanocasting technique as mentioned above. It differs from SiC and Si-C-N in its pyrolysis procedure. The pyrolysis procedure applied to all nitride based systems is similar. Although the pyrolysis procedure is same for both simple nitride and nanocomposite nitride, we explain them separately so as to avoid confusion in naming the systems.

4.3.1 Mesoporous PHPS derived Si₃N₄ monolith

The infiltration of preceramic polymer was done following the same protocols as before and the infiltrated monolith was named as *PHPS/ACM*. For pyrolysis 3 different strategies are applied. In a first strategy, the tube is filled with nitrogen to be subjected to a cycle of ramping at 1°C min⁻¹ to 1000°C; dwelling there for 2 h. Cooling to RT is carried out at 2°C min⁻¹ generating samples *Si₃N₄-Si/ACM*. After the polymer-to-ceramic conversion process, the samples *Si₃N₄-Si/ACM* undergo a further heat-treatment under ammonia (to remove the *ACM*) at 5°C min⁻¹ to 1000°C, dwelling there for 5 h. Cooling produces the mesoporous Si₃N₄ monoliths labelled **mSi₃N₄1010**. In a second strategy, the tube is filled with ammonia to be subjected to a cycle of ramping at 1°C min⁻¹ to 1000°C, dwelling there for 5 h. Cooling directly produces the mesoporous Si₃N₄ monoliths labelled **mSi₃N₄10**. In a third strategy, the tube is filled with nitrogen to be subjected to a cycle of ramping at 1°C min⁻¹ to 400°C, dwelling there for 1 h then under ammonia at 1°C min⁻¹ to 1000°C, dwelling there for 5 h. Cooling directly produces the mesoporous Si₃N₄ monoliths labelled **mSi₃N₄410**. The sample **mSi₃N₄410** undergoes heat-treatment at higher temperature using a graphitic furnace (Gero Model HTK

8) to follow the evolution of its porosity as a function of the pyrolysis temperature. The furnace is pumped out for 30 min then refilled with nitrogen (200 mL min^{-1}) before undergoing a cycle consisting of ramping at 5°C min^{-1} to the final temperature, remaining there for 2 h and then cooling down to RT at 2°C min^{-1} to generate the samples **mSi₃N₄1X** (X being the second number of the temperature, *e.g.*, 2 for 1200°C).

4.3.2 Polymetallosilazane/borane derived mesoporous monoliths

The polymetalosilazane/borane (before extraction from solvent $\sim 5\text{wt}\%$), are infiltrated into the *ACM* under reduced pressure conditions to allow better impregnation in to the porosities of the template. The amount of preceramic polymer infiltrated is calculated using an optimum mass ratio between the polymer and the monolith. The system was sonicated for 24 hours while the being under static vacuum. This was followed by washing off excess polymer from the monoliths by toluene under inert gas flow. The system was again put under dynamic vacuum for one hour to allow the monoliths to dry. The generated monoliths are labelled *NCPMX/ACM* (polymetallosilazane prepared from PHPS), *NCHMX/ACM* (polymetallosilazane prepared from HTT1800) and *NCABMX/ACM* (polymetalloborane prepared from ammonia borane). The infiltrated monoliths were stored in the glove box being transferred into silica tube inserted in a horizontal tube furnace (Thermoconcept® OS50/450/12) under Argon flow. The polymer to ceramic conversion and removal of template was done under a single pyrolysis. The samples were treated under different conditions to find the optimum settings to achieve maximum SSA and mechanical stability. In a first strategy, the tube is filled with nitrogen to be subjected to a cycle of ramping at 1°C min^{-1} to 1000°C ; dwelling there for 2 h. cooling to RT is carried out at 2°C min^{-1} . After the polymer-to-ceramic conversion process, the samples undergo a further heat-treatment under ammonia (to remove the *ACM*) at 5°C min^{-1} to 1000°C , dwelling there for 5 h. Cooling produces the mesoporous Si-M-N or B-M-N monoliths. In a second strategy, the tube is filled with ammonia to be subjected to a cycle of ramping at 1°C min^{-1} to 1000°C , dwelling there for 5 h. Cooling directly produces the mesoporous Si-M-N or B-M-N monoliths. In a third strategy, the tube is filled with nitrogen to be subjected to a cycle of ramping at 1°C min^{-1} to 400°C , dwelling there for 1 h then under ammonia at 1°C min^{-1} to 1000°C , dwelling there for 5 h. Cooling directly produces the mesoporous Si-M-N or B-M-N monoliths labelled **mNCPMX10**, **mNCHMX10** and **mNCABMX10**. The samples **mNCPMX10**, **mNCHMX10** and **mABMX1000** undergo heat-treatment at higher temperature using a graphitic furnace (Gero Model HTK

8) to follow the evolution of its porosity as a function of the pyrolysis temperature. The furnace is pumped out for 30 min then refilled with nitrogen (200 mL/min) before undergoing a cycle consisting of ramping at 5°C/min to the final temperature, remaining there for 2 hours and then cooling down to RT at 2°C/min to generate the samples **mNCPMX-Y**, **mNCHMX-Y** and **mABMX-Y** (M is Ti, Zr, Hf; X is the molar ratio between Si/M and Y is the first two numbers of crystallization temperature of the sample, for eg **mNCPTi2.5-14** stands for Si-Ti-N nanocomposite with a Si/Ti ratio of 2.5 and annealed till 1400°C).

4.4 Deposition of Platinum Nanoparticles (np-Pt) on the ceramic monoliths

The platinum nanoparticles (Pt NPs) synthesized from the precursor $\text{H}_2\text{PtCl}_6 \cdot 6\text{H}_2\text{O}$ were supported over the mesoporous Si-based non-oxide ceramic/nanocomposite monoliths with the highest SSA in each system by wet impregnation followed by heat-treatment under a hydrogen/argon flow. A low platinum loading was targeted (1 wt. %). The platinate was dissolved in 1 ml filtered water (obtained from Millipore systems $\Omega < 18 \text{ S m}^{-2}$) and ultrasonicated for 30 min generating a yellowish solution. The mesoporous Si-based non-oxide ceramic/nanocomposite monoliths were suspended in 2.5 ml of filtered water and the platinate solution was added to this. The mixtures were allowed to age under sonication for 24 hours. The mixtures were then dried at 80°C overnight and then heat treated under diluted H_2 flow (5 % H_2 and 95 % Ar) at 450°C for 4 h to reduce the platinate to platinum and generate the materials labelled **Pt-mSi₃N₄X**, **Pt-mSiCX**, **Pt-mSi-C-NX** where X is the first two numbers of the crystallization temperature of sample with highest specific surface area in case of binary systems and **Pt-mNCPMX-Y** and **Pt/mNCHMX-Y**, where M is Ti, Zr, Hf; X is the molar ratio between Si/M and Y is the first two numbers of crystallization temperature of the sample, for eg. **Pt-mNCPTi2.5-14** stands for Si-Ti-N nanocomposite with a Si/Ti ratio of 2.5 and annealed till 1400°C before Pt deposition. For comparison, **Pt/ACM** was prepared following the same experimental procedure.

5. Preparation of MXene/SiCN composite

2D MAX phase known as MXene is prepared by the following route. Ti_3AlC_2 MAX phases were synthesized using a conventional powder metallurgy technique. Titanium (-200 mesh, 99,95%, Alfa Aesar Karlsruhe Germany), titanium carbide TiC (4 μm , 99,5%, Alfa Aesar) and aluminum (60-100 mesh 99,8%, Alfa Aesar) were used as starting materials. The powders

were weighted according to the desired composition (Ti_3AlC_2) except for Al which was introduced with a 10 wt% excess in order to compensate its loss by evaporation during the sintering process. After mixing for 30 min (Turbula Shaker Mixer), a homogeneous mixture without agglomerates is obtained. This mixture was then packed into a glass tube sealed under vacuum. The sintering has been performed in a Nabertherm furnace under argon atmosphere for 2 h at 1450°C . Finally, the powders were sieved in order to select MAX phases with grain sizes lower than $25\ \mu\text{m}$. The as obtained powder was sonicated for 2 hours in filtered water to open up the structure and form a layered structure. The solution was dried in a hot air oven at 80°C for 24 hours. The powder was then transferred into a 25 mL long Schlenk closed using a septum. The system was put under dynamic vacuum (5×10^{-1} mbar) for 2 hours. HTT1800 (polycarbolsilazane) was injected into the Schlenk under this reduced pressure to allow popper impregnation of the polymer into the spaces between the MXene layers. Various mass ratios between HTT1800 and MXene were synthesized ranging from excess MXene to excess HTT1800. The system was sonicated for 24 hours before being transferred into silica tube inserted in a horizontal tube furnace (Thermoconcept® OS50/450/12) under argon flow. The tube was put under dynamic vacuum for 30 mins before being refilled by argon. The polymer to ceramic conversion was carried out at 800°C under 200 ml/min flow of argon. The temperature was ramped upto 800°C at a rate of $1^\circ\text{C}/\text{min}$. It was held at 800°C for 2 hours before being cooled down to room temperature at a rate of $2^\circ\text{C}/\text{min}$. The prepared sample was labelled as *X-SiCN/MXene* (X is the mass ratio between HTT1800 and MXene).

6. Synthesis of Pt/Si-C-N nanocatalysts

The preparation of Pt/Si-C-N nanocatalysts involved two separate steps: firstly, preparation of Pt complex and secondly preparation of single source polymer. The method is same as described in our paper.⁵

The platinum complex was synthesized adding exchanging existing ligands from a platinum salt with reactive ones. An 8 millimolar solution of Ap^{TMSH} ligand was prepared in diethylether. To this solution we added 8 mmol of n-butyllithium at 0°C . This solution was named L1. The reaction was allowed to continue for two hours with continuous stirring. Another 4 millimolar suspension of $[\text{PtCl}_2(\text{cod})]$ was prepared in diethylether. To this suspension we added the previously prepared L1 solution at 0°C . The mixture was allowed

to warm to room temperature slowly along with continuous stirring for 24 hours. After filtration and crystallization we obtained yellow crystals of the platinum complex ($[\text{Pt}(\text{Ap}^{\text{TMS}})_2]$) with a yield of 85%.

The single source polymer was prepared under inert atmosphere of Ar using a Schlenk line. PEOH was dissolved in toluene at 110°C in round bottom three-necked Schlenk under flow of Argon. HTT1800 was added to this in weight ratio of 30:70 to PEOH. The mixture was held for one hour under static conditions at 110°C. The previously prepared Pt complex was dissolved in toluene and added to the HTT1800-PEOH solution in fixed Pt/Si ratio under Argon flow along with DCP. The mixture was allowed to cross-link at 110°C for 12 hours before being cooled down to room temperature. The solvent was removed under reduced pressure and the single source polymer obtained was named as **NCHPtX**, where X is the ratio between Pt and Si and varies from 1/10 to 1/60.

The samples are transferred into a silica tube inserted in a horizontal tube furnace (Thermoconcept® OS50/450/12) under an argon flow. The tube is pumped under vacuum for 30 min and refilled with argon. The samples were pyrolyzed under a flow of N_2 till 1000°C with a heating ramp of $1^\circ\text{C}\cdot\text{min}^{-1}$ with 2 hour steps each at 200°C, 300°C, 400°C and 500°C. At 1000°C the sample was held only for 30 mins before being cooled down to room temperature at $4^\circ\text{C}\cdot\text{min}^{-1}$. The obtained sample was labelled as **mPt@SiCNX**, where X is the initial Pt:Si ratio in the polymer.

7. Characterization Techniques

7.1 Physico-Chemical Characterizations

a) Elemental Analysis

Elemental analysis was performed on all synthesized pre-ceramic polymers and in some cases intermediate samples at Mikroanalytisches Labor Pascher in Germany. A double determination was performed for all elements present and the samples were handled under inert gas to avoid oxidation.

b) Fourier-transformed Infrared Spectroscopy (FT-IR)

Infrared spectroscopy was performed on all polymer samples at room temperature and samples isolated at intermediate temperatures during pyrolysis. This was done to study the polymer to ceramic conversion mechanism for each polymer.

A Thermofischer Nicolet Nexus FT-IR machine was used to collect the data. Collected data was analyzed using OMNIC32. For samples sensitive to air, the polymer was mixed with KBr and made into pellets to protect it from oxidation, while for ceramic samples the acquisition was done using ATR (Attenuated Total Reflectance) accessory.

c) Raman Spectroscopy

Raman spectroscopy was performed on all ceramic samples treated from 1000°C to 1800°C to study the chemical evolution of ceramic at high temperature and check the presence of free carbon.

It was performed using a M.F.O. microscope from Horiba Scientific. A red laser of wavelength 647.1 nm was used and the reflected signals were collected using a HCX PL FLUOTAR 50x0.55 O/C 8 detector from Leica Microsystems. The data was analyzed using LabSpec software.

d) Nuclear Magnetic Resonance (NMR) Spectroscopy

Liquid-phase NMR analyzes were carried out on Bruker Avance 300 MHz machine using deuterated chloroform as solvent since it is the only solvent in which the polymers dissolve even partially. The data was collected using the software TopSpin and analyzed using Spinwork.

Solid-state NMR is carried out at LCMCP (Université Paris 6) by Dr. Christel Gervais using a Bruker Avance 300MHz. It was used to analyze the nuclei of ^{11}B , ^{29}Si , ^{13}C and ^{15}N .

e) Thermogravimetric analysis (TGA)

TGA was performed on all pre-ceramic polymers to study the polymer to ceramic conversion behavior and to access the yield of the polymer. The experiments were carried out in a SETARAM TGA 92-16-18 apparatus till 1000°C. For TGA analysis between 1000°C and 1800°C a SETRAM Setsys Evolution TGA apparatus was used.

f) Inductively-coupled plasma mass spectrometry

ICP-MS was performed on ceramic samples to know the composition of the ceramics. ICP-MS for Si, Ti, Hf, Zr, B and Pt was carried out by Dr. Johan Alauzun at Institut Charles Gerhardt Montpellier.

g) X-ray diffraction analysis

X-ray diffraction analysis for the ceramic samples was carried out on an X'pert Pro apparatus from Pan Analytical (Philips), using the copper K α line ($= 1.5405\text{\AA}$). Identification of the phases was done using EVA and pdf4+ database provided by ICDD, the diagrams were otherwise processed using LabSpec software.

h) X-ray photoelectron spectroscopy

XPS was carried out on ceramic samples with/without metal nanoparticles to study the interaction between the support and nanoparticles and also to determine the precise amount of nanoparticle loading. It was carried out at Science et Surface Company based in Ecully, France using a PHI Quantera SXM equipment with sputtering upto 20 nm and by Dr. Valérie Flaud at Institut Charles Gerhardt Montpellier using a Thermo Electron ESCLAB 250 and a Al K α line as a monochromatic source of excitation.

i) Brunauer-Emmett-Teller (BET)

Specific surface area for the mesoporous monoliths was determined using the Brunauer-Emmett-Teller (BET) method. The data was collected using a Micromeritics ASAP 2020 apparatus. The pore size distribution was calculated using *Barrett-Joyner-Halenda* (BJH) method. The total pore volume (V_p) is estimated from the amount of N $_2$ adsorbed at a relative pressure of (P/P_0) 0.97.

For samples having Macroporosities a MicroMeritics Autopore IV 9500 was used to perform Hg porosimetry.

7.2 Electron Microscopy

a) Scanning Electron Microscopy

The specimens are observed on a high resolution S4800-FEG SEM from Hitachi. A lower resolution SEM EVO HD 15 from Zeiss was also used to perform Energy dispersive X-ray spectroscopy (EDX) not only for point areas but also for surface mapping of all the elements present.

b) Transmission Electron Microscopy

To analyse the nanocomposite samples with an amorphous matrix and a crystallized second phase TEM was performed at Indian Institute of Technology Madras, Chennai using TECHNAI 20G², FEI instruments, USA using an accelerating voltage of 200 kV & JEOL 3010 (Japan) instrument at an accelerating voltage of 300 kV. It was also used to determine the exact size and agglomeration in the loaded nanoparticles on the support.

References:

1. Birot, M., Pillot, J.-P. & Dunogues, J. Comprehensive Chemistry of Polycarbosilanes, Polysilazanes, and Polycarbosilazanes as Precursors of Ceramics. *Chem. Rev.* **95**, 1443–1477 (1995).
2. Whitmarsh, C. K. & Interrante, L. V. Synthesis and Structure of a Highly Branched Polycarbosilane Derived from (Chloromethyl) trichlorosilane. *Organochemicals* **10**, 1336–1344 (1991).
3. Bernard, S. & Miele, P. Nanostructured and architected boron nitride from boron, nitrogen and hydrogen-containing molecular and polymeric precursors. *Materials Today* **17**, 443–450 (2014).
4. Fazen, P. J. *et al.* Synthesis, Properties, and Ceramic Conversion Reactions of Polyborazylene. A High-Yield Polymeric Precursor to Boron Nitride. *Chem. Mater.* **7**, 1942–1956 (1995).
5. Sachau, S. M. *et al.* Micro-/Mesoporous Platinum@SiCN Nanocomposite Catalysts (Pt@SiCN): From Design to Catalytic Applications. *Chem. - A Eur. J.* **22**, 15508–15512 (2016).

CHAPTER 3
BORON-BASED
NON-OXIDE
CERAMICS



1. Introduction:

In the category of III-V nitrides, boron nitride (BN) is an important compound which is currently considered as a wide band gap semiconductor with a band gap energy corresponding to the UV region. BN is isoelectronic to carbon and thus, in the same way that carbon exists as diamond and graphite, boron nitride can be synthesized in the tetrahedral structure (cubic BN, c-BN) and in a layered structure (hexagonal; h-BN). In h-BN, the in-plane B and N atoms are bounded by strong covalent bonds while the out-of-plane layers are held together by Van der Waals forces. In comparison to graphite, the layered BN hexagons are arranged vertically and each nitrogen atom is surrounded by two boron atoms of the adjacent layers¹. Hexagonal BN (h-BN but expressed in the following discussions as BN) is the most widely studied polymorph. It is the focus of the present chapter.

BN is a synthetic binary compound discovered in the early 19th century and developed as a commercial material at the latter half of the 20th century². This form shows similar physical properties analogous to graphite and like graphite the different bonding cause high anisotropy of the properties of the layered BN. It displays good lubricating properties according to its layered structure (weakly held layers can slide over each other). It displays a very high thermal conductivity (in the direction of hexagons), a high thermal stability, a high resistance to corrosion and oxidation as well as a strong UV emission. It is not wetted by most molten metals such as aluminium, iron and copper as well as hot silicon, glasses and salts and hence has a high resistance to chemical attack. It is nontoxic and it has good environmental compatibility. Unlike graphite, it offers high dielectric breakdown strength and high volume resistivity. As a consequence, the layered BN displays unique combination of properties that distinguish it from graphite and allow it to be potentially applied in a wide range of application.

Because transition metal nitrides in general exhibit extremely high melting points, high hardness and wear resistance, one can anticipate that a B-M-N (M = Ti, Zr, Hf) composite phase may adapt the combined advantages of the two phases and exhibit a better performance than either of the single phases made by metal nitride or boron nitride alone. Furthermore, because of the layered, graphite-like, BN structure, the BN matrix in the B-M-N ceramics is expected to act as solid lubricant in a similar way as the “diamond-like carbon”, DLC, does in the TiC/C coatings. However, the B-M-N ceramics may have some potential

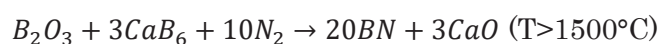
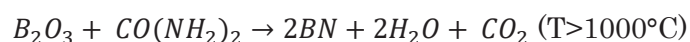
disadvantage in dry machining due to the low oxidation resistance of BN, especially if it is not prepared in its purely hexagonal phase.

In this chapter we discuss the synthesis and characterization of boron nitride (BN) -based nanocomposites. These nanocomposites are made of MN nanocrystals ($M = \text{Ti, Zr, Hf}$) dispersed in a BN matrix. They are prepared by chemical modification of BN precursors like ammonia borane (AB) and polyborazylene (PB) with organometallic precursors. In particular, we will investigate the synthesis pathway to produce these nanocomposites. By the combination of infrared spectroscopy and solid state NMR, we will give a detailed view on the polymer structural characteristics in order to confirm the reproducibility of the synthesis pathway. We will investigate the influence of the amount of metals on the synthesis of polymers with a particular attention on the effect on their ceramic yield to form the B-M-N ($M = \text{Ti, Zr, Hf}$) ceramics and the high temperature thermal behavior of the latter. To better understand the role of the chemistry behind the preparation of these precursors, the part focused on nanocomposites is preceded by a small part which describes the preparation of BN from AB and PB. A last part of the present chapter is focused on the main disadvantage of precursor-derived BN and B-M-N ceramics we highlight in the present chapter: the relatively low degree of crystallinity of the BN phase which can induce high sensitivity to oxidation. We therefore propose a way to improve the BN crystallinity and prepare the hexagonal phase by chemical modification of BN precursors such as AB and PB. The materials are characterized at each step of their process. This chapter is purely fundamental. In particular, by reporting the synthesis, processing and pyrolysis behavior of a series of chemically modified BN precursors, we contribute to build new knowledge toward a more rational approach to the preparation of BN and B-M-N ($M = \text{Ti, Zr, Hf}$) ceramics.

2. Results and Discussion:

2.1. Preparation and characterization of BN from AB and PB:

Conventionally BN is prepared by reaction of B_2O_3 or H_3BO_3 with ammonia or urea^{1,3} in a nitrogen atmosphere by the following reactions:



The resulting BN formed is amorphous and has up to 10% B_2O_3 impurity. To remove the impurity, it needs to be treated above 1500°C. These high temperatures result in crystallization of BN along with grain growth. To allow low temperature synthesis of BN and easier shaping as fibers and nanosheets, its preparation from preceramic polymers has been reported⁴⁻⁷. In this first part, we discuss the preparation of BN from two *single-source* precursors: Ammonia Borane (AB) and Polyborazylene (PB).

2.1.1 BN from ammonia borane:

Ammonia borane (AB, $H_3N \cdot BH_3$) is a molecular solid generally used as hydrogen storage material due to its high hydrogen content (19.6 wt%) as discussed in chapter 1. Here we look at its use as molecular precursor for synthesis of BN (Figure 3.1⁴⁶).

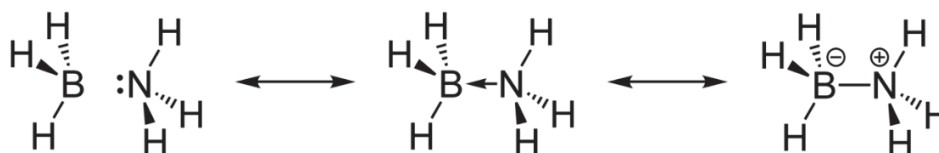


Figure 3.1 Resonance structure of ammonia borane (AB)

AB is a promising precursor for BN due to the fact that it has all the elements required to form stoichiometric BN and the only extra element to be removed is hydrogen. Suib et al⁸ investigated the thermal conversion of AB to BN under nitrogen (N_2) atmosphere as described

in Chapter 1. They reported the formation of a semi-crystalline BN at 1500°C after 24 hours under an N₂ atmosphere. However, loss of nitrogen can occur at high temperature when using N₂ as atmosphere. Furthermore, the B-M-N ceramics prepared in the second part of this chapter are prepared using ammonia (NH₃) as an atmosphere because of the objective to generate purely nitride compounds. Here, we therefore explore the conversion of AB to BN under NH₃ atmosphere to understand the pyrolysis conversion under NH₃ of metal-modified AB compounds that are synthesized to prepare the B-M-N ceramics in the second part of the present chapter.

2.1.1.1 Characterization of Ammonia borane:

Figure 3.1 showed the resonance structure of AB.

Figure 3.2 shows the FTIR spectrum of AB. The FTIR spectrum is similar to that given in the literature⁸. Between 3200 and 3400 cm⁻¹ we have the bands due to stretching of N-H bonds. The broad band centered around 2300 cm⁻¹ corresponds to stretching of B-H bonds. Two sharp bands corresponding to deformation of N-H bonds appear at 1625 and 1375 cm⁻¹. Similarly, bands due to the deformation of B-H bonds come up at 1170 and 1060 cm⁻¹. Finally, there are two intense peaks corresponding to stretching and rocking of B-N bond at 780 cm⁻¹ and 740 cm⁻¹ respectively. However, we should mention that in the literature B-N stretching has been also attributed to peaks at 1440 cm⁻¹, 1380 cm⁻¹ and 850 cm⁻¹⁹⁻¹².

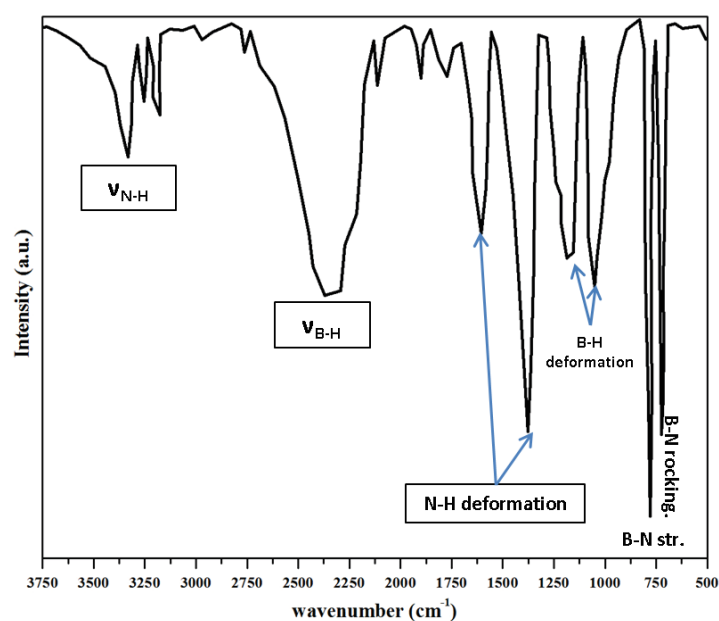


Figure 3.2 FTIR spectrum of AB

2.1.1.2 Conversion of AB into BN:

The pyrolysis of AB under NH_3 flow at 1000°C for 2 hours leads to a poorly crystallized sample we labeled **ABBN-1000** as shown in Fig. 3.3. Unfortunately, it was not possible to measure the weight loss of AB under NH_3 by TGA because of a lot of gaseous by-products are escaped at 120°C which deposited on the cold part of the suspensions significantly altering the measurement.

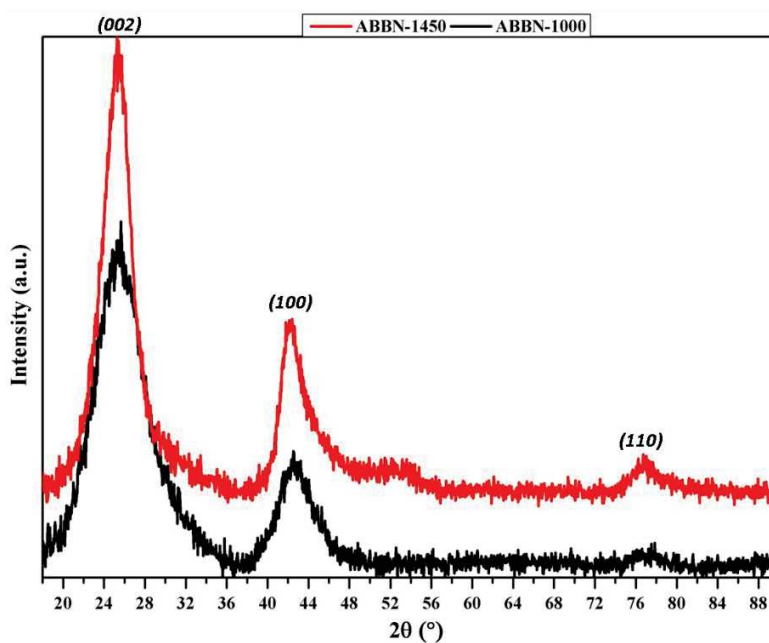


Figure 3.3 XRD of BN produced by pyrolysis of AB at 1000°C and 1450°C

Based on the scheme depicted in Fig. 3.4, it seems that borazine (that polymerizes into polyborazylene in the cold part probably) and polyaminoborane are formed during the pyrolysis of AB into BN.

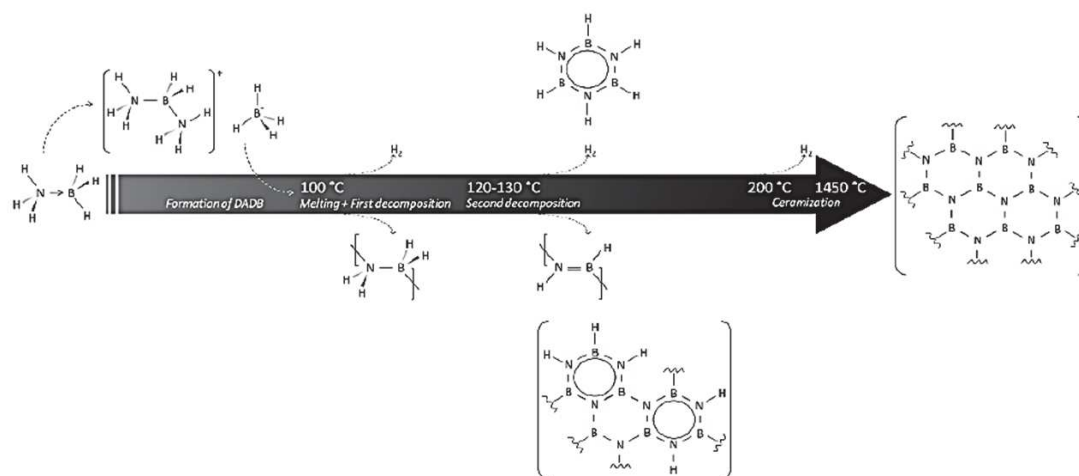


Figure 3.4 Scheme for conversion of AB to BN

2.1.1.3 Structural evolution at high temperature:

Structural evolution of BN derived from ammonia borane was investigated using XRD as shown in Figure 3.3. The samples were named as **ABBN-1000** (sample pyrolyzed at 1000°C under NH₃) and **ABBN-1450** (ammonia-treated sample annealed at 1450°C under N₂). The annealing was stopped at 1450°C because higher temperatures did not allow obtaining higher degree of crystallinity. The XRD pattern of the **ABBN-1450** sample has broad and weak peaks emerging at 25.3°, 42.4° and 76.7°. These coincide in position and intensity with the reflections from a P63/mmc hexagonal phase of BN. This has a graphitic structure where N atoms are stacked in-line between the B atoms of adjacent sheets and vice versa^{13–15}. The XRD pattern for **ABBN-1450** is similar to turbostratic BN (t-BN)¹⁶. The crystallite size calculated using Scherrer equation at the dominant (002) peak was found to be 2.73 nm which clearly indicates a very low degree of crystallization. It should be mentioned that two disordered BN phases, *i.e.*, turbostratic-BN (t-BN) and amorphous-BN (a-BN), are usually found in addition to the hexagonal phase^{6,7,17–19}. The turbostratic BN phase is characterized by a random stacking sequence of the (002) layers and a disorientation of these layers around the *c*-axis, whereas the amorphous BN phase represents a structure disordered at atomic level. XRD patterns of such phases are significantly distinct from that of h-BN.

The poor crystallinity of BN prepared from AB is clearly an advantage to prepare the nanocomposites with the structural organization we targeted (nanocrystalline phase dispersed in an amorphous matrix). However, to prepare pure BN, it appears that the use of

AB as a BN precursor does not allow generating a material with the intrinsic properties of the hexagonal phase of BN.

2.1.2 BN from polyborazylene:

Polyborazylene (PB) as a BN precursor has been also explored. Such a polymer is synthesized with controlled cross-linking degrees by thermolysis of borazine at low temperature inside an autoclave. A large number of studies have been focused on the thermolysis of borazine and the identification of polymerization mechanisms²⁰⁻²². In the fifties and sixties, several authors studied the self-condensation of borazine forming biphenylic and naphthalenic-type structures given the ideal polyborazylene structure proposed in Fig. 3.5^{16,17,22,23}.

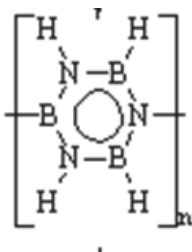


Figure 3.5 Structural formula of PB

In our group, we prepared PB by thermolysis of borazine at 60°C in an autoclave (*See the experimental part in Chapter 2*) we labeled **PB60**.

2.1.2.1 Characterization of Polyborazylene:

Figure 3.6 shows the FTIR comparison of borazine and the **PB60** sample derived from it. Borazine showed absorption bands at 3475 cm⁻¹, 2525 cm⁻¹, 1464 cm⁻¹, 916 cm⁻¹, and 718 cm⁻¹. The absorption bands at 3475 cm⁻¹ and 916 cm⁻¹ are attributed to N-H stretching and B-N bending respectively. The absorption bands at 2525 cm⁻¹ and 718 cm⁻¹ are assigned to B-H stretching and bending, respectively. The absorption band at 1464 cm⁻¹ is attributed to B-N stretching in cyclic B-N ring. In comparison **PB60**, the sharp B-N absorption band at 1464 cm⁻¹ changes to a broad absorption band at 1435 cm⁻¹ in the **PB60** sample, confirming that thermolysis of borazine proceeded through ring condensation forming naphthalene-like derivatives and hydrogen release.

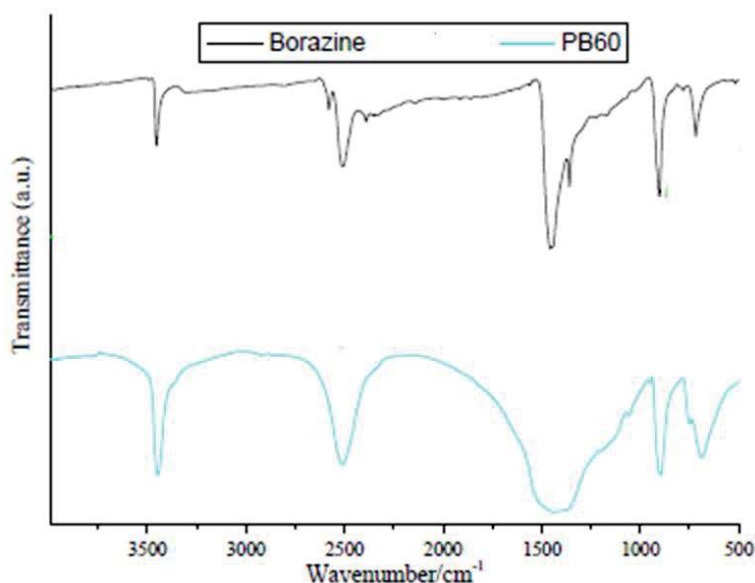


Figure 3.6 FTIR spectra of borazine and the PB60 sample

The ^{11}B solid-state NMR spectrum of **PB60** (Fig. 3.7) recorded at 7 T shows a large signal in the region of tricoordinated boron atoms that was tentatively simulated with two sites at 27 ppm ($C_Q = 2.7$ MHz, $\eta = 0.1$) and 31 ppm ($C_Q = 2.9$ MHz, $\eta = 0.1$) assigned to BN_3 and BN_2H environments respectively. This confirms the naphthalenic-type structure of **PB60**.

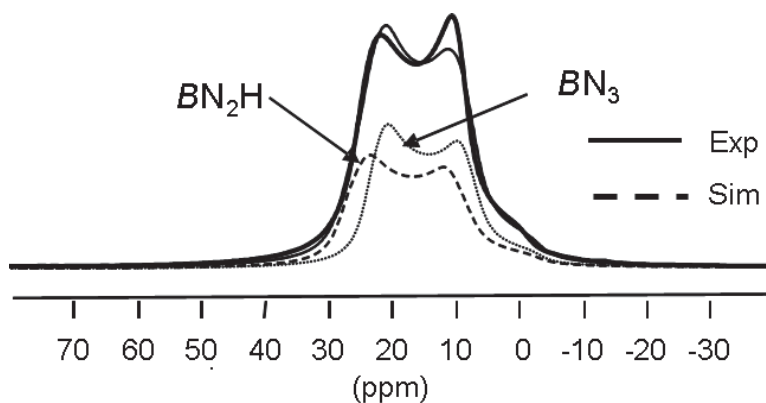


Figure 3.7 ^{11}B SS NMR spectrum for PB60

2.1.2.2 Conversion of polyborazylene to boron nitride:

The polymer to ceramic conversion of **PB60** to BN was carried out under ammonia up to 1000°C. Figure 3.8 shows the TGA curve for conversion of **PB60** to BN. A ceramic yield of 90.9% was obtained with **PB60** which is very high compare to that obtained from AB.

Whereas AB is a molecule, **PB60** is a polymer and therefore, this high ceramic yield is attributed to the highly cross-linked structure of **PB60**.

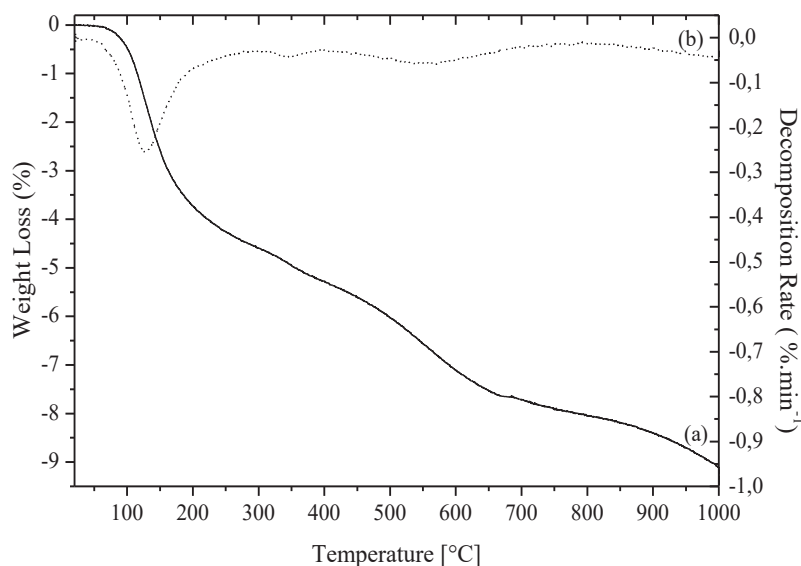


Figure 3.8 a) TGA curve and b) DTG curve of the **PB60** sample

The polymer to ceramic conversion can be divided into three steps. The three-step weight loss starts with an initial weight loss occurring from 70 to 290 °C (4.5 wt%), a second one from 290 to 750 °C (3.5 wt%) and a third one from 750 to 1000 °C (1.1 wt%) which is the maximum temperature of the TG apparatus. The low weight loss of **PB60** is related to its highly cross-linked structure as mentioned previously but also to its ability to further cross-link by dehydrocoupling upon heating according to the presence of reactive B-H and N-H units. Both avoided depolymerization of the **PB60** during the polymer-to-ceramic conversion. However, it is clear that the polymer-to-ceramic conversion is not fully achieved at 1000 °C most probably due to the fact that the polyborazylene-derived material produced at 1000 °C contains residual hydrogen. Hydrogen is completely removed during the further heat-treatment to 1200 °C²⁴.

2.1.2.3 High temperature structural evolution of PB60 derived BN:

The samples are named **PB60BN-X** (where X is the annealing temperature). The **PB60BN-1000** is poorly crystallized with a XRD pattern (Fig. 3.9) similar to that one obtained from

AB at the same temperature as shown on Fig.3.10 although the crystallite size is slightly higher for the PB60BN-1000 sample.

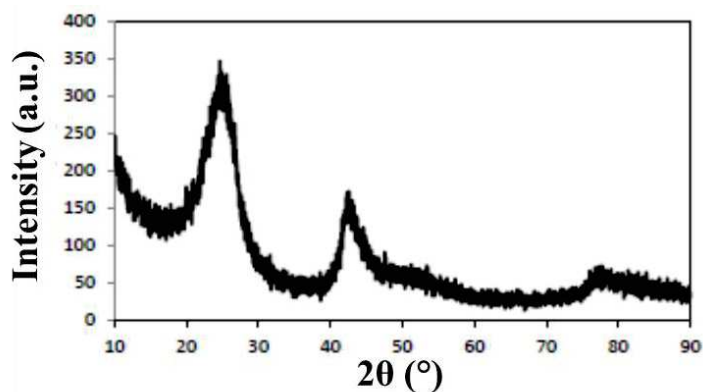


Figure 3.9 X-ray diffractogram of the PB60BN-1000 sample

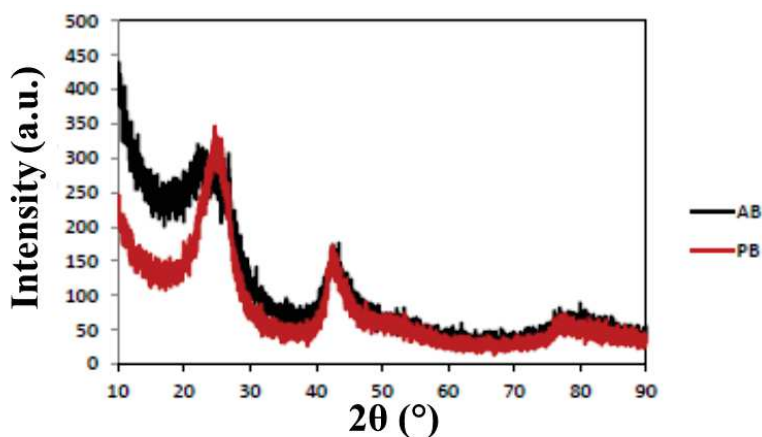


Figure 3.10 X-ray diffractograms of the ABBN-1000 and PB60BN-1000 samples

After annealing to 1450 °C leading to the PB60BN-1450 sample, the presence of the broad (002) peak ($2\theta = 25.35^\circ$; $\text{FWHM} = 3.5^\circ$) and diffuse (10)/(100) and (004) peaks which are shifted from the Bragg angles of h-BN in the XRD pattern (Fig. 3.11) is representative of a disordered structure. In particular, the asymmetric shape of the (002) peak and the absence of the (102) and (112) peaks suggests in a coherent way the presence of t-BN.

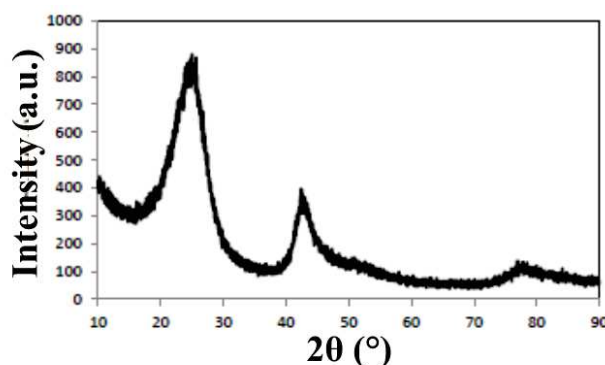


Figure 3.11 X-ray diffractogram of the PB60BN-1450 sample

Again, a comparison of the XRD patterns of the ABBN-1450 and PB60BN-1450 samples shows that the FWHM of the (002) peaks is sharper in the PB60BN-1450 sample which indicates a slightly higher crystallite size for the PB60BN-1450 sample (Fig. 3.12). However, both samples still display the turbostratic phase of BN.

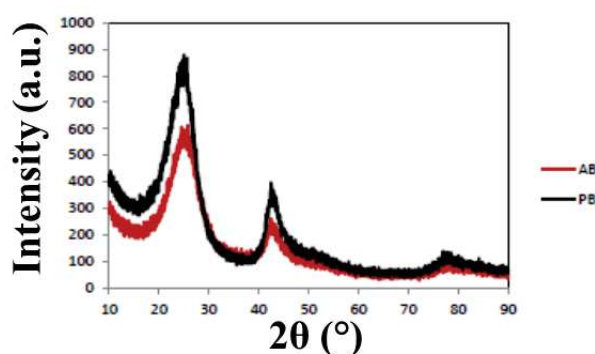


Figure 3.12 X-ray diffractograms of the ABBN-1450 and PB60BN-1450 samples

In this section, we have seen that the formation of the hexagonal phase of BN is not possible using AB and PB as BN precursors. The following section will investigate the effect of the addition of a second metal nitride (MN, M = Ti, Zr, Hf) phase to AB and PB-derived BN. We will investigate the addition of Ti, Zr, Hf to AB and PB at molecular scale and their effect on the polymer synthesis, polymer thermal behaviour and ceramic microstructural evolution at high temperature.

2.2. Preparation and characterization of B-M-N ceramics ($M = \text{Ti, Zr, Hf}$)

Here, we investigated the synthesis of a series of metal-modified compounds from AB and PB; precursors which have been described previously. Because AB is commercially available, a large part of this section is focused on the use of AB as a BN precursor. In our experiments, we focused on the reaction between AB and PB with three liquid molecular entities each containing one transition metal respectively as precursors of the MN nanophase:

- 1) TiN precursor: tetrakis(dimethylamino)titanium (TDMAT, $\text{Ti}[\text{N}(\text{CH}_3)_2]_4$),
- 2) ZrN precursor: tetrakis(diethylamino)zirconium (TDEAZr, $\text{Zr}[\text{N}(\text{CH}_2\text{CH}_3)_2]_4$),
- 3) HfN precursor: tetrakis(methylethylamino)hafnium (TMEAHf, $\text{Hf}[\text{N}(\text{CH}_2\text{CH}_3)(\text{CH}_3)]_4$).

The metal-modified BN precursors are labeled ABMX (synthesized from **AB**) and PB60MX (synthesized from **PB60**) with M the metal (Ti, Zr or Hf) and X the B:M ratio

It is particularly shown by complementary techniques involving solid-state NMR and FTIR spectroscopies that we can modulate/tailor the metal-modified BN precursors characteristics (composition and degree of crosslinking) *via* selection of the BN precursors and control of the B:Ti ratio at molecular scale during the polymer synthesis. This has an effect on the pyrolysis behavior and the nano-/microstructural features of the B-M-N ceramics.

2.2.1 Preparation and characterization of B-Ti-N ceramics

In the present part, we investigate the modification of **AB** and **PB60** with TDMAT at a same intermediate B:Ti ratio (= 3) to identify the mechanisms that govern the polymer synthesis. Then, using a same BN precursor, we investigated the effect of the B:Ti ratio on the polymer thermal behavior and on the high temperature behavior of the resulting B-Ti-N ceramics.

2.2.1.1 Synthesis of titanium-modified BN precursors

Firstly, we compared the effect of the BN precursors on the structure of the derived metal-modified BN precursors keeping a B:Ti ratio constant by FTIR and solid-state NMR spectroscopies. It should be mentioned that amount of B in one mole of **AB** is 1 which is different from that present in one mole of **PB60** (3).

Figure 3.13 shows the FTIR spectra for **ABTi3** and **PB60Ti3** compared with their native precursors **AB** and **PB60**.

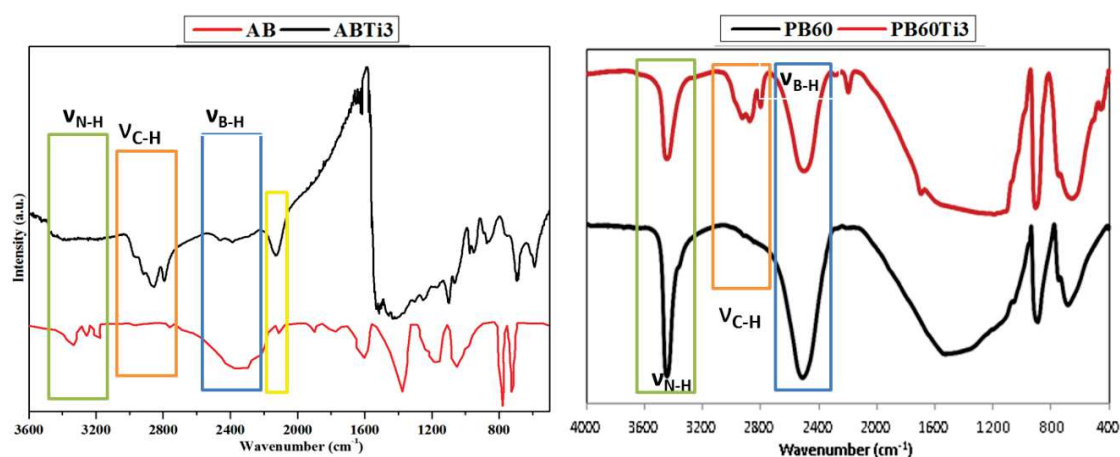
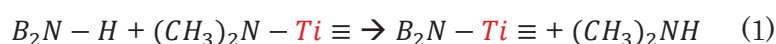
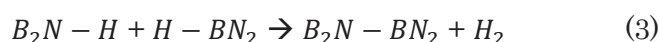


Figure 3.13 FTIR spectra of the **ABTi3** and **PB60Ti3** samples and their native polymers

As expected, FTIR spectroscopy suggests an introduction of $-\text{N}(\text{CH}_3)_2$ groups present in TDMAT in the **ABTi3** and **PB60Ti3** samples by comparing their infrared spectra with those of **AB** and **PB60**. It is found that the intensity of the C-H stretching bands significantly increases while the intensity of the bands assigned to N-H stretching and B-H stretching mode decreases. This clearly suggests that there are reactions involving N-H and B-H bonds in BN precursors and $-\text{N}(\text{CH}_3)_2$ groups in TDMAT according to equations (1) and (2). Such equations represent an amine displacement reaction from TDMAT to **AB** or **PB60** samples with evolution of dimethylamine or methane, respectively.



In addition, the broadening of the bands attributed to B-N stretching in the **ABTi3** sample is indicative of the polymerization of AB into polyamminoborane (PAB). Therefore, in addition to reactions depicted in equations (1) and (2) that occur during synthesis of the **ABTi3** and **PB60Ti3** samples, other reactions, independently of the addition of TDMAT such dehydrocoupling between B-H and N-H units according to equation (3) probably occur to build the molecular weight and degree of cross-linking of BN precursors. This reaction leads to B-N bond formation.



In order to obtain a complete view of the structure of the compounds, solid-state NMR spectroscopy was carried out on the **ABTi3** and **PB60Ti3** samples to probe the local B and C environments. The cross-polarization (CP) technique was used for ^{13}C NMR experiments to obtain spectra with reasonable acquisition times and signal-to-noise ratios. Figure 3.14 shows the ^{11}B MAS NMR spectra of the **ABTi3** and **PB60Ti3** samples. Signals are broadened partially due to the heterogeneity in the local chemical environment of the boron nuclei and line shapes are moreover distorted by quadrupolar interactions since ^{11}B is at spin 3/2. It appears therefore useful to record spectra at different magnetic fields since the intensity of the quadrupolar interaction is inversely proportional to the magnetic field. Therefore, spectra have been recorded at 7 T (for **PB60Ti3**) and 15 T (for **ABTi3**).

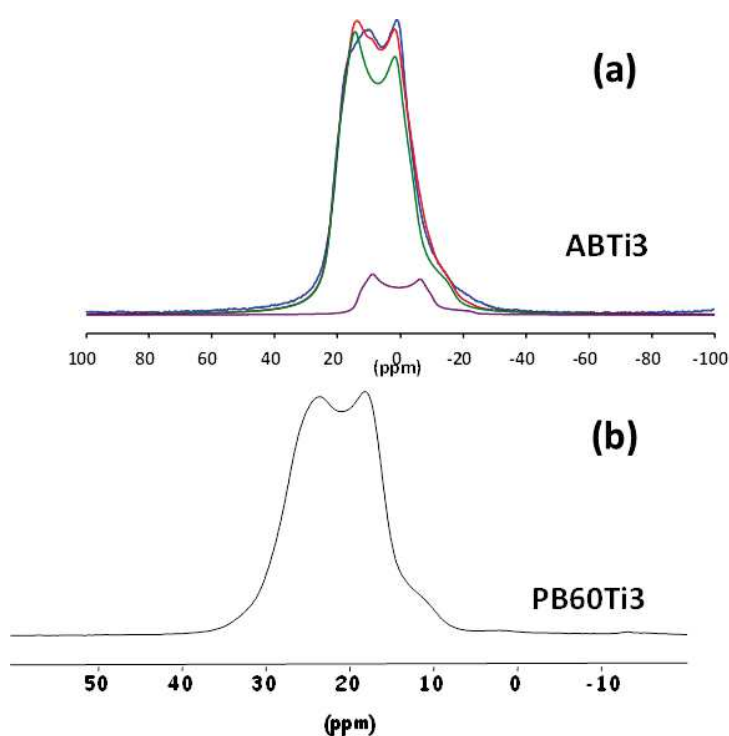


Figure 3.14 ^{11}B MAS NMR spectrum of a) **ABTi3** and b) **PB60Ti3**

^{11}B MAS NMR spectra of both polymers exhibit a broad signal centered in the region of tri-coordinated boron atoms (B[3]) that can be tentatively simulated with two sites as done on the **ABTi3** sample (Figure 3.14). The two signals which can be assigned to BN_3 and BN_2H environments as already identified for **PB60** at $\delta_{\text{iso}} = 31$ ppm (BN_3) and 27 ppm (BN_2H). The signal is shifted with the **ABTi3** sample because it is recorded at a different magnetic field:

the small signal emerging at 18 ppm can be attributed to BN_2H units while the signal at 31 ppm attributed to BN_3 formed by dehydrocoupling process of AB²⁵⁻²⁷.

Figure 3.15 shows the ^{13}C CP MAS NMR spectra for the two samples being discussed.

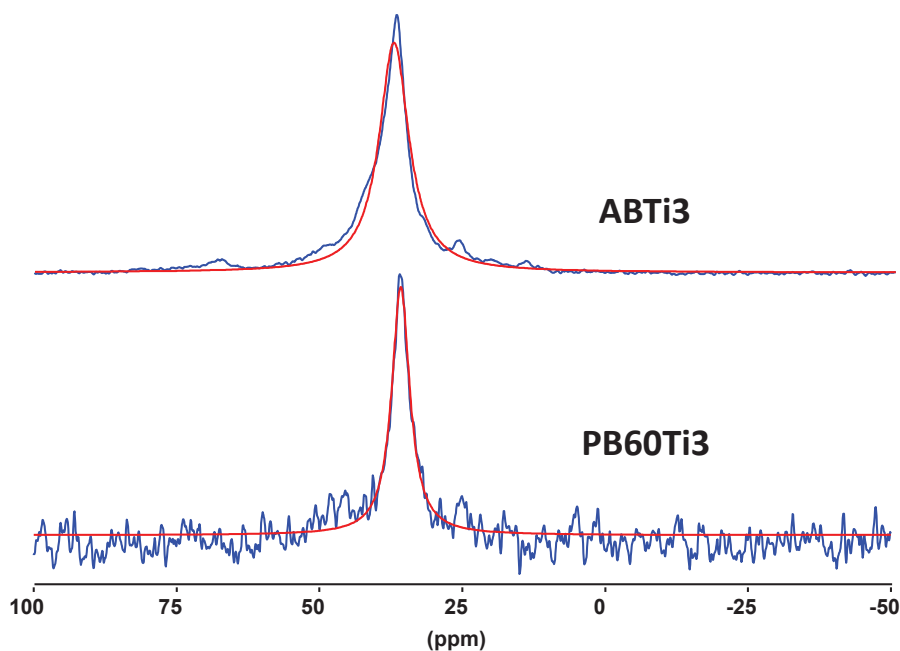


Figure 3.15 ^{13}C CP MAS NMR spectra of a) ABTi3 and b) PB60Ti3

The spectra exhibit a main signal at 39 ppm which is broad suggesting the presence of overlapping components. The signal can be assigned to Ti-N- CH_3 groups regarding their position in good agreement with the position of the signal found in the ^{13}C NMR of $\text{Ti}[\text{N}(\text{CH}_3)_2]_4$ (Fig. 3.16).

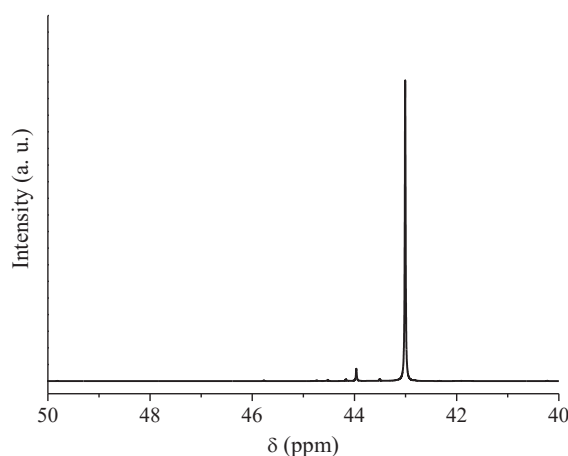
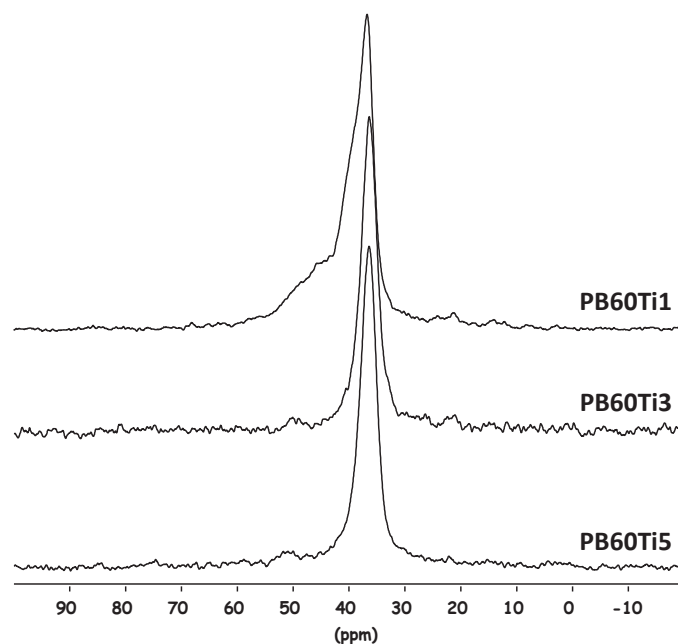


Figure 3.16 ^{13}C CP MAS NMR spectra of TDMAT

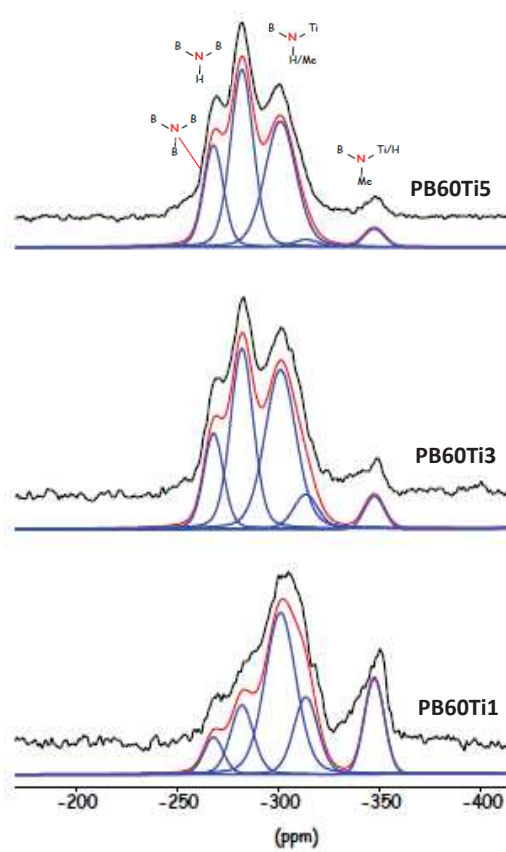
However, the presence of a broad signal suggests, especially in **ABTi3**, more than a single environment. Based on equations (1) and (2) we mentioned previously, $\text{N}(\text{CH}_3)_x$ groups appear as ending group ($x = 2$, eq. (1)) or as a bridge ($x = 1$, eq. (2)) which can involve the presence of two signals. Interesting, the shape of this signal evolves by changing the B:Ti ratio in PB60TiX ($X = \text{B:Ti} = 1 \rightarrow 5$) (Fig. 3.17). In particular a high-field signal as a broadened shoulder emerges around 50 ppm and its intensity increased from **PB60Ti5** to **PB60Ti1** (Fig. 3.17a). As a consequence, the main signal is clearly attributed to $\equiv\text{Ti-N-CH}_3$ groups regarding their position in good agreement with the position of the signal found in the ^{13}C NMR of $\text{Ti}[\text{N}(\text{CH}_3)_2]_4$ as mentioned previously whereas the signal at around 50 ppm is attributed to $=\text{B-N}(\text{CH}_3)\text{-Ti}\equiv$.

The ^{15}N CP MAS NMR spectra (Fig. 3.17b) show a composite signal made of overlapping peaks ranging from -250 to -330 ppm which is inherently difficult to interpret. In addition, we can see that the samples exhibit a more resolved signal at -347 ppm. The intensity of this signal decreases in line with the increase of the B:Ti ratio; thereby with the decreased amount of used $\text{Ti}[\text{N}(\text{CH}_3)_2]_4$ during the synthesis. Therefore, we suggest that it corresponds either to $\text{Ti-M}(\text{CH}_3)_2$ or $\text{B}_2\text{N-Ti}[\text{N}(\text{CH}_3)_2]_3$ environments. The signal with the higher chemical shift value (-268 ppm) can be assigned to a MB_3 environment because a ^{15}N signal with a similar chemical shift ($\delta_{\text{iso}}(^{15}\text{N}) = -268$ ppm) has been already observed in PB^{28} . Another signal at -285 ppm can be assigned to B_2MH units of borazine rings based on previous observations in PB^{28} . A broad component centered at -307 ppm can be simulated with two signals at -302 and -313 ppm which are most probably attributed to Ti-based nitrogen environment according to

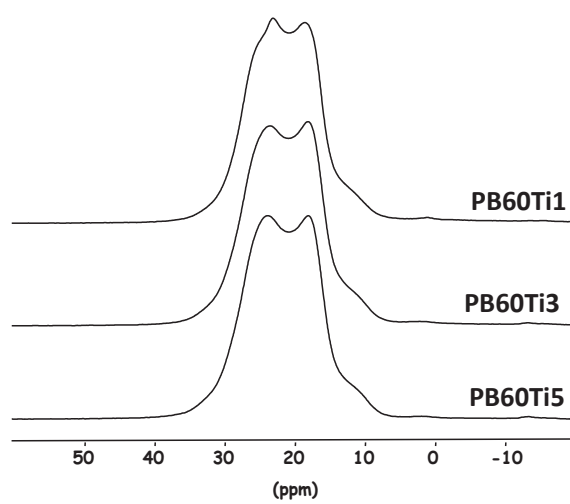
the change in their intensity with the evolution of the B:Ti ratio. Regarding the reactions we have suggested based on IR spectroscopy (Eq. (1) and (2)), they can be assigned to either $B_2N-Ti\equiv$ or $N_2B-N(CH_3)-Ti\equiv$ sites. The signal at -313 ppm could be ascribed to a $B-NCH_3-Ti$ bridge based on an assignment performed in a previous study in which $N(CH_3)$ bridges connecting boron atoms have been observed at -317 ppm in a borylborazine molecule²⁹. The signal at -302 ppm has been therefore attributed to $B_2N-Ti\equiv$ sites. As a consequence of the reaction process, it turns out that Ti-modified BN precursors are composed of at least five structural nitrogen sites that are consistent with FTIR, ^{11}B and ^{13}C NMR data.



(a)



(b)



(c)

Figure 3.17 ^{15}N (a), ^{15}N (b) and ^{13}C CP (c) MAS NMR spectra of PB60TiX (X = B:Ti = 1→5)

It appears therefore that the change of the B:Ti ratio has no effect on the nature of the mechanisms that govern the polymer synthesis. As an illustration, the boron, environment in PB60TiX (X = B:Ti = 1→5) does not evolve in the ^{11}B MAS, spectra (Fig. 3.17c). However, it changes the extent of the reactions and probably modifies the degree of crosslinking of the polymer as we observed by investigating the polymer-to-ceramic conversion in the following part.

2.2.1.2 Polymer-to-ceramic conversion:

The direct pyrolysis of titanium-modified BN precursors leads to colored powders depending on both the B:Ti ratio and temperature. Such materials propose a range of different colors which makes these compounds ideal candidates for decorative applications. Such variations of color can be explained by the growth of the titanium nitride nanocrystals and the change in the crystalline plane orientation with increasing annealing temperature. The chemistry involved during the polymer-to-ceramic conversion includes a complex sequence of structural and chemical changes based on molecular rearrangements and the release of gaseous by-products which are inherently related to the molecular structure and chemistry of preceramic polymers. Therefore, it is particularly essential to control as much as possible thermally induced molecular rearrangements by carefully adjusting the molecular structure of preceramic polymers.

Here, we have investigated the pyrolytic decomposition of titanium-modified BN precursors under NH_3 by thermogravimetric analyses (TGA). This part is shared into two studies. Firstly, we followed the thermal behavior of the **ABTi3** sample under NH_3 from room temperature (RT) to 1000 °C. We compared this sample with the analogs with a B:Ti ratio of 1 (**ABTi1**) and 5 (**ABTi5**). As pyrolysis atmosphere, NH_3 is well known to remove carbon-based groups, $\text{N}(\text{CH}_3)_x$ ($1 \leq x \leq 2$) groups, linked to the basal polymer network and also to involve rearrangements of the structure. Furthermore, NH_3 is used to adjust the nitrogen content in our sample by nitridation and generate PDCs free of carbon and even enriched with nitrogen.

Figure 3.18 shows the TGA curves of ABTiX samples with $X = 1 \rightarrow 5$ during decomposition up to 1000 °C under NH_3 .

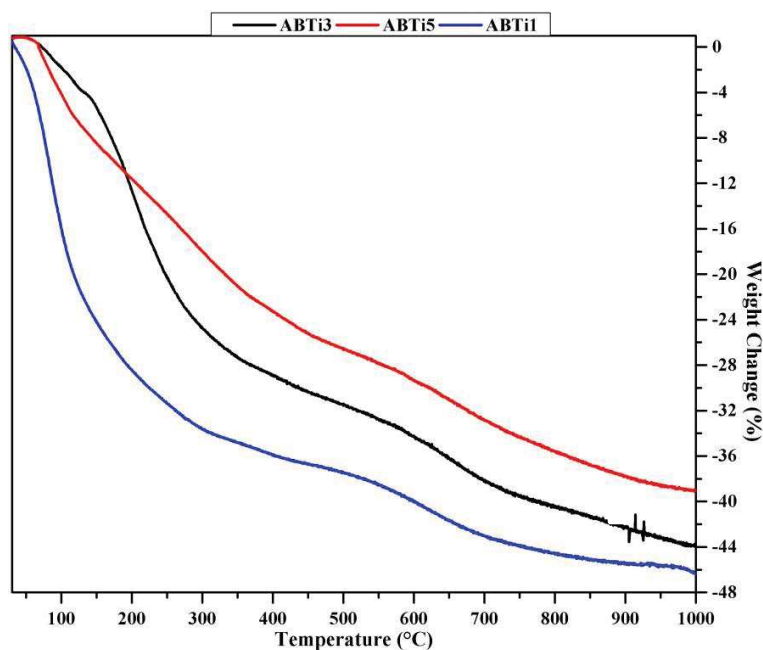


Figure 3. 18 TGA for ABTiX samples with $X = 1 \rightarrow 5$ under NH_3 up to 1000°C

The ceramic yield of the ABTiX samples with $X = 1 \rightarrow 5$ increases with increasing the B:Ti ratio in the polymer from 53.5 % for ABTi1 to 61 % for ABTi5. The ceramic yield of the ABTi3 sample is 53.5 %. This tends to demonstrate that the crosslinking degree of the ABTiX samples with $X = 1 \rightarrow 5$ increased from 1 to 5. To further confirm this tendency, a similar study was performed for PB60Ti1→5 under NH_3 . Figure 3.19 shows the TGA for PB60TiX samples with $X = 1 \rightarrow 5$ under NH_3 .

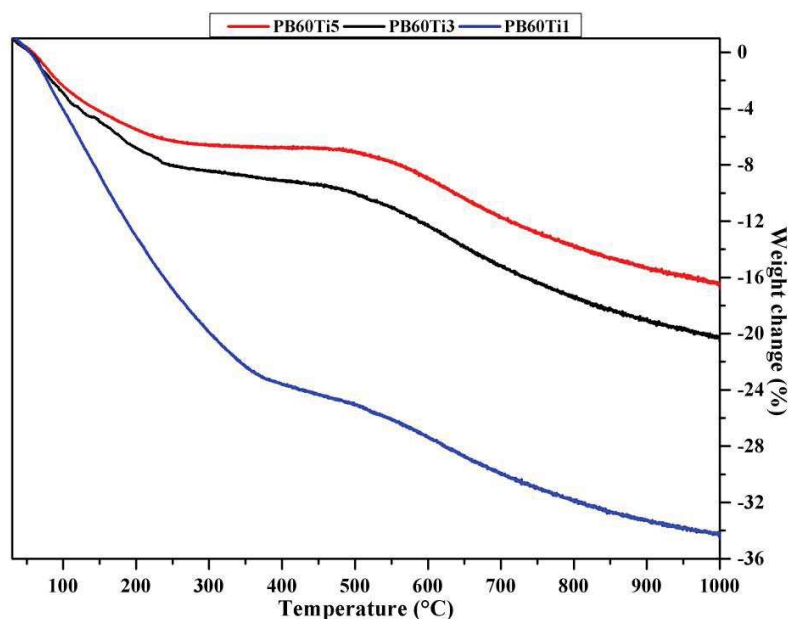


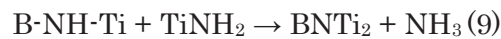
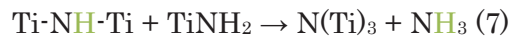
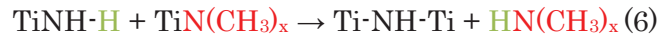
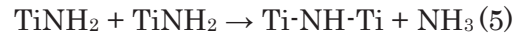
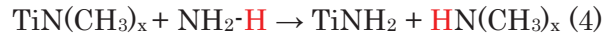
Figure 3. 17 TGA for PB60TiX samples with X = 1-->5 under NH₃ up to 1000°C

It is also obvious that the weight loss of the PB60TiX samples with X = 1 → 5 depends on the B:Ti ratio fixed during synthesis: the weight loss of PB60TiX samples with X = 1 → 5 increases with the decrease of the B:Ti ratio, from 16.7 % (**PB60Ti5**) to 34.4 % (**PB60Ti1**). The highest ceramic yield of PB60TiX samples with X = 1 → 5 than ABTiX samples with X = 1 → 5 is clearly attributed to the fact that PB60TiX samples with X = 1 → 5 are prepared from a relatively highly cross-linked polymer, *i.e.*, **PB60**, whereas ABTiX samples with X = 1 → 5 are prepared from a “monomer” *i.e.*, **AB**, although AB most probably polymerizes into a polyaminoborane during the synthesis.

The TGA behavior can be understood as follows: with the decrease of the B:Ti ratio, the quantity Ti increases; thereby the amount of -N(CH₃)_x (1 ≤ x ≤ 2) groups introduced in the structure of BN precursors increases. Such groups are evolved during the polymer-to-ceramic conversion under NH₃ to form dimethylamine ((CH₃)₂NH). This explains why the strongest presence of these groups involves the highest weight loss.

As a consequence, the behavior of titanium-modified BN precursors is relatively simple to understand through equations shown below. Initially, -N(CH₃)_x (1 ≤ x ≤ 2) groups are displaced by amido group (-NH₂) by reaction with NH₃, whereby -Ti-NH₂ units form and (CH₃)₂NH is released involving mass loss: the higher quantity of -N(CH₃)₂ group is, the higher the weight loss will be. With the increase of the pyrolysis temperature, as-formed moieties

subsequently condense with elimination of NH_3 and/or $((\text{CH}_3)_2\text{NH})$ leading to secondary units, then $\text{N}(\text{B})_{3-x}(\text{Ti})_x$ units ($0 < x \leq 3$).



Beside these reactions, there are reactions involving only the groups present in the BN precursors such as BH and NH units that can condense to form BN_3 groups. A poorly crystallized ceramic network is thus produced at 1000 °C according to the extremely diffuse peaks in the corresponding XRD pattern which is reported in the following section.

2.2.1.3 Microstructural evolution and high temperature crystallization behavior of B-Ti-N ceramics

Ammonia-treated B-Ti-N ceramics derived from ABTiX samples with $X = 1 \rightarrow 5$ have been annealed under N_2 flow at high temperature to investigate their microstructural evolution and their crystallization behavior. After pyrolysis at 1000°C under NH_3 , ABTiX-1000 samples with $X = 1 \rightarrow 5$ are poorly crystallized according to the extremely diffuse peaks identified in the corresponding XRD pattern (Fig. 3.20a, b and c). These peaks correspond to the face-centered cubic (*fcc*) TiN phase (JCPDS file 00-038-1420) which appear at $2\theta = 36.7^\circ$ (111), 42.72° (200), 62.11° (220), 74.42° (311) and 77.97° (222) in the XRD pattern of the **ABTi1-1000** sample. Phase identification is achieved by locating the characteristic diffraction peaks of the respective phases in the XRD spectra. With the increase of the B:Ti ratio, the peak become more and more diffuse and those corresponding to (220), (311) and even (111) (in the **ABTi5-1000** sample) planes gradually disappear. This clearly indicates a decrease of the crystallinity and the degree of crystallization of the samples with the increased B:Ti ratio. Through annealing at 1450°C leading to the **ABTi1-1450**, **ABTi3-1450** and **ABTi5-1450** samples, crystallization of the nanophase occurred. As an illustration, the XRD pattern of

the **ABTi3-1450** sample (Fig. 3.20b) shows sharp intense peaks at the position described previously, *i.e.*, $2\theta = 36.7^\circ$, 42.6° , 61.8° , 74.12° and 77.98° . The crystallite size, calculated at the dominant (200) peak, increased from 3.8 nm (**ABTi3-1000**) to 27 nm (**ABTi3-1450**) (Table 3.1). The small peak belonging at 26.5° is attributed to the (002) plane of the BN matrix. Interesting this peak is not present in the **ABTi1-1450** sample (Fig. 3.20a) whereas it is relatively intense in the **ABTi5-1450** sample (Fig. 3.20c). A further annealing at 1600°C confirms the observations made for the XRD pattern of the **ABTi1-1450**, **ABTi3-1450** and **ABTi5-1450** samples: the crystallite size continues to increase as shown in the Table 3.1, a slight shift towards right of the TiN peaks occurs and the (002) peak corresponding to BN becomes more intense in samples. Interestingly, the TiN peaks at 61.8° , 74.12° and 77.98° identified in all samples reveal the presence of a shoulder peak which could be attributed to TiB_x phase. Further confirmation of this was done with the **ABTi3-1600** sample which could not be spun during solid-state NMR experiments most probably due to the presence of a metallic phase (TiB_x).

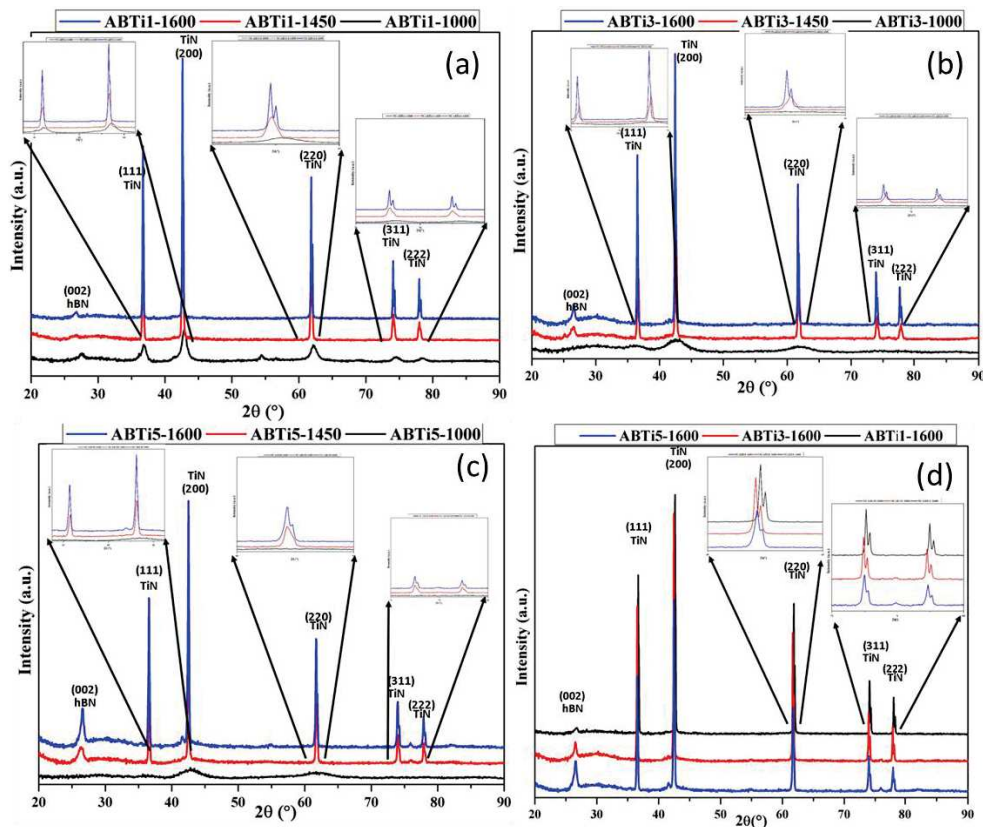


Figure 3. 20 XRD patterns of a) **ABTi1**, b) **ABTi3**, c) **ABTi5**-derived ceramics with temperature and d) comparison of XRD patterns of **ABTiX-1600** with $X = 1 \rightarrow 5$ samples.

In Fig. 3.20d, it can be clearly seen that the intensity of peak belonging to BN (26.5°) decreases with the decreased B:Ti ratio from **ABTi5-1600** to **ABTi1-1600**. Furthermore, in the insets of the figures 3.20d, it can be seen that the separation of shoulder peaks at 61.8°, 74.12° and 77.98° from the TiN peaks increases with the decreased B:Ti ratio from 5 to 1, *i.e.*, increase of the TiN content in the system. It therefore seems that the increase of the Ti content in the precursor increases the TiN content in the final material which is expected but it tends also to stabilize the amorphous structure of BN and shift its crystallization to higher temperatures.

Table 3.1 Crystallite size calculated in the ABTiX-Y samples with X = 1→5 and Y = 1000, 1450 and 1600

System (B:Ti) ratio in nanocomposite (ABTiX)	Crystallite size (nm)		
	1000°C	1450°C	1600°C
ABTi5	3.71	26.9	45
ABTi3	3.8	27	68
ABTi1	10.39	33.7	45

A same behavior was observed using **PB60** as a BN precursor. Figure 3.21 investigates the Raman spectra of ABTi1→5 samples pyrolyzed at 1000 °C under NH₃ then annealed at 1450 and 1600 °C in flowing N₂. Raman spectroscopy confirms the observations made by X-ray diffraction for the samples: the signal appearing around 1360 cm⁻¹ corresponds to the typical vibration frequency observed in h-BN materials³⁰. It is due to the E_{2g} symmetric vibration mode in h-BN (B-N in plane atomic displacements). This signal is the most intense and the sharpest in the Raman spectrum of the **ABTi5-1600** sample which means that the BN matrix displays the highest degree of crystallization among all samples. Beside this, we confirmed the growth of the TiN nanophase in the samples. As illustrated in Fig. 3.21, the Raman spectra of the samples are characteristic of the face-centered cubic (*fcc*) TiN phase. The low frequency peaks below 400 cm⁻¹ can be attributed to acoustical phonons, whereas the high frequency mode around 540 cm⁻¹ is due to optical phonons³¹. Both Raman peaks at 209 and

300 cm^{-1} are representative of the transverse acoustic (TA) and longitudinal acoustic (LA) modes of TiN, respectively³². The Raman peak at 410 cm^{-1} can be attributed to the 2A mode and the Raman peak centered at 539 cm^{-1} completed by the shoulder at 600 cm^{-1} correspond to the transverse optic/longitudinal optic (TO)/LO modes³². The phonon bands in the acoustic and optic range are due to vibrations of the heavy Ti^{4+} ions and the lighter N^{3-} ions, respectively. In the 817-1075 cm^{-1} wavenumber range, we can assign the Raman peaks to the A+O and 2O modes.

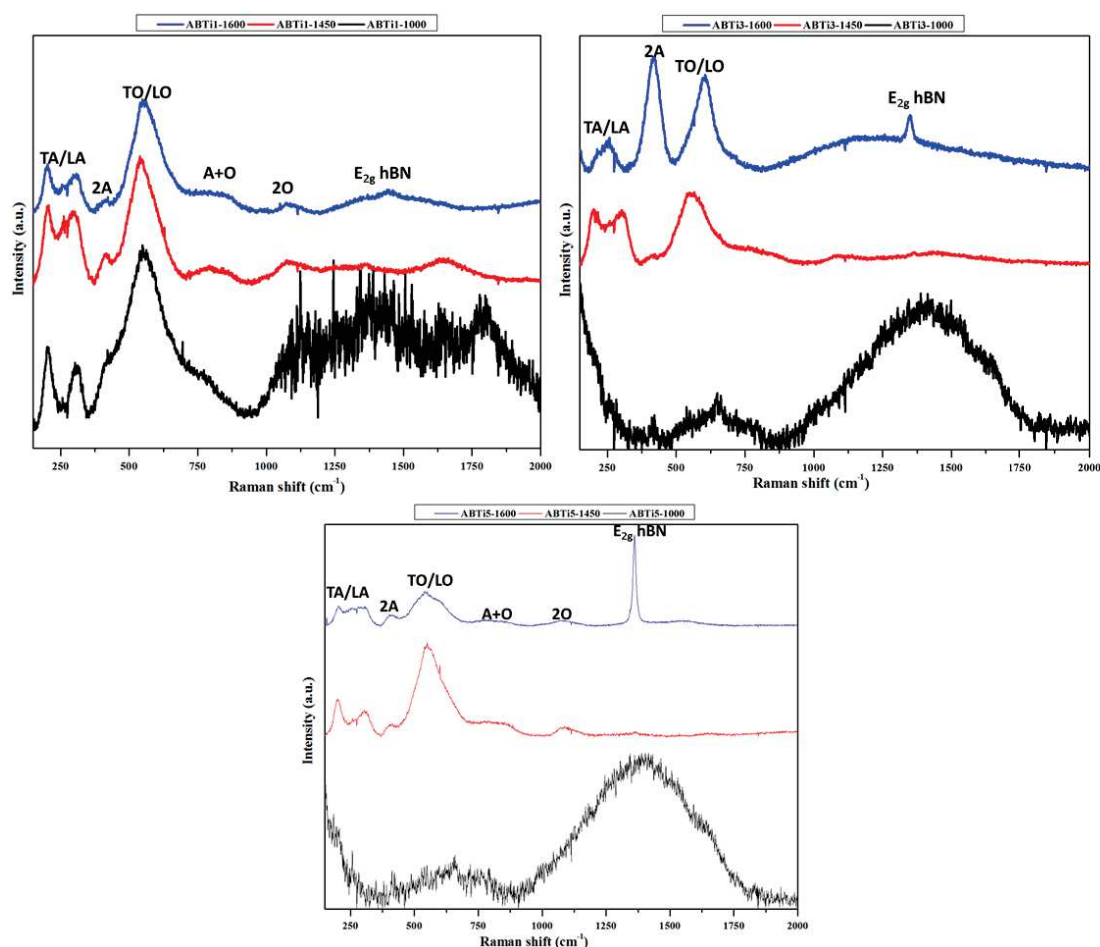


Figure 3.21 Evolution of the Raman spectra of a) ABTi1, b) ABTi3, c) ABTi5-derived ceramics with temperature

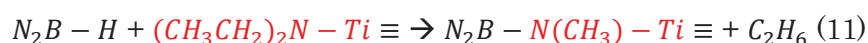
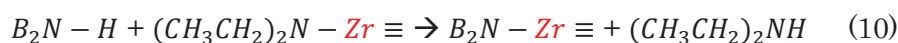
This study showed the strong effect on the B:Ti ratio fixed at the polymer synthesis level on the extent of the reactions occurring during the polymer synthesis. This changes the degree of crosslinking of polymers which influences the weight loss measured during the subsequent pyrolysis under NH_3 . Ammonia-treated samples are X-ray amorphous and evolve toward a nanocomposite structure with the annealing under N_2 up to 1600°C. The nanocomposite

structural organization changes with the B:Ti ratio fixed at molecular scale. Below, we investigate the effect of the nature of the metal introduced at molecular scale in the metal-modified BN precursors.

2.2.2 Preparation and characterization of B-Zr-N and B-Hf-N ceramics

2.2.2.1 Polymer synthesis and pyrolysis

The mechanisms that govern the polymer synthesis and the polymer to ceramic conversion for Zr- and Hf-modified BN precursors are similar to those identified for Ti-modified BN precursors. The unknown is the extent of the reactions which take place and the only difference is the nature of the dialkylamino groups linked to Zr (diethylamino) and Hf (methyl/ethylamino) which are different of those linked to Ti (dimethylamino): diethylamine/ethane (for Zr, Eqs. (10 and (11)), methylamine/ethylamine/methane/ethane (for Hf) are evolved as gaseous by-products during the polymers synthesis. We have also such reactions during the polymer-to-ceramic conversion.



The thermal conversion of the polymers into ceramic materials is accompanied by the formation of gaseous byproducts and therefore weight loss during the polymer-to-ceramic conversion as shown previously. Because of the difference in the nature of the gaseous by-products, the weight change upon pyrolysis must be different. The ceramic yields for Zr- and Hf-modified BN precursors were determined using TGA and the results compared with the TGA of the Ti-modified BN precursors. The data in Figure 3.22 suggest that the substitution of Ti in polymers with Zr does not change the pyrolysis behavior: the ceramic yield of the **ABZr3** under NH_3 up to $1000^\circ C$ is found to be 56 %, a value close to the ceramic yield calculated for the **ABTi-3** sample (56,5 %) although the lower weight substituents ($N(CH_3)_2$) in **ABTi3** that split off as gaseous by-products are expected to cause a lower weight loss than bulk groups ($N(CH_2CH_3)_2$) in **ABZr3**. The ceramic yield calculated for the **ABHf3** sample is unexpectedly high (82 %) as shown in Figure 3.22.

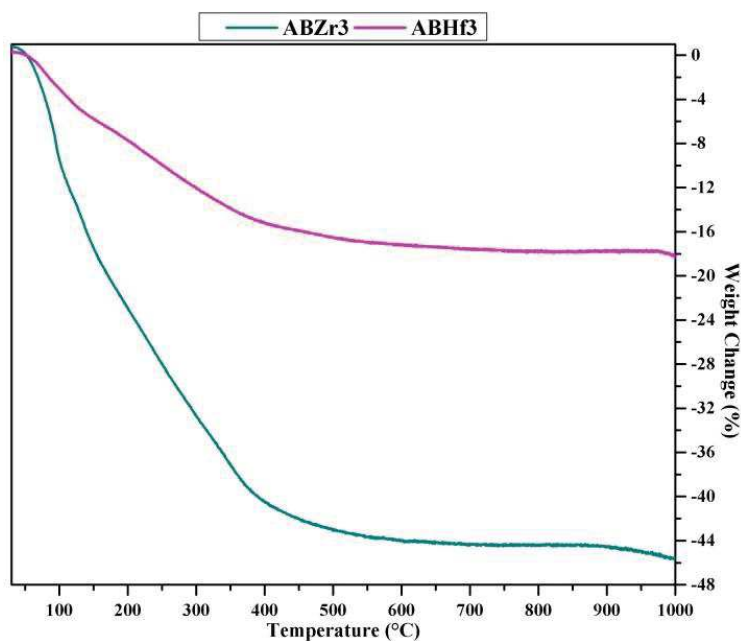


Figure 3.22 TGA profile of the ABZr3 and ABHf3 sample recorded under NH₃ up to 1000°C

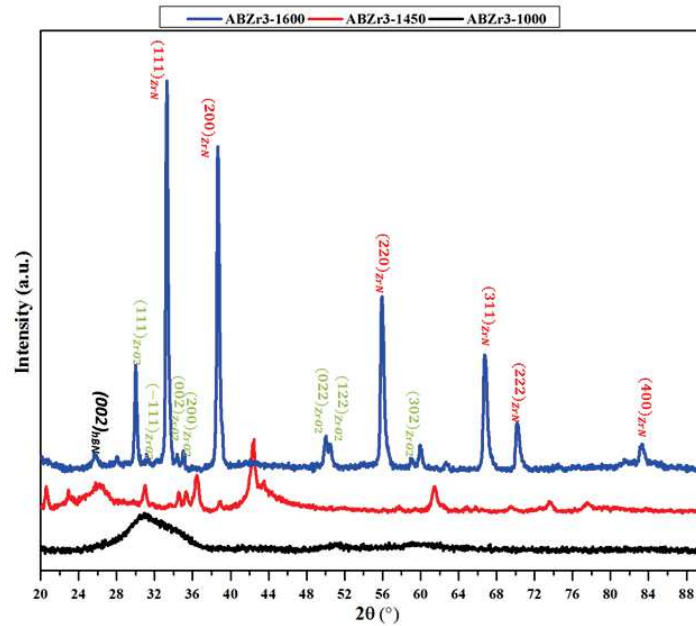
A number of factors, such as polymer structure, molecular weight, the degree of cross-linking, *i.e.* the structure of the polymer backbone and the nature of the functional groups that are attached to boron and/or nitrogen strongly influence the ceramic yields. An additional important issue in this regard is the decomposition chemistry of the precursors, including the ability to cross-link further during the heat treatment. Taking these factors into account and considering that the reaction occurring during the polymer synthesis lead to the same polymer degree of crosslinking, the ceramic yields should increase in the expected sequence **ABZr3**, **ABHf3**, **ABTi3**. **ABHf3** does not fit in this sequence. This is most probably a consequence of the extent of the reactions which occur between TDMAHf and BN precursors. Reactions between NH and BH groups in BN precursors and N(CH₃)(CH₂CH₃) probably occur with more efficiency to generate a more highly cross-linked polymer. Such a behavior is documented in case of Si-based polymers modified with TDMAHf as reported by Ionescu et al³³. The evaluation of structural intermediates that arise during the various stages of thermolysis will be performed by using multinuclear solid-state NMR and FT-IR spectroscopy and will be available soon. This will help us to confirm such observations.

2.2.2.2 Microstructural evolution and high temperature crystallization behavior of B-Zr-N and B-Hf-N ceramics

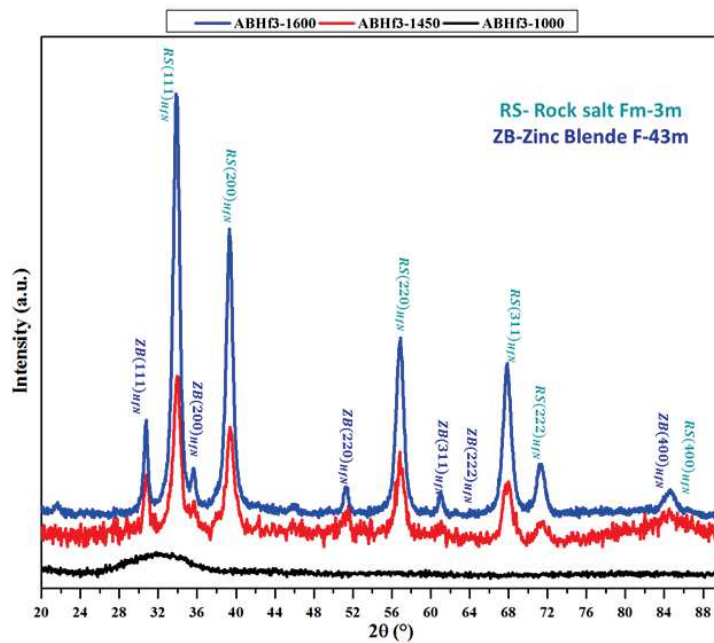
Ammonia-treated B-Zr-N and B-Hf-N ceramics derived from the **ABZr3** and **ABHf3** samples have been annealed under N₂ flow at high temperature to investigate their microstructural evolution and their crystallization behavior. After pyrolysis at 1000°C under NH₃, samples labeled **ABZr3-1000** and **ABHf3-1000** are poorly crystallized according to the extremely diffuse peaks identified in the corresponding XRD pattern (Fig. 3.23). Upon further annealing to 1450°C, the XRD pattern of the **ABZr3-1450** sample (Fig. 3.23a) has number of sharp peaks corresponding to monoclinic ZrO₂ appear (marked in green) along with (002) peak attributed to h-BN. The ZrO₂ peaks, usually observed in such system because of the high sensitivity of the polymers, are due to the extremely high sensitivity of the polymer toward oxidation. Final annealing at 1600°C (**ABZr3-1600**) leads to further crystallization of ZrO₂ but along with that sharp and intense peaks corresponding to ZrN (JCPDS file: 04-004-2860) at 33.3°, 38.6°, 55.94°, 66.8°, 70.1° and 83.3° (Fig. 3.23a). The crystallite size calculated using Scherrer equation at the dominant (111) peak is found to be 32.82 nm.

Figure 3.23b shows the phase evolution for of the **ABHf3-1000** sample at 1450 and 1600°C. Further annealing at 1450°C leads to the **ABHf3-1450** Sample. The XRD pattern has a number of sharp peaks at 30.76°, 33.82°, 35.64°, 39.34°, 51.22°, 56.89°, 61.1°, 67.85°, 71.4° and 84.6°. These belong to two different cubic structures of HfN, rock salt (JCPDS file: 00-033-0592) and zinc blende (JCPDS file: 01-079-5779). The two HfN phases differ from each other in terms of their space groups. The crystallite size calculated at the dominant peaks (111) peak in both cases was found to be 10.71 nm for (Zinc blende)_{HfN} and 8.1 nm for (Rock salt)_{HfN}. At 1600°C, the crystallite size of the **ABHf3-1600** sample increases to 16.13 nm (zinc blende structure) and to 11.95 nm (rock salt structure). There are no peaks corresponding to BN suggesting that the matrix is still amorphous at this temperature which demonstrated the very high stability of the B-Hf-N ceramics, *i.e.*, HfN/BN nanocomposites, as we observed with the B-Ti-N ceramics with a B:Ti ratio of 1. This clearly shows that, at a same B:M ratio, the B-Hf-N ceramics are more stable at high temperature than B-Ti-N ceramics. We attributed this phenomenon to the high efficient reactions which occur between AB and TDMAHf allowing introducing more Hf in the polymer structure than the reaction between AB and TDMAT at a same B:M ratio. This increases the HfN content in the final materials which stabilize the amorphous phase of BN. Elemental analyses of the polymers and final

ceramics and HRTEM investigations should help us to confirm our observations. This will be performed soon.



(a)



(b)

Figure 3.23 Evolution of the XRD patterns of the a) ABZr3 and b) ABHf3 samples with temperature from 1000°C to 1600°C

Raman spectroscopy allowed us to confirm the presence of BN. Figure 3.24 shows the Raman spectra of ceramics derived from **ABZr3** and **ABHf3**. The presence of the E_{2g} peak of the B-N bond vibration in the **ABZr/Hf3-1200** and **ABZr/Hf3-1600** is visible in both cases at around 1360 cm^{-1} which confirms the presence of BN in the systems even though it may not be crystallized.

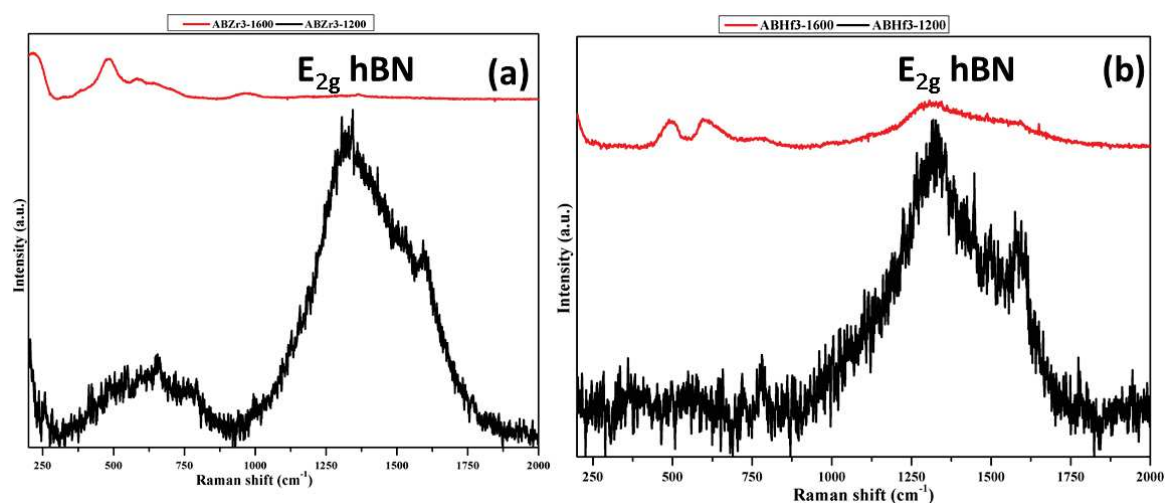


Figure 3.24 Raman spectra with temperature for a) **ABZr3** and b) **ABHf3**

In this section, we showed that the presence of metal nitride nanocrystals in a BN matrix can suppress the crystallization of the latter if the B:M ratio is sufficiently low. However, the nc-MN/a-BN (nc for nanocrystalline and a for amorphous) nanocomposites especially with $M = \text{Ti}$ and Hf may have some potential disadvantage in some application due to the low BN crystallinity which can involve a low oxidation resistance. To overcome this problem, we focused the last part of the present chapter on the investigation of the improvement of the BN crystallinity using AB and PB as BN precursors and then, we changed the nature of the matrix toward Si_3N_4 in chapter 4 which is well known as a ceramic highly resistant to oxidation.

2.3. Preparation and characterization of highly crystallized BN

In the previous section we discussed synthesis of boron nitride from ammonia borane (AB) and polyborazylene (PB60). Under standard conditions, both the precursors give a semi-crystalline and turbostratic BN at $1450\text{ }^\circ\text{C}$ and it is almost impossible to generate the hexagonal phase even at higher temperatures. The use of such high temperatures defeats

one of the major reasons of using the PDC route, *i.e.*, processability at low temperatures. However, we can take advantage of the PDC route by modifying the BN precursors with further elements that improve the BN crystallinity in contrast to Ti and Hf that hinder BN crystallisation.

The crystallization of h-BN at low temperature has been reported in metal fluxes, such as in sodium at 700–800 °C^{34,35} and in molten hydrogen saturated nickel below 1000 °C³⁶. The synthesis and growth of h-BN crystallites at low temperature have been investigated by carrying out in a lithium bromide (LiBr) melt in 600–700 °C³⁷. The molten salt was found to have a strong effect on the crystal growth.

Li₃N is traditionally known to be an additive which lowers the conversion temperature of h-BN to cubic- (c-)BN^{38–42}. Yuan *et al* explored its use as an additive to polymer in order to lower the crystallization temperature of BN obtained from precursor route. Li₃N was mixed as a powder with the precursor thus leading to a physical mixing, *i.e.*, precursor blend, not a *single-source* precursor. This inherently led to a poor reactivity between both compounds and certain inefficiency.

Use of Li based compounds which can react with the polymer and modify the polymer at a molecular level to lead to a homogeneous distribution of the crystallization promoter in the system is the focus on the present chapter part. For this purpose, we have explored the reaction between BN precursors and lithium amide (LiNH₂) in solution and by reactive ball-milling. We showed that this reaction can occur also with lithium hydride (LiH).

2.3.1 Synthesis in solution

The synthesis in solution consists of adding LiNH₂ to a solution of AB in THF drop by drop with a molar B:Li ratio of 1:1. A white powder labelled **ABLi1** was obtained after drying. Figure 3.25 compares the FTIR spectra of AB and the **ABLi1** sample.

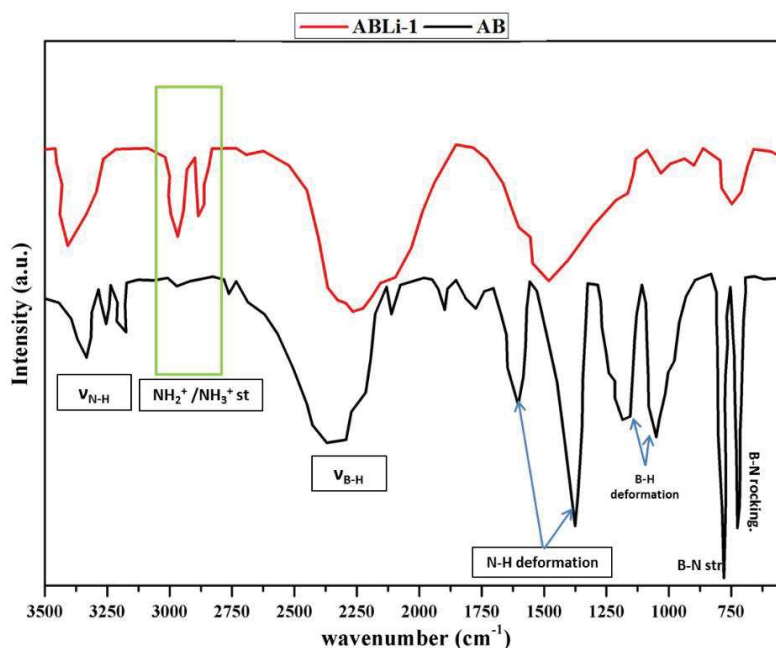


Figure 3.25 FTIR spectra of AB and ABLi1 samples.

Modification of AB with LiNH_2 leads to a lot changes in its structure. The two bands at 780 cm^{-1} and 740 cm^{-1} representing the stretching and rocking of BN bond drastically reduces in intensity and appears as one broad band. As mentioned before, B-N stretching/elongation bonds have been reported at different wavenumbers also. The bands relating to deformation of B-H bonds at 1125 and 1070 cm^{-1} completely reduce in intensity and are nearly lost behind the broad band for B-N bond stretching. The broad band of B-H bond stretching is slightly shifted to the right and the N-H bond stretching bands become into one broad band. There is appearance of two new bands in the range of 2800 to 300 cm^{-1} . These are attributed to stretching of ammonium bonds of NH_2^+ and NH_3^+ which are formed after reaction with LiNH_2 . The presence of broad bands suggests the formation of a polymer as it occurs when AB is transformed into a PAB. By the way, a branched or cyclized PAB displays a very similar IR spectrum without significant shifts in stretching frequencies from the purely linear case.

To have a better idea of the reaction between AB and LiNH_2 in solution we performed ^{11}B MAS solid-state NMR of the **ABLi1** sample (Figure 3.26).

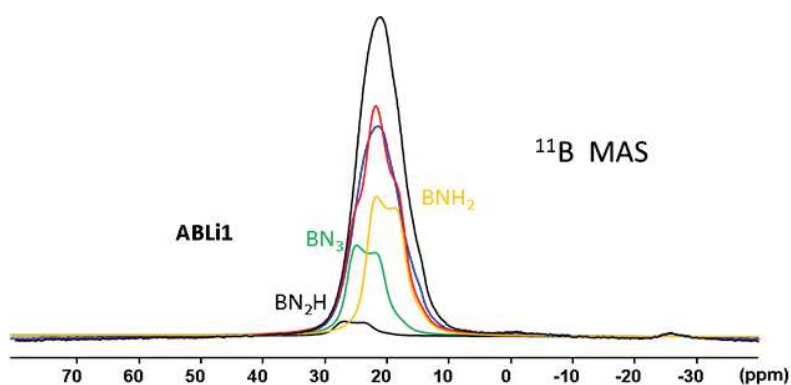


Figure 3.26 ^{11}B MAS solid state NMR spectrum of the **ABLi1** sample

Similar to the FTIR spectrum, the ^{11}B MAS NMR spectrum of the **ABLi1** sample significantly changes in comparison to the spectrum of AB (Fig. 3.27). In particular, the signals observed in the ^{11}B spectrum of AB between -20 and -30 ppm is significantly reduced which means that BH_3 units are mostly absent. In contrast, it shows the presence of three different B environments namely BN_2H , BN_3 and BNH_2 ⁴³ which tends to demonstrate that the sample is in an oligomeric or polymeric state.

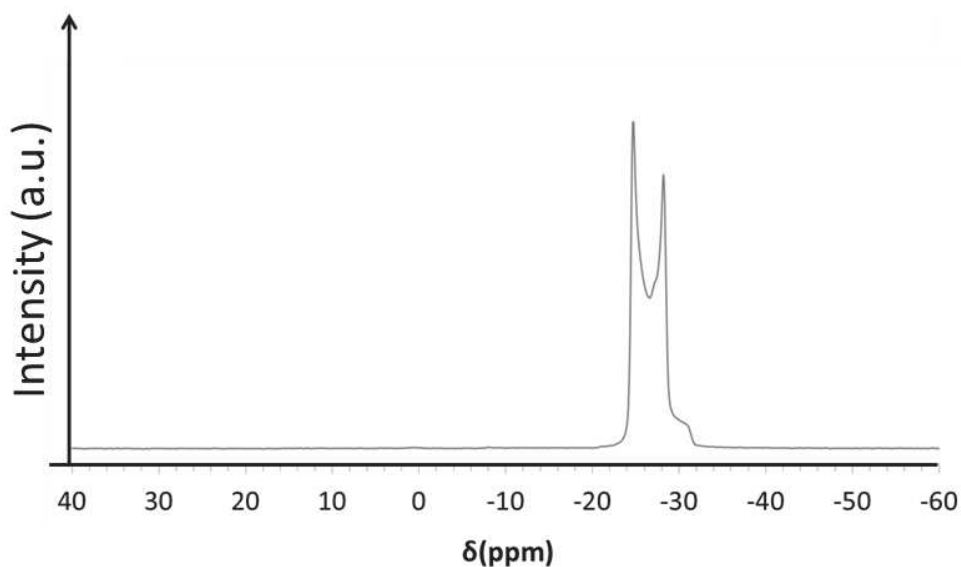


Figure 3.27 ^{11}B MAS solid state NMR spectrum of AB.

To complement the data, we investigated ^{15}N CP MAS NMR (Figure 3.28).

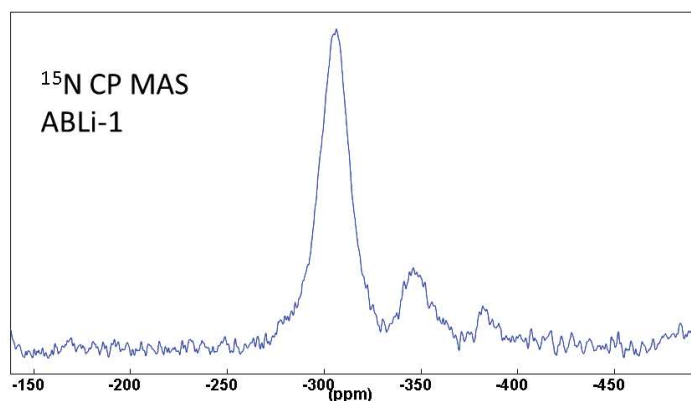


Figure 3.28 ^{15}N CP MAS NMR spectrum of the **ABLi1** sample

The ^{15}N CP MAS NMR spectrum of the **ABLi1** sample displays three major peaks centered at -310 ppm, -350 ppm and -380 ppm. The peak at -310 ppm is very broad and most probably represents a composite signal made of overlapping signals. In this chemical shift, non-protonated NB_3 sites (-294 ppm) and NB_2H groups (-311, -326 ppm) can be identified²⁸. The signal at -350 ppm is usually attributed to $-\text{N}(\text{H})\text{CH}_3$ groups⁴⁴ but we do not have such groups in our system. In the chemical shift range around -364 ppm, AB displays a signal⁴⁵. In addition, the signals relative to $-\text{NH}_2\text{-BH}_2$ in PAB are in this chemical shift range. We may therefore suggest the identification of tetracoordinated nitrogen for both signals.

2.3.1.1 Precursor-to-ceramic conversion:

The polymer to ceramic conversion of the **ABLi1** sample has been achieved at 1000°C under NH_3 for 2 hours. In contrast to AB, we could measure the weight loss that occurs during the pyrolysis up to 1000 °C under NH_3 . The ceramic yield has been calculated to be around 69 % at 1000 °C but, as seen in Fig. 3.29, the weight loss continues above 1000 °C.

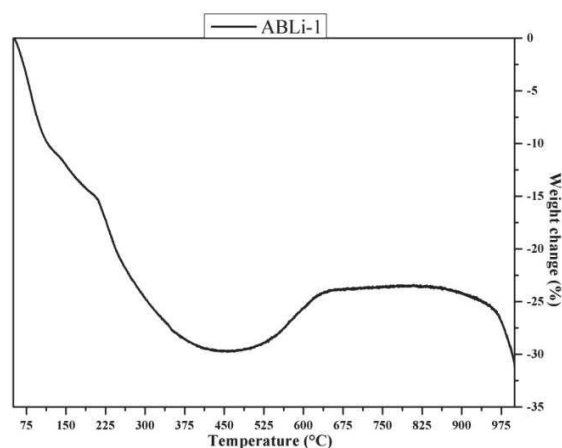


Figure 3. 29 TGA curve recorded for the ABLi1 sample under NH₃ up to 1000°C

The weight loss profile is very complex: the precursor displays a first weight loss up to 125 °C which is similar to the weight loss recorded under nitrogen for AB⁵⁰: it is attributed to loss of H₂ due to formation of PAB. Here, it probably forms a Li-containing PAB. This first weight loss is followed by a second weight loss up to 225 °C which may again be due to loss H₂ and formation of a lithium-containing polyiminoborane (PIB) up to 450 °C. Then, a weight gain is recorded between 450 and 675 °C. The weight is then stable over around 300 °C before a third weight loss that most probably continues above 1000 °C. The weight loss above 900°C has been reported to be due to evaporation of Li₃BN₂ liquid phase formed during the pyrolysis as reported for Li₃N mixed with PB.⁴⁶

To learn more about the mechanisms involved in the precursor-to-ceramic conversion, *ex-situ* analyses of intermediates isolated during pyrolysis up to 1000 °C under NH₃ have been carried out by solid-state NMR. The ¹¹B MAS NMR on the intermediate pyrolysis product isolated at 450 °C (end of the second weight loss, **ABLi-450**) shows the complete vanishing of the signal attributed to **BNH₂** environments, most probably because of their self-condensation ($=\text{BNH}_2 + =\text{BNH}_2 \rightarrow =\text{BN}_2\text{H} + \text{BH}_3$). As-formed $=\text{BN}_2\text{H}$ units can react with $=\text{BNH}_2$ groups to form BN₃ units. Because ¹⁵N NMR has identified NB₂H groups, ammonia is also probably removed. This is in good agreement with the increase of the intensity of the signals attributed to $=\text{BN}_2\text{H}$ and BN₃ environments which tends to demonstrate the formation of borazine-type rings in the product. The continuous increase of the intensity of the signal attributed to BN₃ units up to 1000°C (**ABLi-1000**) confirms condensation reactions.

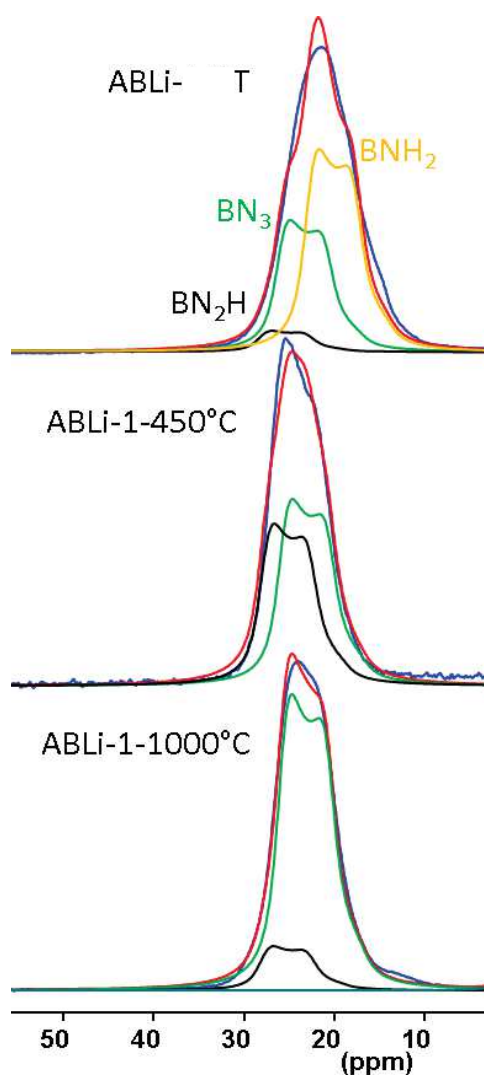


Figure 3.30 ^{11}B MAS NMR for pyrolysis intermediate prepared from the **ABLi1** sample under ammonia

The solid-state NMR highlights the TG results that showed a weight loss occurring above 1000 °C: it identifies the presence of the BHN_2 environments in the **ABLi-1000** sample which are expected to be released at higher temperatures.

2.3.1.2 High temperature behavior of Li modified AB based BN

The phase evolution of the **ABLi1-1000** sample has been studied using XRD and Raman spectroscopy. Figure 3.31 depicts the XRD patterns of the **ABLi1-1000**, **ABLi1-14500**, **ABLi1-1600** samples with temperature increase from 1000 to 1600 °C under N_2 .

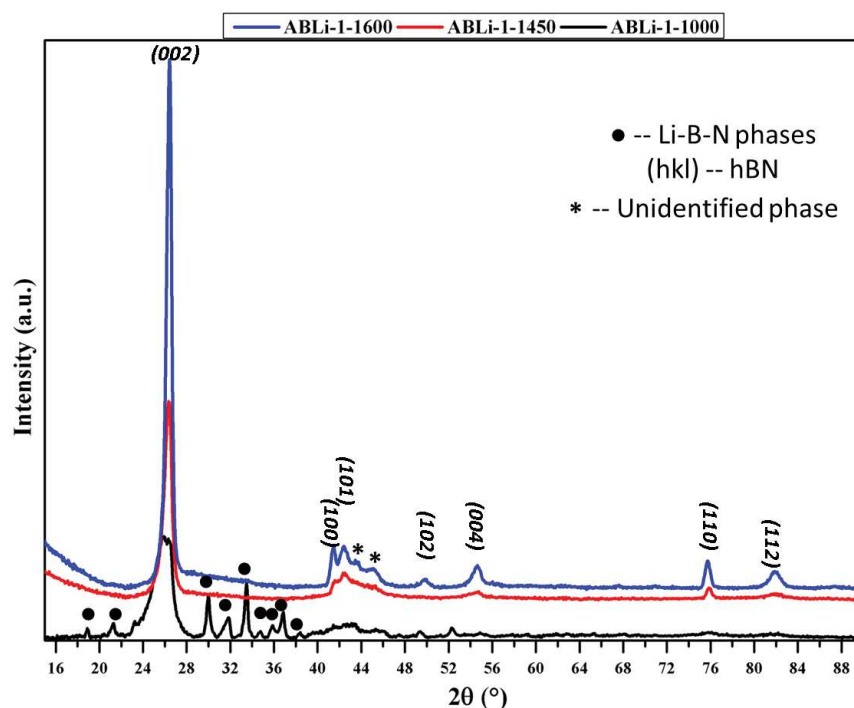


Figure 3.31 XRD patterns of ABLi-1000, ABLi-1450 and ABLi-1600 samples.

The XRD pattern of the **ABLi-1000** sample display a broad peak centered around 26.74° corresponding to the (002) reflection of BN with a lot of small peaks on the left and right sides between $2\theta = 28^\circ$ to 40° which are attributed to a Li-B-N phase. There are some peaks which are difficult to identify between 42° and 46° . Upon further annealing, the XRD pattern of the **ABLi-1450** sample was found to have a more intense and sharper peak at 26.74° as well as small broad peaks at around 43° , 54.5° and 75.9° which are all attributed to BN. The XRD peaks attributed to the Li-B-N phase disappear which can explain the weight loss we suggested to occur above 1000°C . Compared to the XRD pattern of the **ABBN-1450** sample (See Fig. 3.3), a significant increase of the BN crystallinity occurred. At 1600°C , we obtain a fully crystallized **ABLi-1600** sample with a sharp and intense peak at 26.4° (002) followed by harp but small peaks at 41.6° (100), 43.87° (101), 50.15° (102), 55.1° (004), 75.93° (110) and 82.18° (112). The pattern was matched with JCPDS file number 04-003-6253 of the hexagonal phase of BN suggesting a centrosymmetric crystal structure and a P63/mmc space group. The crystallite size calculated using Scherrer formula at the dominant (002) peak increases from 5.1 nm for **ABLi-1000** to 12.5 nm at **ABLi-1450** and finally 16.15 nm at **ABLi-1600**. Increase in degree of crystallization of BN due to addition of LiNH_2 to AB can be clearly seen upon comparing the crystallite sizes. For the **ABBN-1450**, we observed an

average crystallite size of 2.73 nm at (002) peaks. Hence we see a 7 fold increase in size of the crystal due to this process. Yuan et al reported a crystallite size of 9.27 nm at the same peak after addition of Li₃N powder to PB⁴⁶. The larger crystallite size in our case suggests the better efficiency of the intimate reaction between AB and LiNH₂, i.e., modification at a molecular level, over physical mixing of powders.

Two XRD peaks are also identified in the XRD pattern of the **ABBN-1600** sample around 44°. The c-BN and the t-Li₃BN₂ phase displays a XRD peak around this position but an annealing at 1600°C is expected to decompose the t-Li₃BN₂ phase whereas the formation of c-BN from h-BN needs high pressure. As a consequence, it was not possible to attribute these two peaks.

Here, we successfully demonstrated the interest to modify BN precursors with LiNH₂ to significantly improve the BN crystallinity at high temperature. However, a temperature of 1600 °C can be still considered as too high to find this approach interesting. As a consequence and because both precursors, *i.e.*, AB and LiNH₂, are solid, we tentatively applied a reactive ball-milling.

2.3.2 Reactive ball-milling

Ball milling (BM) is a simple and relatively inexpensive processing technique that is generally used for applying extensive plastic deformation to metallic powders through multiple impact events in a rotating vial containing hardened steel or ceramic balls. BM can produce extremely fine microstructures and form non-equilibrium phases (i.e. amorphous) or intermetallic compounds, when powder mixtures of different metals are used. Parameters that affect milling are particle size, compositional ratio of elements, ball-to-material ratio, rotation speed and milling time. Although BM has been carried out to mainly produce materials with superior high-temperature mechanical properties, there are only few reports on the preparation of BN by reactive ball-milling.

BN nanotubes have been produced by thermal annealing at 1000°C of elemental boron powders which were previously ball milled in NH₃ for 150 h at room temperature⁴⁷. As a proof of concept, we report for the first time the application of reactive BM to synthesize BN from *single-source* precursors. We performed the reaction between AB and LiNH₂ in a ball milling reactor (solid state reaction) at 200 rpm for 4 hours (*See chapter 2 for more details*). This process is called mechano-synthesis. The polymer (**ABLi1-BM**) powders obtained after this

process have been pyrolyzed at 1000 °C under NH_3 then annealed up to 1450°C in flowing N_2 . Figure 3.32 shows the XRD patterns of the **ABLi1-1000-BM** and **ABLi1-1450-BM** samples.

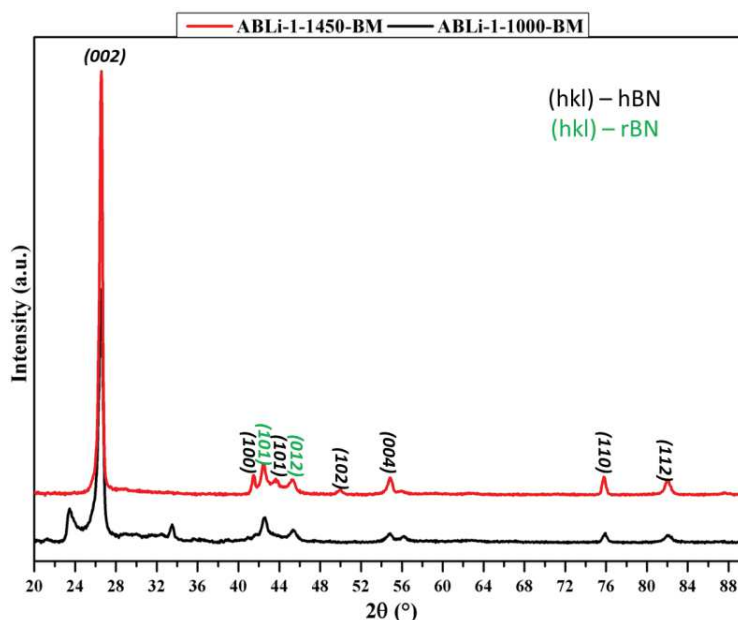


Figure 3. 32 XRD patterns of the **ABLi1-1000-BM** and **ABLi1-1450-BM** samples

The **ABLi1-1000-BM** sample is more crystalline as compared to its analog prepared by solution reaction. The crystallite size calculated at the dominant (002) peak using Scherrer equation was found to be 18.5 nm which upon annealing to 1450 °C (**ABLi1-1450-BM**) increased to 25.9 nm. Values above 17 nm generally indicate good degree of crystallinity⁴⁸. More interesting, the **ABLi1-1450-BM** sample crystallized as hexagonal boron nitride. The peaks were matched using JCPDS file number 04-003-6253. The most important peak which suggests the complete crystallization of BN at 1450 °C is the (102) peak. This peak did not crystallize for the previous **ABLi1-1450** sample in Figure 3.31. Therefore, we proved that reactive ball-milling is a promising approach to prepare highly crystallized BN at relatively low temperatures from *single-source* precursors. The process of mechano-synthesis also shows good promise in synthesizing polymers effectively. This process needs further investigation to understand its mechanism, advantages and drawbacks. Indeed, two unknown XRD peaks are still present in the XRD pattern of the **ABLi1-1450-BM** sample.

We also applied BM using **PB60** as a BN precursor using the same parameters. Pyrolysis was also done under NH_3 and annealing up to 1450 °C was performed under N_2 . Figure 3.33 shows

the XRD for the **PB60Li1-1450** sample. Because of the strongly intense (002) peak, it is difficult to see other peaks. Therefore, Fig. 3.34 presents a zoom of the 2θ range 35-90°. The majority of the peaks is attributed to the hexagonal phase of BN. However, it seems that the reactivity between **PB60** and LiNH_2 is better to generate highly crystallized BN.

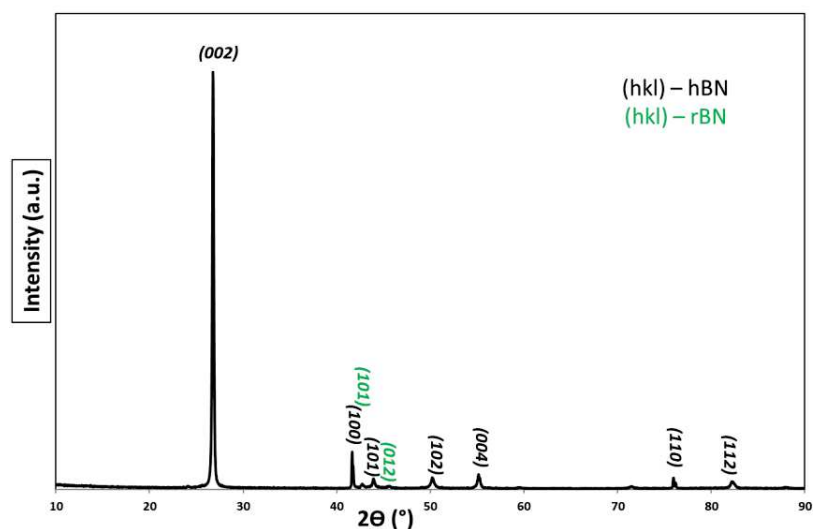


Figure 3.33 XRD pattern of the **PB60Li1-1450-BM** sample

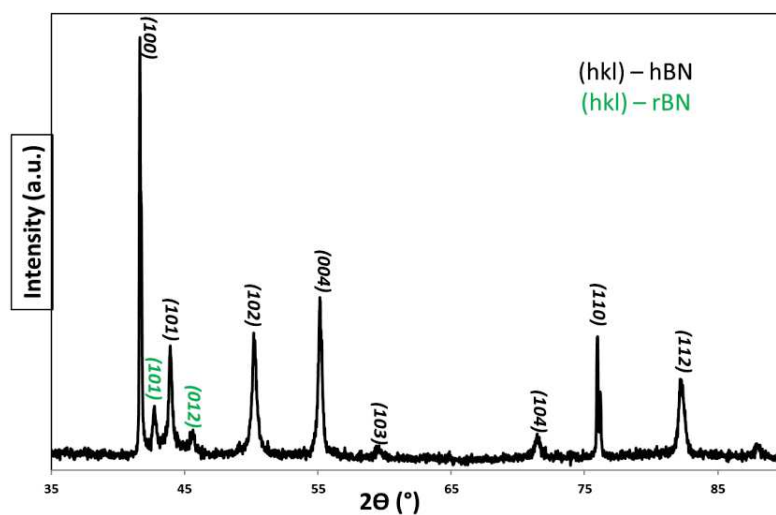


Figure 3.34 Zoom of the XRD pattern of the **PB60Li1-1450-BM** sample

By changing the chemistry of the Li-based compound and selecting LiH, we can observe a same behavior in the XRD patterns of the samples prepared at 1450 °C with a better BN crystallinity using **PB60** as a BN precursor.

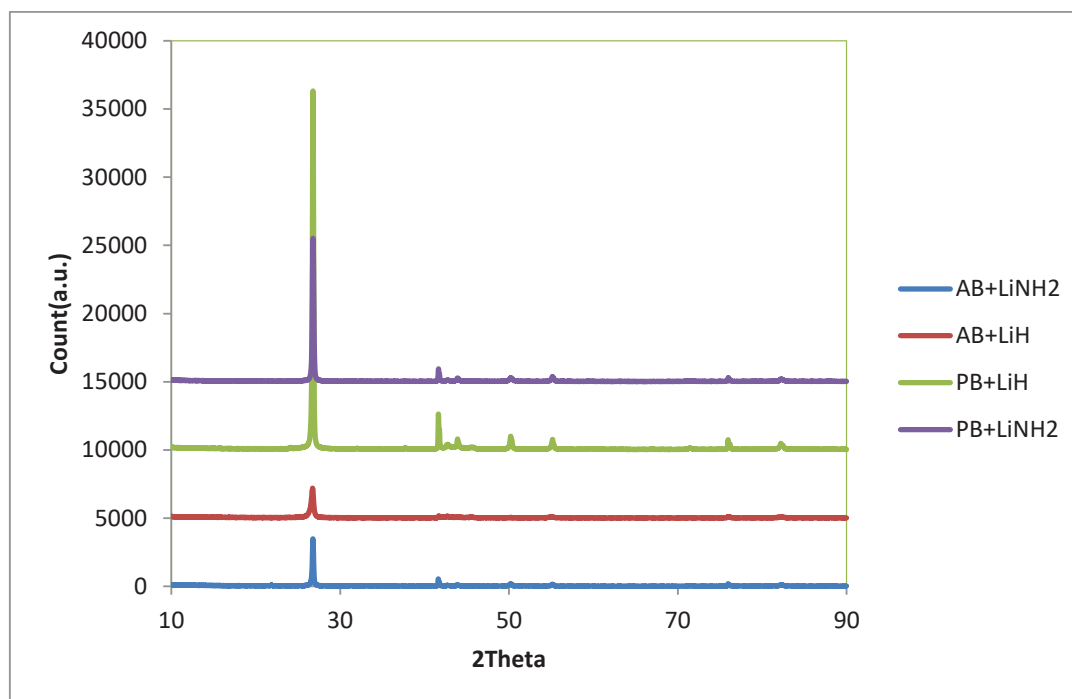


Figure 3.35 XRD patterns of the samples using LiH and LiNH₂ as Li-containing compounds.

4. Conclusion

In this chapter, we investigated the synthesis of boron nitride (BN) and B-M-N (M = Ti, Zr, Hf) ceramics from two different BN precursor namely, ammonia borane (AB) and polyborazylene (PB). In the first part of the chapter, we briefly introduced the preparation of BN from these two precursors and showed that the formation of the hexagonal phase of BN was not possible using these two precursors which represents an advantage to prepare the nanocomposites with the nanostructural organization we targeted in the second part of the present chapter: MN nanophase distributed in an amorphous matrix. In the second part, the major part, we discussed on the introduction of transition metals such as titanium, zirconium and hafnium at molecular scale in BN precursor. The polymer synthesis and pyrolysis have been investigated through complementary tools such as FTIR, solid-state NMR and TGA. It has been shown that the synthesis of polymers occurred through two reactions involving NH and BH groups in BN precursors but such reactions occurred more efficiently with Hf-based

compounds. As a consequence, Hf-containing polymers displayed the highest crosslinking degree; thus resulting in a very high ceramic yield. After pyrolysis under NH_3 at 1000°C , samples were amorphous and the subsequent annealing to 1450°C under N_2 formed nanocomposites in which MN nanocrystals are dispersed in the BN matrix. We found out that increasing the Ti content in the polymer almost suppressed the crystallization of BN in the final nanocomposites at high temperature but only Hf is able to fully suppress the crystallization of BN for a B:Hf ratio of 3 resulting in the formation of highly stable nanocomposite structures. However, such nc-MN/a-BN nanocomposites especially with $M = \text{Ti}$ and Hf may have some potential disadvantage due to the low BN crystallinity which can involve oxidation. To overcome this problem, we focused the last part of the present chapter on the investigation of the improvement of the BN crystallinity through the modification of BN precursors with LiNH_2 through a solution route and reactive ball-milling. Reactive ball-milling allowed generating a highly crystallized BN after pyrolysis under NH_3 at 1000°C then annealed at 1450°C under N_2 .

References

1. Paine, R. T. & Narula, C. K. Synthetic routes to boron nitride. *Chem. Rev.* **90**, 73–91 (1990).
2. Balmain, W. H. Bemerkungen über die Bildung von Verbindungen des Bors und Siliciums mit Stickstoff und gewissen Metallen. *J. für Prakt. Chemie* **27**, 422–430 (1842).
3. Haubner, R., Wilhelm, M., Weissenbacher, R. & Lux, B. in 1–45 (Springer Berlin Heidelberg, 2002). doi:10.1007/3-540-45623-6_1
4. Bernard, S., Salles, V., Foucaud, S. & Miele, P. Boron Nitride Nanoparticles: One-Step Synthesis from Single-Source Pre-ceramic Precursors. *Adv. Sci. Technol.* **62**, 1–7 (2010).
5. Li, J., Bernard, S., Salles, V., Gervais, C. & Miele, P. Preparation of Polyborazylene-Derived Bulk Boron Nitride with Tunable Properties by Warm-Pressing and Pressureless Pyrolysis. *Chem. Mater.* **22**, 2010–2019 (2010).
6. Miele, P., Toury, B., Cornu, D. & Bernard, S. Borylborazines as new precursors for boron nitride fibres. *J. Organomet. Chem.* **690**, 2809–2814 (2005).
7. Bernard, S., Chassagneux, F., Berthet, M.-P., Vincent, H. & Bouix, J. Structural and mechanical properties of a high-performance BN fibre. *J. Eur. Ceram. Soc.* **22**, 2047–2059 (2002).
8. Frueh, S. *et al.* Pyrolytic Decomposition of Ammonia Borane to Boron Nitride. (2010). doi:10.1021/IC101020K
9. Brame, E. G., Margrave, J. L. & Meloche, V. W. Infra-red spectra of inorganic solids—II oxides, nitrides, carbides, and borides. *J. Inorg. Nucl. Chem.* **5**, 48–52 (1957).
10. Baumann, J., Baitalow, F. & Wolf, G. Thermal decomposition of polymeric aminoborane (H₂NBH₂)_x under hydrogen release. *Thermochim. Acta* **430**, 9–14 (2005).
11. Komm, R., Geanangel, R. A. & Liepins, R. Synthesis and studies of poly(aminoborane), (H₂NBH₂)_x. *Inorg. Chem.* **22**, 1684–1686 (1983).
12. Fazen, P. J. *et al.* Synthesis, Properties, and Ceramic Conversion Reactions of Polyborazylene. A High-Yield Polymeric Precursor to Boron Nitride. *Chem. Mater.* **7**, 1942–1956 (1995).
13. Pease, R. S. An X-ray study of boron nitride. *Acta Crystallogr.* **5**, 356–361 (1952).
14. Ooi, N., Rairkar, A., Lindsley, L. & Adams, J. B. Electronic structure and bonding in hexagonal boron nitride. *J. Phys. Condens. Matter* **18**, 97–115 (2006).
15. Coleburn, N. L. & Forbes, J. W. Irreversible Transformation of Hexagonal Boron Nitride by Shock Compression. *J. Chem. Phys.* **48**, 555–559 (1968).
16. Thomas, J., Weston, N. E. & O'Connor, T. E. Turbostratic ¹ Boron Nitride, Thermal Transformation to Ordered-layer-lattice Boron Nitride. *J. Am. Chem. Soc.* **84**, 4619–4622 (1962).
17. Schaeffer, R. *et al.* Preparation of Borazole by the Reduction of Trichloroborazole ^{1a}. *J. Am. Chem. Soc.* **76**, 3303–3306 (1954).

18. Bernard, S. *et al.* Evolution of structural features and mechanical properties during the conversion of poly[(methylamino)borazine] fibers into boron nitride fibers. *J. Solid State Chem.* **177**, 1803–1810 (2004).
19. Jeschke, G., Hoffbauer, W. & Jansen, M. A comprehensive NMR study of cubic and hexagonal boron nitride. *Solid State Nucl. Magn. Reson.* **12**, 1–7 (1998).
20. Beck, J. S., Albani, C. R., McGhie, A. R., Rothman, J. B. & Sneddon, L. G. Dibromoborane-dimethyl sulfide: a simple molecular precursor for the formation of bulk powders and fiber coatings of boron nitride. *Chem. Mater.* **1**, 433–438 (1989).
21. Termoss, H. *et al.* Preparation of boron nitride-based coatings on metallic substrates via infrared irradiation of dip-coated polyborazylene. *J. Mater. Chem.* **19**, 2671 (2009).
22. Laubengayer, A. W., Moews, P. C. & Porter, R. F. The Condensation of Borazine to Polycyclic Boron-Nitrogen Frameworks by Pyrolytic Dehydrogenation¹. *J. Am. Chem. Soc.* **83**, 1337–1342 (1961).
23. Fazen, P. J., Beck, J. S., Lynch, A. T., Remsen, E. E. & Sneddon, L. G. Thermally induced borazine dehydropolymerization reactions. Synthesis and ceramic conversion reactions of a new high-yield polymeric precursor to boron nitride. *Chem. Mater.* **2**, 96–97 (1990).
24. Kim, D. & Economy, J. Occurrence of Liquid Crystallinity in a Borazine Polymer. *Chem. Mater.* **6**, 395–400 (1994).
25. Diwan, M., Hanna, D. & Varma, A. Method to release hydrogen from ammonia borane for portable fuel cell applications. *Int. J. Hydrogen Energy* **35**, 577–584 (2010).
26. Heldebrant, D. J. *et al.* The Effects of Chemical Additives on the Induction Phase in Solid-State Thermal Decomposition of Ammonia Borane. *Chem. Mater.* **20**, 5332–5336 (2008).
27. Sepehri, S. *et al.* Spectroscopic studies of dehydrogenation of ammonia borane in carbon cryogel. *J. Phys. Chem. B* **111**, 14285–14289 (2007).
28. Gervais, C. *et al.* Chemically derived BN ceramics: Extensive ¹¹B and ¹⁵N solid-state NMR study of a preceramic polyborazylene. *Chem. Mater.* **13**, 1700–1707 (2001).
29. Toury, B. *et al.* High-resolution ¹⁵N solid-state NMR investigations on borazine-based precursors. *Appl. Organomet. Chem.* **18**, 227–232 (2004).
30. Nemanich, R. J., Solin, S. A. & Martin, R. M. Light scattering study of boron nitride microcrystals. *Phys. Rev. B* **23**, 6348–6356 (1981).
31. Spengler, W., Kaiser, R. & Bilz, H. Resonant Raman scattering in a superconducting transition metal compound—TiN. *Solid State Commun.* **17**, 19–22 (1975).
32. Ding, Z. H., Yao, B., Qiu, L. X. & Lv, T. Q. Raman scattering investigation of nanocrystalline δ -TiN_x synthesized by solid-state reaction. *J. Alloys Compd.* **421**, 247–251 (2006).
33. Zhou, C. *et al.* Synthesis and high-temperature evolution of single-phase amorphous Si₃Hf₂N₃ ceramics. *J. Eur. Ceram. Soc.* **35**, 2007–2015 (2015).

34. Yano, M. *et al.* Growth of nitride crystals, BN, AlN and GaN by using a Na flux. *Diam. Relat. Mater.* **9**, 512–515 (2000).
35. Yano, M. *et al.* Na: A New Flux for Growing Hexagonal Boron Nitride Crystals at Low Temperature. *Jpn. J. Appl. Phys.* **39**, L300–L302 (2000).
36. Yang, P. C., Prater, J. T., Liu, W., Glass, J. T. & Davis, R. F. The formation of epitaxial hexagonal boron nitride on nickel substrates. *J. Electron. Mater.* **34**, 1558–1564 (2005).
37. Gu, Y., Zheng, M., Liu, Y. & Xu, Z. Low-Temperature Synthesis and Growth of Hexagonal Boron-Nitride in a Lithium Bromide Melt. *J. Am. Ceram. Soc.* **90**, 1589–1591 (2007).
38. Solozhenko, V. L. & Turkevich, V. Z. Kinetics of cBN crystallization in the Li₃N-BN system at 6.6 GPa. *Diam. Relat. Mater.* **7**, 43–46 (1998).
39. Shipilo, V. B., Ignatenko, O. V., Shempel, N. A., Azarko, I. I. & Lebedev, S. A. Crystallization of cubic boron nitride in the system Li₃N-BN (4–10 wt % Li₃N). *Inorg. Mater.* **44**, 258–262 (2008).
40. Guo, X.-F. *et al.* Thermodynamic Analysis about Nucleation and Growth of Cubic Boron Nitride Crystals in the hBN-Li₃N System under High Pressure and High Temperature. *Entropy* **17**, 755–762 (2015).
41. von der Gönna, J. *et al.* In-situ investigations of the reversible hBN-cBN-hBN-transformation in the Li₃N-BN catalyst system using synchrotron radiation. *Mater. Lett.* **33**, 321–326 (1998).
42. Du, Y. *et al.* Synthesis of black cBN single crystal in hBN-Li₃N-B system. *Mater. Lett.* **61**, 3409–3412 (2007).
43. Nöth, H. & Wrackmeyer, B. *Nuclear Magnetic Resonance Spectroscopy of Boron Compounds*. (Springer Berlin Heidelberg, 1978). doi:10.1007/978-3-642-66757-2
44. Duperrier, S. *et al.* Design of a Series of Pre-ceramic B-Tri(methylamino)borazine-Based Polymers as Fiber Precursors: Shear Rheology Investigations. *Macromolecules* **40**, 1028–1034 (2007).
45. Gunaydin-Sen, O., Achey, R., Dalal, N. S., Stowe, A. & Autrey, T. High resolution ¹⁵N NMR of the 225 K phase transition of ammonia borane (NH₃BH₃): Mixed order-disorder and displacive behavior. *J. Phys. Chem. B* **111**, 677–681 (2007).
46. Yuan, S. *et al.* Low-Temperature Synthesis of Highly Crystallized Hexagonal Boron Nitride Sheets with Li₃N as Additive Agent. *Eur. J. Inorg. Chem.* **2014**, 5507–5513 (2014).
47. Chen, Y., Fitz Gerald, J., Williams, J. S. & Bulcock, S. Synthesis of boron nitride nanotubes at low temperatures using reactive ball milling. *Chem. Phys. Lett.* **299**, 260–264 (1999).
48. Yuan, S. *et al.* New potential for preparation of performing h-BN coatings via polymer pyrolysis in RTA furnace. *J. Eur. Ceram. Soc.* **33**, 393–402 (2013).
49. by Ben Mills - Own work, Public Domain, <https://commons.wikimedia.org/w/index.php?curid=6323282>
50. PhD thesis of Gorges Moussa; 2014

CHAPTER 4
SILICON-BASED
NON-OXIDE
CERAMICS



1. Introduction

For most industrial purposes, technical ceramics are produced from conventional powder metallurgy routes which involve shaping and consolidation of inorganic powders. Although the process is well established at industrial scale, it has some limitations such as high operating temperatures, especially as non-oxide ceramics, inability to generate complex shapes and difficulties to design the porosity, at least the mesoporosity of materials. Furthermore, when the preparation of nanocomposites is targeted, a uniform distribution of elements is difficult to achieve, owing to the low diffusion coefficient of elements. One of the ways to design such materials is to control the structure at very small length scales in an early stage of their synthesis. Within this context, it appeared obvious to us that improving the control of compositional homogeneity, the purity as well as the processability of ceramics should be achieved using *single-source* precursors, polymers and/or solution techniques. This viewpoint focused on, the polymer-derived ceramics (PDC) route has been exploited in our work. As we observed in the chapter 3, the PDC route is well adapted to multi-element systems including MN/BN (M: Ti, Zr, Hf) nanocomposites.

This chapter is based on the same concept with the difference being change in the nature of the matrix from BN to Si_3N_4 . It is divided in two parts; the first part deals with the chemistry, the polymer-to-ceramic conversion and the high temperature behavior of polysilazane-derived Si_3N_4 . This study will allow us to understand the impact of the addition of a second phase, *i.e.*, MN with M = Ti, Zr, Hf, in these ceramics to form nanocomposites which are discussed in the second (major) part of the present chapter. In this second part, we discuss the synthesis and properties of Si-M-N (M=Ti, Zr, Hf) ceramics using the PDC route. We firstly characterize the *single-source* polymetallosilazane, then document the polymer-to-ceramic conversion and finally characterize the microstructure of the ceramics, especially its evolution at high temperature.

The main objective behind the preparation of these nanocomposites is to understand the influence of the chemistry of precursor on the structural behavior of Si-M-N ceramics at high temperature.

2. Preparation of polysilazane-derived Si_3N_4

The objective of this part is to characterize the preceramic polymers like Si_3N_4 and Si-C-N which are used to prepare the Si-M-N (M: Ti, Zr, Hf) ceramics in the second part of this chapter. We investigate the chemistry, thermal behavior and study the microstructure evolution of the as-obtained ceramics at high temperature.

2.1 Perhydropolysilazane (PHPS)-derived Si_3N_4

PHPS is a highly reactive preceramic polymer containing two Si-H and one N-H functions in its structure as illustrated in Figure 4.1.

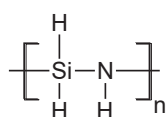


Figure 4.1 Formula of perhydropolysilazane (PHPS)

Figure 4.2a show the FTIR and ^1H NMR spectra of PHPS.

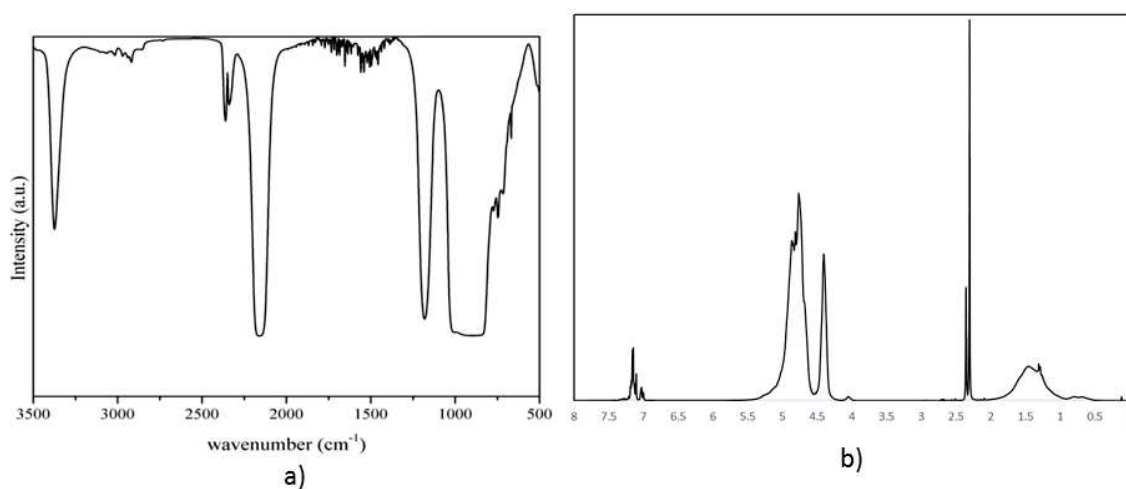


Figure 4.2 a) FTIR spectrum (taken using KBr windows) and b) ^1H liquid NMR spectrum (in CDCl_3) of PHPS

The FTIR spectrum of PHPS involves only three types of bonds corresponding to its structure shown in Figure 4.2, *i.e.*, N-H, Si-N-Si, and Si-H. The bands in the range of 3200-3400 cm^{-1} (stretching) and 1180 cm^{-1} (bending) correspond to N-H bonds. The sharp nature of the band in the former range indicates the absence of hydrogen bonding in the system thus the polymer has a very open chain structure. The very strong band at 2150 cm^{-1} corresponds to stretching of Si-H bonds whereas the strong band from 800 to 1000 cm^{-1} corresponds to the Si-N-Si

network. A group of very weak signals can be seen in the range of 2900 to 3000 cm^{-1} which corresponds to the C-H bond. Although PHPS does not have any C in its backbone structure, the signal of C-H bonds can be attributed to protective end groups added to the main chain/backbone to stabilize PHPS and/or the presence of residual solvent as PHPS is commercially available as 20% solution in xylene. The doublet of sharp peaks at 2300 cm^{-1} is due to the CO_2 and H_2O correction, so are the small bands in the range of 1500 to 1750 cm^{-1} .

Apart from FT-IR, we investigated ^1H liquid NMR on PHPS to determine the structure of the polymer (Figure 4.2b).

The liquid ^1H NMR spectrum of PHPS shows signals at 7.26 ppm, 7.10 ppm, 4.8 ppm, 4.34 ppm, 2.4 ppm, 2.3 ppm, a broad peak from 0.5-2.0 ppm and 0.1 ppm. Analysis of trace compounds in NMR done by Fulmer et al¹ showed that the peaks at 7.26 ppm and 7.10 ppm are multiplet peaks of CH in *m*-xylene while the signals emerging at 2.4 ppm and 2.3 ppm belong to the CH_3 in *m*-xylene. The rest of the signals belong to the proton in PHPS with the signals from 0.5 to 2.0 ppm attributing to Si_2NH , at 4.8 ppm ($\text{N}_3\text{SiH}/\text{N}_2\text{SiH}_2$), at 4.34 ppm (NSiH_3) and at 0.1 ppm ($\text{NSi}(\text{CH}_3)_3$). Through pyrolysis under nitrogen, PHPS leads to a composite material composed of a majority of Si_3N_4 and around 13 wt% of silicon (Si)². Using ammonia as atmosphere, PHPS leads to Si_3N_4 in a measured weight loss of 32 % (Figure 4.3); therefore, the ceramic yield is calculated to be 68 %. We particularly focused on the use of ammonia as atmosphere of pyrolysis because Si-M-N (M: Ti, Zr, Hf) ceramics designed in the second part of the chapter are prepared under ammonia.

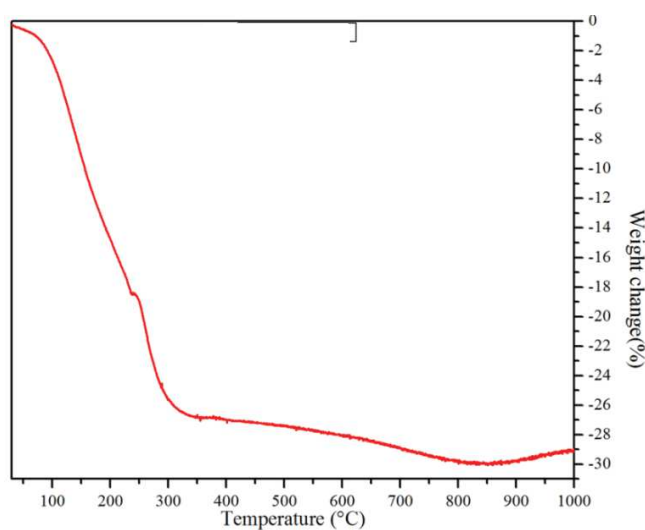


Figure 4.3 TGA of PHPS under NH_3

Under ammonia the major weight loss occurs in the range of 100° to 350°C and is due to dehydrogenation of Si-H/N-H and Si-H/Si-H bonds leading to formation of Si-N and Si-Si bonds forming the backbone structure of the ceramic. There is no weight loss from 350°C to 550°C after which we have a drop of another 3% due to ceramization. There is loss of dangling hydrogen from N-H groups in this range. Ideally, there is nitridation occurring in the temperature range of 350 to 450°C which should lead to weight gain as reported by Isoda et al³ but no such gain is observed. This contradictory result can be attributed to the fact that we use a commercial PHPS which generally has heavy carbon based end groups for stability which are lost in the previously mentioned temperature range whereas Isoda *et al* used a homemade PHPS which did not have such groups. At 1000°C, the material labelled PHPS-1000 is amorphous as shown on XRD pattern represented in Figure 4.4. Further annealing in flowing nitrogen up to 1700°C involved the crystallization of α - and β -Si₃N₄. The major peaks start crystallizing at 1200°C and by 1400°C we achieved complete crystallization of Si₃N₄ which is a little higher than what was reported by Schwab et al, where they obtained a completely crystalline matrix at 1270 °C under N₂.⁴

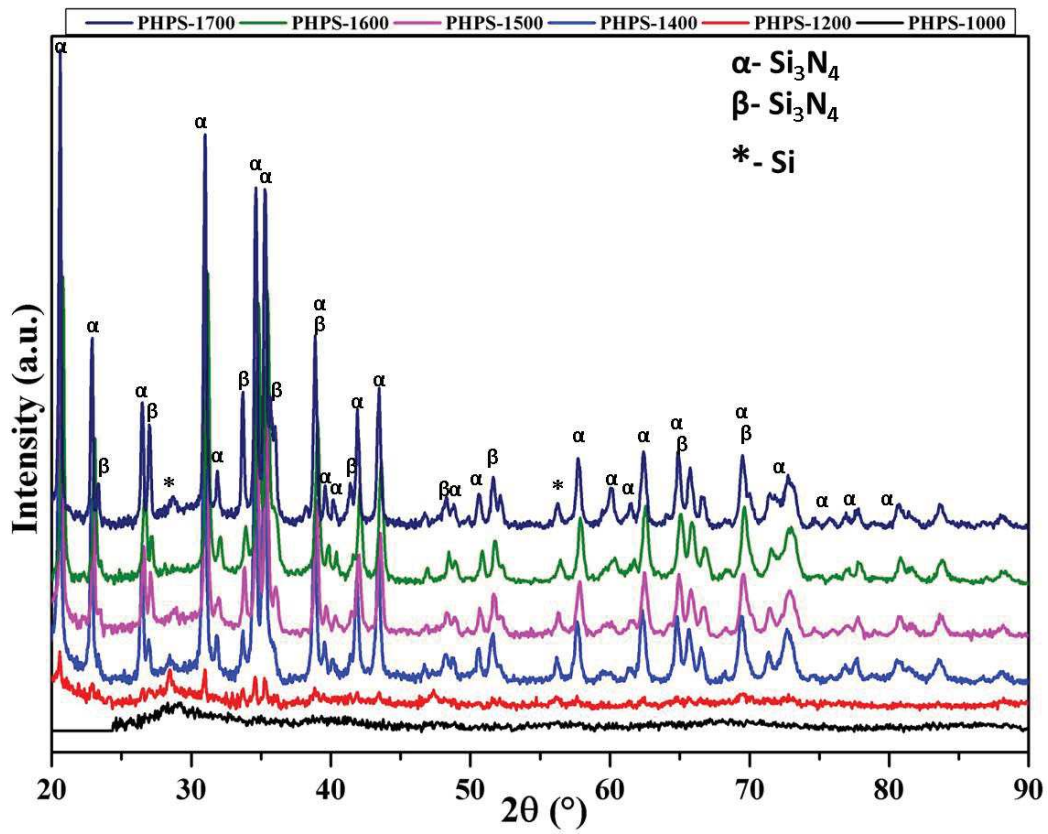


Figure 4.4 XRD patterns of ammonia-treated PHPS derived Si₃N₄ in the temperature range 1000-1700°C

2.2 Poly(vinylmethyl-co-methyl)silazane (HTT1800)-derived Si_3N_4

HTT1800 is a commercially available copolymer containing 20 % of methyl/vinyl and 80 % of methyl/hydride substituted silazane units (Figure 4.5)⁵.

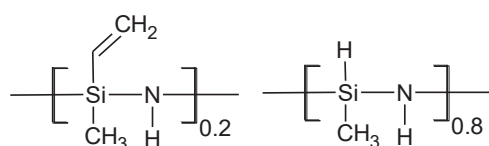


Figure 4.5 Structure for HTT1800

The precursor can be used to prepare both Si_3N_4 and Si-C-N ceramics depending on the gaseous atmosphere used during the polymer-to-ceramic conversion.

The FTIR spectrum (Figure 4.6a) of HTT1800 shows the expected absorption bands of polyorganosilazanes, as reported in the literature^{6,7}: Si-N-H stretching at 3382 cm^{-1} coupled with Si-N vibrations at 1166 cm^{-1} , the stretching of C-H bonds in CH_x units at 2957 cm^{-1} (CH_3 asymmetric stretching), 2916 cm^{-1} (CH_2 stretching), 2898 cm^{-1} (CH stretching), and 2849 cm^{-1} (CH_3 symmetric stretching), a typical absorption band arising from the stretching of C=C double bonds in vinyl groups and CH_x deformations at 1593 and 1400 cm^{-1} , respectively as well as the corresponding C-H bond stretching at 3047 and 3005 cm^{-1} , respectively was also visible. The bands at 2126 and 1253 cm^{-1} are attributed to the stretching of Si-H bonds and deformations of C-H bonds in SiCH_3 units, respectively. Below 1000 cm^{-1} , absorption bands attributed to stretching and deformation vibrations that involve Si-C, Si-N, C-H, and C-C bonds overlap and cannot be assigned unambiguously.

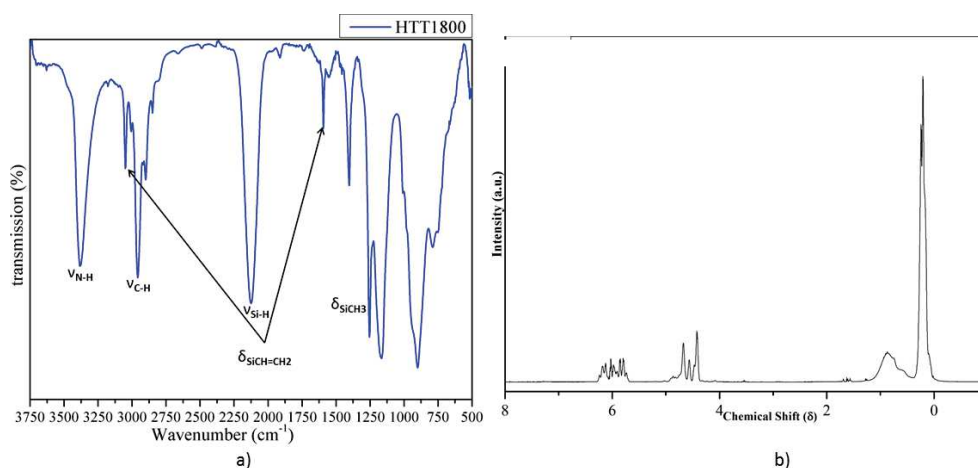


Figure 4.6 a) FTIR and b) ^1H liquid NMR spectrum of HTT1800

The ^1H NMR spectrum is typical of a vinyl-containing polyorganosilazane. ^1H signals were detected at $\delta=0.20$ (SiCH_3), 0.5 to 1.1 (SiNHSi), 4.35 to 4.7 (SiH), 5.65 to 5.95 ($\text{SiCH}=\text{CH}_2$), and 6.00 to 6.25 ppm ($\text{SiCH}=\text{CH}_2$). In ^{13}C NMR spectrum a broad signal was observed at $\delta = -4.0$ to 4 ppm which can be assigned to Si bonded CH_3 sites and signal relating to olefin carbon was observed from $\delta = 125$ to 142 ppm. For ^{29}Si NMR spectra, a signal at $\delta = -21$ ppm was attributed to $(\text{CH}_3)\text{Si}(\text{CH}=\text{CH}_2)\text{N}_2$ units. Peak related to $\text{HSi}(\text{CH}_3)\text{N}_2$ units should appear at $\delta = -15$ ppm, but this component was superimposed by the main peak at $\delta = -21$ ppm.

The polymer-to-ceramic conversion of HTT1800 leads to either Si-C-N ceramics or Si_3N_4 depending on the pyrolysis atmosphere. Under N_2 , HTT1800 exhibits three different weight losses during the pyrolysis (Figure 4.7). A first major weight loss occurs up to 250°C , which mainly corresponds to the volatilization of low-molecular-weight organosilicon species, but also crosslinking reactions of the precursor through transamination and bond redistribution. However, hydrogen is also identified as a gaseous byproduct, most probably due to the dehydrocoupling reaction of $-\text{SiH}/-\text{SiH}$ and $-\text{SiH}=\text{NH}$ groups. The TGA profile after the first stage is nearly same for both N_2 and NH_3 as is evident from the figure. A second weight loss takes place between 250 and 450°C , which is possibly due to transamination because of the presence of NH groups, which removes ammonia. HTT1800 is converted into a ceramic through a third weight loss occurring between 450 and 1000°C , in which rearrangements occur through radical formation and recombination. Evolution of methane is mainly detected in this temperature range⁷ because of the decomposition of SiCH_3 groups or the cleavage of C=C bonds. However, the thermal decomposition of HTT1800 probably occurs through

mechanisms that are superimposed rather than well separated in clear temperature ranges as proposed.

Under ammonia (Figure 4.7), the weight loss is lower most probably because volatilization of low molecular weight species in the low temperature regime of the decomposition is reduced.

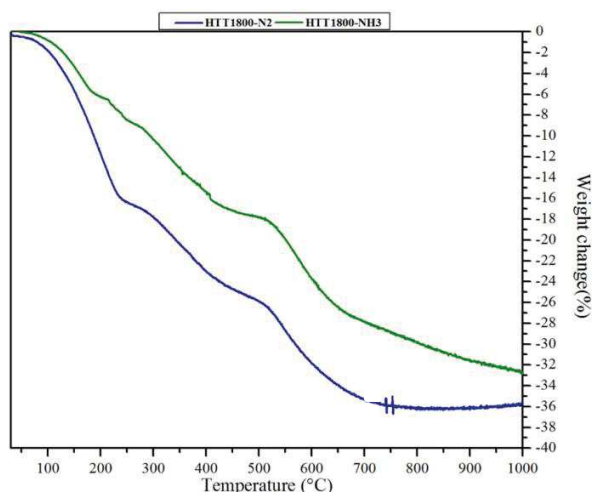


Figure 4.7 TGA of HTT1800 under NH_3 and N_2

After pyrolysis at 1000°C , ammonia-treated samples are X-ray amorphous as shown in Fig 4.8. By increasing the temperature up to 1700°C under nitrogen, ammonia-treated samples are shown to remain completely amorphous until 1400°C . After annealing at 1500°C , we can distinguish peaks attributed to $\alpha\text{-Si}_3\text{N}_4$ and $\beta\text{-Si}_3\text{N}_4$. Major peaks for $\alpha\text{-Si}_3\text{N}_4$ peaks are found at 20.62° (101), 31.02° (201), 34.617° (102), 35.376° (210) and 38.94° (-2-10) while $\beta\text{-Si}_3\text{N}_4$ peaks are found at 23.397° (110), 27.06° (200) and 33.693° (101). The crystallization temperature of HTT1800-derived Si_3N_4 is shifted by 230°C in comparison to PHPS-derived Si_3N_4 . This is probably due to the more complex reaction sites which occur during pyrolysis because of the presence of carbon-based groups. After annealing to 1700°C , we obtained fully crystallized $\alpha\text{-Si}_3\text{N}_4$ and $\beta\text{-Si}_3\text{N}_4$.

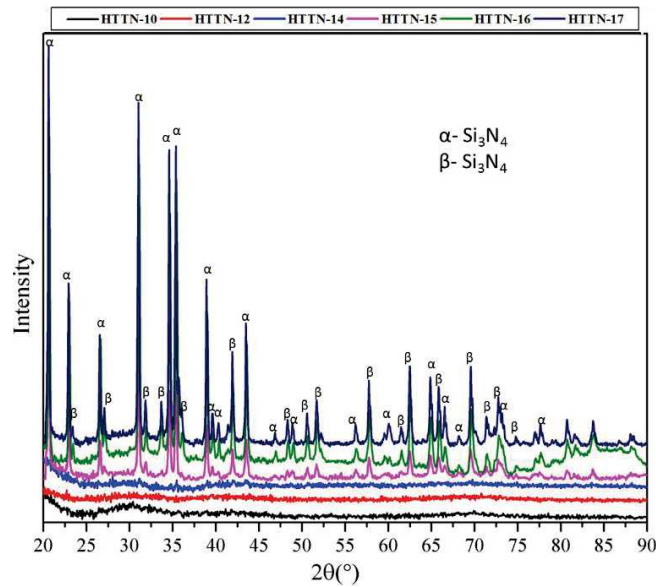


Figure 4.8 XRD patterns of ammonia-treated HTT1800 derived Si_3N_4 in the temperature range 1000-1700°C

2.3 Conclusion

The objective of this part was to follow the thermal decomposition of PHPS and HTT1800, two commercially available preceramic polymers, into Si_3N_4 using ammonia as gaseous atmosphere. Then, we investigated the microstructural evolution at high temperature. Such a study was required to understand and highlight the effect of the introduction of a third element, *i.e.*, $M = \text{Ti}, \text{Zr}, \text{Hf}$ to these ceramics to form Si-M-N ceramics. This is the subject of the second part of the present chapter.

3. Preparation of Si-Ti-N ceramics

Ternary Si-M-N (M = early transition metal) materials have attracted the attention of researchers in recent years, especially as coatings with very interesting physical properties such as their hardness and wear resistance, their high-temperature stability and their oxidation resistance. Such materials form multiphase compounds with a uniform distribution of elements in which early transition metal nitride nanocrystals are homogeneously dispersed in a silicon nitride (Si_3N_4) matrix. They are denoted as $nc\text{-MN}/a\text{-Si}_3\text{N}_4$ films (nc for nanocrystalline, a for amorphous). CVD (chemical vapor deposition), ALD (atomic layer deposition) and reactive magnetron sputtering methods are reported to be applied in the fabrication of Si-M-N materials. However, these techniques are mostly applied to produce films whereas for many applications, there is a pressing need to generate other shapes and textures to make practical devices. This is the way to further explore the properties of these materials and exploit their widespread interest in industry, in cutting-edge technology and in our daily life. Here we used the previously described preceramic polymers, *i.e.*, PHPS and HTT1800 to react with titanium containing precursor, tertakisdimethylaminotitanium (TDMAT), to prepare ternary Si-Ti-N materials using the procedure depicted in Figure 4.9 and already exploited in chapter 3 using BN precursors as matrix precursors.

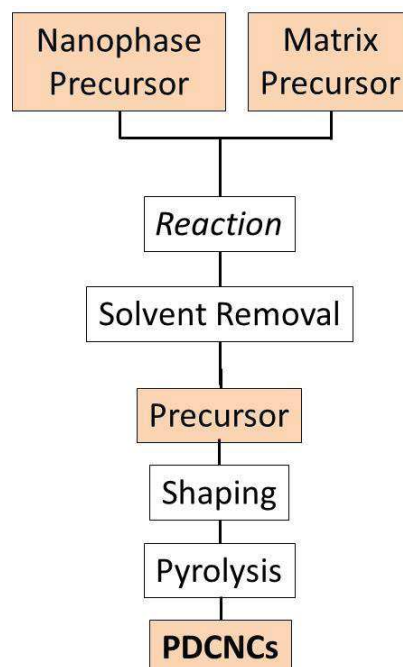


Figure 4.9 Schematic of PDC route to synthesize nanocomposites

In the following sections we discuss the synthesis of the polytitanosilazanes from PHPS and HTT1800 by fixing a Si:Ti ratio of 2.5, the polymer-to-ceramic conversion, the crystallization behavior and the microstructural evolution of the ceramics and the nanostructure of ceramics. In particular, we will highlight that the polymer chemistry has a strong impact on the properties of the ceramics.

3.1. Polytitanosilazane synthesis

The liquid tetrakis(dimethylamido)titanium precursor (TDMAT, Figure 4.10) was used as the nanophase precursor to modify the polysilazanes such as PHPS and HTT1800. This modification leads to the synthesis of a *single source* Si-Ti-N precursor we call polytitanosilazanes.

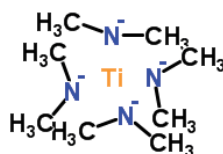


Figure 4.10 Molecular formula of TDMAT

We already investigated the reaction between TDMAT and polyorganosilazanes such as polymethylsilazane (PMSZ) in the PhD thesis of Mirna Bechelany³³. This work was recently published in *Chem. Eur. J.*⁸

In particular, a series of polytitanosilazanes has prepared from PMSZ (Figure 4.11) through several ratios from 1 to 10 and the role of the chemistry behind their synthesis has studied in details.

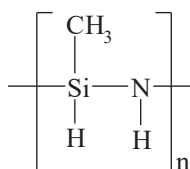


Figure 4.11 Molecular formula of polymethylsilazane (PMSZ)

It has been demonstrated based on FTIR and solid-state NMR spectroscopies coupled with mass spectrometry and elemental analyses that the reaction of TDMAT and polyorganosilazanes involves N-H and Si-H bonds in polysilazanes as well as $N(CH_3)_2$ groups in TDMAT according to Eq. (1) and Eq. (2).

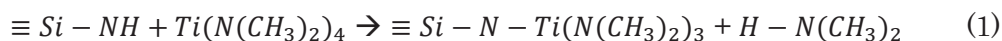


Figure 4.12 proposed a molecular structure for the polytitanosilazane prepared from PMSZ with a Si:Ti ratio of 2.5 based on chemical composition, FTIR, solid-state NMR and molecular weight measurements.

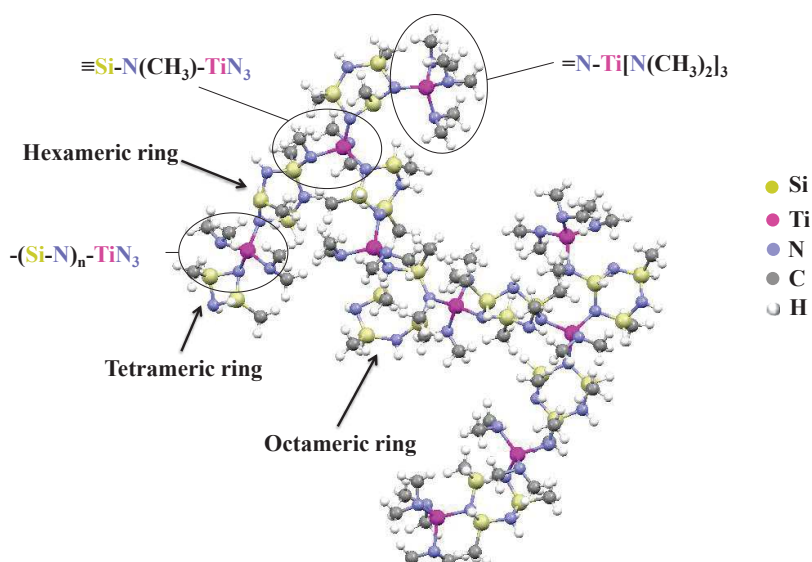


Figure 4.12 Molecular structure proposed for the polytitanosilazane synthesized from PMSZ and TDMAT

Titanium atoms allow increasing the crosslinking degree of the polymeric backbone. They are homogeneously distributed within the polysilazane structure as bridges linking silazane units as well as terminal units. There are two types of bridges *i.e.* those involving $-(Si-N)_n-TiN_3$ units (Eq. (1)) which are built by $HNMe_2$ and NH condensation and those involving $SiN(CH_3)TiN_3$ units (Eq. (2)) which arise due to reaction between $Si-H$ and $(CH_3)_2NTi$ moieties. The proposed structure is consistent with the analyzed polymer structure although it shows a slight deviation in the nitrogen content in comparison to experimental chemical compositions.

We confirmed such reactions with the polytitanosilazanes prepared from PHPS (labeled **NCPTi2.5**) and HTT1800 (labeled **NCHTi2.5**) according to a Si:Ti ratio of 2.5 based on FTIR and solid NMR spectroscopies coupled with elemental analyses.

The FTIR spectra of the **NCPTi2.5** and **NCHTi2.5** samples are compared with PHPS and HTT1800, respectively. To better understand the chemistry behind the synthesis of polytitanosilazane from HTT1800, we compared its FTIR spectrum with the FTIR spectrum of HTT1800 and HTT1800 having undergone a similar synthesis procedure than polytitanosilazane but without TDMAT. It is labelled HTT1800-R120 (Figure 4.13).

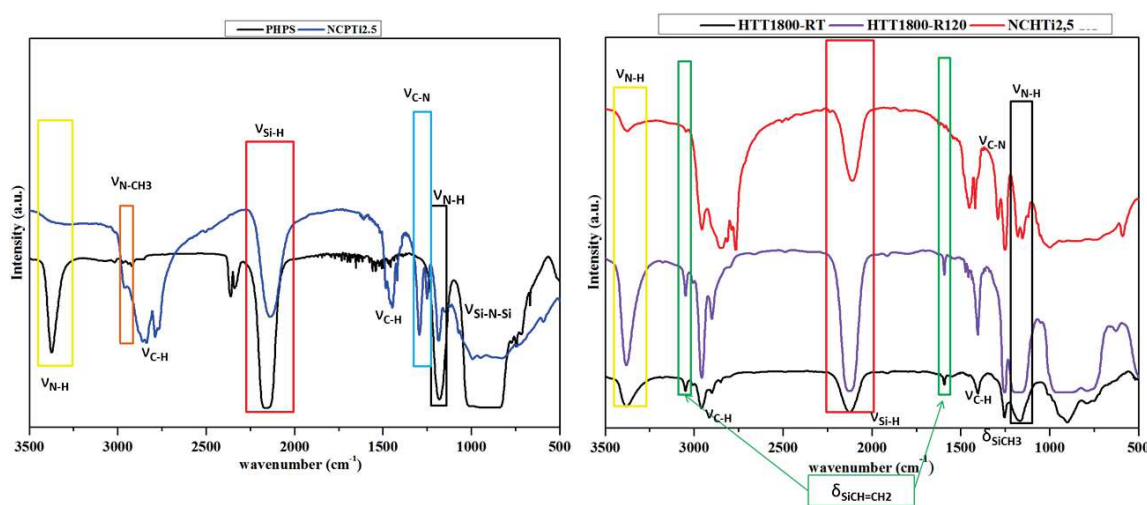
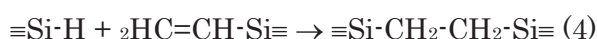
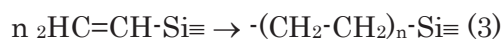


Figure 4.13 FTIR spectra of **NCPTi2.5** and **NCHTi2.5** compared with PHPS, HTT1800 and HTT1800-R120

At higher wavenumbers of around $3400\text{--}3300\text{ cm}^{-1}$ we observe the disappearance of the N-H stretching band after reaction between PHPS and TDMAT. The N-H vibration band at 1180 cm^{-1} , marked by the black box, decreases in intensity in both systems. This confirms that NH groups participate to the building of the polytitanosilazane network as proposed in Eq. (1). The highly intense Si-H peak decreases in intensity after reaction of PHPS with TDMAT suggesting the occurrence of the reaction depicted through Eq. (2). In the **NCPTi2.5** sample, there is appearance of a set of broad bands in the range of $2800\text{--}3000\text{ cm}^{-1}$. This is attributed to the vibration of C-H bonds from the dimethyl group present in TDMAT. Another set of bands that can be attributed to deformation of C-H bands appears at around 1360 and 1450 cm^{-1} . The band at 1280 cm^{-1} can be assigned to the N-C bonds in $\text{N}(\text{CH}_3)$ groups. In the **NCHTi2.5** sample, the bands attributed to the vinyl groups at 1620 cm^{-1} present in HTT1800 disappeared. Interesting, they are still present in the HTT1800-R120 sample. This could

demonstrate that TDMAT reacts with the vinyl groups of HTT1800 but such a reaction cannot occur. We rather propose that TDMAT acts as a catalyst for the polymerization of the vinyl groups (Eq. (3)) and/or hydrosilylation reactions (Eq. (4)).



In order to obtain a complete view of the polytitanosilazane structure, we investigated solid-state NMR spectroscopy to probe the local carbon, nitrogen and silicon environments of the samples. The CP technique has been used to obtain spectra with a reasonable signal-to-noise (S/N) ratio. Solid-state ^{13}C CP MAS NMR spectra of the **NCPTi2.5** and **NCHTi2.5** samples (Figure 4.14a) exhibit signals which can be simulated into two and four signals, respectively. The spectrum of the **NCHTi2.5** sample (Figure 4.14a) is similar to the spectrum of polytitanosilazanes prepared from PMSZ⁸. The signal emerging at 6 ppm is very broad with a shoulder emerging at 0 ppm. ^{13}C NMR signals at around 0 ppm are generally assigned to carbon atoms of aliphatic groups bonded to a silicon atom, *i.e.* in this case SiCH_3 units as identified in HTT1800. In **NCPTi2.5**, such units are logically absent (Figure 4.15b). Therefore, the resonances at 39 and 45 ppm, present in both systems, have been assigned to TiNCH_3 groups. In particular, the peak at 45 ppm can tentatively be attributed to NCH_3 groups linked to titanium, *i.e.*, $\text{Si}_2\text{N-Ti}[\text{NCH}_3]_2$ units, resulting from reaction between NH units and $\text{N}(\text{CH}_3)_2$ groups with dimethylamine elimination (Eq. (1)). Indeed, its position is similar to the position of the signal of TDMAT being thermolyzed at toluene reflux for 3 days identified in the liquid-state ^{13}C NMR spectrum (Figure 4.15).

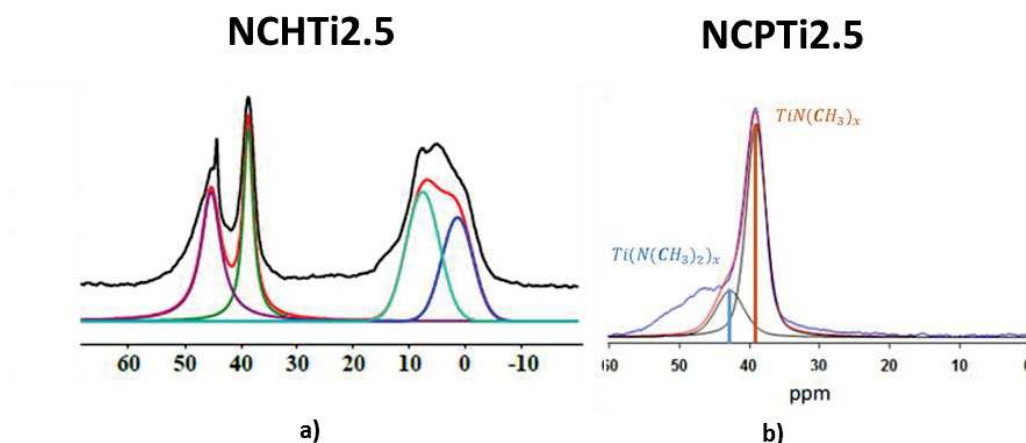


Figure 4.14 Solid-state ^{13}C CP MAS NMR spectra of the **NCPTi2.5** and **NCHTi2.5** samples

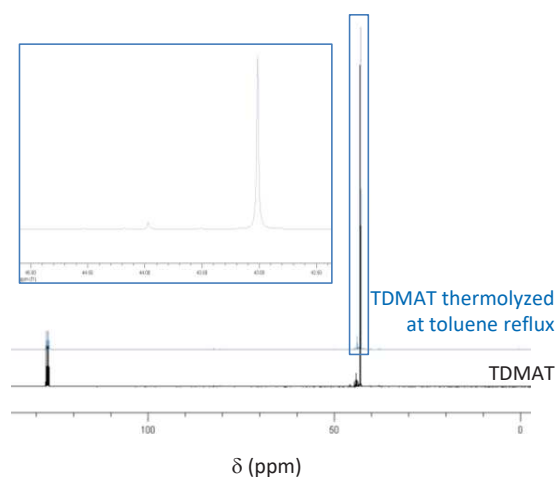


Figure 4.15 Liquid ^{13}C NMR for TDMAT thermolysed at toluene reflux for 3 days

The signal at 39 ppm has been therefore assigned to $\text{N}_2\text{Si}(\text{CH}_3)\text{-N}(\text{CH}_3)\text{-TiN}_3$ units resulting from the reaction between SiH units and $\text{N}(\text{CH}_3)_2$ groups with methane elimination (Eq. (2)).

Regarding the signal around 0 ppm deconvoluted into two components centered at 0 and 6, it is possibly due to CH_3 groups linked to SiN_2H (Eq. (1)) and SiN_3 (Eq. (2)) environments.

The solid-state ^{15}N CP MAS NMR spectra (Figure 4.16) of the **NCPTi2.5** and **NCHTi2.5** samples display two broad signals centered at -350 and -370 ppm. The signal at -350 ppm corresponds to HNSi_2 environments whereas the additional signal centered around -370 ppm is assigned to NCH_3 environment based on our data collected for polytitanosilazanes prepared from PMSZ⁸.

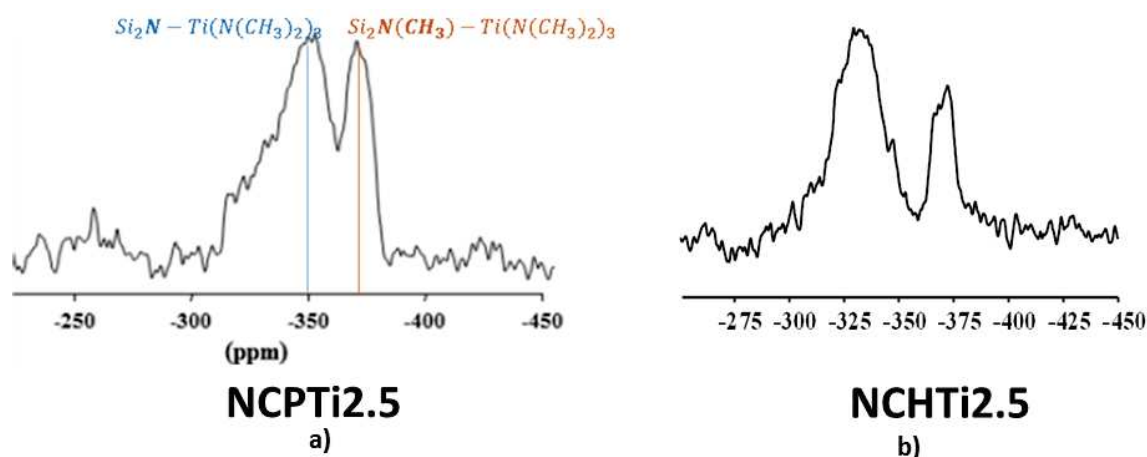


Figure 4.16 Solid-state ^{15}N CP MAS NMR spectra of the **NCPTi2.5** and **NCHTi2.5** samples

^{29}Si CP MAS NMR spectra are shown in Figure 4.17. The ^{29}Si MAS NMR spectrum of the **NCPTi2.5** sample (Figure 4.17a) exhibits a broad line with a maximum around -36 ppm assigned to both N_2SiH_2 and N_3SiH environments⁹. Their presence highlights reactions between Si-H units and $\text{N}(\text{CH}_3)_2$ groups. The **NCHTi2.5** sample (Figure 4.17b) exhibits a main broad resonance centered around -24 ppm that can be simulated with two components at -21 and -29 ppm similarly to polytitanosilazanes prepared from PMSZ⁸. The signal at -21 ppm is related to $\text{CH}_3\text{-Si}(\text{H})\text{N}_2$. This ^{29}Si chemical shift value is consistent with those published previously for a boron-modified polyhydridovinylsilazane which exhibited broad signals at -13 ppm, attributed to silicon atoms in a $\text{SiHC}(\text{sp}^3)\text{N}_2$ environment¹⁰. The other signal at -29 ppm could correspond to a SiN_3C group and more precisely to $\text{CH}_3\text{-Si}(\text{NCH}_3)\text{N}_2$ resulting from the reaction between SiH units and NCH_3 groups present in $\text{Ti}[\text{N}(\text{CH}_3)_2]_4$ (Eq. (2)). It definitely approves the occurrence of this reaction. Finally, the signal at -7 ppm can be attributed to SiC_2N_2 environments. Indeed, the ^{29}Si chemical shift depends on the conformation of the silazane¹³. For example, a ^{29}Si chemical shift value of -5 ppm is expected for SiC_2N_2 units within six-membered cyclosilazanes¹⁴ while those of SiC_2N_2 groups in four- or eight-membered rings would appear at 3.3 ppm or -8.7 ppm, respectively¹⁴. In conclusion, the **NCHTi2.5** sample is preferentially composed of six- and eight-membered Si-N rings as well as Si-N chains.

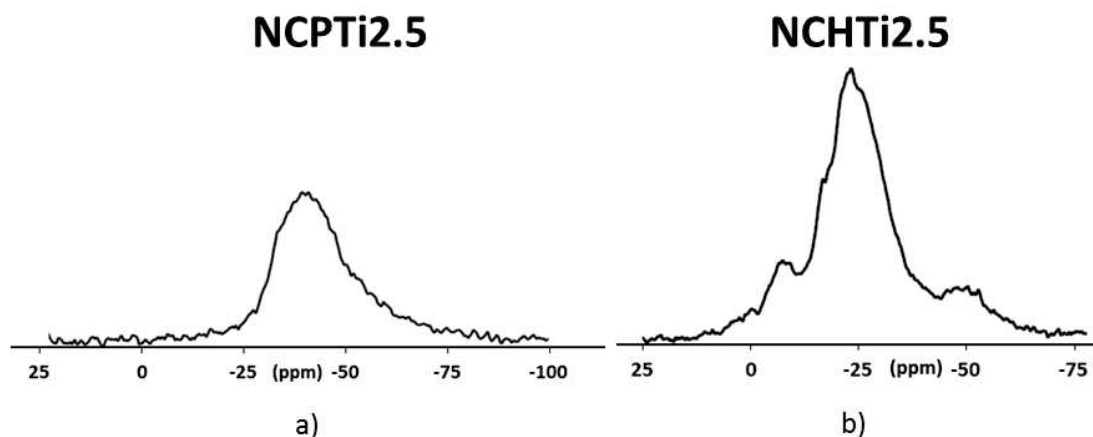


Figure 4.17 ^{29}Si CP MAS NMR spectra of a) **NCPTi2.5**, b) **NCHTi2.5** samples

As suggested by FTIR and solid-state NMR spectra, the synthesis of polytitanosilazanes gives rise to a large variety of structural components which are formed by the mechanism described in Eq. (1)→(4). Even though highly suitable for probing the local chemical environment of NMR-active nuclei, NMR spectroscopy does not give information on the chemical composition of the polymers. Such data are, however, strictly required for having a complete view of the polymer synthesis.

Polytitanosilazanes synthesized from PMSZ displayed a chemical composition of $\text{Si}_{1.0}\text{Ti}_{0.37}\text{C}_{2.0}\text{N}_{0.7}\text{H}_{7.1}$ (20.3 wt% of Ti for a Si:Ti ratio of 2.5)⁸. In comparison, the presence of two SiH groups (one more in comparison to PMSZ) and one NH group (like PMSZ) in the monomeric unit of PHPS did not allow significantly increasing the Ti content in polytitanosilazanes prepared from PHPS, *i.e.*, **NCPTi2.5** sample. A chemical composition of $\text{Si}_{1.0}\text{Ti}_{0.4}\text{C}_{2.0}\text{N}_{1.0}\text{H}_{5.6}$ has been calculated for **NCPTi2.5**. This corresponds to 20.6 wt% of Ti which has been introduced in PHPS. These results prove that the precursor synthesis occurs in the expected manner since they agree reasonably well with the fixed Si:Ti ratio. HTT1800, in its given structure, contains a lower SiH site content (0.8) than in PMSZ (1) and PHPS (2) while the NH group content is the same. However, the steric hindrance imposed by vinyl groups can reduce the reactivity of this polymer with TDMAT in comparison to PMSZ and PHPS. This is confirmed through the Ti content of the **NCHTi2.5** sample: a chemical composition of $\text{Si}_{1.0}\text{Ti}_{0.3}\text{C}_{3.0}\text{N}_{1.6}\text{H}_{8.5}$ has been calculated corresponding to only 12.9 wt% of Ti which has been introduced in HTT1800 taking into account a Si:Ti ratio of 2.5. This proves that the reactions described in eqs (1) to (4) occur more effectively under PHPS and PMSZ.

This will have clearly an effect on the polymer-to-ceramic conversion as well as on the microstructural evolution and crystallization behavior of the ceramics.

3.2. Polytitanosilazane-to-amorphous ceramic conversion

The thermal conversion of preceramic polymers into ceramics occurs through the evolution of gaseous byproducts involving a weight loss upon the heat treatment. The ceramic yield, which is the share of $(m_{\text{ceramic}}/m_{\text{precursor}}) \times 100\%$ is a subject of major importance as it proves the general applicability of preceramic polymers as ceramic precursors. A common method for monitoring the progress during pyrolysis and for determining ceramic yields is thermogravimetric analysis (TGA). Here, we firstly discuss the polymer-to-ceramic conversion of the **NCPTi2.5** and **NCHTi2.5** samples from room temperature (RT) to 1000 °C in flowing ammonia as followed by TGA (Figure 4.18). Results are compared data recorded from PHPS and HTT1800.

In both cases, the weight loss of the **NCPTi2.5** and **NCHTi2.5** samples are higher than the native polymer, *i.e.*, PHPS and HTT1800, respectively.

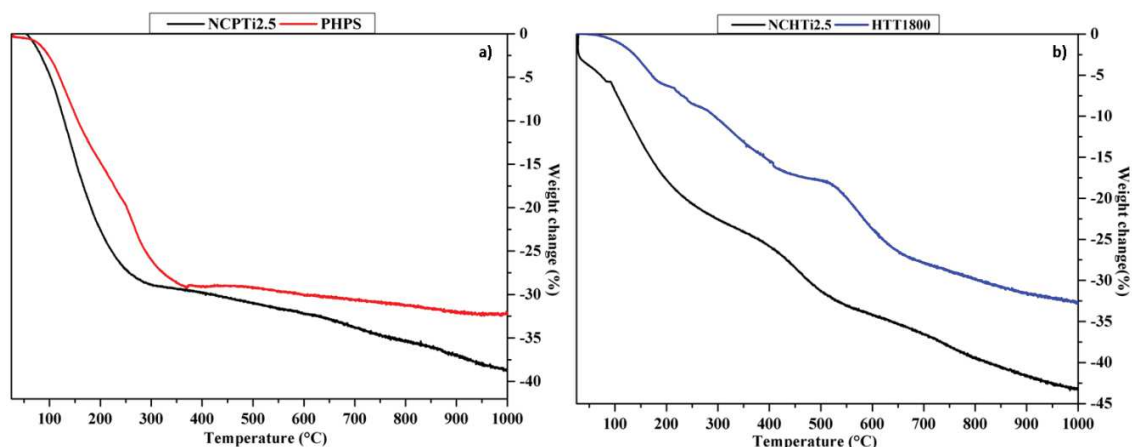
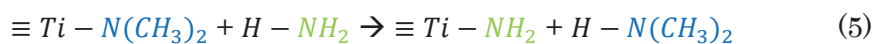
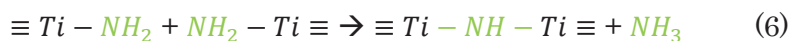


Figure 4.18 TGA of a) **NCPTi2.5** and b) **NCHTi2.5** samples under NH_3

As a first speculation, this is mainly attributed to the presence of dimethylamino groups in the **NCPTi2.5** and **NCHTi2.5** samples that form NH_2 groups by reaction with ammonia (transamination reactions^{15,16}) and release dimethylamine (Eq. (5)). Then, the NH_2 groups immediately condense to form NH groups by releasing ammonia (Eq. (6)).





However, only speculations can be made at this stage on the mechanisms governing the polymer-to-ceramic conversion. Within this context, spectroscopic analyses (FTIR and solid-state NMR) of intermediates isolated during pyrolysis have been carried out to learn more about the chemistry involved in each step of the polymer-to-ceramic conversion and to set up the procedure parameters. This is discussed in details below.

FTIR and solid-state NMR spectroscopies were performed on both **NCPTi2.5** and **NCHTi2.5** samples heat-treated at 200, 450, 700 and 1000 °C in an ammonia atmosphere with a dwelling time of 2 hours at each temperature. Pyrolysis intermediates are labeled **NCPTi2.5-Y/NCHTi2.5-Y** (Y being the temperature at which the sample was exposed: Y = 200 for 200 °C and 1000 for 1000 °C). On the basis of the structural assignment of the spectral features, the pyrolytic decomposition pathways are outlined. Representative FTIR spectra recorded from the two samples are shown in Figure 4.19.

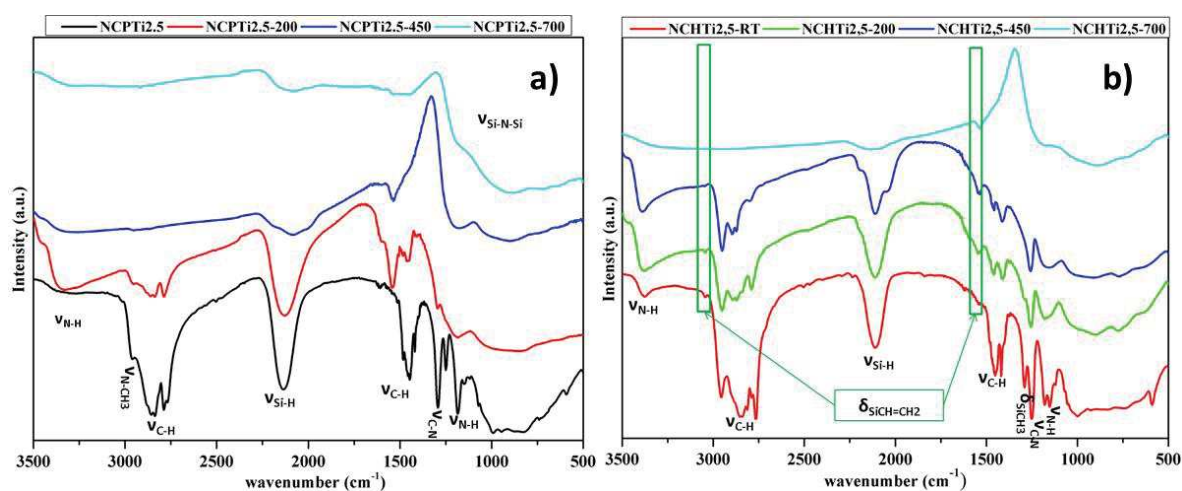


Figure 4.19 FTIR spectra of pyrolysis intermediates derived from **NCPTi2.5** and **NCHTi2.5** under NH_3

Upon pyrolysis under NH_3 up to 200°C (**NCPTi2.5-200/NCHTi2.5-200**), there is a main decrease in intensity of the C-H vibration bands in both systems which tend to confirm the occurrence of transamination reactions (Eq. (5)) during the decomposition of the **NCPTi2.5** and **NCHTi2.5** samples in the low temperature regime of the pyrolysis. There are no major changes between 200 and 450°C as shown on the FTIR spectra. Only the band assigned to the stretching of N-H bonds increases in intensity, in particular in the **NCPTi2.5-450** sample

most probably because of the condensation of as-formed -NH_2 groups forming NH units (Eq. (6)).

From 450°C (**NCPTi2.5-450/NCHTi2.5-450**) to 700°C (**NCPTi2.5-700/NCHTi2.5-700**) the N-H, C-H and Si-H bond stretching bands disappear which indicates that the conversion of the polymer into ceramic is almost achieved. At 1000°C , we finally have an amorphous Si-N-Si network with N-Ti-N bridges.

FTIR spectroscopy gives a good overview of the evolution of chemical structure of preceramic polymers during their pyrolytic conversion but is not sufficient to fully understand the reactions taking place. Multinuclear solid-state NMR spectroscopy is another extremely helpful tool to investigate the structural rearrangements of the pyrolysis intermediates at the atomic scale during the polymer-to-ceramic transformation, by probing the local environment of the various NMR-active nuclei. Here, we give a detailed picture of the structural changes of both **NCPTi2.5** and **NCHTi2.5** samples during their ceramic conversion up to 1000°C under ammonia, based on ^{29}Si , ^{14}N and ^{13}C solid-state NMR spectroscopies. The samples pyrolyzed at 450°C (**NCPTi2.5-450** and **NCHTi2.5-450**) and 1000°C (**NCPTi2.5-1000** and **NCHTi2.5-1000**) have been investigated.

^{29}Si MAS spectra of **NCPTi2.5-450** and **NCHTi2.5-450** samples (Figure 4.20) result in a small shift of the main signal. For the **NCPTi2.5-450** sample, this suggests a predominantly covalent material in which silicon is mainly present in SiN_4 environments. For the **NCHTi2.5-450** sample, the main signal shifts toward the resonance at -28 ppm (SiN_3C) suggesting that the chemical environment of the silicon atoms is not strongly affected by the pyrolysis under ammonia. Whereas the silicon environment is similar for the **NCPTi2.5-10** sample, more changes occur in the **NCHTi2.5-10** sample. Obviously, nucleophilic substitutions and rearrangements occur in the temperature range $450\text{-}1000^\circ\text{C}$ that cause a modification of the chemical environment of the silicon atoms: The signal corresponding to SiCHN_2 environments almost disappears while a broad signal centered at -48 ppm appears. It suggests a predominantly covalent material in which silicon is mainly present in SiN_4 environments like in the **NCPTi2.5-10** sample. As a consequence, the ^{29}Si MAS NMR signals confirm the formation of silicon nitride.

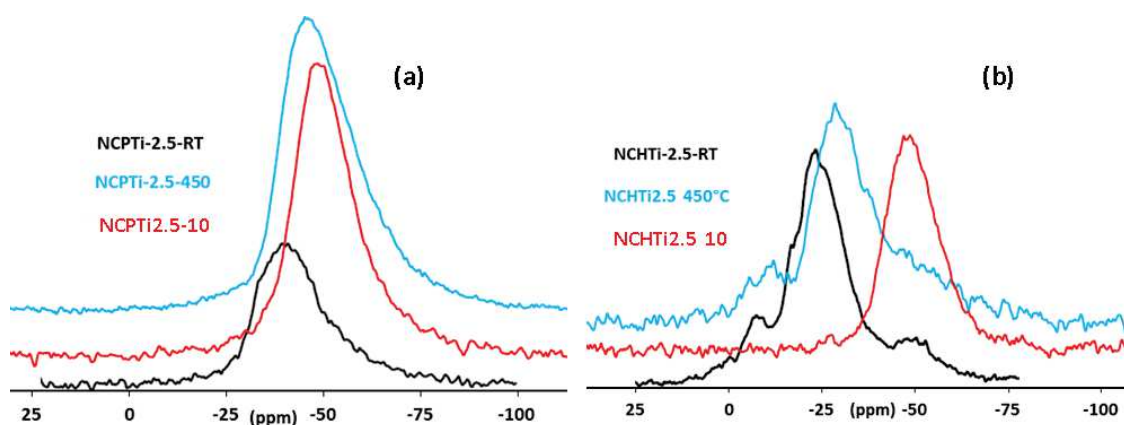


Figure 4.20 ^{29}Si MAS NMR spectra of pyrolysis intermediates derived from **NCPTi2.5** and **NCHTi2.5** under NH_3

The experimental ^{13}C CP MAS NMR spectra of **NCPTi2.5-450/NCHTi2.5-450** samples are reported in Figure 4.21. The experimental ^{13}C CP MAS NMR spectra of **NCPTi2.5-10/NCHTi2.5-10** samples could not be recorded with CP due to the low amount of remaining protons). The signals at 39 and 45 ppm which have been attributed to TiNCH_3 units in different environment almost disappear. This points to the fact that such units react during the first step of the pyrolysis under ammonia. The spectra of **NCPTi2.5-450/NCHTi2.5-450** samples show one main signal in the aliphatic region that can be assigned to $\text{CH}_x\text{Si}_{4-x}$ units (with $x = 0, 1, 2, 3$) in the **NCHTi2.5-450** sample.

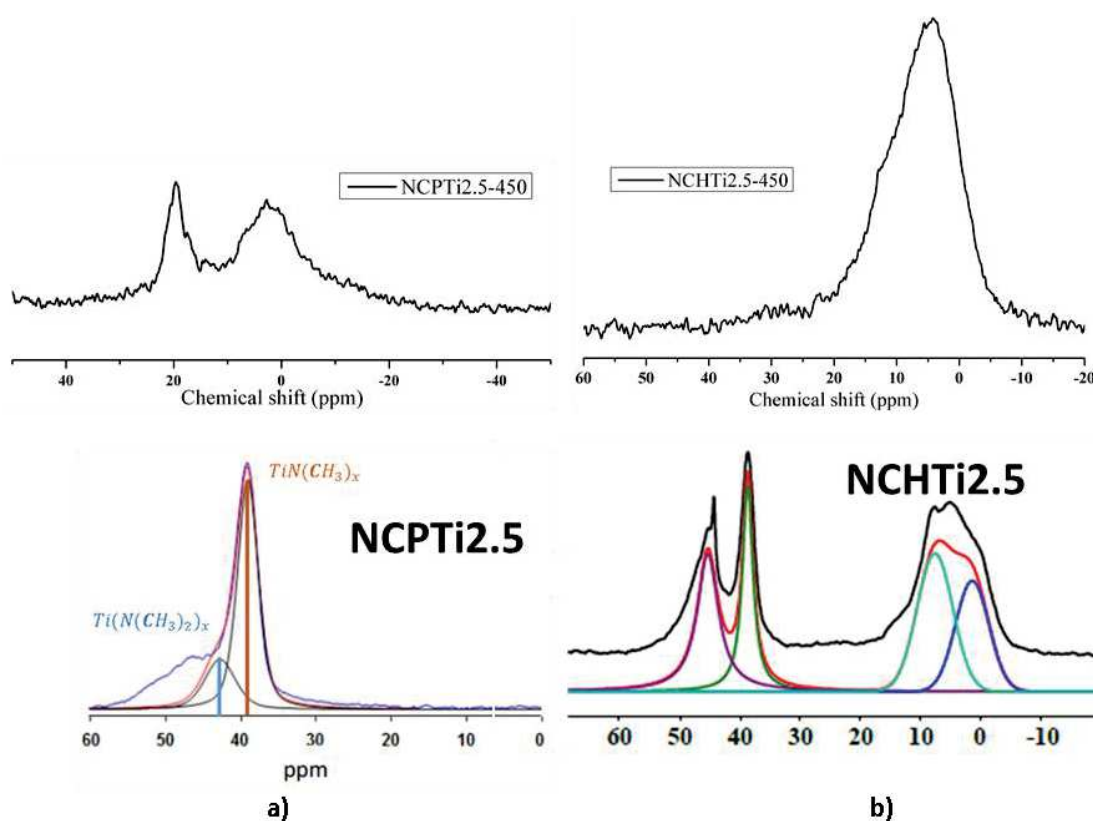


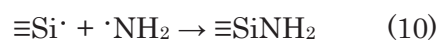
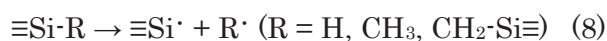
Figure 4.21 ^{13}C CP MAS NMR spectra of a) NCPTi2.5 and NCPTi2.5-450 and b) NCHTi2.5 and NCHTi2.5-450

FTIR and solid state NMR spectroscopies allow us to understand the pyrolysis behavior of polytitanosilazanes prepared from PHPS and HTT1800.

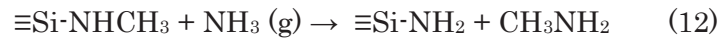
Mutin *et al*⁷ showed that Si-H and Si-CH₃ as well as Si-CH₂-Si units in polycarbosilane are easily modified by ammonia according to Eq. (7). This mechanism is quite favored with polymers containing Si-H units which are sensitive to nucleophilic substitution.



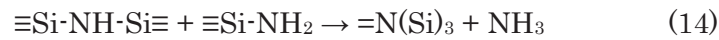
Homolytic cleavages probably occur in a parallel way according to Eqs (8)-(10).



Such mechanisms have also been proposed by Interrante *et al.* for vinyl-substituted polysilanes¹⁸, and by Mutin *et al.* for polysilazanes¹⁷. They probably occur below 500 °C. In the presence of N-CH₃ groups in the preceramic network, *e.g.* in N-CH₃ polysilazanes¹⁷, release of methylamine is detected around 450 °C. It arises from the substitution of N-CH₃ groups by ammonia, *i.e.*, a *trans*-amination according to Eqs (11)-(12).



Si-NMe-Si units are thus cleaved by formation of Si-NH₂ and Si-N-CH₃H entities. The latter are subsequently transformed into SiNH₂ and CH₃NH₂ which is released. Si-NH₂ groups condense with formation of Si-NH-Si and N(Si)₃ units by release of ammonia according to Eqs (13) and (14).



We suggest that *trans*-amination reactions of internal Si-NCH₃-Si units as depicted in Eqs (11) and (12) forming Si-NH₂ groups (Eq (7)) occur during the pyrolysis under ammonia up to 450 °C. Besides, we cannot exclude the possibility of an ammonolysis of SiCH₃ groups according to Eqs (7) to (10) resulting in the elimination of methane and the formation of Si-NH₂ units. As-formed Si-NH₂ units self-condense during further heat treatment to release ammonia according to Eqs (13) and (14) forming the ceramic network at 1000 °C

3.3. Crystallization behavior:

Si-Ti-N materials prepared from NCPTi2.5/NCHTi2.5 samples after pyrolysis at 1000°C under ammonia (NCPTi2.5-10/NCHTi2.5-10) are predominantly amorphous according to the extremely diffuse peaks in the corresponding XRD pattern (Figure 4.22). Through annealing at higher temperatures, crystallization occurred in both systems. The X-ray diffraction patterns of the samples annealed between 1200 and 1600 °C, *i.e.*, NCPTi2.5-12/NCHTi2.5-12, NCPTi2.5-14/NCHTi2.5-14, NCPTi2.5-15/NCHTi2.5-15 and NCPTi2.5-16/NCHTi2.5-16 samples, are given in Figure 4.24. Phase identification is achieved by locating the characteristic diffraction peaks of the respective phases in the XRD spectra.

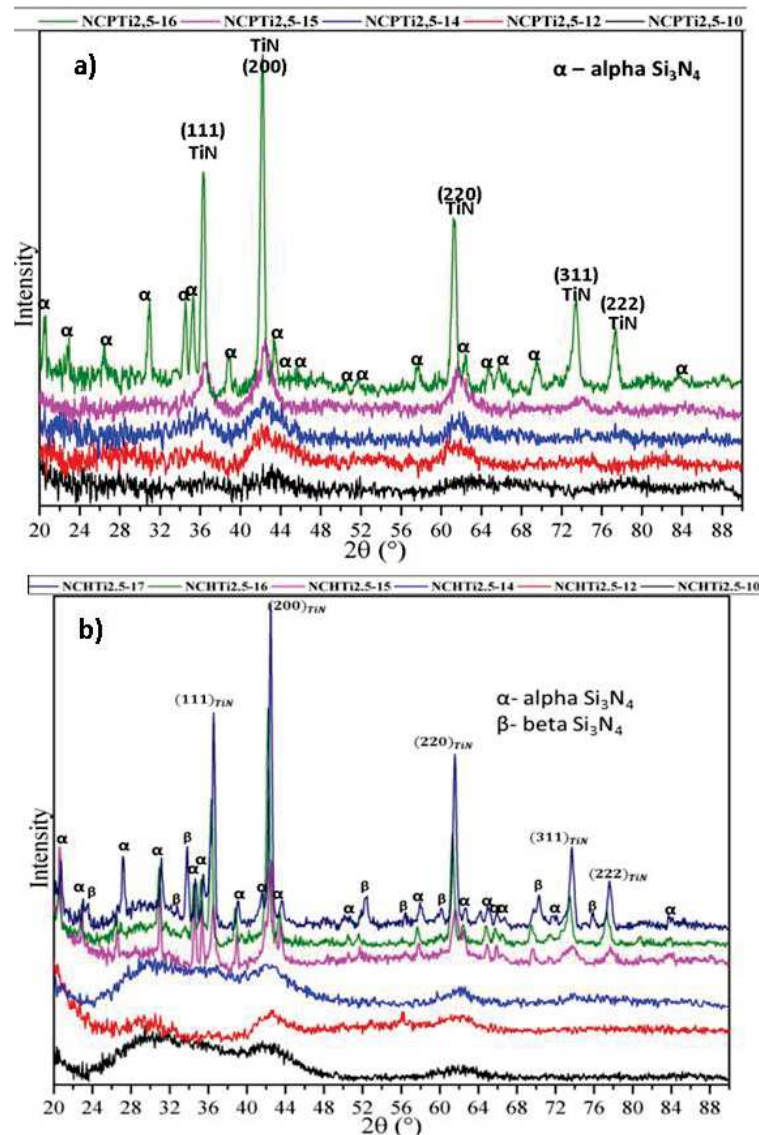


Figure 4.22 XRD patterns of a) NCPTi2.5-10 \rightarrow NCPTi2.5-16 and b) NCHTi2.5-10 \rightarrow NCHTi2.5-17

The XRD pattern of the NCPTi2.5-12/NCHTi2.5-12 and NCPTi2.5-14/NCHTi2.5-14 samples show broad peaks corresponding to the nucleation of the face-centered cubic (fcc) TiN phase (The peaks match with the JCPDS: 00-038-1420, corresponding to cubic structure of TiN.). TiN is identified by the presence of peaks at $2\theta = 36.5^\circ$, 42.63° and 62.11° which are attributed to the (111), (200) and (220) reflections. The 2θ values indicated above are based on the $\text{CuK}\alpha$ radiation. The XRD patterns of the NCPTi2.5-15/NCHTi2.5-15 samples are different. The XRD pattern of the NCPTi2.5-15 sample show sharper and more intense TiN peaks with two

additional broad peaks attributed to TiN at and 74.00° and 78.30° corresponding to the (311) (222) reflections, respectively. As we move up to 1500°C with the **NCPTi2.5-15** sample, sharper TiN XRD peaks appear at 36.5° , 42.4° , 61.3° , 73.4° and 77.2°C . In addition, the matrix starts crystallizing as peaks corresponding to $\alpha\text{-Si}_3\text{N}_4$ appear at 21.5° , 23.5° , 26.5° , 31° , 34.5° , 35.5° , 38.9° , 43.48° , 44.62° , 50.51° , 51.72° , 57.82° , 62.44° , 64.92° , 65.86° , 69.68° and 84.2° . As the annealing temperature was increased to 1600°C , *i.e.*, the **NCPTi2.5-16/NCPTi2.5-16** samples, crystallization of $\alpha\text{-Si}_3\text{N}_4$ proceeded together with an increased extent of the crystallization of the TiN phase. The β phase is difficult to identify in those samples. Only by increasing the temperature to 1700°C with the **NCPTi2.5-17** sample, we could identify the $\beta\text{-Si}_3\text{N}_4$ phase appearing at 23.6° , 32.8° , 33.8° , 52.5° , 56.5° , 60.2° , 70.3° and 75.9° along with the previous peaks of $\alpha\text{-Si}_3\text{N}_4$. As a confirmation of the marked improvement of the extent of crystallization and TiN crystallite growth from 1500 to 1600°C , the average TiN nanocrystal size has been calculated by applying the Scherrer formula to measure the FWHM of the dominant TiN peak (111) in the XRD patterns. It increases from $2.6/1.9$ nm (**NCPTi2.5-14/NCPTi2.5-14**) to $27.6/22.4$ nm (**NCPTi2.5-16/NCPTi2.5-16**). Hence, we have shown that the amorphous matrix in TiN/Si₃N₄ nanocomposites is more stable using PHPS than HTT1800 as matrix precursors. The crystallization behavior of materials prepared from PHPS is similar to those prepared from PMSZ. This clearly shows that the chemistry of the polyorganosilazane plays a key role in the crystallization behavior at high temperature. Let's discuss on the reactivity of these polyorganosilazanes

As a consequence, and in contrast to other systems, Si₃N₄ nucleation already occurred at 1500°C in the HTT1800-derived **NCPTi2.5-15** sample because of the lowest reactivity of HTT1800 with TDMAT in comparison to PMSZ and PHPS. As a consequence, the TiN volume fraction increases from HTT1800-derived Si-Ti-N ceramics to PMSZ and PHPS-derived Si-Ti-N ceramics. We observed that this shifts the onset of the crystallization of the Si₃N₄ phase to higher temperatures from HTT1800-derived Si-Ti-N ceramics to PMSZ and PHPS-derived Si-Ti-N ceramics. The XRD results allowed us to demonstrate that PHPS offers more latitude in the control of the crystallization of the Si₃N₄ matrix in Si-Ti-N ceramics. After pyrolysis up to 1600°C and 1700°C , we confirm the formation of nanocomposites with three crystallized phases: the fcc TiN and the α -/ β -Si₃N₄ in the three systems.

To highlight the interest of PHPS to limit or even suppress the crystallization of Si_3N_4 , the effect of the Si:Ti ratio on the high temperature structural evolution of PHPS-derived nanocomposites has been studied.

The X-ray diffraction patterns of the samples with Si:Ti ratios of 5 (**NCPTi5-14** → **NCPTi5-17**) and 1 (**NCPTi1-12** → **NCPTi1-18**) have been investigated in the temperature range 1400-1700°C (Figure 4.23) and 1200-1800°C (Figure 4.24), respectively. We performed XRD of the **NCPTi1-12** sample because it can be already considered as a $nc\text{-TiN}/a\text{-Si}_3\text{N}_4$ nanocomposite (Figure 4.24). After a pyrolysis at 1400°C, all samples are nanocomposites made of a TiN nanophase and an amorphous Si_3N_4 matrix. At a pyrolysis temperature > 1400°C, the crystallization behavior changed: the XRD peaks attributed to Si_3N_4 showed a progressive decrease in intensity as the Si:Ti ratio of the sample decreased. Indeed, Si_3N_4 nucleation already occurred at 1500°C in the **NCPTi5-15** samples (Figure 4.23). This confirms the strong influence of the Ti content in SiTiN ceramics on the onset of the crystallization of Si_3N_4 . Interestingly, a mixture of α - and β -phases is identified in the **NCPTi5-17** sample while only the α -phase is identified in the **NCPTi5-16** sample (Figure 4.23).

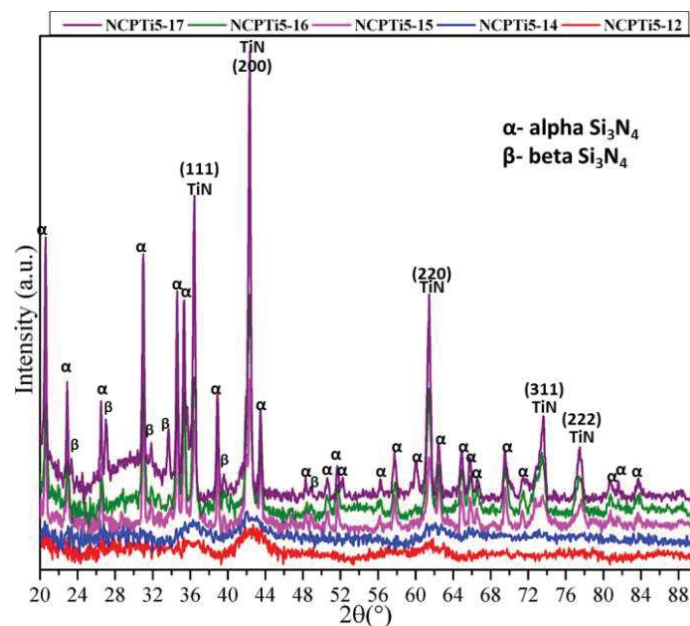


Figure 4.23 XRD patterns depicting evolution of phases for the **NCPTi5** sample with temperature

In comparison, a β - Si_3N_4 phase is obtained in the the **NCPTi1-16** sample (Figure 4.24). This showed that the Si:Ti ratio has also a strong effect on the nature of the Si_3N_4 phases even by using a same polyorganosilazane, *i.e.*, PHPS.

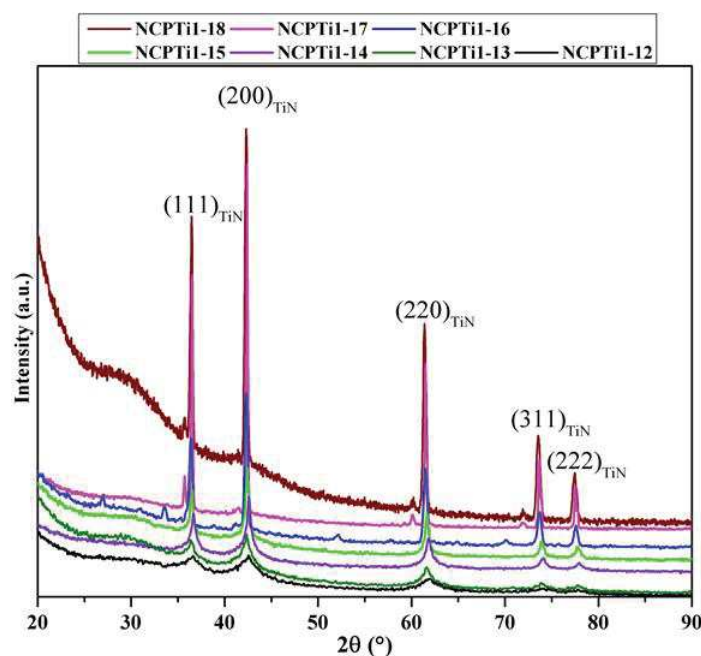


Figure 4.24 XRD depicting evolution of phases for **NCPTi1** sample with temperature

However, the crystallization of the Si_3N_4 phase is significantly reduced in the **NCPTi1-17** and **NCPTi1-18** samples. Indeed, it is remarkable to observe that the crystallization of Si_3N_4 is extremely limited even after a pyrolysis at 1800 °C for a Si:Ti ratio of 1, *i.e.*, the **NCPTi1-18** sample (Figure 4.24). A semi-quantitative estimation of the extent of crystallization has been done by calculating the integrated intensity of the selected diffraction $(111)_{\text{TiN}}$ line. The crystallite size of TiN increased from (a) **NCPTi1-12** (6.2 nm) to **NCPTi1-18** (60 nm) samples.

Based on this detailed XRD study on Si-Ti-N ceramics, we demonstrated that *nc*-TiN/*a*- Si_3N_4 nanocomposites prepared from a series of polyorganosilazanes can be prepared after a pyrolysis performed under ammonia at 1000 °C then under nitrogen at 1400 °C. By increasing the temperature of pyrolysis to 1500 °C, a strong effect of both the polysilazane chemistry and the Si:Ti ratios is identified. PHPS offers more latitude in the control of the crystallization of the Si_3N_4 matrix in Si-Ti-N ceramics and could produce nanocomposites with a limited crystallization of the Si_3N_4 phase at 1800 °C with a Si:Ti ratio of 1.

We confirmed the growth of the TiN nanophase by Raman spectroscopy. The Raman spectra from the **NCPTi2.5-10** to **NCPTi2.5-16** samples are presented in Figure 4.25. We can really identify the TiN phase in the **NCPTi2.5-14**, **NCPTi2.5-15** and **NCPTi2.5-16** samples.

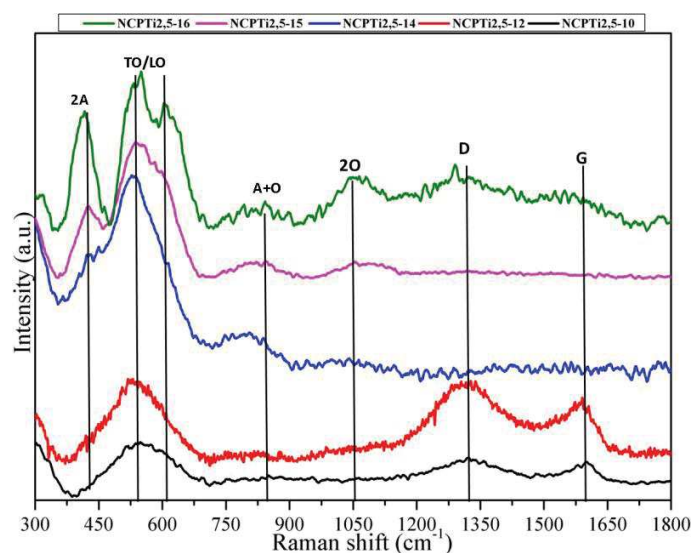


Figure 4.25 Raman spectra from the **NCPTi2.5-10** to **NCPTi2.5-16**

The peaks below 400 cm^{-1} can be attributed to acoustical phonons whereas those in the high frequency mode, above 500 cm^{-1} , can be attributed to optical phonons. The peaks corresponding to 296.6 cm^{-1} belong to longitudinal acoustic (LA) node. This node is generally accompanied by transverse acoustic (TA) node at around 210 cm^{-1} but due to poor signal strength the node seems to be absent. The 2A mode of vibration which is centered around 410 cm^{-1} becomes visible only at 1500°C . For temperatures below 1500°C the peak is not visible although its contribution to the adjacent broad peak can be seen upon deconvolution of the broad peak. The peak at 540 cm^{-1} along with a very slight shoulder at 600 cm^{-1} (visible only at 1600°C) corresponds to the transverse optic/longitudinal optic (TO/LO) mode. The phonon bands in the lower acoustic range correspond to the heavier Ti^{4+} ions while in the higher optical range they correspond to the lighter N^{3-} ions. The two broad peaks in the $817\text{-}1075\text{ cm}^{-1}$ wavenumber range can be assigned to the A+O and 2O modes.

No contribution from Si_3N_4 is visible for this system. $\alpha\text{-Si}_3\text{N}_4$ has close to 20 peaks in the wavenumber range of $400\text{ to }1000\text{ cm}^{-1}$. The absence of these peaks can be attributed to the fact that they may be covered by TiN peaks.

Interestingly, D and G peaks corresponding to free carbon emerge in the **NCPTi2.5-10** and **NCPTi2.5-12** samples. The peaks disappear in the **NCPTi2.5-14** and **NCPTi2.5-15** samples then tend to re-appear in in the **NCPTi2.5-16** sample. The presence of free carbon at 1000°C goes contrary to the observations of elemental analysis at the same temperature. The chemical composition of the **NCPTi2.5-10** sample as calculated by elemental analysis is $\text{Si}_{1.9}\text{N}_{3.8}\text{Ti}_{1.0}\text{C}_{0.01}\text{O}_{0.03}$. This shows that only a very negligible amount of carbon is present in the system. The Raman bands attributed to free carbon then can be attributed to carbon impurity arising from the graphite furnace used for high temperature (>1000°C) treatment of the samples.

As we move to the lowest Si:Ti ratio of 1 (Figure 4.26), we see a stark difference between the Raman spectra for this system and the previous systems at 1600°C. The modes corresponding to both transverse acoustic/ longitudinal acoustic and transverse optical/ longitudinal optical phonons are shifted by nearly 75 cm^{-1} . While the A+O and 2O bands are completely missing at 1600°C. 2A band centered around 410 cm^{-1} is very sharp at 1600°C while it is just visible as a shoulder at lower temperatures.

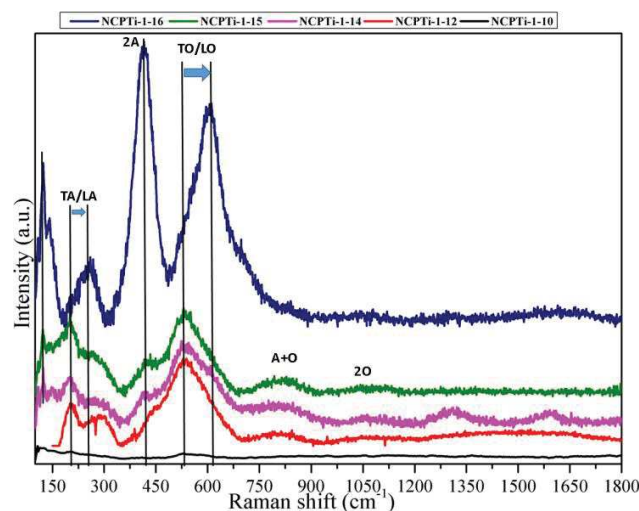


Figure 4.26 Raman spectra from the **NCPTi1-10** to **NCPTi1-16**

3.4 Microstructural characterization using Transmission Electron Microscopy

The microstructure of the **NCPTi2.5** derived ceramics was observed by a HRTEM for samples crystallized at 1400°C (**NCPTi2.5-14**) and 1500°C (**NCPTi2.5-15**). From XRD, it was observed

that the matrix (Si_3N_4) is amorphous and the TiN nanocrystals were crystallized out from the amorphous system. The TEM images confirm this observation. The HRTEM image showed that the **NCPTi2.5-14** sample (Figure 4.27) consists of nanocrystals with sizes ranging from 2 to 5 nm embedded in a bright-appearing network which revealed the typical phase contrast of amorphous materials. The low magnification TEM image (inset) demonstrated the homogeneous distribution of nanocrystals in the matrix. Based on the selected area electron diffraction (SAED) pattern, the indexation of *fcc* TiN is confirmed but the continuous rings demonstrated the relatively low degree of crystallinity of TiN nanocrystals as shown by X-ray diffraction.

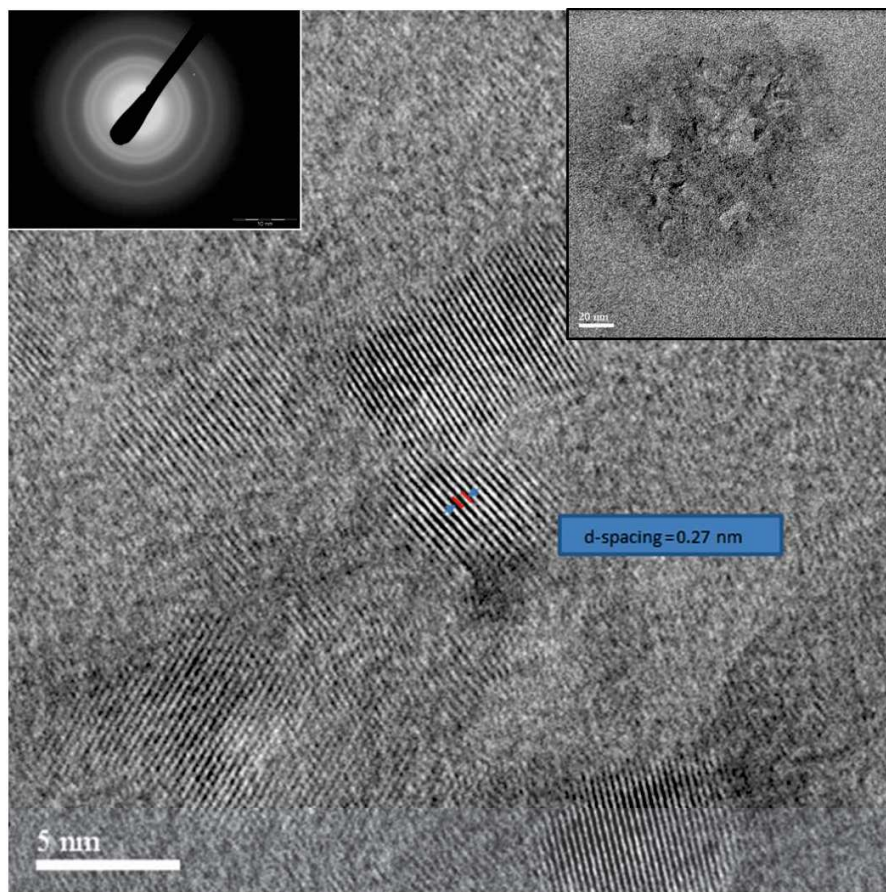


Figure 4.27 HR-TEM image for **NCPTi2.5-14** with SAED pattern inset

The TEM observation results of the **NCPTi2.5-15** sample (Figure 4.28) also shows small nuclei (around 8 nm); again embedded in a bright-appearing network which reveals the typical phase contrast of amorphous materials (inset). We can clearly distinguish the *fcc* structure of TiN nanocrystals with a fringe spacing of 0.225 nm, corresponding to the *d*

spacing of the lattice plane of the TiN structure *i.e.* the [111] direction of the *fcc* cubic rocksalt TiN structure. As in Fig, the low magnification TEM image (inset) demonstrated the homogeneous distribution of nanocrystals in the matrix. The SAED pattern (inset) is in general composed of continuous rings (but spots can be identified) demonstrating an extent of the TiN crystallization similar to the sample prepared at 1400°C as shown by X-ray diffraction.

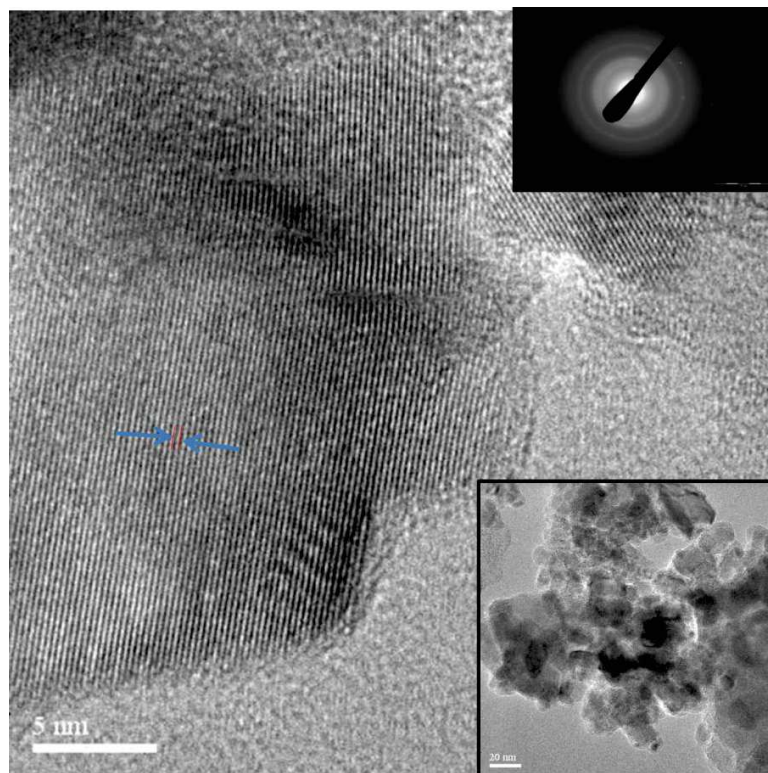


Figure 4.28 HR-TEM image for NCPTi2.5-15 with SAED pattern inset

The macro/microstructure was observed by a HRTEM for samples crystallized at 1400°C (NCHTi2.5-14) and 1500°C (NCHTi2.5-15). From XRD it was already known that at 1400°C the matrix of Si₃N₄ was still amorphous and the TiN nanocrystals were crystallizing out from the amorphous system while at 1500°C the matrix was also crystallizing as α-Si₃N₄ and TiN crystals have crystallized sufficiently and are growing in size. The TEM images confirm this observation. The HRTEM image showed that the NCHTi2.5-14 sample (Figure 4.29) consists of nanocrystals with sizes ranging from 1.5 to 4 nm embedded in a bright-appearing network which revealed the typical phase contrast of amorphous materials. The low magnification TEM image (inset) demonstrated the homogeneous distribution of nanocrystals in the matrix.

Based on the selected area electron diffraction (SAED) pattern (inset in Figure 4.29), the indexation of *fcc* TiN is confirmed but the continuous rings demonstrated the relatively low degree of crystallinity of TiN nanocrystals as shown by X-ray diffraction. The average $d_{(200)}$ for TiN nanocrystal was found to be 0.26 nm

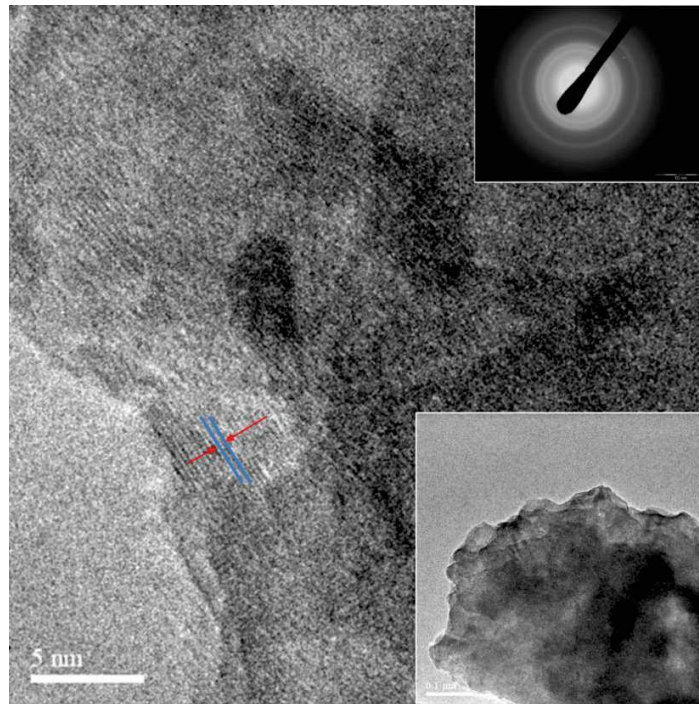


Figure 4.29 HR-TEM image for NCHTi2.5-14 with SAED pattern inset

In the NCHTi2.5-15 sample we can see crystallization of alpha phase of Si_3N_4 along with TiN nanocrystals (Figure 4.30). The $d_{(100)}$ for Si_3N_4 (green arrows) was matched with literature and found to be 0.66 nm while $d_{(200)}$ (red arrows) for TiN was gain confirmed to be 0.25 nm. The TEM image agrees with the XRD study for the system at 1500°C.

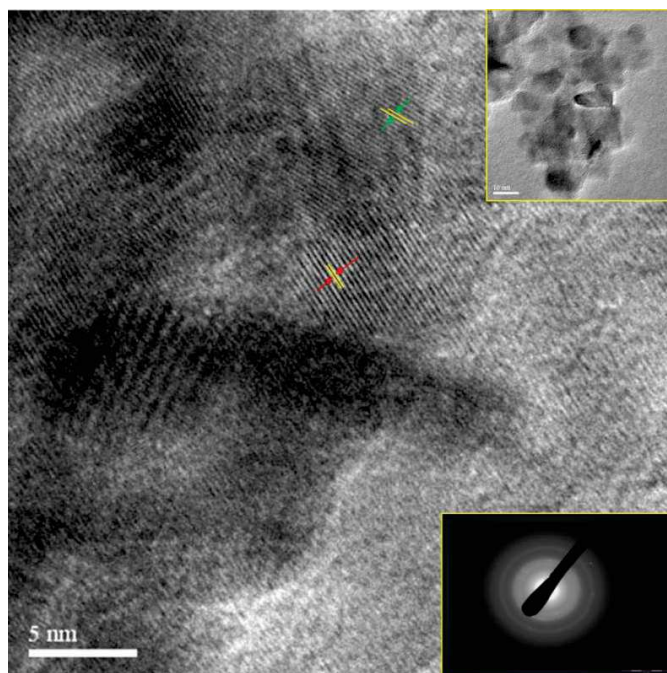


Figure 4.30 HR-TEM image for NCHTi2.5-15 with SAED pattern inset

4 Preparation of Si-Zr-N and Si-Hf-N ceramics

Zirconium ($Z=40$) and Hafnium ($Z=72$) lie below Titanium in the same group IVB. Having similar electronic configuration in the outermost shell, ZrN and HfN are expected to have similar electronic and thermal properties than TiN. The section is divided into two groups, first modification of polysilazanes, PHPS and HTT1800, with tetrakisdiethylamidoZirconium(IV) (TDEAZr) and second modification of the same polysilazanes with tetrakisdimethylamidoHafnium(IV) (TDMAHf).

4.1 Si-Zr-N ceramics

4.1.1 Synthesis and characterization of Zr modified polysilazanes

As discussed in chapter 2, Si-Zr-N are synthesized using tetrakisdiethylamidoZirconium(IV) (TDEAZr). In this case an alkyl amino group with a bigger ethyl group is considered instead of methyl as in TDMAT. TDEAZr is in liquid state thereby facilitating easy handling, although steric hindrance can occur due to larger size of side chain. After the reaction, a yellowish-orange powder is obtained using PHPS and HTT1800 as Si_3N_4 precursors and Si/Zr molar ratio of 2.5.

The polymer systems **NCPZr2.5** (PHPS with TDEAZr) and **NCHZr2.5** (HTT1800 with TDEAZr) have the following elemental composition in wt%.

Table 4.1 Elemental analysis for **NCPZr2.5** and **NCHZr2.5**

	Si	Zr	N	C	O	H	Chemical formula
NCPZr2.5	14.45	24.7	14.35	27.55	13.85	6.5	$Si_{2.69}Zr_{1.0}N_{3.79}C_{8.48}O_{1.5}H_{23.86}$
NCHZr2.5	19.55	19.3	16.25	31.19	6.5	7.2	$Si_{3.26}Zr_{1.0}N_{5.45}C_{12.21}O_{1.91}H_{33.56}$

The compositional analysis brings up some interesting observations. Firstly, the Si:Zr ratio of 2.5 fixed before the reaction is obtained with the **NCPZr2.5** sample. It shows a ratio of 2.69 which is very close to the theoretical value. In contrast, the **NCHZr2.5** sample displays a ratio of 3.26. This implies that the extent of reaction in **NCPZr2.5** sample is higher than in the **NCHZr2.5** sample. This is attributed to the high steric hindrance faced by the vinyl groups in HTT1800 as we demonstrated for the **NCHTi2.5** sample. The presence of small amount of oxygen is due to the highly volatile and sensitive nature of TDEAZr precursor. Figure 4.31 shows FTIR spectra of **NCPZr2.5** and **NCHZr2.5** with comparison to PHPS and HTT1800. For the **NCPZr2.5** sample it can be clearly seen that the reaction has occurred at both N-H (3400 cm^{-1} and 1180 cm^{-1}) and Si-H (2100 cm^{-1}) bonds as the intensity of these bonds decreases. The extent of reaction in **NCHZr2.5** sample is lower as the N-H bonds at 3400 cm^{-1} and 1180 cm^{-1} are still visible in the polymer. Even the intensity of Si-H bonds between the **NCHZr2.5** and HTT1800 does not decrease much.

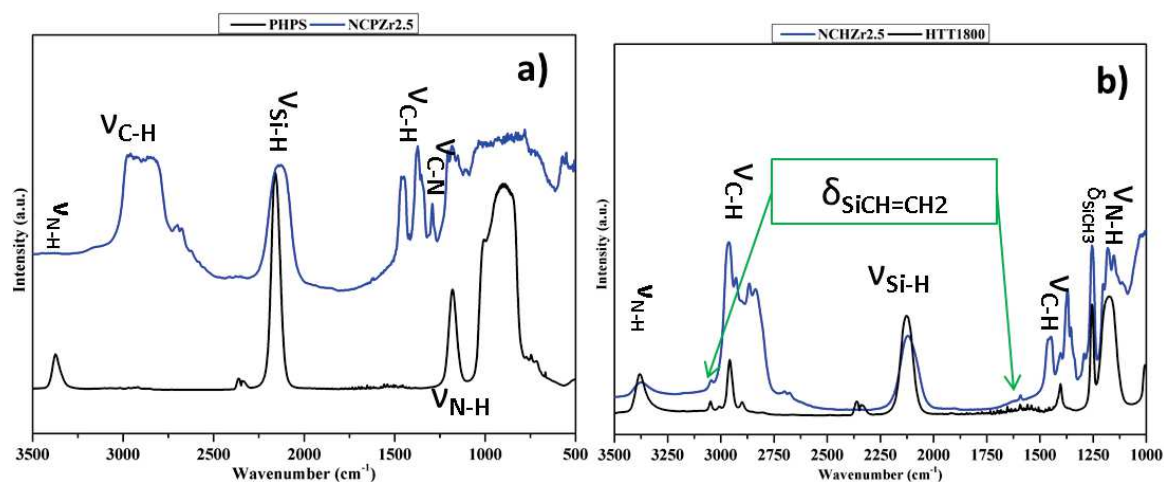


Figure 4.31 FTIR spectra of a) NCPZr2.5 and b) NCHZr2.5 samples

4.1.2 Polymer to ceramic conversion

The ceramic yield of both polymers was investigated under NH_3 using TGA and compared with the native polymer (Figure 4.32).

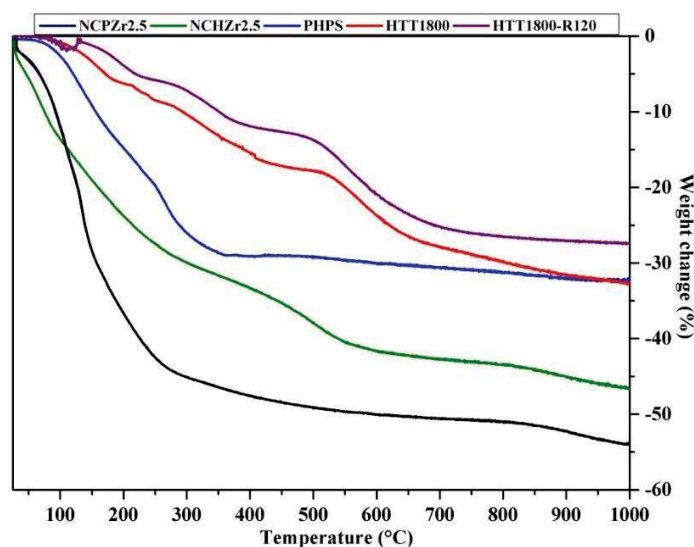


Figure 4.32 TGA under NH_3 of NCPZr2.5 and NCHZr2.5 samples and comparison with native polymers

The NCPZr2.5 sample displays a ceramic yield of 46% while the NCHZr2.5 sample exhibits a higher ceramic yield of about 53.5%. This is contrary to what was expected as in case of the NCPTi2.5 and NCHTi2.5 samples. The latter had a lower ceramic yield. We can suggest that the NCHZr2.5 sample has less Zr-based groups than NCPZr2.5 sample due to lower extent of reaction between TDEAZr and HTT1800 as explained in the previous section. The behavior

of decomposition for **NCHZr2.5** sample is very similar to HTT1800-R120 as shown in the Figure 4.32. It should be noted that the TGA of HTT1800-R120 is performed under N_2 but we expect the profile under NH_3 to be similar but with a higher weight loss. The polymer to ceramic conversion mechanism for **NCPZr2.5** and **NCHZr2.5** systems under ammonia is similar to those for Ti modified PHPS and HTT1800 and hence are not discussed again

4.1.3 Microstructural evolution and high temperature behavior

The microstructural evolution of both **NCPZr2.5-10** and **NCHZr2.5-10** system with annealing temperature was studied using XRD.

After thermal decomposition under NH_3 , the samples labelled **NCPZr2.5-10** and **NCHZr2.5-10** are x-ray amorphous as shown in Figure 4.33. The following section investigates the annealing treatment of these samples. As we move up to $1400^\circ C$, sharp peaks corresponding to nanocrystalline phase appear at 33.8° , 39.3° , 56.75° , 67.75° , 71.15° and 84.5° . The peaks matched with cubic ZrN phase (JCPDS file: 04-004-2860) with space group $Fm\bar{3}m(225)$. The crystallite calculated at the dominant (111) peak was found to be 28.92 nm. Small peaks corresponding to alpha phase of Si_3N_4 start appearing at this temperature. This tends to suggest that the interaction of Zr at the molecular scale does not shift the crystallization of the matrix to higher temperature as Ti can do it. This can be attributed to the fact that with the same Si/M ratio, the quantity of Zr introduced in PHPS is lower than the quantity of Ti introduced in the same polymer. Upon further annealing for **NCPZr2.5-15** sample we observe an increase in the crystallite size of the nanophase along with a leftward shift for the peaks. After annealing at $1600^\circ C$ (**NCPZr2.5-16**) the nanophase peak shift to 33.36° , 38.74° , 56.06° , 66.89° , 70.32° and 83.42° which correspond to cubic $ZrC_{0.5}N_{0.5}$ cubic phase (JCPDS file: 04-001-6512). The crystallite size calculated at dominant (111) peak of ZrCN was found to be 32.82 nm.

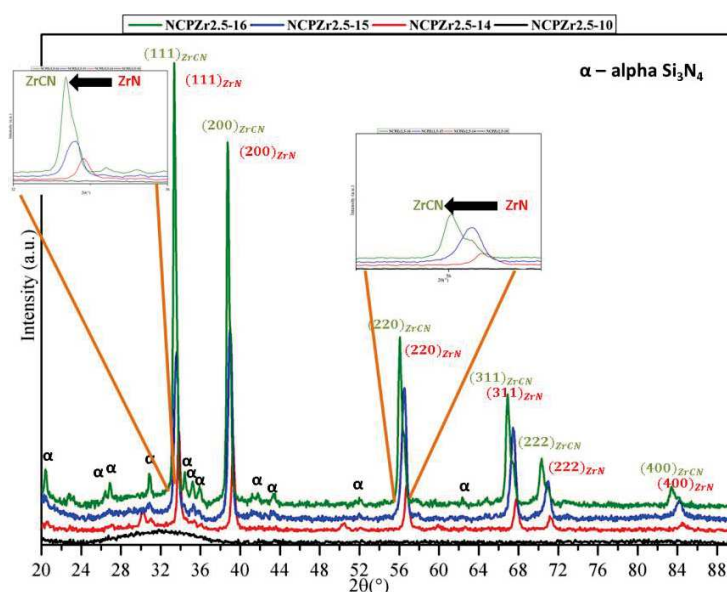


Figure 4.33 XRD depicting the phase evolution for NCPZr2.5-10 with temperature above 1000°C

This movement of nanophase peaks with temperature can be clearly seen in the inset of Figure 4.33. The observation is very contrary to what was expected. This implies that due to the large size of the ethyl side chain in TDEAZr, some carbon is trapped in the polymer network and does not react with NH_3 during the pyrolysis up to 1000°C. Above 1400°C the carbon in the matrix dissolves in the crystallizing nanophase and forms carbonitride via solid solution mixing and reactions.

The annealing behavior of NCHZr2.5-10 sample was different (Figure 4.34). The NCHZr2.5-12 sample is x-ray amorphous; followed by appearance of peaks for both ZrN nanophase and $\alpha\text{-Si}_3\text{N}_4$ for NCHZr2.5-14, similar to NCPZr2.5-14. Upon further annealing up to 1600°C (NCHZr2.5-16), $\beta\text{-Si}_3\text{N}_4$ crystallizes along with increase in intensity for the ZrN nanophase. The peaks for ZrN were obtained at same positions as for NCPZr2.5-14 sample from 1400°C to 1600°C; these were matched with JCPDS file: 04-004-2860. The crystallite size calculated at the dominant (111) peak varies from 16.2 nm at 1400°C to 21.58 nm at 1600°C. Crystallite size of the nanophase is markedly different for both NCPZr2.5-16 and NCHZr2.5-16. This may be due to the bigger size required for ZrCN crystals formed in the former case.

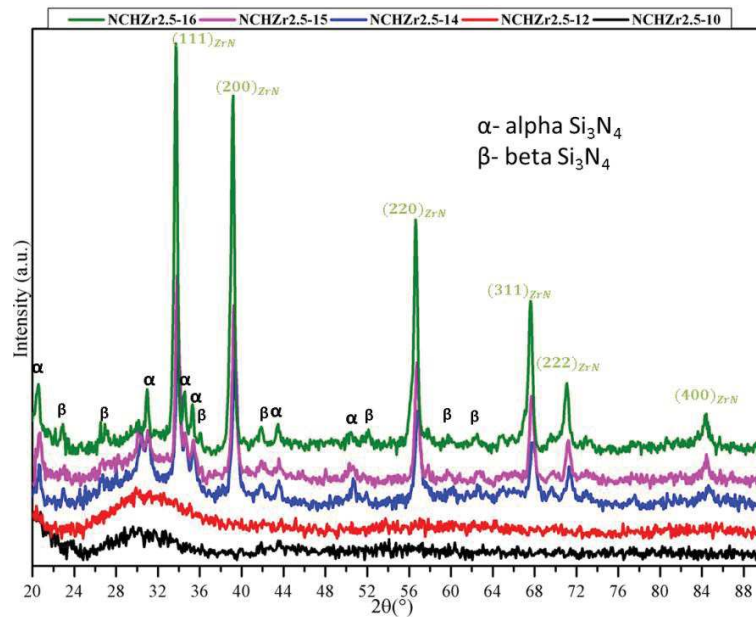


Figure 4.34 XRD depicting the phase evolution for NCHZr2.5-10 temperature above 1000°C

The Si-Zr-N ceramics derived from using PHPS and HTT1800 are compared those derived from PMSZ. The nanophase at 1500°C for PMSZr2.5-15 is similar to NCHZr2.5-15, i.e., ZrN (Figure 4.35). It was observed that the crystallization of both matrix and nanophase in for the PMSZ derived Si-Zr-N ceramic begins only at 1500°C while for the HTT1800 and PHPS derived systems it begins at a lower temperature, i.e., 1400°C. The average crystallite size for ZrN nanophase calculated at (111) peak at 1500°C was 52 nm. Comparing with other Zr modified polysilazanes, PMSZr2.5-15 has the biggest average crystallite size. Also at 1500°C, PMSZr2.5-15 has the most crystallized matrix in comparison to other two polysilazanes based systems implying that the quantity of Zr introduced at molecular level in PMSZ is the least compared to PHPS and HTT1800 for the same Si/M ratio.

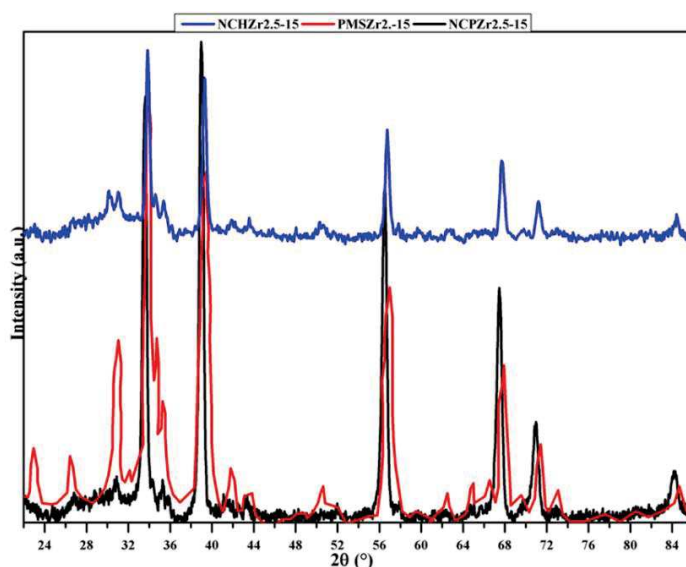


Figure 4.35 XRD comparison for NCHZr2.5-15, PMSZr2.5-15 and NCPZr2.5-15

Raman spectroscopy was performed on both systems to confirm the formation of carbonitride/nitrides of the nanophase and the atom vacancies in the nanophase system. Figure 4.36 shows the Raman spectra for NCPZr2.5-10 and NCHZr2.5-10 sample above 1000°C.

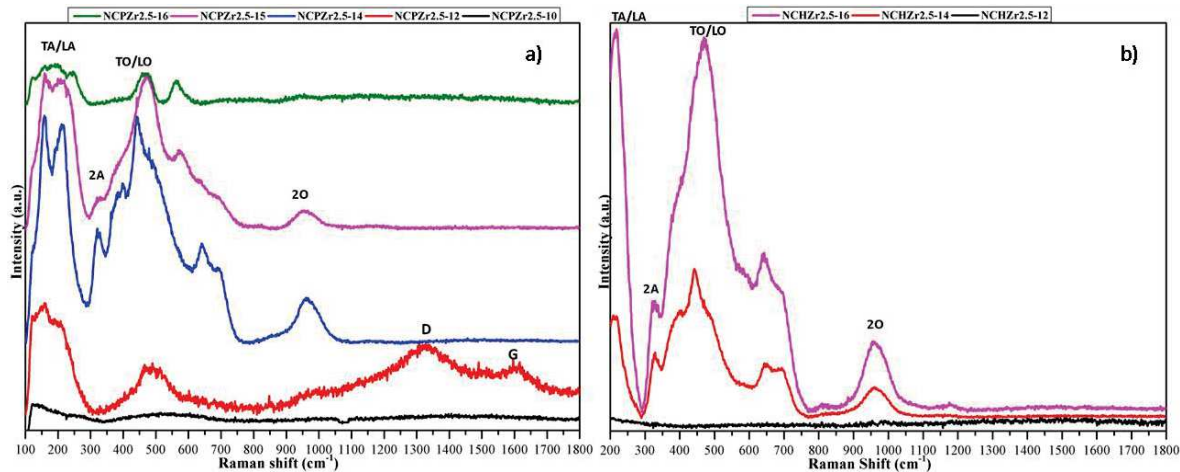


Figure 4.36 Raman spectra depicting phase evolution with temperature above 1000°C for a) NCPZr2.5-10 and b) NCHZr2.5-10 samples

For the NCPZr2.5-10 sample the Raman spectra shows no peaks. The appearance of TA/LA and TO/LO peaks for NCPZr2.5-12 is at similar positions as observed for NCPTi2.5 sample thus signifying presence of nitrogen and zirconium vacancies. The D and G bands at 1320 cm^{-1} and 1605 cm^{-1} respectively show the presence of graphitic carbon. The presence of carbon

in this case can be due to carbon from the ethyl group of TDEAZr trapped in the matrix during polymer to ceramic conversion. Upon further annealing to 1400°C (**NCPZr2.5-14**), the TA/LA peaks deconvolute with the appearance of 2A peak due to second order Raman scattering appears at 320.9 cm⁻¹ and the TO/LO peak centered at 441.2cm⁻¹ with shoulders at 397.8cm⁻¹, 479.2cm⁻¹ and 640.43cm⁻¹ match with the work of Constable et al²⁰ confirming the formation of ZrN as the nanophase. Surprisingly the D and G bands disappear. For the **NCPZr2.5-16** sample the second order scattering peaks disappear completely, TA/LA convolutes into one broad peak and TO/LO separates into two peaks signifying the formation of ZrC_xN_{1-x} system. The disappearance of graphitic peaks can thus be attributed to formation of solid solution of Zr-C-N system.

The Raman spectrum **NCHZr2.5-12** (Figure 4.36b) is quite different from its PHPS derived analog. The appearance of deconvoluted TA/LA and TO/LO peaks for **NCHZr2.5-14** sample suggests the formation of ZrN nanophase. Thus the formation of vacancies of Zr and N occur simultaneously. Upon further annealing at 1600°C the system does not change much and retains the same ZrN nanophase unlike **NCPZr2.5-16** sample.

4.1.4 Microstructure analysis using TEM

TEM analysis for the microstructure was performed on a representative sample of **NCPZr2.5-14**. Figure 4.37 shows the formation of ZrN nanophase crystals with the SAED pattern in the inset (top right corner) confirm the formation of ZrN. The d-spacing between planes marked by the blue lines was found to be 0.25 nm which was found to be in close agreement with that reported for (111) peak for ZrN in the JCPDS file 04-004-2860. On an average the crystallite size calculated at 111 peak as 28 nm is confirmed by the crystals observed in TEM.

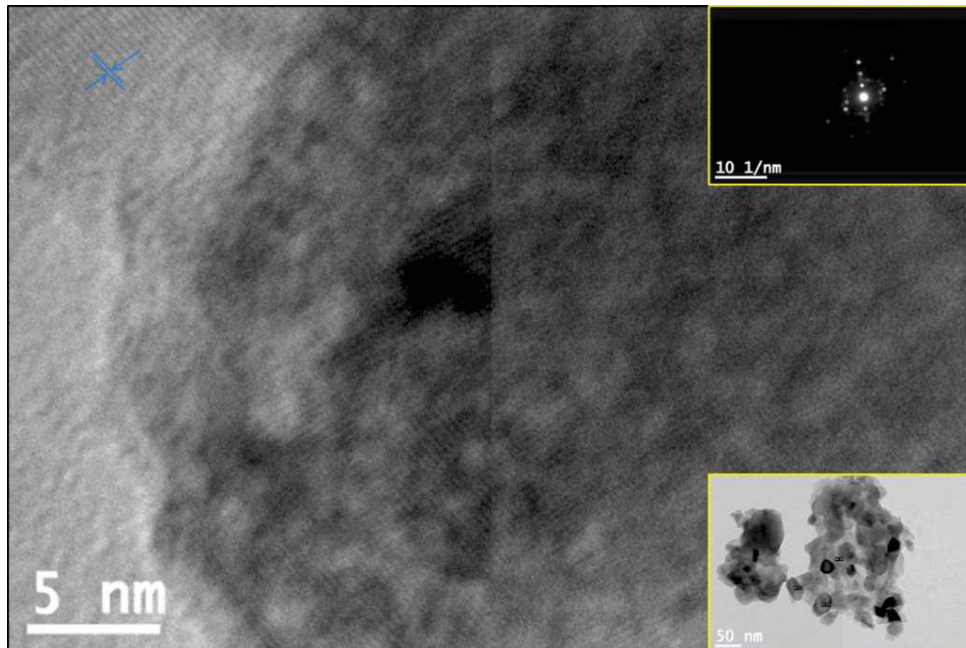


Figure 4.37 HR-TEM image for NCPzr2.5-14 with SAED pattern for ZrN as inset

As the XRD suggests that there is crystallization of matrix as well at this temperature; we find this to be true as shown in the following Figure 4.38. We can see the crystallized matrix for alpha silicon nitride with the d-spacing calculated for the planes marked with blue lines to be 0.42 nm which matches with d-spacing for silicon nitride calculated at (101) plane in the JCPDS file 04-013-5606. The inset figure shows the homogeneous distribution of ZrN nanocrystals in a crystallizing Si_3N_4 matrix.

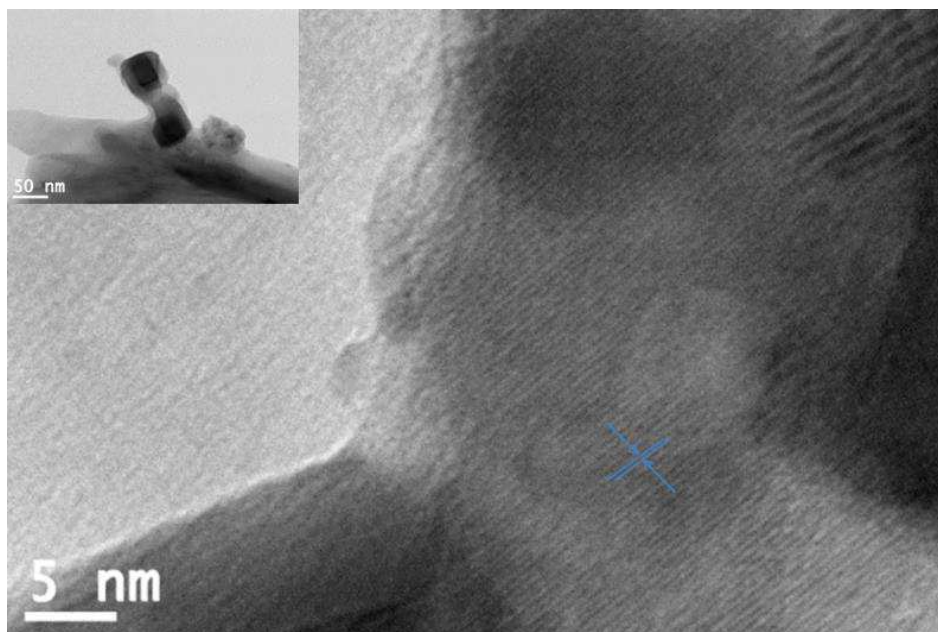


Figure 4.38 HR-TEM image for NCPzr2.5-14 showing crystallizing matrix

4.2 Si-Hf-N ceramics

As discussed in chapter 2, the Si-Hf-N ceramics are synthesized using tetrakisdimethylamidoHafnium. After the reaction a whitish-green powder was obtained using PHPS and HTT1800 as Si_3N_4 precursor and a Si/Hf molar ratio of 2.5

4.2.1 Synthesis and characterization of Hf modified polysilazanes

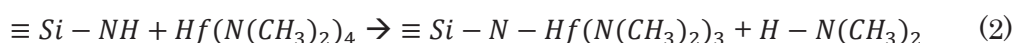
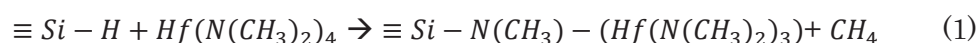
The polymer systems **NCPHf2.5** (PHPS with TDMAHf) and **NCHHf2.5** (HTT1800 with TDMAHf) have the following elemental composition (Table 4.2)

Table 4.2 Elemental analysis for **NCPHf2.5** and **NCHHf2.5**

	Si(at%)	Hf(at%)	N(at%)	C(at%)	O(at%)	H(at%)	Chemical formula
NCPHf2.5	13.95	37.25	14.45	17.6	9.43	4.6	$\text{Si}_{2.38}\text{Hf}_{1.0}\text{N}_{4.94}\text{C}_{7.01}\text{O}_{2.82}\text{H}_{21.84}$
NCHHf2.5	13.9	35.45	10	18.6	13.5	4.82	$\text{Si}_{2.49}\text{Hf}_{1.0}\text{N}_{4.85}\text{C}_{7.8}\text{O}_{3.17}\text{H}_{24.05}$

The Hf content in the polymers is very close to the ratio we set implying good reaction of TDMAHf with both PHPS and HTT1800 which was not the case with TDEAZr due to issues of steric hindrance. The polymers have a slightly higher content of O because of highly reactive nature of Hf precursor.

Figure 4.39 compares the FTIR spectra of the polyhafnosilazanes with their native polymers. For **NCPHf2.5** we see that the reaction takes place at both N-H (3400 cm^{-1} and 1180 cm^{-1}) and Si-H (2100 cm^{-1}) bonds by reactions similar to that occurring in **NCPTi2.5** polymer. Ionescu et al²¹ have done studies on the Si-Hf-N ceramics derived from PHPS albeit with higher Si/Hf ratios, i.e., lower Hf content in the polymer. They found that in case of Hf modified PHPS, the Si-H bond is more involved in the reaction as compared to in Ti modified PHPS via equation (1) mentioned below. For the **NCHHf2.5** sample the reaction seems to occur more prominently at the N-H bond rather than the Si-H bond.



The extent of this reaction is higher in case of **NCPHF2.5** as compared to **NCHHF2.5** because there are 2 moles of Si-H bonds per one mole of PHPS while there is only one mole of Si-H in one mole of HTT1800. Also any group approaching Si-H in HTT1800 will face higher steric hindrance as compared to those approaching in PHPS because of the presence of larger vinyl and methyl groups on Si.

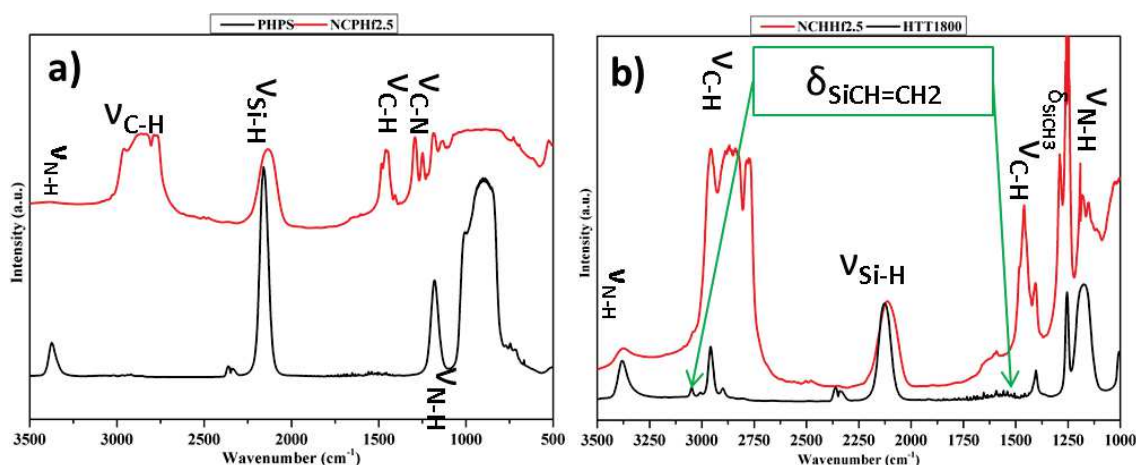


Figure 4.39 FTIR spectra of a) **NCPHF2.5** and b) **NCHHF2.5** samples

This was confirmed by the ^{13}C MAS NMR (Figure 4.40) for **NCPHF2.5**. **NCPHF2.5** has signals quite similar to **NCPTi2.5** suggesting occurrence of similar type of reactions. The intensity of the signal at 43.5ppm is greater than in the case of **NCPTi2.5** sample suggesting higher reaction at the Si-H bond (equation 1) as also suggested by Ionescu et al.

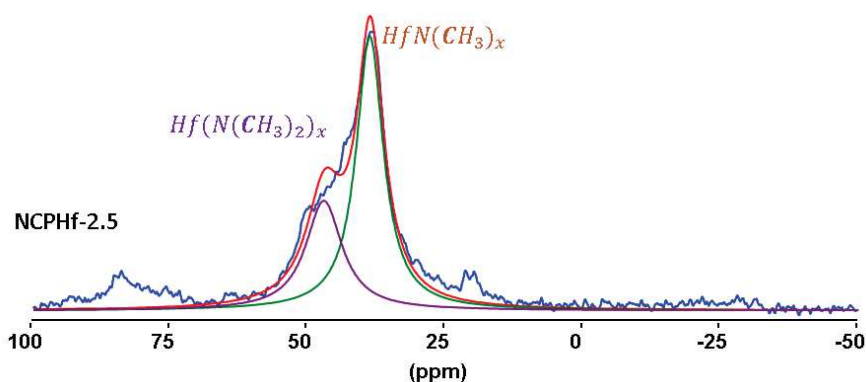


Figure 4.40 ^{13}C MAS NMR for **NCPHF2.5**

Figure 4.41 shows the ^{29}Si MAS for the polymer. It is very similar to that observed for **NCPTi2.5**. Around -36 ppm we have signals due to presence of proton rich environments of

N_2SiH_2 and N_3SiH . These signals confirm the reaction sites of Si-H and $N(CH_3)_2$. Another very weak signal at -48ppm suggests the presence of SiN_4 environment.

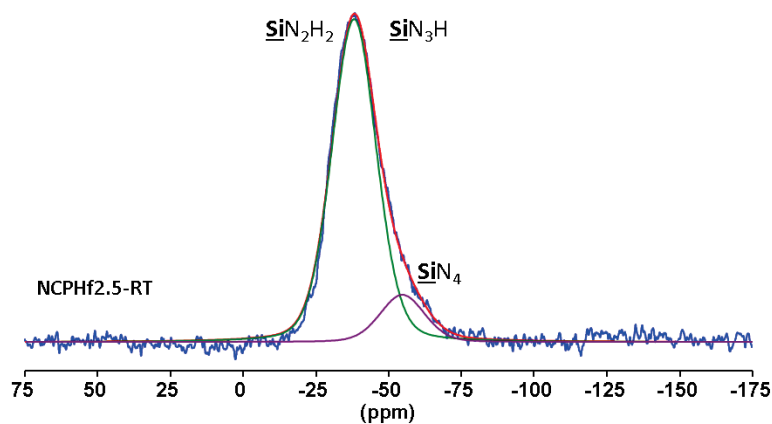


Figure 4.41 ^{29}Si MAS for NCPHf2.5 polymer

For the NCHHf2.5 sample (Figure 4.39b) the reaction occurs mainly at N-H (3400 cm^{-1} and 1180 cm^{-1}) and only slightly at Si-H bond. The disappearance of vinyl bonds after the reaction can be attributed to hydrosilylation reaction facilitated by presence of Hf (as explained in case of NCHTi2.5 system).

4.2.2 Polymer to ceramic conversion analysis with TGA

The polymer to ceramic conversion for both NCPHf2.5 and NCHHf2.5 samples was carried out under ammonia atmosphere at 1000°C . Figure 4.42 compares the TGA profile and ceramic yield for both systems along with their precursor polysilazane.

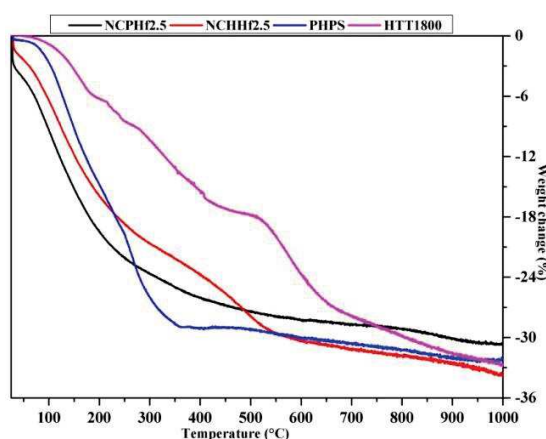


Figure 4.42 TGA under NH_3 for NCPHf2.5 and NCHHf2.5

The **NCPHf2.5** has a ceramic yield of 69.26% while **NCHHf2.5** has a ceramic yield of 66.33%. The overall higher yield in this case as compared to Zr modified polysilazanes is due to presence of methyl groups instead of ethyl in the metal precursors and higher degree of cross-linking as a result of more reaction at Si-H bonds. These Hf based single source precursors have ceramic yields even higher than their Ti based analogues due to similar reason. Upon comparing **NCPHf2.5** sample with PHPS we observed an increase in ceramic yield by 1.2%; this implies that presence of Hf enhances the cross-linking due to higher reaction at Si-H bonds which decreases the loss of low molecular oligomers after 250°C as reported by Ionescu et al also. According to solid-state NMR and FTIR studies done by Ionescu et al.²¹ the reaction forms a Si-N-Hf bond (equation 1) with removal of methane via reaction at Si-H bond along with reaction at N-H. This lead to higher degree of cross-linking which in turn leads to lower loss of low weight oligomers. Even though the initial weight loss for **NCPHf2.5** sample is higher compared to PHPS, the profile changes once the conversion reaches temperatures where we have hydrosilylation taking place and the latter crosses over the former with a less slop. The rest of the mechanism is very similar in both.

While for **NCHHf2.5** sample, the profile all along the conversion is very much similar to HTT1800 except in the very beginning where it experiences a sudden drop. There is difference of 1% in the ceramic yield of **NCHHf2.5** sample and pure HTT1800.

4.2.3 High Temperature microstructural analysis

The microstructural evolution of both **NCPHf2.5** and **NCHHf2.5** sample with annealing temperature was studied using X-Ray.

At 1000°C, the **NCPHf2.5-10** is mostly x-ray amorphous with four broad peaks centered at 30.5°, 35.1°, 51.2° and 60.5° as shown in Figure 4.43.

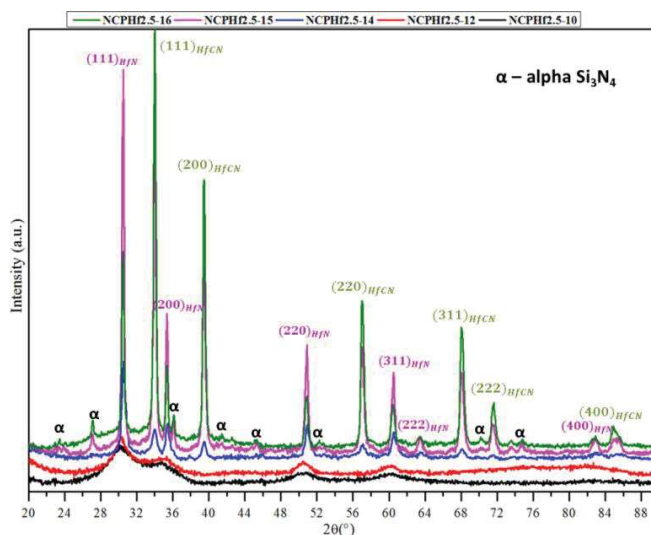


Figure 4.43 XRD patterns depicting phase evolution for **NCPHf2.5** with temperature

Upon further annealing, the **NCPHf2.5-14** sample had peaks which became sharper along with appearance of other peaks at 33.99°, 39.47°, 57.02°, 68.08°, 71.48° and 84.87°. By comparing with X-ray patterns in the literature and database it was found that the first set of peaks belonged to Hafnium nitride (HfN; JCPDS file: 01-079-5779) while the second set of peaks could be attributed to HfC_{0.5}N_{0.5} phase (JCPDS file: 04-001-6516). The presence of nitride and carbonitride of the same metal in nanophase with the matrix still being amorphous was an unexpected result as it deviates from the previously discussed Si-Ti-N and Si-Zr-N ceramics. Ionescu et al have studied the Hf modified PHPS system with various mass ratios between Si and Hf but did not report formation of such phase at high temperature. They reported that with increasing Hf content in the polymer the crystallization of silicon nitride matrix was pushed up. Our system, with Si/Hf molar ratio of 2.5 confirms the trend as the amount of Hf in our system is higher than that present in their systems. We observe that the crystallization of the matrix begins at 1500°C with just peaks of α -Si₃N₄ appearing as marked in the Figure 4.43. The intensity of the matrix peaks is dwarfed as the nanophase

becomes highly crystalline and hence has high intensity. At 1500°C for the **NCPHf2.5-15** sample, HfN has the most intense peaks with dominant (111) peak at 30.53° with a crystallite size of 32.59 nm while the crystallite size for HfCN calculated at the dominant (111) peak at 33.99° was found to be 21.72 nm. For the **NCPHf2.5-16** sample the HfCN peaks became more intense than HfN with crystallite size increasing to 26.31 nm for HfCN while for HfN the crystallite size decreases to 26.07 nm. For **NCPHf2.5-15**, the matrix starts crystallizing as α - Si_3N_4 . The intensity of the matrix peaks is low even after crystallization at 1600°C due to the highly intense nanophase peaks. The increase in HfCN peak intensity can be attributed to consumption of free carbon in the system in to the Hf-C-N solid solution as is indicated by the Raman spectra for **NCPHf2.5-16** sample (Figure 4.44)

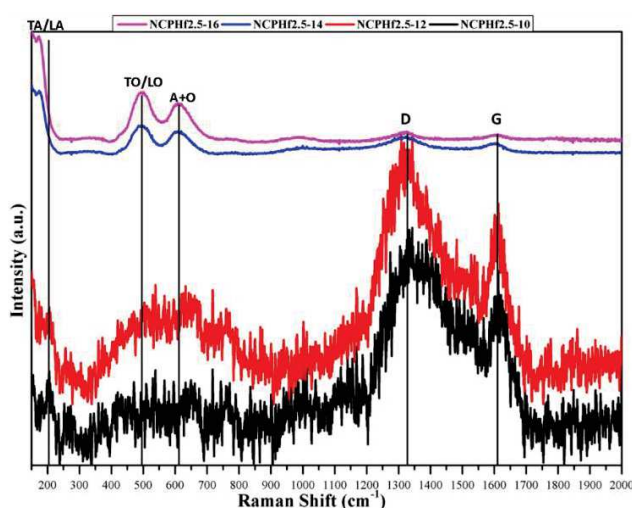


Figure 4.44 Raman spectra for **NCPHf2.5** system from 1000°C to 1600°C

The Raman spectrum for **NCPHf2.5-16** sample displays two distinct peaks for optical phonons around 500 cm^{-1} and 600 cm^{-1} along with decrease in intensity of D and G bands of graphitic free carbon suggesting formation of a metal carbonitride system, thereby confirming the results obtained by XRD.

Following the trend from previous metal modifies HTT1800 polymers we expected the formation of HfN and crystallization of silicon nitride matrix by 1500°C. Figure 4.45 shows the XRD for **NCHHf2.5-10** \rightarrow **NCHHf2.5-16**.

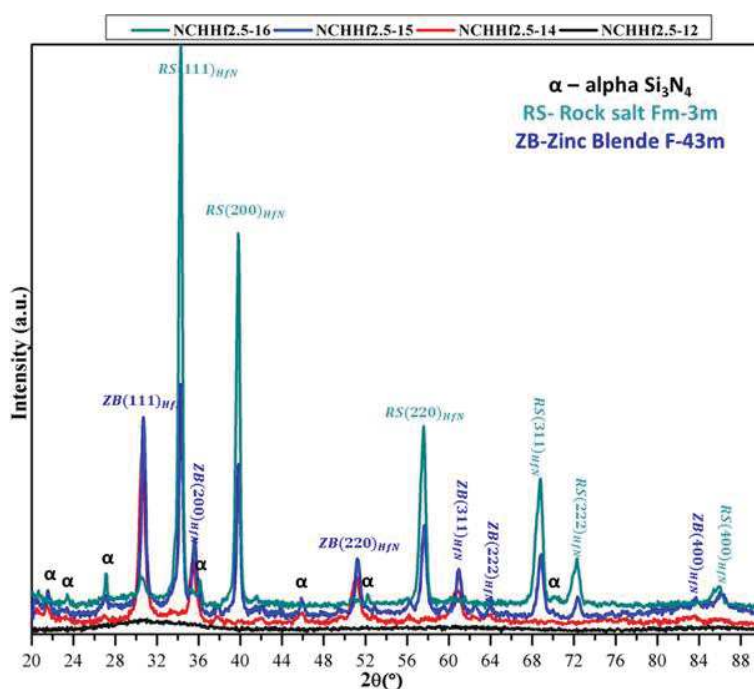


Figure 4.45 XRD patterns depicting phase evolution for NCHHf2.5 with temperature

The system upon annealing to 1400°C (NCHHf2.5-14) gave sharp peaks corresponding to the HfN having a zinc blende structure as expected (JCPDS file: 01-079-5779). It is a non-centrosymmetric crystal structure. The crystallite size calculated at the dominant (111) peak was found to be 12.84 nm. Upon further annealing till 1500°C under N₂ the existing peaks become sharper along with appearance of a new set of intense peaks at 34.3°, 39.85°, 57.65°, 68.85° and 72.35°. The positions of the peaks were found to be similar to carbonitride belonging to Hf as was observed in the previous system but upon further investigation the peaks were found to belong to another cubic phase of HfN with a rock salt structure. (JCPDS file: 00-033-0592). The two HfN phases differ from each other in terms of their space groups. The crystallite size in NCHHf2.5-15 for ZB-HfN₍₁₀₀₎ was calculated to be 17.22 nm while for RS-HfN₍₁₀₀₎ was calculated to be 21.72 nm. In NCHHf2.5-16, we observe the disappearance of ZB-HfN phase while the RS-HfN phase peak increase in intensity and sharpness. The crystallite size for RS-HfN₍₁₀₀₎ was calculated to be 21.72 nm. The disappearance of the second phase, ZB-HfN, can be explained by looking at the work of Jiang and Chen on 4d and 5d transition metal nitride²². They simulated the metal nitrides of the 4d and 5d series in the rock salt and zinc blende structure and compared the calculated values of properties like elastic modulus, bulk modulus and lattice parameters with those obtained experimentally.

They compared the cohesive energy of the various metal nitrides in their rock salt and zinc blende structure. For HfN, it was found that rock salt has higher cohesive energy than zinc blende implying that zinc blende structure is more energetically stable. Also they estimated that under 5GPa of pressure ZB converts to RS structure. Thus the disappearance of ZB at 1600°C may attributed to the energy provided by increases temperature and the pressure encountered by the nanophase from the surrounding matrix as it tries to grow.

The Raman spectroscopy analysis of **NCHHf2.5** samples at temperatures above 1000°C allows us to confirm the difference in crystallization behavior of this system and the previous system. Figure 4.46 shows a number of extra peaks as compared to the previous system.

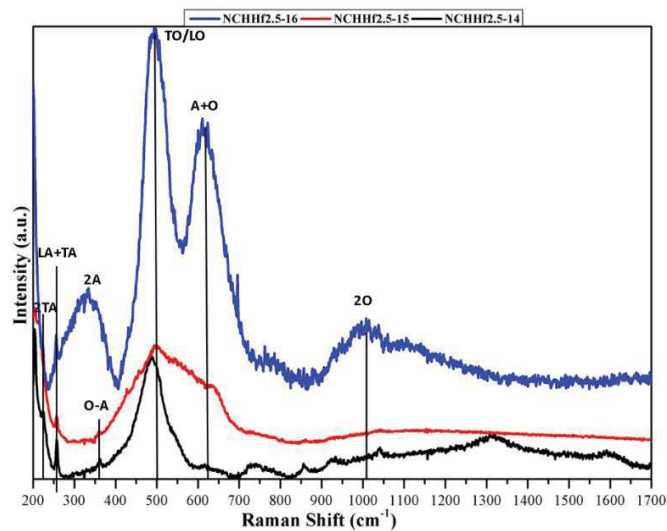


Figure 4.46 Raman spectra for **NCHHf2.5** system from 1000°C to 1600°C

For **NCHHf2.5-14**, a broad peak centered around 500 cm^{-1} can be attributed to the first order optical phonon scattering caused due to N^{3-} ions. The presence of first order peaks confirms our result of the presence of non-symmetric²⁵ HfN phase (Zinc Blende structure). Second order acoustic scattering peaks 2TA, LA+TA and O-A are visible around 230 cm^{-1} , 262 cm^{-1} and 360 cm^{-1} respectively. For **NCHHf2.5-15**, the previously mentioned second order acoustic peaks are still visible but the optical phonon peak appears broadened. After annealing at 1600°C for **NCHHf2.5-16** sample, we see reappearance of TO/LO peak centered around 500 cm^{-1} and the second order optical phonon peak A+O centered around 630 cm^{-1} . The XRD suggests the presence of symmetric HfN crystal at this temperature which implies that the first order scattering peaks should disappear. The retention of the first order peaks in

NCHHf2.5-16 sample can be attributed to two things; either the presence of small amount of non-symmetric ZB structured HfN or the crystallization of small amount of Si_3N_4 matrix.

The two systems were compared with **PMSZHf2.5-15** sample at 1500°C to see the microstructural difference between them. It was expected that since addition of carbon based groups in the polysilazane does not affect the appearance of the two different HfN structures same would be expected in **PMSZHf2.5-15** but the XRD comparison (Figure 4.47) shows that the only one phase of HfN crystallizes at 1500°C in case of Hf modified PMSZ. The HfN crystallizes only in high energy rock salt structure with the matrix nearly amorphous. Thus it is observed that presence of carbon in the polysilazane leads to formation of nitride while a polysilazane without carbon in its structures results in formation of a carbonitride contrary to what would be expected.

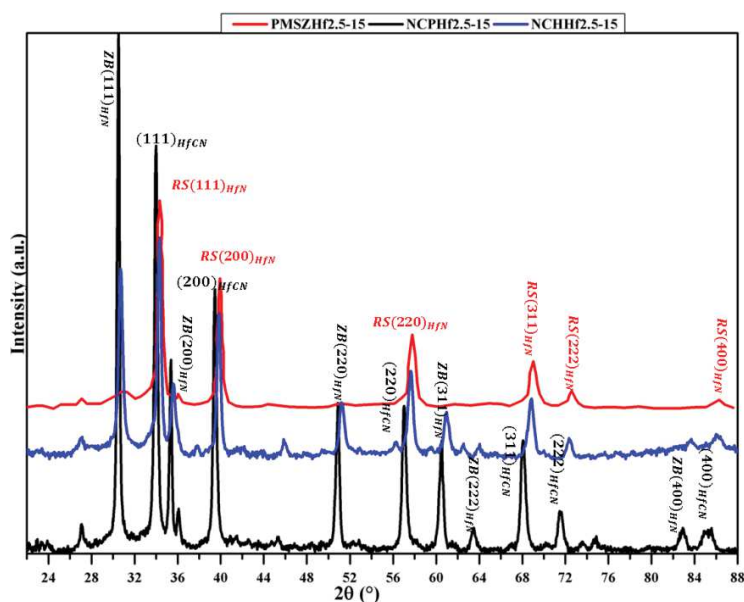


Figure 4.47 Comparison between **PMSZHf2.5-15**, **NCPHf2.5-15** and **NCHHf2.5-15**

4.2.4 Microstructural analysis through TEM

The microstructure of the nanocomposite system was studied using TEM for the representative system **NCPHf2.5-14**. The Figure 4.48 shows the microstructure of **NCPHf2.5-14**. The TEM image shows the presence of two different nanocrystals in an amorphous matrix. The set of planes depicted by pink color belong to HfN (JCPDS file: 01-079-5779) with a d-spacing calculated at the (200) set of planes as 2.21 Å while the set HfCN of planes depicted by green lines at (111) set of planes was found to be 2.68 Å. The inset figure on bottom right shows the SAED pattern for both HfN and HfCN. The inset top right image shows the continuous rings for an amorphous Si_3N_4 phase.

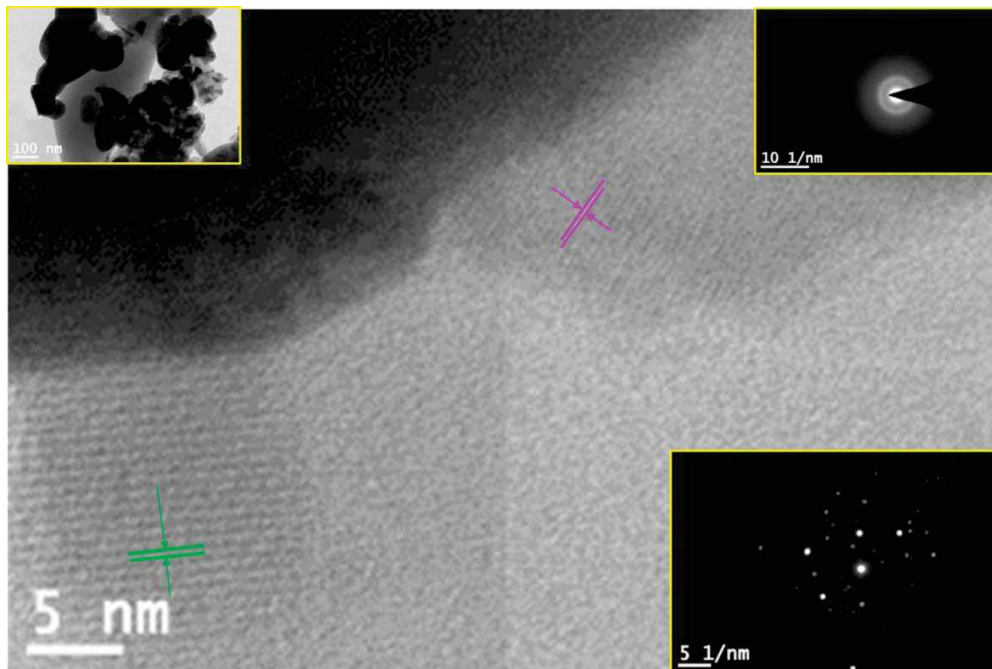


Figure 4.48 HR-TEM image for **NCPHf2.5-14** with SAED for HfN and HfCN (bottom right) and SAED for Si_3N_4 (top right)

4. Conclusion

In this chapter we focused on Si_3N_4 and Si-M-N (M = Ti, Zr, Hf) ceramics. We firstly sequenced a one-step synthetic method to obtain polymetallosilazanes. The synthesis consisted to perform the reaction between commercially available polysilazanes such as PHPS and HTT1800 and the low molecular weight metal-containing molecules (which have been already used in chapter 3) with controlled Si:M ratios. The role of chemistry behind their synthesis was studied by FTIR, solid-state NMR and elemental analyses. Two mechanisms involving N-H and Si-H bonds in polysilazanes as well as $\text{N}(\text{CH}_3)_2$ groups in metal-containing precursors have been identified. It has been shown that PHPS is the most reactive polysilazane while Hf-based molecules were highly reactive with SiH groups of polysilazanes. Such a difference has an effect on the ceramic conversion and the high temperature behavior of ceramics. Thus, we provided a comprehensive mechanistic study of the polymetallosilazane to Si-M-N ceramic transformation under ammonia based on solid-state NMR coupled with TG experiments. Pyrolysis under ammonia generated X-ray amorphous ceramics

The subsequent annealing of ammonia-treated samples under nitrogen at 1400 °C led to nanocomposites made of MN nanocrystals dispersed in an amorphous or crystallized matrix depending on the nature of the metal and the Si:M ratio fixed at molecular scale. After annealing to 1500°C, the effect of the chemistry of the polysilazane on the matrix crystallization was demonstrated. We found that the addition of Ti or Hf to PHPS in the correct Si:M molar ratio led to suppression of the matrix crystallization up to 1800°C. This generates a system where we have controlled growth of nanostructured metal nitride crystals within an amorphous ceramic matrix. These materials have been prepared as mesoporous components in the chapter 5.

References

1. Fulmer, G. R. *et al.* NMR chemical shifts of trace impurities: Common laboratory solvents, organics, and gases in deuterated solvents relevant to the organometallic chemist. *Organometallics* **29**, 2176–2179 (2010).
2. Günthner, M. *et al.* Advanced coatings on the basis of Si(C)N precursors for protection of steel against oxidation. *J. Eur. Ceram. Soc.* **29**, 2061–2068 (2009).
3. Isoda, T. *et al.* Perhydropolysilazane precursors to silicon nitride ceramics. *J. Inorg. Organomet. Polym.* **2**, 151–160 (1992).
4. Blanchard, C. R. & Schwab, S. T. X-ray Diffraction Analysis of the Pyrolytic Conversion of Perhydropolysilazane into Silicon Nitride. *J. Am. Ceram. Soc.* **77**, 1729–1739 (1994).
5. Günthner, M. *et al.* High performance environmental barrier coatings, Part I: Passive filler loaded SiCN system for steel. *J. Eur. Ceram. Soc.* **31**, 3003–3010 (2011).
6. Lücke, J., Hacker, J., Suttor, D. & Ziegler, G. Synthesis and Characterization of Silazane-Based Polymers as Precursors for Ceramic Matrix Composites. *Appl. Organomet. Chem.* **11**, 181–194 (1997).
7. Seifollahi Bazarjani, M. *et al.* Nanoporous Silicon Oxycarbonitride Ceramics Derived from Polysilazanes In situ Modified with Nickel Nanoparticles. *Chem. Mater.* **23**, 4112–4123 (2011).
8. Bechelany, M. C. *et al.* Nanocomposites through the Chemistry of Single-Source Precursors: Understanding the Role of Chemistry behind the Design of Monolith-Type Nanostructured Titanium Nitride/Silicon Nitride. *Chem. - A Eur. J.* **23**, 832–845 (2017).
9. Löffelholz, J., Engering, J. & Jansen, M. Sol-Gel-Process in the Ammono-System – a Novel Access to Silicon Based Nitrides. *Zeitschrift für Anorg. und Allg. Chemie* **626**, 963–968 (2000).
10. Engelhardt, G., Radeaglia, R., Jancke, H., Lippmaa, E. & Mägi, M. Zur Interpretation²⁹Si-NMR-chemischer Verschiebungen. *Org. Magn. Reson.* **5**, 561–566 (1973).
11. Hering, N., Schreiber, K., Riedel, R., Lichtenberger, O. & Woltersdorf, J. Synthesis of polymeric precursors for the formation of nanocrystalline Ti-C-N/amorphous Si-C-N composites. *Appl. Organomet. Chem.* **15**, 879–886 (2001).
12. Lichtenberger, O., Pippel, E., Woltersdorf, J. & Riedel, R. Formation of nanocrystalline titanium carbonitride by pyrolysis of poly(titanylcarbodiimide). *Mater. Chem. Phys.* **81**, 195–201 (2003).
13. Seitz, J., Bill, J., Egger, N. & Aldinger, F. Structural investigations of Si/C/N-ceramics from polysilazane precursors by nuclear magnetic resonance. *J. Eur. Ceram. Soc.* **16**, 885–891 (1996).
14. YIVE, N. S. C. K., LECLERCQ, D., MUTIN, P. H. & VIOUX, A. Polyvinylsilazane: a novel precursor to silicon carbonitride. *New J. Chem.* **15**, 85–92 (1991).
15. Choong Kwet Yive, N. S., Corriu, R. J. P., Leclercq, D., Mutin, P. H. & Vioux, A. Silicon carbonitride from polymeric precursors: thermal cross-linking and pyrolysis of oligosilazane model compounds. *Chem. Mater.* **4**, 141–146 (1992).

16. BROWN, G. M. & MAYA, L. Ammonolysis Products of the Dialkylamides of Titanium, Zirconium, and Niobium as Precursors to Metal Nitrides. *J. Am. Ceram. Soc.* **71**, 78–82 (1988).
17. Choong Kwet Yive, N. S., Corriu, R. J. P., Leclercq, D., Mutin, P. H. & Vioux, A. Thermogravimetric analysis/mass spectrometry investigation of the thermal conversion of organosilicon precursors into ceramics under argon and ammonia. 2. Poly(silazanes). *Chem. Mater.* **4**, 1263–1271 (1992).
18. Schmidt, W. R. *et al.* Ammonia-induced pyrolytic conversion of a vinylic polysilane to silicon nitride. *Chem. Mater.* **4**, 937–947 (1992).
19. Duwez, P. & Odell, F. Phase Relationships in the Binary Systems of Nitrides and Carbides of Zirconium, Columbium, Titanium, and Vanadium. *J. Electrochem. Soc.* **97**, 299 (1950).
20. Constable, C. P., Yarwood, J. & Münz, W.-D. Raman microscopic studies of PVD hard coatings. *Surf. Coatings Technol.* **116–119**, 155–159 (1999).
21. Zhou, C. *et al.* Synthesis and high-temperature evolution of single-phase amorphous Si-Hf-N ceramics. *J. Eur. Ceram. Soc.* **35**, 2007–2015 (2015).
22. Chen, W. & Jiang, J. Z. Elastic properties and electronic structures of 4d- and 5d-transition metal mononitrides. *J. Alloys Compd.* **499**, 243–254 (2010).
23. Spengler, W., Kaiser, R. & Bilz, H. Resonant Raman scattering in a superconducting transition metal compound—TiN. *Solid State Commun.* **17**, 19–22 (1975).
24. Spengler, W., Kaiser, R., Christensen, A. N. & Müller-Vogt, G. Raman scattering, superconductivity, and phonon density of states of stoichiometric and nonstoichiometric TiN. *Phys. Rev. B* **17**, 1095–1101 (1978).
25. Spengler, W. & Kaiser, R. First and second order Raman scattering in transition metal compounds. *Solid State Commun.* **18**, 881–884 (1976).
26. Hodak, S. K., Seppänen, T. & Tungasmita, S. Growth of (Zr,Ti)N Thin Films by Ion-Assisted Dual D.C. Reactive Magnetron Sputtering. *Solid State Phenom.* **136**, 133–138 (2008).
27. Uglov, V. V. *et al.* Structural characterization and mechanical properties of Ti–Zr–N coatings, deposited by vacuum arc. *Surf. Coatings Technol.* **180–181**, 519–525 (2004).
28. Purushotham, K. P. *et al.* Tribological studies of Zr-implanted PVD TiN coatings deposited on stainless steel substrates. *Wear* **254**, 589–596 (2003).
29. Lugscheider, E. *et al.* PVD hard coated reamers in lubricant-free cutting. *Surf. Coatings Technol.* **112**, 146–151 (1999).
30. Nowotny, H., Benesovsky, F. & Rudy, E. Hochschmelzende Systeme mit Hafniumkarbid und -nitrid. *Monatshefte für Chemie* **91**, 348–356 (1960).
31. Kieffer, R., Ettmayer, P., Dufek, G. & Nowotny, H. Recent investigations on the miscibility of transition element nitrides and carbides. *Metall* **26**, 701–708 (1972).
32. Kieffer, R., Nowotny, H., Neckel, A., Ettmayer, P. & Usner, L. Zur Entmischung von kubischen Mehrstoffcarbiden. *Monatshefte für Chemie* **99**, 1020–1027 (1968).

33. PhD. Thesis Mirna Bechelany, University of Lyon, 2011

CHAPTER 5

SHAPING AND

APPLICATION



1. Introduction

The emerging hydrogen economy addresses environmental and energy challenges faced by society by envisaging the production of electricity using fuel cells. The success of this approach relies heavily on the broad availability of high-purity hydrogen (H_2). However, hydrogen is mainly produced by methane reforming; a high temperature process yet expensive and requiring separation techniques to purify it. This is one of the first issues which limit the large scale development of these technologies. Furthermore, the mature technologies for fuel cells involve platinum-based nanoparticles (Pt-NPs) dispersed on a carbon substrate as electrode catalysts for performing the electrochemical reactions (oxygen reduction reaction -ORR-, hydrogen evolution reaction -HER-, alcohol oxidation reaction -AOR-, hydrogen oxidation reaction -HOR-). But, platinum is a rare, strategic and expensive material and classical carbon supports having a low graphitization degree are sensitive to corrosion at low and medium potentials, which limits the large scale development of these technologies because of cost (catalysts represents 50 % of a fuel cell cost and more than 20 % of the whole system) and durability issues. Moreover, carbon supports are inactive. Within this context, a major part of the present chapter deals with the processing of the materials developed and characterized in chapters 3 (Si-C-N, Si_3N_4 , Si-Ti-N(C)) and 4 (BN, B-Ti-N). These materials are prepared as mesoporous compounds for use as supports of platinum (Pt) nanoparticles: i) in the hydrolysis of sodium borohydride ($NaBH_4$) to produce hydrogen as an alternative to methane reforming. For these applications, highly stable and catalytically active materials are expected. This is the reason of using Si- and B-based ceramics such as SiC, Si-C-N, Si_3N_4 and BN compounds. Furthermore, TiN has a number of desirable properties that make it uniquely suited as a catalyst support, especially when synthesized at nanoscale¹⁻⁴. However, TiN may suffer from corrosion in harsh environments. Therefore, TiN alone may not propose the necessary stability for the application we target. The design of mixed nitrides in the Si-Ti-N and/or B-Ti-N systems can provide useful properties derived from their component nitrides such as catalytic properties, robustness and chemical stability for catalysis-assisted reactions in harsh environment. In addition, there is a particular interest in controlled synthetic approaches for monolithic structures that provide nanosized materials (because they show improved properties compared with bulk materials), three-dimensional (3D) porosity, connectivity and accessibility. In particular, we pay attention to

tailor the pore size in the mesoscale range (2-50 nm), namely mesopores, to warrant high surface area in order to maximize the contact of catalyst with the fuels such as NaBH_4 .

With the structural viewpoints focused on, we describe the synthesis and characterization of monoliths that bear mesopores and provide a very high specific surface area through the template-assisted Polymer-Derived Ceramics (PDCs) route in the systems explored in chapters 3 and 4. We start with the preparation and detailed characterization of mesoporous ceramics including binary (SiC , Si_3N_4 , BN) and ternary/quaternary (Si-C-N , Si-Ti-N(C) , B-Ti-N) materials using activated carbon monoliths as templates. Supported platinum (Pt) catalysts were prepared by reduction of Pt precursors with hydrogen as a reducing agent and the different systems as supports. A 1 wt% of Pt was targeted. The catalytic behavior of the nanocomposite supported Pt catalyst for the hydrolysis of NaBH_4 was investigated and compared.

2. Design of mesoporous components

The possibility to develop materials bearing tailored mesoporosity can be envisioned by coupling the PDCs route with a templating approach⁵⁻⁷. This process is in general applied to prepare mesoporous PDC powders through impregnation of hard template powders such as ordered mesoporous silica (SBA-15), derived carbon (CMK-3) or zeolite-derived carbon. However, powders have limited practical use. One of the solutions could be to sinter these powders at low temperature by Spark Plasma Sintering (SPS) and generate 3D structures as the preferred configuration^{8,9}. However, this strategy reduces the micro/mesoporosity and develops the macroporosity of the materials. Here, we propose to i) impregnate the porous structure of monolith-type templates (activated carbon monoliths labeled *ACM*) with particular mesoporosity with a preceramic polymer solution, (ii) performing the subsequent pyrolysis to achieve the precursor-to-ceramic conversion, and then (iii) removing the mold while generating a monolith with tailored mesoporosity.

Firstly, we use three different commercial organosilicon polymers including the PHPS (Si₃N₄ precursor) and HTT1800 (Si-C-N precursor) already detailed in chapter 3 and AHPCS (SiC precursors) to form mesoporous 3D structures. Then, we will briefly speak about mesoporous BN monoliths. In the third section, we will describe Si-Ti-N and B-Ti-N ceramics designed as mesoporous components. The pore architecture of all samples has been assessed at the mesoscopic scale by nitrogen gas adsorption-desorption measurements at 77 °K.

2.1. Preparation of mesoporous SiC, Si-C-N and Si₃N₄ monoliths

Herein, we used three commercially available liquid precursors to produce mesoporous 3D structures (Fig. 5.1).

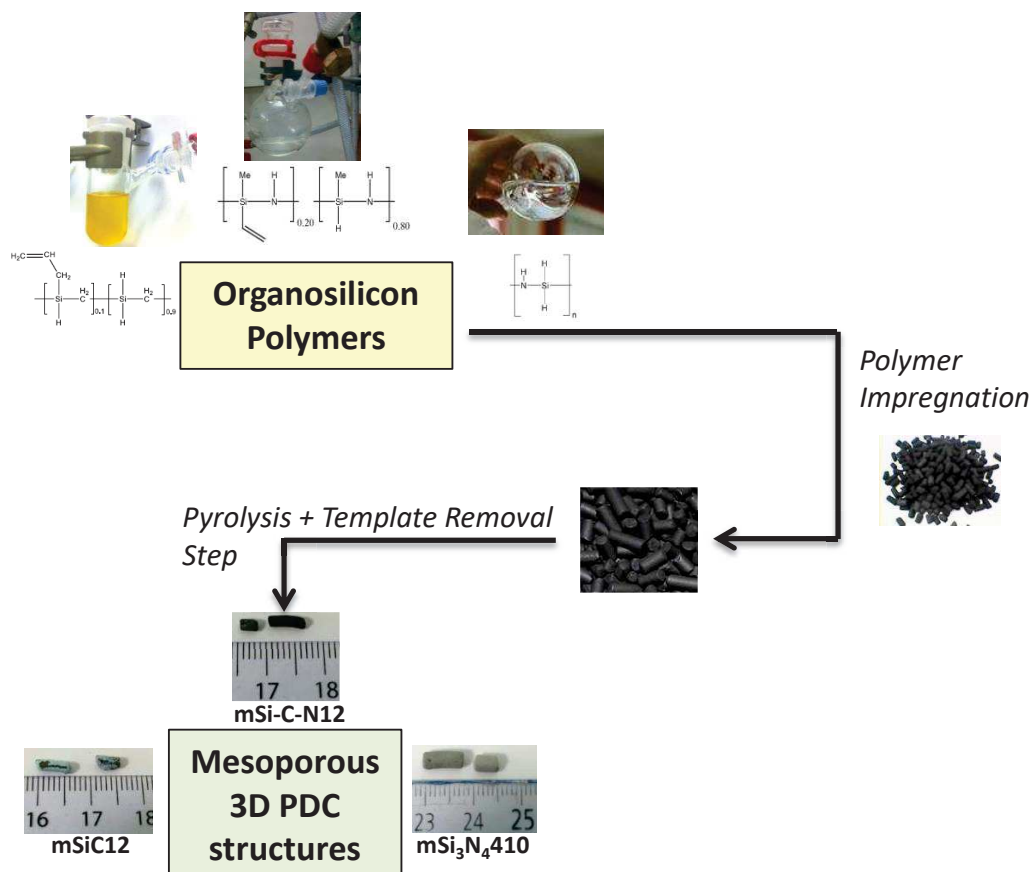


Figure 5.1 Scheme for preparation of mesoporous Si based carbide/carbonitrides/nitrides

AHPCS (SiC precursor) has a nominal structure of $[\text{Si}(\text{CH}_2\text{CH}=\text{CH}_2)\text{HCH}_2]_{0.1}[\text{SiH}_2\text{CH}_2]_{0.9}$ (Fig. 5.1)¹⁰. The presence of allyl groups in its structure results in a precursor with improved thermal cure characteristics, as well as enhanced ceramic yield. AHPCS exhibits a three-step decomposition starting from 70 °C to provide SiC and free carbon in a weight loss of 28 % corresponding to 72.0 wt% ceramic yield. The polycarbosilazane HTT1800 (Si-C-N precursor) is a copolymer containing 20 % of methyl/vinyl and 80 % of methyl/hydride substituted silazane units (Fig. 5.1)¹¹. HTT1800 can be crosslinked by heating to 180–200 °C then pyrolyzed under nitrogen to produce Si-C-N ceramics with free carbon with a weight loss of 32 % corresponding to a ceramic yield of 68 %. PHPS (Si₃N₄ precursor, Fig. 5.1) is a highly

reactive preceramic polymer containing two Si-H and N-H functions in its structure^{12,13}. Through pyrolysis under nitrogen, PHPS leads to a composite material composed of a majority of Si₃N₄ and around 13 wt% of silicon (Si). Using ammonia as atmosphere, PHPS leads to Si₃N₄ in a measured weight loss of 30 %; therefore, the ceramic yield is calculated to be 70 %.

In the present paper, nanocasting provides access to mesopores by replicating the nanostructure of activated carbon monoliths labeled *ACM* into mesoporous 3D structures. Two key factors need to be appropriately selected during the processing of the mesoporous 3D structures from AHPCS, HTT1800 and PHPS. They are the mass ratio between the preceramic polymers and the template as well as the heat treatment conditions to convert the corresponding ceramics and remove the template. These two factors have a strong impact on the structural properties of the final materials and the cohesion of the materials after pyrolysis and template removal. The most appropriate processing parameters have been selected based on the specific surface area (SSA) and the structural stability of the well representative mesoporous 3D Si₃N₄ structure after pyrolysis of *PHPS/ACM* and the template removal step. Table 5.1 shows the effect of the mass ratio for the sample **mSi₃N₄10**.

Table 5.1 Effect of the mass polymer-to-template ratio fixed during impregnation of PHPS in ACMs

Mass Ratio (PHPS:ACMs)	Specific surface area ($\text{m}^2 \text{g}^{-1}$)	Pyrolysis and template removal step
0.5 (<i>product collapsed during processing</i>)	511.0	1°C min^{-1} heating rate till 1000°C , dwell time of 10 hours and cool to RT at 1°C min^{-1} ; atmosphere NH_3
1	216.3	1°C min^{-1} heating rate till 1000°C , dwell time of 10 hours and cool to RT at 1°C min^{-1} ; atmosphere NH_3
1.4	494.1	1°C min^{-1} heating rate till 1000°C , dwell time of 10 hours and cool to RT at 1°C min^{-1} ; atmosphere NH_3
1.8	501.7	1°C/min heating rate till 1000°C , dwell time of 10 hours and cool to RT at 1°C/min ; atmosphere NH_3

Based on the values of the SSA, a mass polymer-to-template ratio of 1.4 has been fixed. It represents the minimal ratio to avoid the collapse of the structure of monoliths during the pyrolysis. Above this ratio, the monoliths display low SSA values. This means that a mass polymer-to-template ratio of 1.4 brings about an appropriate combination of voids in the pore walls which can generate a large porosity and in turn a large pore volume without altering the mechanical robustness of the materials. Based on the results obtained with PHPS, we apply the same ratio using AHPCS and HTT1800 as SiC and Si-C-N precursors, respectively. The composites *AHPCS/ACM*, *HTT1800/ACM* and *PHPS/ACM* have been subjected to various final pyrolysis programs and pyrolysis temperatures to select the ideal ones which allowed obtaining 3D structures with a sufficient structural integrity, high SSA as well as pore volumes after template removal. Here, we need to distinguish the couple *AHPCS/ACM* and *HTT1800/ACM* from *PHPS/ACM*. Within this context, we discuss firstly on the characterization of SiC and Si-C-N 3D structures then on the characterization of Si_3N_4 3D

structures combining nitrogen gas adsorption-desorption measurements, X-ray diffraction and/or SEM. Complete characterization is done at mesoscale. The objective is to select the best material in terms of SSA and pore volume in each composition.

2.1.1 Mesoporous SiC and Si-C-N monoliths:

2.1.1.1 Synthesis strategy

For *AHPCS/ACM* and *HTT1800/ACM*, the formation of mesoporous 3D structures is achieved within two steps including the pyrolysis to convert AHPCS into SiC and HTT1800 into Si-C-N ceramics and the template removal step. The determination of the final pyrolysis temperature in the first step is crucial because it is expected to produce a material which is sufficiently stable (thermally and chemically) for the second heat-treatment performed under air (template removal step). Within this context, the samples *AHPCS/ACM* and *HTT1800/ACM* are heat-treated at different temperatures in the range 1000-1600 °C before the template removal step which has been fixed at 600 °C for 5 hours. The temperature is selected after performing TGA on the sample in which a sudden drop in weight is observed in the temperature range 500-600 °C due to oxidation of carbon template.

2.1.1.2 Characterization:

The monoliths prepared by nanocasting were characterized using BET technique to measure the specific surface area of the samples and to confirm the type of porosity created in the system. XRD on the crushed monoliths was done to confirm the formation of intended ceramic phase.

The pore architecture of samples **mSiCX** (from *AHPCS/ACM*) and **mSi-C-NX** (from *HTT1800/ACM*) (X being the two first numbers of the final temperature, *e.g.*, 12 for 1200) is assessed at the mesoscopic length scale by nitrogen gas adsorption-desorption measurements at 77 K (Figure 5.2. (for **mSiCX**) and Figure 5.5. (for **mSi-C-NX**)).

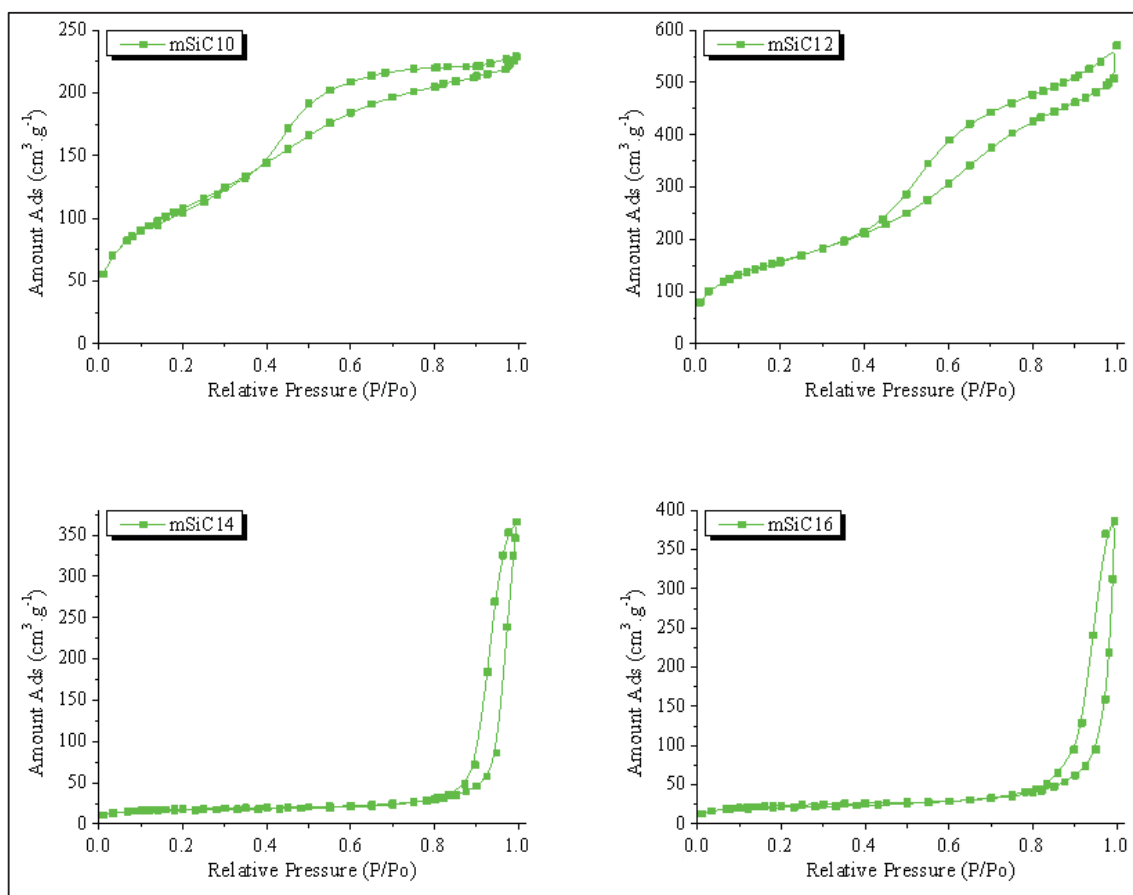


Figure 5.2 Evolution of BET isotherm for mesoporous SiC monoliths with temperature

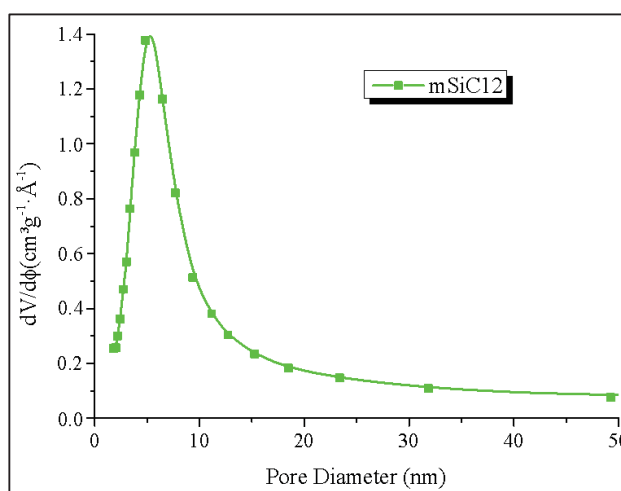


Figure 5.3 Pore size distributions for mSiC12 sample

As expected, the structure of monoliths as well as the pore dimensions may be tailored by the choice of the final temperature. This is highly reflected through the shapes of the isotherms of the mSiCX samples. The **mSiC10** and **mSiC12** samples show two similar IV type-curves in

which the adsorption and desorption curves do not coincide over the region of relative pressure $P/P_0 = 0.4-0.99$ indicative of H2 hysteresis loops for these samples. The IV-type isotherms suggest that the samples have uniform mesoporous channels^{13,14} while H2 hysteresis loops are generally found in disordered porous materials or in ordered mesoporous material with 3-D cage-like pores and interconnected pores¹⁵. Based on the structure of *ACM*, we can consider that **mSiC10** and **mSiC12** are mesoporous materials bearing interconnected porosity. The specific BET surface area is $396.5 \text{ m}^2 \text{ g}^{-1}$ for the sample **mSiC10** and $581.4 \text{ m}^2 \text{ g}^{-1}$ for the sample **mSiC12**. The SSA of the sample **mSiC12** is close to that one reported by Zhao *et al.* on ordered mesoporous PCS-derived SiC powders when temperature of pyrolysis of $1200 \text{ }^\circ\text{C}$ ¹⁶. The micropore area for **mSiC10** is $244.2 \text{ m}^2 \text{ g}^{-1}$, whereas there are no micropores in the sample **mSiC12**. The total pore volume determined from the amount of nitrogen adsorbed at $P/P_0 = 0.97$ for **mSiC10** is $0.34 \text{ cm}^3 \text{ g}^{-1}$ and it increases to $0.76 \text{ cm}^3 \text{ g}^{-1}$ for the fully mesoporous **mSiC12**. The pore size distribution (PSD) calculated from desorption branch by means of the *Barett-Joyner-Halenda* method gives an average pore diameter of 5.26 nm (Figure 5.3). It should be mentioned that the SiC composition of the sample **mSiC10** cannot be retained under the air-treatment to remove *ACM*. Silica is generated. A treatment at $1200 \text{ }^\circ\text{C}$ before template removal enhances the thermal stability during the subsequent air-treatment.

Figure 5.4 shows that the profiles of isotherms significantly change for the samples **mSiC14** and **mSiC16** and correspond to II-type isotherms suggesting the formation of macroporous or non-porous samples. The samples exhibit specific BET surface areas ranging from $63 \text{ m}^2 \text{ g}^{-1}$ to $83 \text{ m}^2 \text{ g}^{-1}$ which significantly decrease in comparison to **mSiC10** and **mSiC12**. The total pore volume determined from the amount of nitrogen adsorbed at $P/P_0 = 0.97$ decreases to $0.36 \text{ cm}^3 \text{ g}^{-1}$ and $0.24 \text{ cm}^3 \text{ g}^{-1}$ for **mSiC14** and **mSiC16**, respectively. We suggest that the possible reason is the mesostructural/framework shrinkage of the *ACM* host accompanied by a tremendous decrease in the volume of the pores due to the high-temperature treatment. The high-temperature treatment involves the crystallization of the β -SiC phase above $1200 \text{ }^\circ\text{C}$ as shown in the X-ray diffraction patterns of these materials. The samples **mSiC10** and **mSiC12** are X-ray amorphous whereas the samples **mSiC14** and **mSiC16** show the main diffraction peaks of the β -SiC phase ((111) at 35.6° , (220) at 59.9° and (311) at 71.7°) as well as of β -SiC and β -SiC through the two poorly intense peaks at 41.5° and 76° .

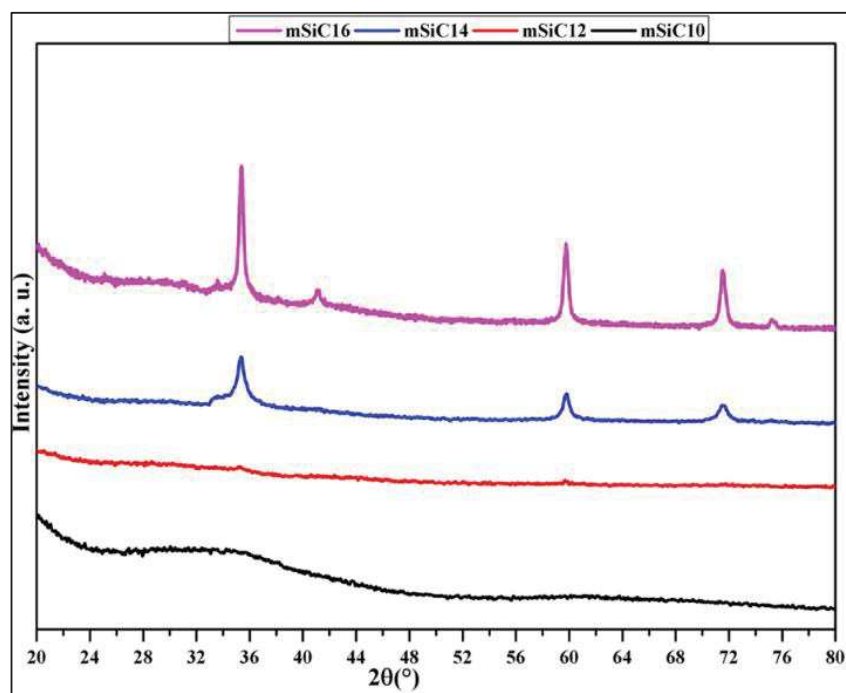


Figure 5.4 XRD patterns of mSiCX monoliths with temperature

The same behavior is observed with the samples **mSi-C-NX** (X= first two numbers of annealing temperature for eg. At 1200°C the sample is labelled **mSi-C-N12**) in the nitrogen adsorption desorption isotherms (Fig. 5.5).

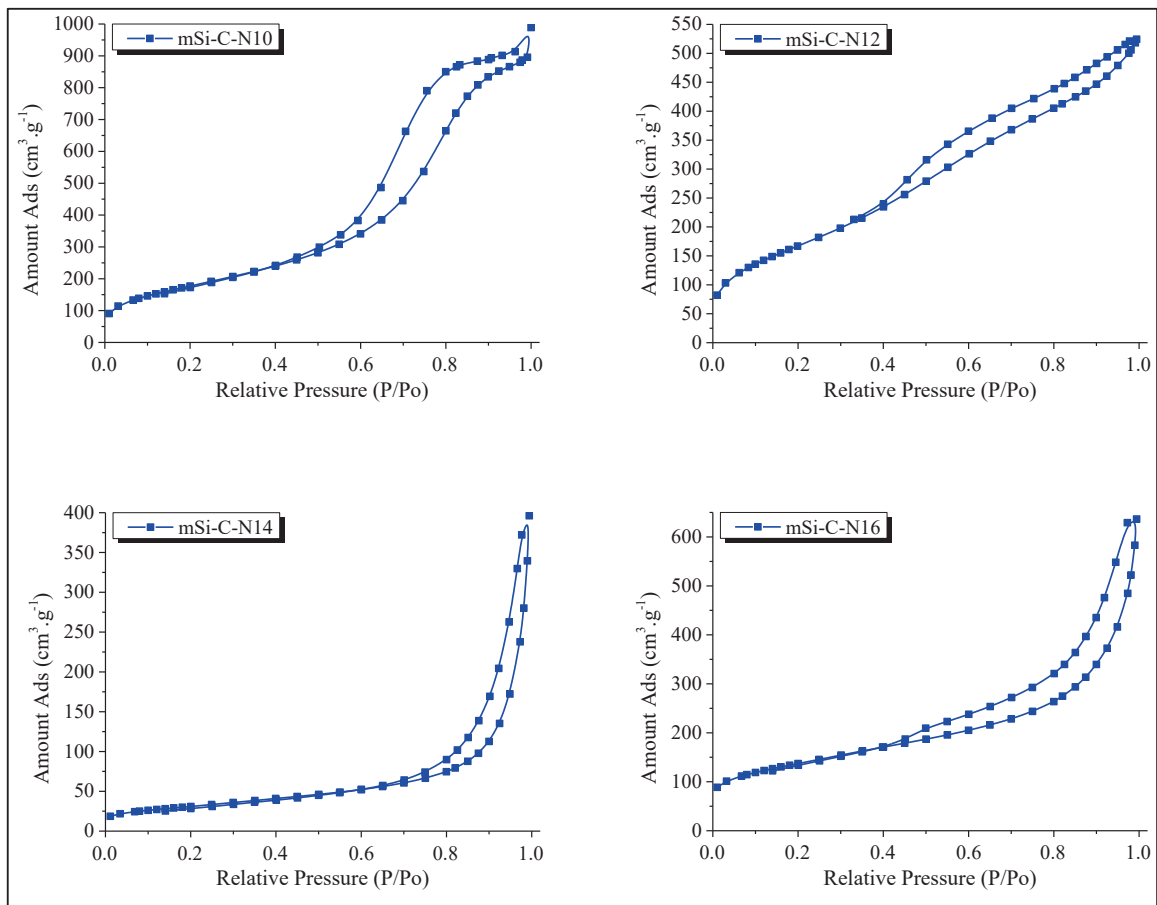


Figure 5.5 BET isotherm for mSi-C-NX monoliths with temperature

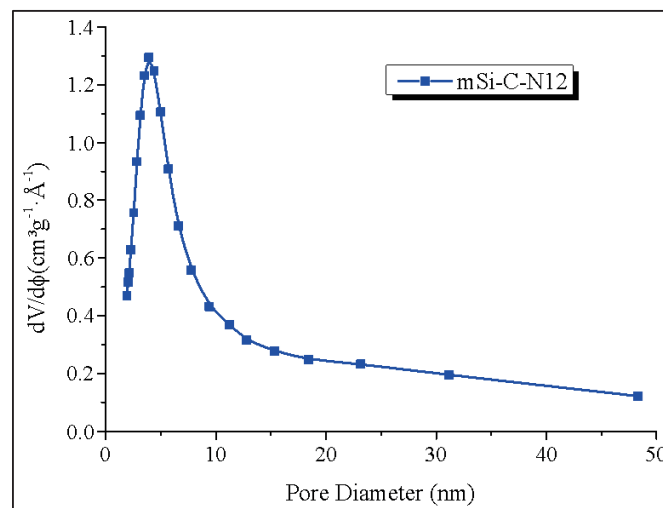


Figure 5.6 Pore size distribution of mSi-C-N12 monolith

The isotherms of **mSi-C-N10** and **mSi-C-N12** show IV type-curves in which the adsorption and desorption curves do not coincide over the region of relative pressure $P/P_0=0.4-0.99$. We can suggest that the adsorption hysteresis represents a H2-type for both samples. Therefore, we suggest that the samples **mSi-C-N10** and **mSi-C-N12** are mesoporous materials with interconnected pores similarly to **mSiC10** and **mSiC12**. A specific BET surface area as high as $623.7\text{m}^2\text{ g}^{-1}$ is measured for the sample **mSi-C-N12** which is significantly higher than the values reported by Kim *et al.* on HTT1800-derived Si-C-N powders using CMK-3 and CMK-8 as templates¹⁷. The total pore volume determined from the amount of nitrogen adsorbed at $P/P_0 = 0.97$ is $0.77\text{cm}^3\text{ g}^{-1}$. The pore size distribution (PSD) is calculated from the desorption branch (Figure 5.6) by means of the *Barett-Joyner-Halenda* method. A uniform diameter of 4.9 nm is found. In contrast, the sample **mSi-C-N14** proposes II-type isotherms suggesting the formation of macroporous or non-porous samples. The specific BET surface area decreases to $111.4\text{m}^2\text{ g}^{-1}$ in line with the total pore volume decreasing to $0.36\text{cm}^3\text{ g}^{-1}$. These results confirm the behavior observed with the samples **mSiC14**. However, the sample **mSi-C-N14** is X-ray amorphous as shown on the corresponding X-ray diffraction patterns. This confirms that the decrease of the SSA in the samples **mSiC14** and **mSi-C-N14** is mainly due to the high temperature heat-treatment which probably involves framework shrinkage. Surprisingly, the sample **mSi-C-N16** shows a IV-type curve suggesting that the sample displays uniform mesoporous channels. Furthermore, at relative pressures below 0.1, the relatively high uptake implies the presence of micropores. The shape of the isotherm is asymmetrical with a desorption branch steeper than the adsorption branch at a relative pressure (P/P_0) from 0.4 to 0.99 indicative of H2 hysteresis loop. The sample displays a SSA of $490.7\text{ m}^2\text{ g}^{-1}$ and a pore volume of $0.74\text{ cm}^3\text{ g}^{-1}$; the reason of this behavior may be understood through the XRD patterns (Figure 5.7). Like the samples **mSiCX**, the heat-treatment of the samples **mSi-C-NX** at high temperature involves the nucleation of the β -SiC phase as shown in the X-ray diffraction patterns of these materials. The samples **mSi-C-N10**, **mSi-C-N12** and **mSi-C-N14** are X-ray amorphous whereas **mSi-C-N16** shows the main diffraction peaks of β -SiC and small peaks of mixture of β - Si_3N_4 and α - Si_3N_4 phases. β -SiC is formed through the carboreduction of Si_3N_4 in the sample **mSi-C-N14**³. This involves the removal of nitrogen from the volume of the component while SiC is formed. As a consequence, we suggest that nitrogen leaves pores in the samples **mSi-C-N16** to increase its SSA and pore volume. The main disadvantage is the lack of control over total mesoporosity.

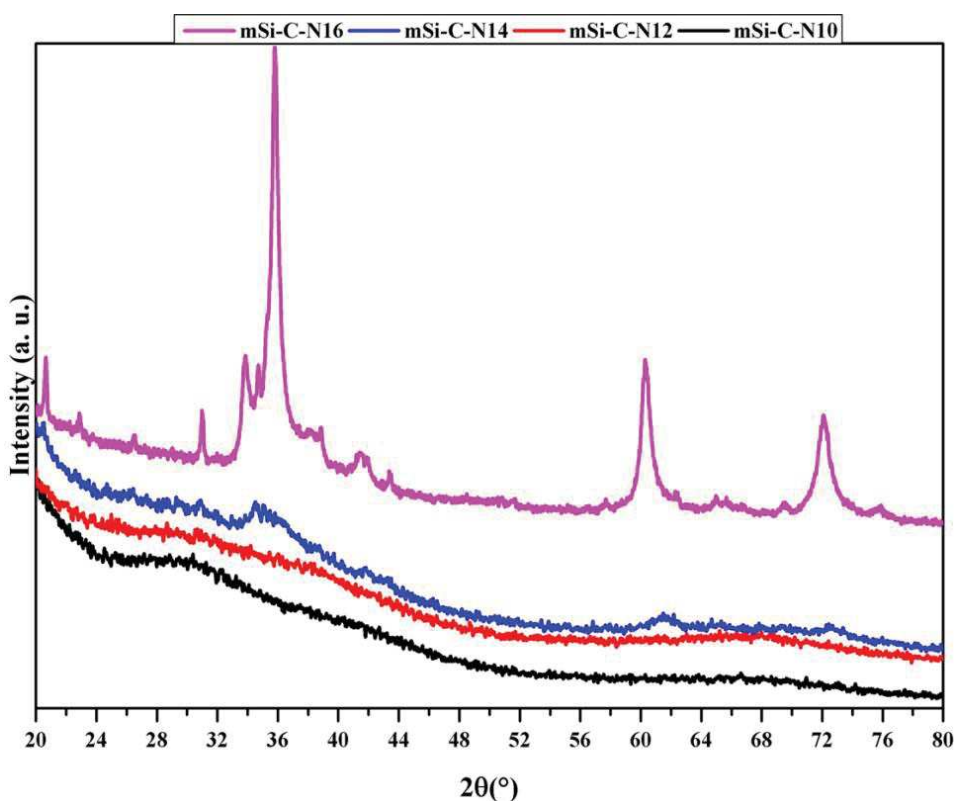


Figure 5.7 XRD patterns of mSi-C-NX monoliths with temperature

2.1.2 Mesoporous Si_3N_4 monoliths

2.1.2.1 Synthesis strategy

Three strategies are investigated to prepare mesoporous Si_3N_4 3D structures. Firstly, we should mention that heat-treatment in air to remove *ACM* after the polymer-to-ceramic conversion systematically leads to silica. As a consequence, the template removal step is performed under ammonia according to our previous work¹⁸. The first strategy consists to pyrolyze *PHPS/ACM* under nitrogen at 1000 °C for 2 h followed by removal of template under ammonia at 1000 °C for 5 h. In the second strategy, conversion and removal of template are achieved in the same step under ammonia. In the third strategy, the pyrolysis is first performed under nitrogen up to 400 °C then under ammonia up to 1000 °C.

The first strategy does not allow fully removing the template whereas the second strategy is effective in both conversions of PHPS into Si_3N_4 and removal of the carbonaceous template. However, it leads to the formation of a monolith with a very poor robustness. As a consequence, we applied the third strategy which involves the use of both nitrogen and ammonia in the same heat treatment process. This leads to the best results in terms of SSA

($653.8 \text{ m}^2 \text{ g}^{-1}$), structural integrity and template removal. Such a SSA value is close to the values we got for ordered mesoporous PHPS-derived Si_3N_4 powders using CMK3 as a template¹². The system is first treated in flowing nitrogen up to $400 \text{ }^\circ\text{C}$ to ensure sufficient conversion of the preceramic polymer to a cross-linked state which has some structural stability and then the gas is changed to ammonia through a continuous pyrolysis up to $1000 \text{ }^\circ\text{C}$. A dwell time of 1 h at $400 \text{ }^\circ\text{C}$ is employed to switch the gas and a dwell time of 5 h is employed at $1000 \text{ }^\circ\text{C}$ for effective conversion and template removal. The pore architecture of the sample **mSi₃N₄410** by BET (micropores and mesopores scale) is discussed below based on the BET isotherms reported in Figure 5.8.

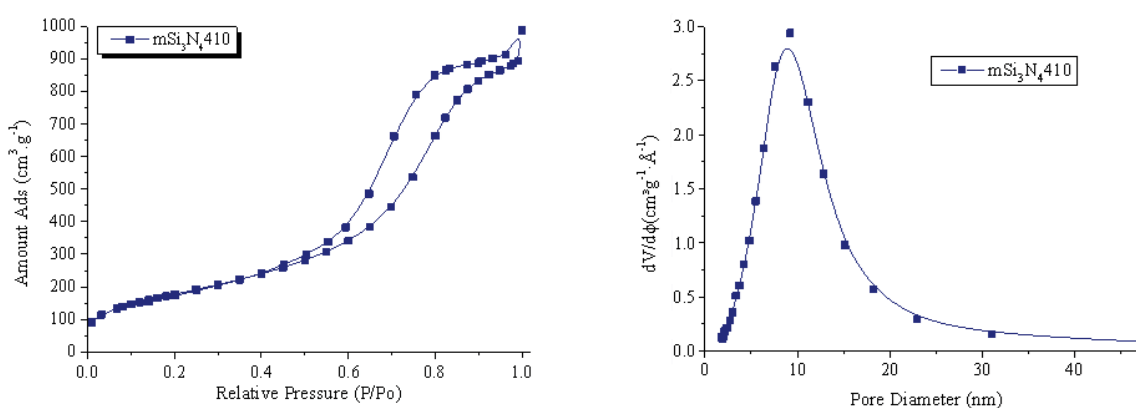


Figure 5.8 BET isotherm for the **mSi₃N₄410** sample and its PSD

The sample **mSi₃N₄410** demonstrates mesoporosity according to the nitrogen sorption isotherms (Fig. 5.8). Analysis of the isotherms allows identifying a IV type-curve typical for mesoporous adsorbents with distinct capillary condensation branches. The shape of the isotherms is asymmetrical with a desorption branch steeper than the adsorption branch at a relative pressure (P/P_0) from 0.4 to 0.9 indicative of H2 hysteresis loops.

It is observed that the sample **mSi₃N₄410**, which is X-ray amorphous is not stable though heat-treatments at temperatures higher than $1000 \text{ }^\circ\text{C}$ under nitrogen. Its specific surface area (as well as mesoporosity) falls drastically with the increased temperature. The reason for this is attributed to the formation of Si_3N_4 nanowires in the porosity starting from $1200 \text{ }^\circ\text{C}$ (Figure 5.9) while crystallization of $\alpha\text{-Si}_3\text{N}_4$ occurs.

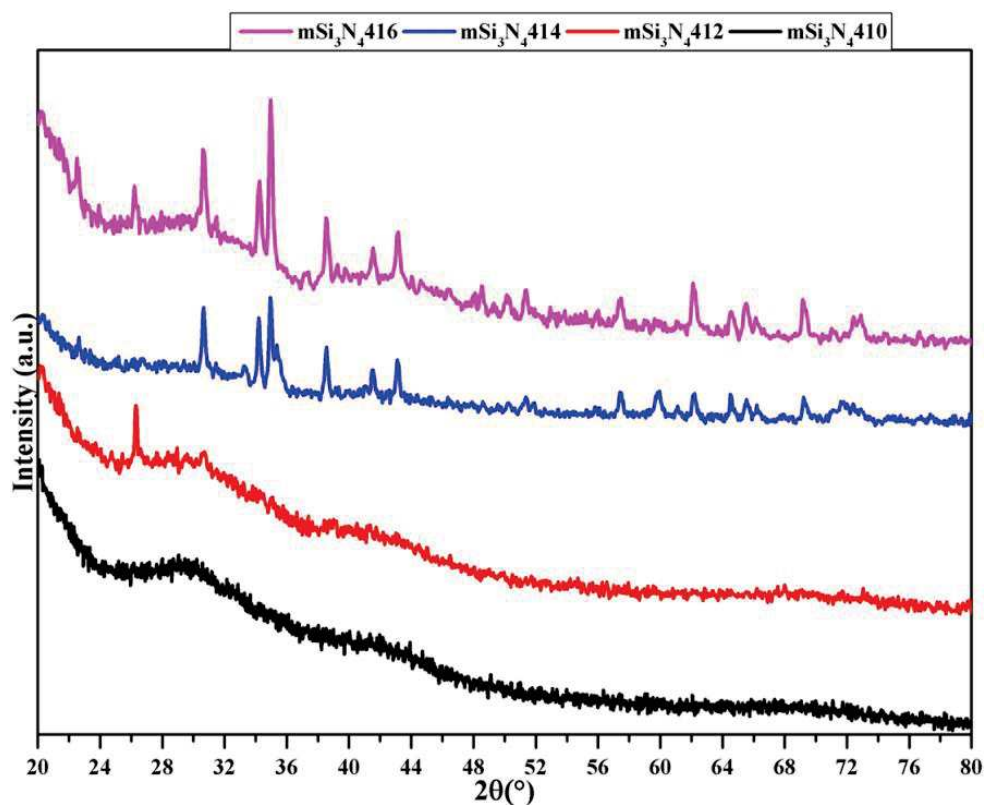


Figure 5.9 XRD patterns of mesoporous Si_3N_4 monoliths with temperature

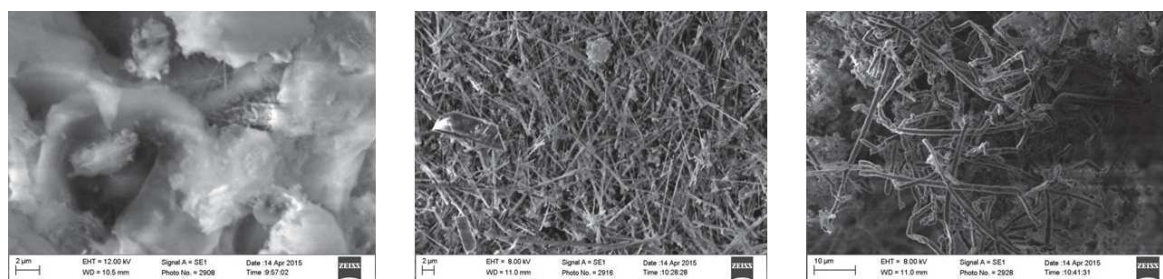


Figure 5.10 SEM image for $\text{mSi}_3\text{N}_4412$ to $\text{mSi}_3\text{N}_4416$ depicting the growth of nanowires

The formation of nanowires at these temperatures for silicon nitride made via polymer derived ceramic route has been well documented⁸. Hence for Si_3N_4 supports, the optimum specific surface area of $653.8 \text{ m}^2 \text{ g}^{-1}$ was obtained for the sample $\text{mSi}_3\text{N}_4410$.

2.2. Preparation of mesoporous BN monoliths

The design of mesoporous BN monoliths has been submitted for publication to *J. Mater. Chem. A* and was demonstrated in the PhD thesis of Chrystelle Salameh. Here, we briefly described the process and the main characterization of samples.

2.2.1 Synthesis strategy

We used polyborazylene (PB) (synthesized through thermolysis of borazine at 60°C in an autoclave) to produce the mesoporous 3D BN structures (Fig. 5.11).

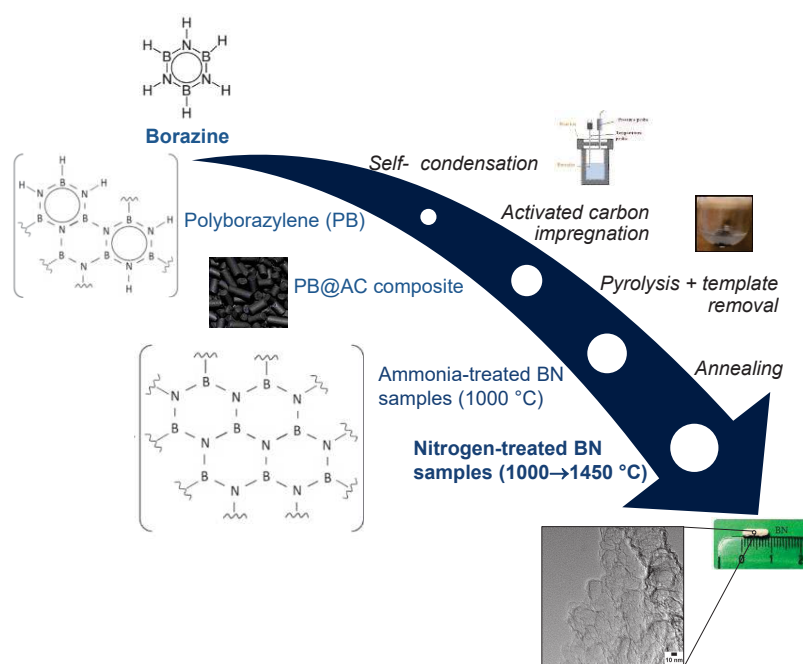


Figure 5.11 Synthesis of mesoporous 3D BN structures from polyborazylene

It has the nominal structure $[B_{3.0}N_{3.5}H_{4.5}O_{0.04}]_n$. In the present work, we have prepared a series of mesoporous samples in the temperature range 1000-1450 °C to tune the textural and structural properties. We labeled as-obtained samples mBNX (with X being the temperature), *i.e.*, **mBN1000**, **mBN1200** and **mBN1450**. Based on the different attempts, a polymer-to-template ratio, *i.e.*, a PB:AC ratio of 0.75, has been fixed during the impregnation step. It represents the minimal ratio to avoid the collapse of the structure of monoliths during the pyrolysis. Above this ratio, the monoliths display low SSA values. After 2 days of aging, washing and drying of the impregnated AC, a two-step pyrolysis allows transforming PB into BN while removing the template. An appropriate heat-treatment procedure consists in a pyrolysis under N₂ then under ammonia at 1000 °C (dwelling time of 5 h) delivering the

sample labeled **mBN1000**. Then the latter is annealed at different temperatures under N_2 up to 1450°C to generate the **mBN1450** sample. An intermediate sample labeled **mBN1200** has been isolated after annealing at 1200°C .

2.2.2 Characterization

All the BN samples discussed have an excellent cylinder-like appearance and replicate the monolithic shape of AC (Fig. 5.11). More interestingly, the samples did not reveal any shrinkage and retained the dimension of the template. We investigated Raman spectroscopy to provide information about the lattice vibration modes of the samples and to confirm that AC was removed during the ammonia treatment. The Raman spectrum of the **mBN1450** sample shows a signal at 1366 cm^{-1} which indicates the presence of BN (Fig. 5.12). The D and G peaks related to carbon are not identified indicating the complete removal of the carbon template.

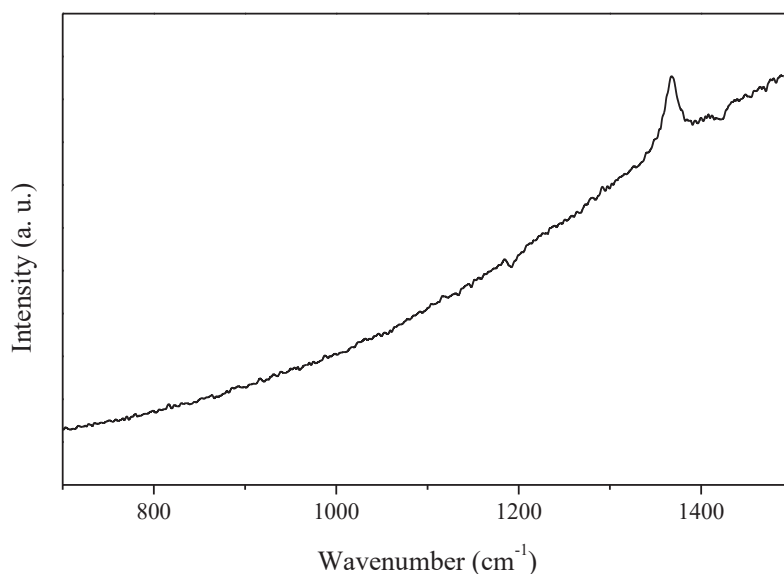


Figure 5.12 Raman spectrum of the mBN1450 sample

We used the semi-quantitative EDX to characterize the elemental composition of the BN samples. A nearly stoichiometric composition (42.5 at% (N) and 57.2 at% (B)) is confirmed with a neglected oxygen content (0.32 at%). We then characterized the **mBN1000**, **mBN1200** and **mBN1450** samples at mesoscopic length scale by N_2 physisorption measurements at 77K (Fig. 5.13).

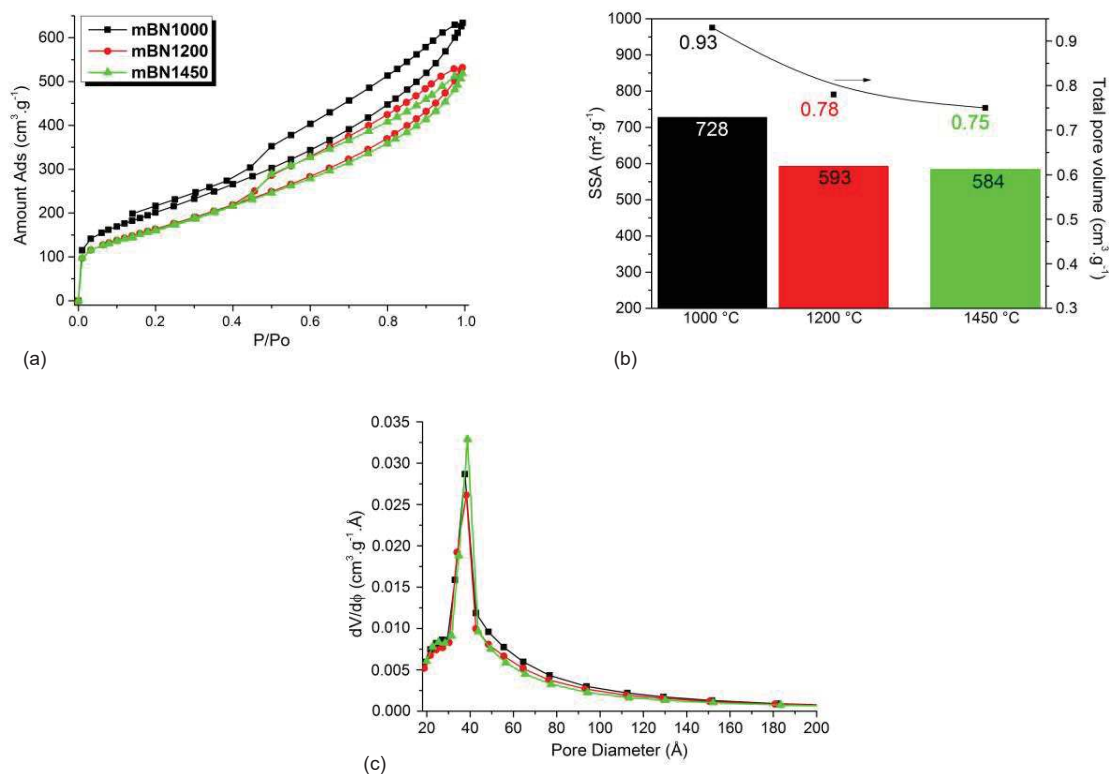


Figure 5.13 (a) N₂ adsorption-desorption isotherms with (b) evolution of the SSA and pore volume vs annealing temperature and (c) BJH pore diameter distribution curves at adsorption branch of **mBN1000**, **mBN1200** and **mBN1450** samples.

As expected, the structure of the monoliths as well as the pore dimensions may be tailored by the annealing temperature. This is not reflected through the shapes of the isotherms of the BN samples because they display similar isotherms that follow the typical behavior of type IV. This suggests that the samples have uniform mesoporous channels (Fig. 5.13 a). Above a relative pressure P/P_0 of 0.4-0.45 and up to 1, the distinct hysteresis loops observed between the adsorption and desorption curves confirm the presence of mesopores. It is identifiable to a H₂-type which is generally found in disordered porous materials or in ordered mesoporous material with 3-D cage-like pores and interconnected pores. Based on the structure of ACM, we can consider that the BN samples are disordered mesoporous materials bearing interconnected porosity which was targeted for an efficient nanoconfinement.

The BET SSA (Fig. 5.13 b) and the pore volume (less than 78.08 nm determined from the amount of nitrogen adsorbed at $P/P_0 = 0.975$) are very high. In particular, the pore volume changes from 0.93 (**mBN1000**) to 0.75 (**mBN1450**) cm³.g⁻¹ (Fig. 5.13 b). The SSA and pore volume values of the BN samples decrease with the increase of the temperature. We suggest

that the possible reasons are the crystallization of the BN phase from 1000 to 1450 °C concomitantly with the mesostructural/framework shrinkage of the materials accompanied by a decrease in the volume of the pores due to the high-temperature treatment. The samples exhibit uniform mesopore dimensions according to the N₂ desorption calculated from desorption branch by means of the *Barett-Joyner-Halenda* method (Fig. 5.13 c). The TEM images of the **mBN1000** and **mBN1450** samples are presented in Fig. 3 and well reflect the above discussion.

A high porosity level is particularly revealed by HRTEM and the local pore diameter matches the pore diameter calculated by the BJH method (See above). The low-magnification TEM (Figure 5.14 a) of the **mBN1000** sample confirms its porous character made of randomly distributed voids surrounded by a very thin wall. The corresponding SAED pattern which reveals diffuse haloes, as a general feature, has been indexed as the *P6₃/mmc* space group and suggests a poorly crystallized BN structure. HRTEM observations (Fig. 5.14 b) reveal the presence of BN layers with a lack of a long range ordering confirming that the structure is rather turbostratic (t-BN). The average number of layers in the walls is comprised between 5 and 10. The HRTEM investigations also confirm the locally high degree of porosity of the **mBN1450** sample (Fig. 5.14 c). However, a significant change in the crystallinity occurs. The **mBN1450** sample is made of strongly faceted nanopolyhedral shapes comprising highly crystalline BN layers (Fig. 5.14 d). The degree of crystallinity of the walls appears to be very high in contrast to the observations made by XRD. Figure 5.14d shows that there is a clear continuity between layers of adjacent facets even if locally a discontinuity in the walls and a mismatch within the wall structure can be encountered for this sample. The polyhedron wall thickness has been found to vary from 6 to more than 30 layers with an interlayer spacing found to be 0.34 ± 0.05 nm which is highly constant throughout the sample. The SAED pattern exhibits spots that indicate the formation of a highly crystalline structure presuming a well-ordered B and N-alternating hexagonal pattern belonging to the *P6₃/mmc* space group. Such a nanocrystalline quality made of highly crystallized hexagonal BN polyhedra is unusual for polymer-derived BN. The reason is difficult to explain but the use of activated carbon most probably promoted the crystallite growth of BN.

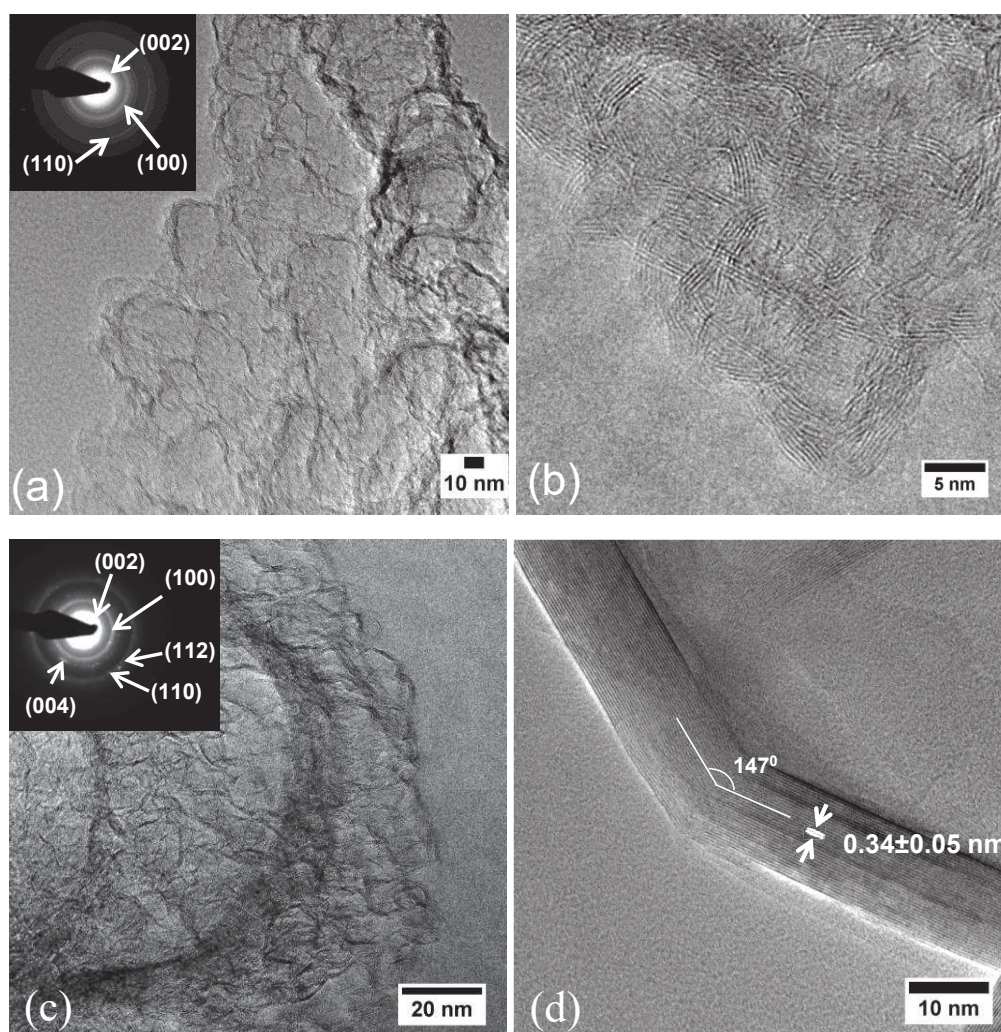


Figure 5.14 Low and high magnification HRTEM images with the SAED patterns as inset of the (a,b) **mBN1000** and (c,d) **mBN1450** samples.

A value of the helium density was found to be equal to 1.95 and 2.03 for **mBN1000** and **mBN1450** samples, respectively. This is relatively close to the theoretical value of 2.27. The bulk density determined through the ratio of the mass of the monolith samples and its total volume (ten replicate determinations was achieved for the determination of this property) was calculated to be 0.52 (**mBN1000**) and 0.57 (**mBN1450**) which indicate 73.3 and 71.9% of porosity, respectively. Interestingly, through this high porosity, mesoporous BN monoliths can be compressed. As an illustration, the **mBN1450** sample exhibits a load bearing capacity of the order of 14 N. The calculated values of the ultimate compressive stress are found to be 3.3 MPa which is around 6 times lower than the value found for AC. This is inherently due to the significantly higher porous volume found in the BN samples. However, such a value is the highest ever reported for a monolith of BN with high SSA and pore volumes.²³

2.3. Preparation of mesoporous Si-Ti-N monoliths

2.3.1. Synthesis strategy:

Mesoporous Si-Ti-N ceramics are prepared by impregnation of *ACM* with the **NCPTi2.5** (synthesized from PHPS) and **NCHTi2.5** (synthesized from HTT1800) polytitanosilazane sexperimentally described in chapter 2 and studied in chapter 4. The Si:Ti ratio of 2.5 is chosen for various reasons. As seen in chapter 3, the **NCPTi2.5** and **NCHTi2.5** samples are able to produce a nanocomposite at 1400°C where the matrix is still amorphous while the nanophase of TiN starts to crystallize out of the matrix. Any Si:Ti ratio greater than 2.5 does not lead to such a tailored microstructure at high temperature. Although a Si:Ti ratio 1 leads to highly stable amorphous matrix as shown in chapter 4; the viscosity of the polymer increases thereby making it more difficult to impregnate in activated carbon.

To prepare the mesoporous components, we applied the strategy used for mesoporous Si₃N₄ monoliths. The system is first treated in flowing nitrogen up to 400 °C to ensure sufficient conversion of the preceramic polymer to a cross-linked state which has some structural stability and then the gas is changed to ammonia through a continuous pyrolysis up to 1000 °C. A dwell time of 1 h at 400 °C is employed to switch the gas and a dwell time of 5 h is employed at 1000 °C for effective conversion and template removal.

2.3.2. Characterization:

2.3.2.1. PHPS-derived Si-Ti-N ceramics:

Figure 5.15 shows the evolution of BET isotherm with temperature for mesoporous Si-Ti-N ceramics prepared from NCPTi2.5 precursors (synthesized from PHPS) we label mNCPTi2.5-X (X being the two first numbers of the temperature: 10 for 1000°C).

We note that the samples display similar complex isotherms which represent a mixture of type IV and type II suggesting the presence of microporosity at lower relative pressures and mesoporosity at higher values of relative pressures with 3-D cage-like pores and interconnected pores being disordered¹⁶. Above a relative pressure P/P_0 of 0.45 and up to 1, the distinct hysteresis loops observed between the adsorption and desorption curves confirmed the presence of mesopores. It is identifiable to a type H2 which is generally found in disordered porous materials or in ordered mesoporous material with 3-D cage-like pores and interconnected pores. Based on the structure of AC, we can consider that the samples

are a micro-/mesoporous material bearing interconnected porosity which was targeted for an efficient use as a catalyst support.

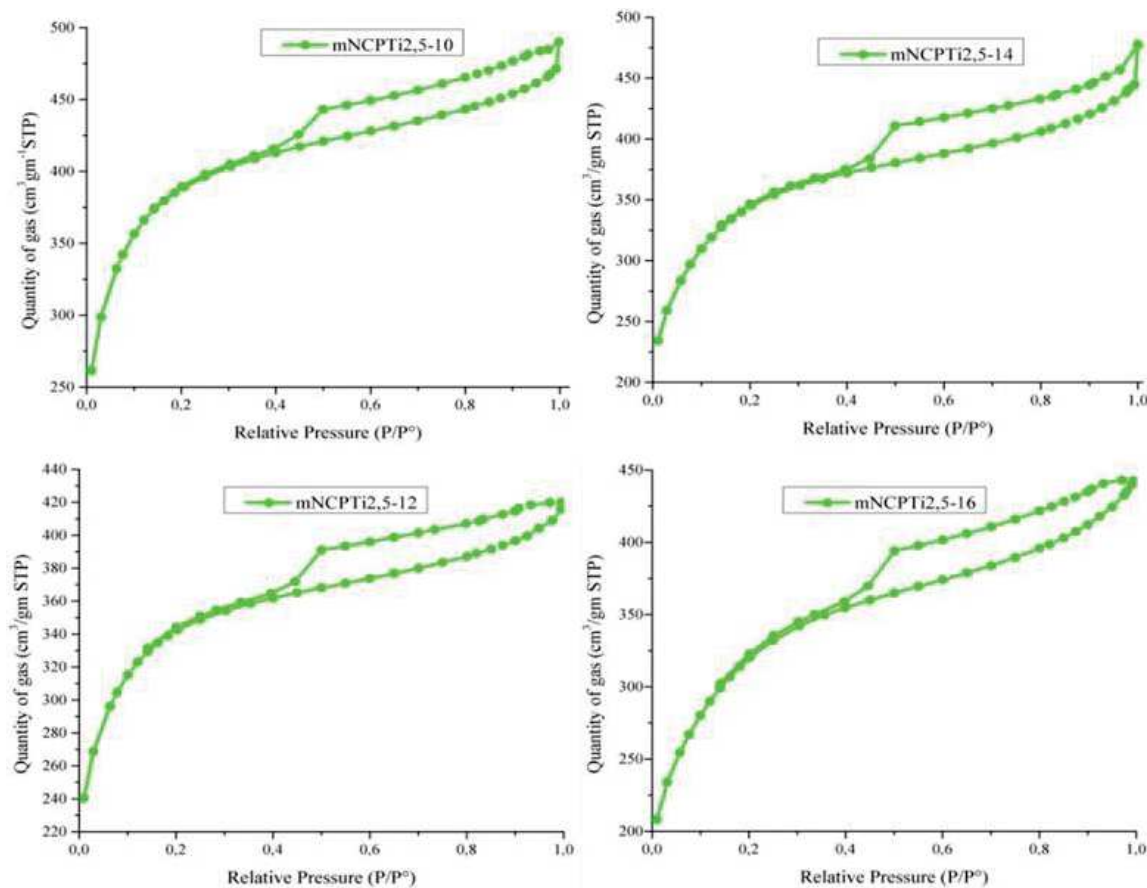


Figure 5.15 Evolution of BET isotherm for mNCPTi2.5-X samples with temperature

The Table 5.2 shows the SSA values along with the pore volume and pore size for monoliths. SSA values are very high for such compounds and are the highest values reported in the literature for mesoporous PDCs. Furthermore, there is no specific trend observed in the values but unlike previously reported for Si_3N_4 made using similar procedure there is no drop in the SSA values with the increased annealing temperature. To understand such high values, we investigated SEM and, although it is difficult to observe, it appeared that the template is still present in monoliths which means that the general procedure we applied for Si_3N_4 ceramics does not work with Si-Ti-N ceramics whereas the matrix precursor is the same, *i.e.*, PHPS. This means that the extremely high SSA of these samples are attributed to the retention of the template. In this case, the Si-Ti-N material forms a coating over the template and surrounds it preventing its decompositions. Because this phenomenon does not occur with mesoporous Si_3N_4 samples, we decided to prepare mesoporous TiN sample

using the same strategy from TDMAT (TiN precursor that has been used to react with matrix precursors, *i.e.*, PHTS and HTT1800 forming the polytitanosilazanes).

Table 5. 2 Evolution of SSA, pore volume and pore diameter for mNCPTi2.5 samples

Sample Name	SSA (m ² /g)	Pore volume (cm ³ .g ⁻¹)	Pore size (nm)
mNCPTi2.5-10	1345	0.72	3.4
mNCPTi2.5-12	1189	0.63	3.2
mNCPTi2.5-14	1217	0.67	3.3
mNCPTi2.5-16	1143	0.66	3.2

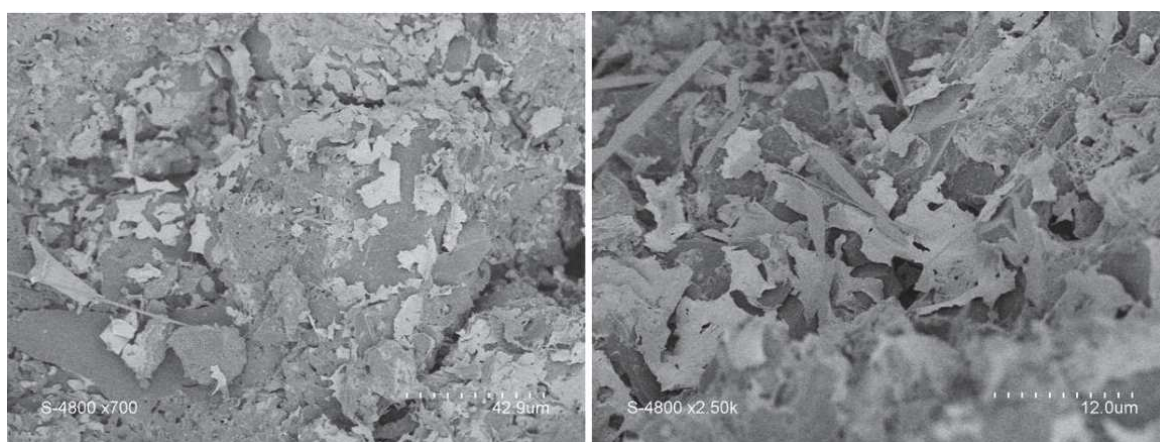


Figure 5. 16 Nanocomposite coating over activated carbon template

2.3.2.2. TDMAT-derived TiN:

As described before the monoliths were prepared using the same heat treatment as Si₃N₄ monoliths. The monoliths obtained after pyrolysis were black in color with a golden tinge on the surface. The pore architecture of the mesoporous TiN sample was assessed at the mesoscopic scale by nitrogen gas adsorption-desorption measurements at 77 °K. Figure 5.17 shows the BET isotherm for the TiN monoliths prepared at 1000°C and 1400 °C.

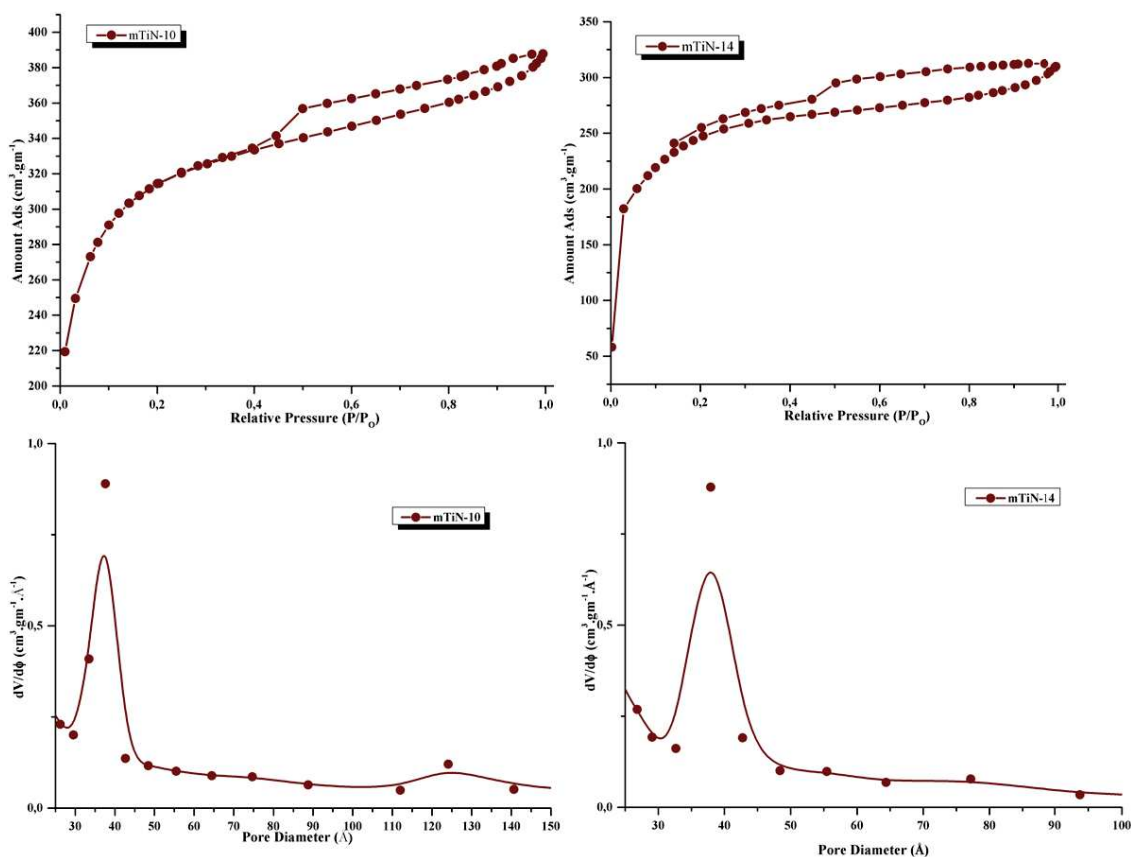


Figure 5. 17 BET isotherm and PSD for mesoporous TiN at 1000°C and 1400°C

The BET isotherm for TiN (Figure 5.17) prepared at 1000°C, i.e., **mTiN-10**, is a mixture of type II and type IV isotherms. At low pressures (below $P/P_0 = 0.4$) the curve represents type II isotherm indicating a presence of micropores in the system. While in the higher pressure regime it looks like type IV isotherm with H2 hysteresis suggesting the presence of disordered interconnected mesopores. The BET adsorption isotherm of the **mTiN-14** sample, although distorted with a thinner hysteresis, still retains its character as a mixture of type II and IV isotherms with H2 hysteresis. The SSA and pore volume for the former is found to be $1088 \text{ m}^2 \text{ g}^{-1}$ and $0.58 \text{ cm}^3 \text{ g}^{-1}$ while for the latter the SSA decreased to $872 \text{ m}^2 \text{ g}^{-1}$ and the pore volume to $0.46 \text{ cm}^3 \text{ g}^{-1}$. Values for SSA at 1000 °C exceed that of the activated carbon template by close to $100 \text{ m}^2 \text{ g}^{-1}$. The average pore diameter calculated using the desorption branch of BJH curve is found to be 3.33 nm in the **mTiN-10** sample and 3.8 nm in the **mTiN-14** sample. Therefore, the behaviour of the mesoporous TiN sample is close to that of the mesoporous Si-Ti-N ceramics and different from the mesoporous Si_3N_4 sample. We therefore suggest that TiN can act as a diffusion barrier for NH_3 , as it acts as a barrier for diffusion of metals^{19–22}. Thus it is possible that the initial treatment performed under N_2 during the preparation of TiN

and Si-Ti-N ceramics forms a coating over the surface of activated carbon to protect it from being eaten away by NH_3 . TGA of activated carbon under NH_3 revealed the beginning of mass loss to be above 500°C . This supports our hypothesis that the activated carbon is protected by a coating over it.

2.3.2.3. HTT1800-derived Si-Ti-N ceramics:

The adsorption–desorption isotherms of the Si-Ti-N ceramics prepared from NCHTi2.5 precursors (synthesized from HTT1800) we label mNCHTi2.5-X (X being the two first numbers of the temperature: 10 for 1000°C) are similar to mNCPTi2.5-X samples (Figure 5.18). The SSA value for the **mNCHTi2.5-10** sample is obtained to be $1326 \text{ m}^2\cdot\text{g}^{-1}$ with a pore volume of $0.69 \text{ cm}^3/\text{g}$. The pore size distribution (PSD) calculated from desorption branch by means of the *BJH* method gives an average pore diameter of 3.45 nm. Although there is a small drop in the SSA value in the **mNCHTi2.5-14** sample ($1028 \text{ m}^2\cdot\text{g}^{-1}$), the isotherm profiles still remain the same with mixture of types II and IV with H2 hysteresis and a similar pore size of 3.5 nm.

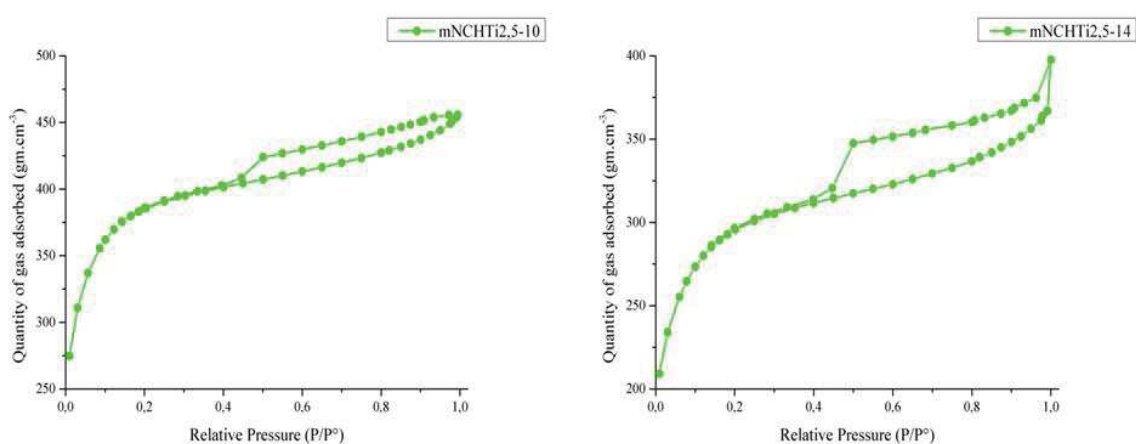


Figure 5.18 BET isotherm for mNCHTi2.5-X with temperature.

2.3. Preparation of mesoporous B-Ti-N monoliths

2.3.1. Synthesis strategy

The preparation of mesoporous components in the B-Ti-N system was only possible with polytitanoborazine synthesized from ammonia borane (AB). In particular, they have been prepared using the ABTi_3 precursor (synthesized from ammonia borane with a B:Ti ratio of 3). The BET isotherms (Figure 5.19) are similar to those of Si based nanocomposite. The SSA

and pore volume for the 1000°C and 1400 °C systems are 1326 m².g⁻¹, 0.7 cm³.g⁻¹ and 1028 m².g⁻¹, 0.55 cm³.g⁻¹, respectively. The nature of the porosity is same as the previous case, a complex mix of type IV and type II isotherms representing microporosity at low pressure (P/P₀<0.45) and mesoporosity at high pressures (P/P₀>0.45) with a H2 type hysteresis curve suggesting interconnected porosity, and the retention of the activated carbon template can be attributed to the presence of titanium nitride in the system. The evolution is studied only till 1400°C as BN matrix is known to crystallize at 1450°C and we prefer a system with an amorphous matrix and crystallizing nanophase. Such a system is preferred since the amorphous matrix protects the metal nitride nanocrystal and hinders grain growth. These metal nitride nanocrystals are known to exhibit interesting catalytic and photocatalytic properties at such low sizes²³ as discussed in chapter 1.

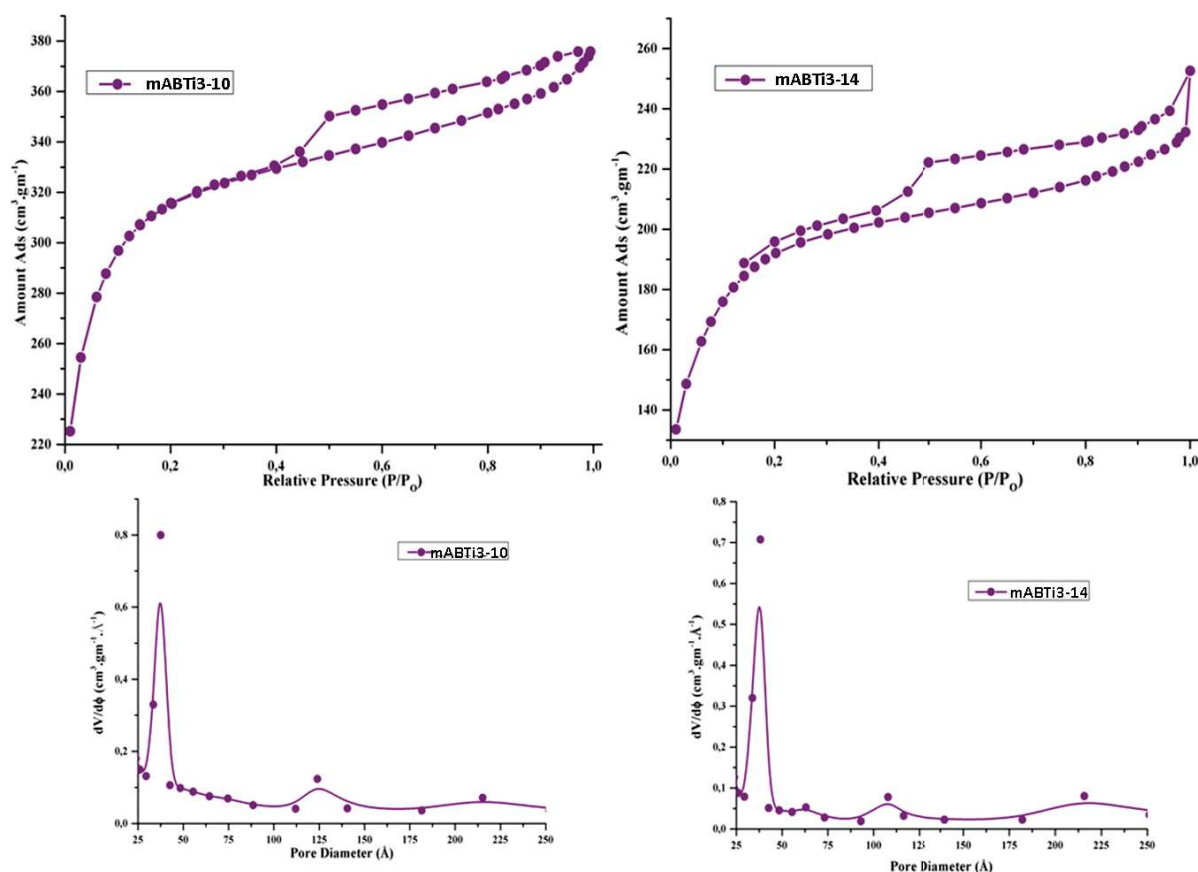


Figure 5.19 BET isotherm and PSD for mABTi3 at 1000°C and 1400°C

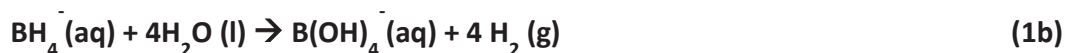
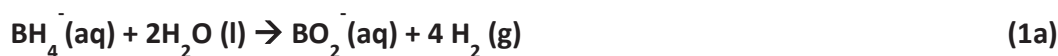
As-obtained high SSA and pore volume mesoporous samples have been used as platform to grow catalytically-active platinum nanoparticles (NPs). Then, to assess the catalytic activity

of the Pt-supported mesoporous samples, these systems are tested for hydrolysis of NaBH₄ to generate hydrogen in aqueous medium; the performances have been finally compared.

3. Design of Pt-supported mesoporous Components-Catalytic application

Catalytic activity of metal nanoparticles is dependent on their shape, size, crystal structure and textural parameters. Furthermore, it can be suitably increased by selecting a support system on which nanoparticles are preferentially synthesized with tailored shapes, sizes and crystalline structure without agglomeration. Because the transport of materials to active sites of catalyst is controlled by diffusion through the pores of the support system²⁴, the support is expected to be prepared with tunable pore morphologies, accessible porosity²⁵. In particular, the high specific surface area (SSA) of mesopores in the samples prepared in the previous part should provide selectivity and active sites to be effectively accessed for catalysis.

Pt NPs are deposited on mesoporous samples using hexahydrated chloroplatinic acid as Pt precursor by wet impregnation followed by chemical reduction in hydrogen/argon flow (*See experimental part in chapter 2*). The attractiveness of a supported catalyst lies in the low amount of Pt loaded. We supported 1 wt% of Pt only. The successful loading of Pt on the supports has been verified by BET and ICP/EDXS. The activity of Pt-supported mesoporous samples for the hydrolysis of sodium borohydride is investigated at 80 °C, in a very alkaline solution (pH > 10; 2% NaOH), and with the presence of water (1 mL such as 1 mol NaBH₄ for 17.5 mol H₂O; water excess of 438%) according to Eq. (1a and 1b).



By hydrolysis, molecular hydrogen is spontaneously released by reaction of one hydridic hydrogen (H^{δ-}) of NaBH₄ with one protic hydrogen (H^{δ+}) of H₂O, which thus provides half of the H₂ generated. The volume of hydrogen generated during the synthesis is calculated. The by-product, sodium tetrahydroxyborate, may be recycled back into NaBH₄ *via* a complex process but this is not the subject of the present study. The imposed conditions are considered as being harsh for any catalyst support. It should be mentioned that we synthesized a Pt-supported activated carbon monoliths for comparing the performance of the mesoporous

samples we prepared in the first part of the present chapter. However, the mesoporous BN and B-Ti-N samples have been no longer investigated because their performance as catalytic support was poor. In the following section, we firstly describe the preparation, characterization and catalytic activity of Pt-supported SiC, Si-C-N and Si₃N₄ samples before investigating Pt-supported Si-Ti-N samples.

3.1. Catalytic activity of Pt-supported SiC, Si-C-N and Si₃N₄ samples

3.1.1. Pt impregnation

Based on the previous results and discussion, the samples **mSiC12**, **mSi-C-N12**, **mSi₃N₄410** have been selected according to their high BET SSA values, large pore volume and tailored mesoporous structure. These characteristics are positive features for the growth of Pt NPs which is investigated in the following section of this paper. Pt NPs are deposited on **mSiC12**, **mSi-C-N12** and **mSi₃N₄410** to form nanocatalysts labelled **Pt-mSiC12**, **Pt-mSi-C-N12** and **Pt-mSi₃N₄410**. These materials are used to catalytically activate the hydrolysis of NaBH₄. The successful loading of Pt on the supports has been verified by BET (Figure 5.20) and EDXS.

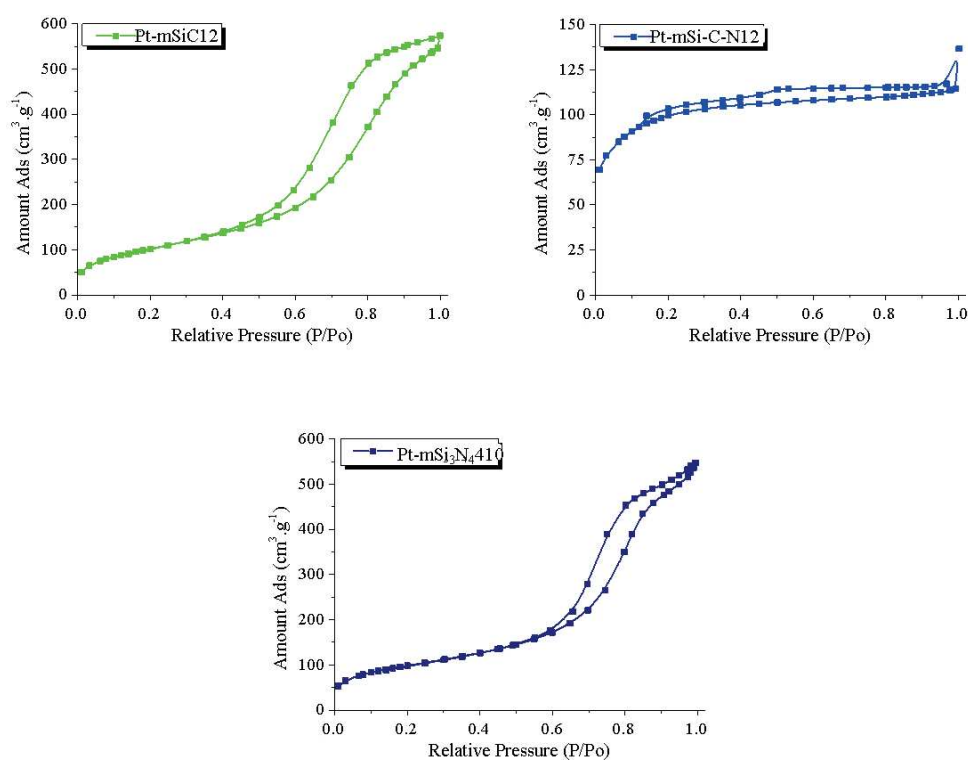


Figure 5.20 Evolution of BET adsorption isotherms for Pt/mSiC12, Pt/mSi-C-N12 and Pt/mSi₃N₄410.

As mentioned previously, we targeted 1 wt% of Pt. This was confirmed by EDXS: EDXS spectroscopy indicates the presence of 1.54 wt%, 1.79 wt% and 1.12 wt% for Pt-mSiC12, Pt-mSi-C-N12 and Pt-mSi₃N₄410, respectively. Since the loading content is low, it is necessary to continuously ultra-sonicate the solution containing the platinum salt and the support system for 24 h. The heat treatment of the supported samples under hydrogen to reduce the palatinate to metallic platinum is done at 450 °C²⁶. The process does not affect the structural stability in any way and allows keeping the mesoporosity of the support with a decrease of the SSA values as shown in Figure 5.20 and Table 5.3.

Table 5. 3 SSA values of samples Pt-mSiC12, Pt-mSi-C-N12 and Pt-mSi₃N₄410.

Samples	SSA (m ² g ⁻¹)	
	Before impregnation	After impregnation
mSiC12	581.4	378.2
mSi-C-N12	623.7	347.8
mSi ₃ N ₄ 410	653.8	357.7

After Pt growth, the shape of the isotherms and the hysteresis loop of the **Pt-mSiC12**, **Pt-mSi-C-N12** and **Pt-mSi₃N₄410** samples are similar to the isotherms of the parent **mSiC12**, **mSi-C-N12** and **mSi₃N₄410**. It can be observed that growth of Pt NPs decreases the SSA to reach values that are close for all the samples as indicated in Table 5.3. This suggests the encapsulation of NPs inside the pore channels. However, the relatively high SSA value after Pt impregnation further proves that the pores of the support are not blocked by nanoparticles larger than the pore size of the support, revealing that the **mSiC12**, **mSi-C-N12** and **mSi₃N₄410** samples hinder the agglomeration or migration of the nanoparticles. This is also fundamental to allow diffusion of borates through the porosity during hydrolysis of NaBH₄.

3.1.2. Hydrolysis of NaBH₄

The activity of **Pt-mSiC12**, **Pt-mSi-C-N12** and **Pt-mSi₃N₄410** for the hydrolysis of sodium borohydride is investigated at 80 °C, in a very alkaline solution (pH > 10), and with the presence of water. The hydrogen generation results are presented in Figure 5.21. It should be mentioned that we synthesized a Pt-supported activated carbon monoliths labelled **Pt-ACM** through the same process we applied to prepare **Pt-mSiC12**, **Pt-mSi-C-N12** and **Pt-mSi₃N₄410**.

Figure 5.21 demonstrated the highest performance obtained with the **Pt-mSi₃N₄410** sample. A hydrogen generation rate (slope of the curves at a conversion < 50 %) of 4.3 mL min⁻¹ was measured. Expressed per gram of Pt, the rate is as high as 24.2 L min⁻¹ g_{Pt}⁻¹ which is the maximum value reported in the literature²⁻³. The hydrolysis starts immediately; no induction period is observed, which is in agreement with the metallic state of Pt. This is also the case for the **Pt-mSiC12** and **Pt-mSi-C-N12** samples but the hydrogen evolution rate is significantly lower: at 50 % conversion, 2.016 mL min⁻¹ and 0.68 mL min⁻¹ are measured for the **Pt-mSiC12** and **Pt-mSi-C-N12** samples, respectively. The results obtained with the **Pt-ACM** sample is comparable to those obtained with the **Pt-mSiC12** and **Pt-mSi-C-N12** samples. During the first minutes, hydrogen release is fast because **ACM** is well known to contain acid groups available on the surface which can contribute to the generation of hydrogen. However, this fast step is rapidly followed by a process with slow kinetics most probably due to absorption of water that affects the diffusion of the anions BH₄⁻ and B(OH)₄⁻.

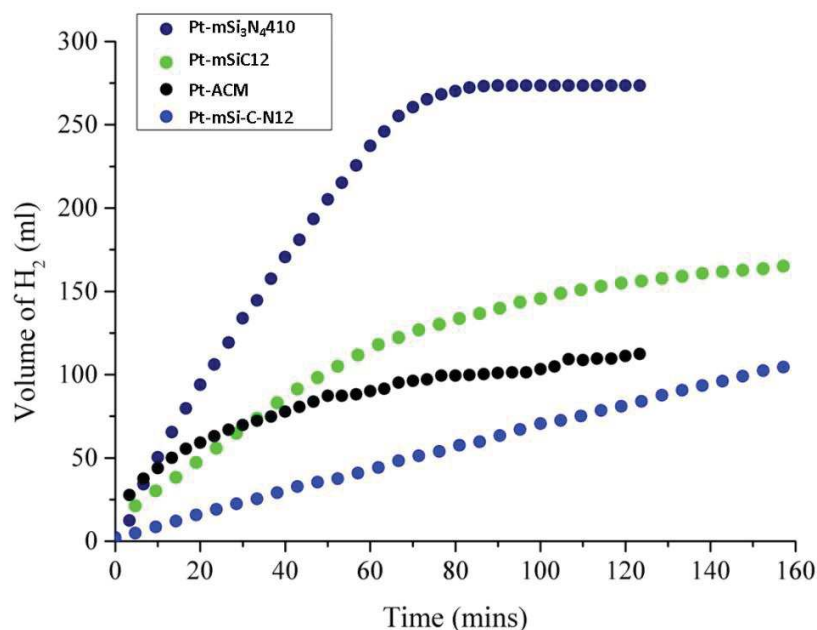


Figure 5.21 Volume of hydrogen measured after 150 min during hydrolysis of sodium borohydride at 80 °C, in a very alkaline solution (pH > 10), and in the presence of **Pt-mSiC12**, **Pt-mSi-C-N12**, **Pt-mSi₃N₄410** and **Pt-ACM**

Whereas the SSA of the **Pt-mSiC12**, **Pt-mSi-C-N12** and **Pt-mSi₃N₄410** samples are close, we may suggest that silicon-based nitride ceramics are the most appropriate candidates to be used as supports of platinum for the hydrolysis of an alkaline solution of sodium borohydride. This can be due to the interactions with the adsorbed reacting species. Theoretical and computational investigations should make tremendous advances in the understanding of the interest to use silicon nitride as catalytic supports. Further works are under investigation to study the beneficial effect of silicon nitride on the catalytic activity of Pt in comparison to other Si-based supports. Because it displays the highest performance, the microstructure and composition of the **Pt-mSi₃N₄410** sample has been analyzed by elemental mapping and TEM (Figure 5.22a-b), EDXS and elemental mapping (Figure 5.22 c-g).

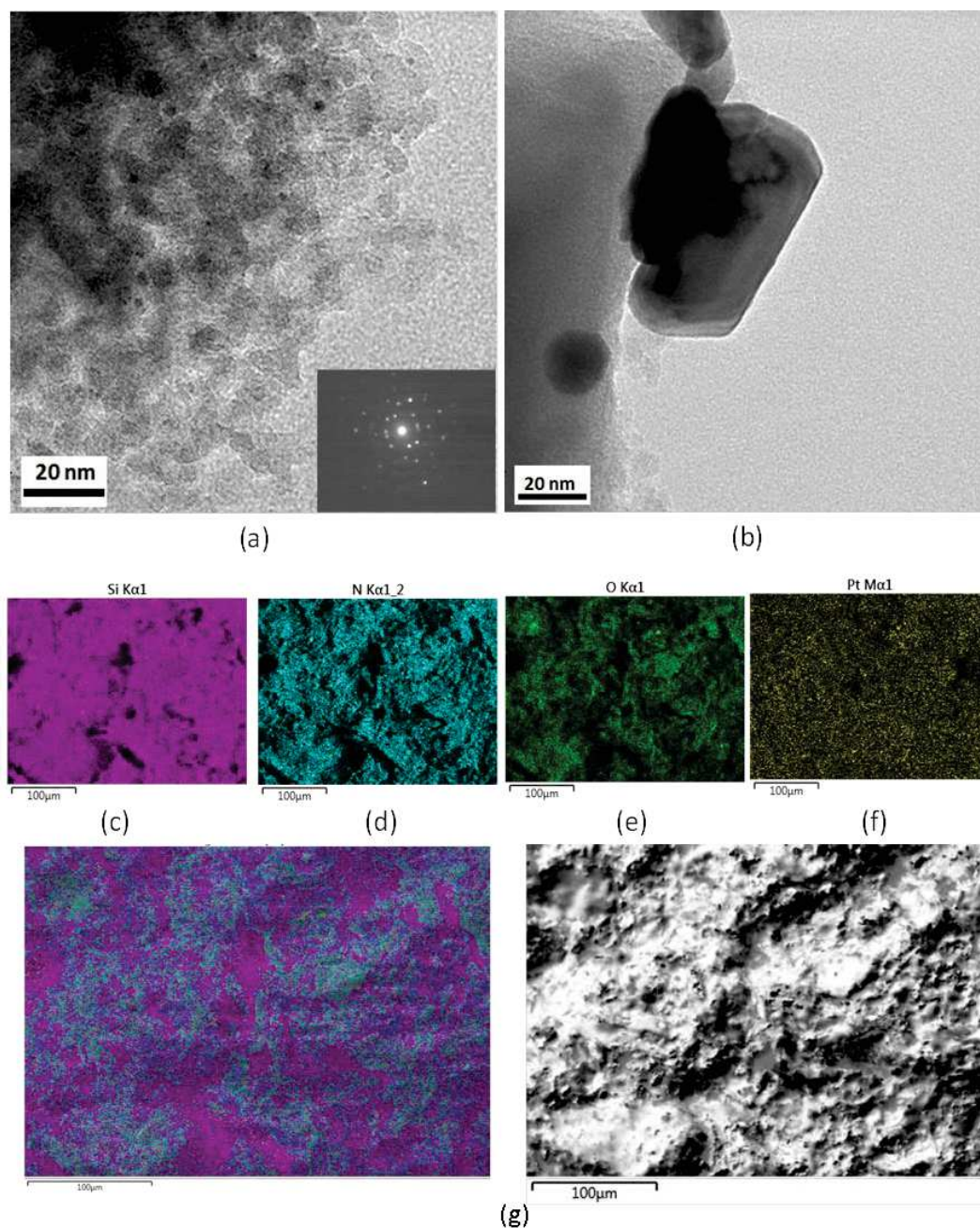


Figure 5.22 (a-b) TEM images and (c-g) elemental mapping of the Pt- $m\text{Si}_3\text{N}_4410$ sample.

The $m\text{Si}_3\text{N}_4410$ sample exhibits a mesoporosity with a lack of ordering as expected. It does not show any crystallinity in the Selected Area Electron Diffraction (SAED) pattern (not shown) confirming its amorphous structure as previously observed by XRD. After Pt growth (Figure 18a), HRTEM investigation allows observing Pt NPs with a spherical shape and we clearly observe their homogeneous distribution on the surface of the $m\text{Si}_3\text{N}_4410$ sample forming the Pt- $m\text{Si}_3\text{N}_4410$ sample. We observe spots belonging to Pt, which crystallizes in

the fcc system (Figure 5.22a). Figure 5.22b shows that a few ones tend to be agglomerated. Then cross-sections have been prepared by using a focused ion beam unit, and EDXS maps were superimposed on the cross-sectional images (Figure 5.22g). Elemental mapping (Figure 5.22c-f) reveals the uniform distribution of silicon and nitrogen from the support as well as Pt on **Pt-mSi₃N₄10**. The sample **mSi₃N₄10** displays a typical chemical formula determined by Energy Dispersive X-ray Spectroscopy (EDXS) of Si_{3.0}O_{0.8}N_{4.1}. The relatively low O content level is mainly associated with physisorbed/chemisorbed water from the internal and external surface of the samples.

However, we should point to the fact the hydrogen production under the reaction conditions we imposed was very vigorous. The **Pt-mSi₃N₄10** sample collapsed after reaction and in fact, none of the three catalyst support systems were able to withstand the vigorous bubbling of hydrogen and collapsed after reaction. The **Pt-mSiC12** and **Pt-mSi-C-N12** samples (which survived the platinum impregnation) collapsed into coarse powders which mostly settled at the bottom of the reaction chamber even with stirring. In contrast, the **Pt-mSi₃N₄10** sample formed a suspension with stirring and was stable for a long time even after the stirring was stopped.

Although all materials collapsed after reaction, the performance of the **Pt-mSi₃N₄10** sample is significantly superior to platinum-supported silicon carbide and carbonitride confirming the interest of nitride for heterogeneous catalysis. Indeed, nitrides as catalytic supports (or even as co-catalysts) are an exciting and vibrant field with a number of significant advances reported recently. In terms of catalysis, it is clear that nanostructuration is an important aspect. Furthermore, surface area considerations play a key role. Finally, the design of multi-element-containing nitrides displaying synergetic effects with the metal catalyst is one of the best strategies to optimize the catalytic properties we present in the following section.

3.2. Catalytic activity of Pt-supported Si-Ti-N samples

In the previous section we demonstrated the superior performance of silicon nitride over carbonitride and carbide counterparts. As mentioned in the introduction, we focus on the Si-Ti-N system because of the presence of TiN that can act as a co-catalyst in some reactions, reducing the required quantity of Pt.

3.2.1. Pt impregnation

The change in the pore architecture of the Pt-supported Si-Ti-N samples including those prepared from NCPTi2.5 precursors (synthesized from PHPS) labelled Pt-mNCPTi2.5-X (X being the two first numbers of the temperature: 10 for 1000°C) and from NCHTi2.5 precursors (synthesized from HTT1800) labeled Pt-mNCHTi2.5-X (X being the two first numbers of the temperature: 10 for 1000°C) has been assessed at the mesoscopic scale by nitrogen gas adsorption-desorption measurements at 77 °K. Figure 5.23 and 5.24 show the BET isotherms of **Pt-mNCPTi2.5-10**, **Pt-mNCPTi2.5-14**, **Pt-mNCPTi2.5-16**, **Pt-mNCHTi2.5-10** and **Pt-mNCHTi2.5-14**. The isotherms retain the types II and IV with a H2 hysteresis.

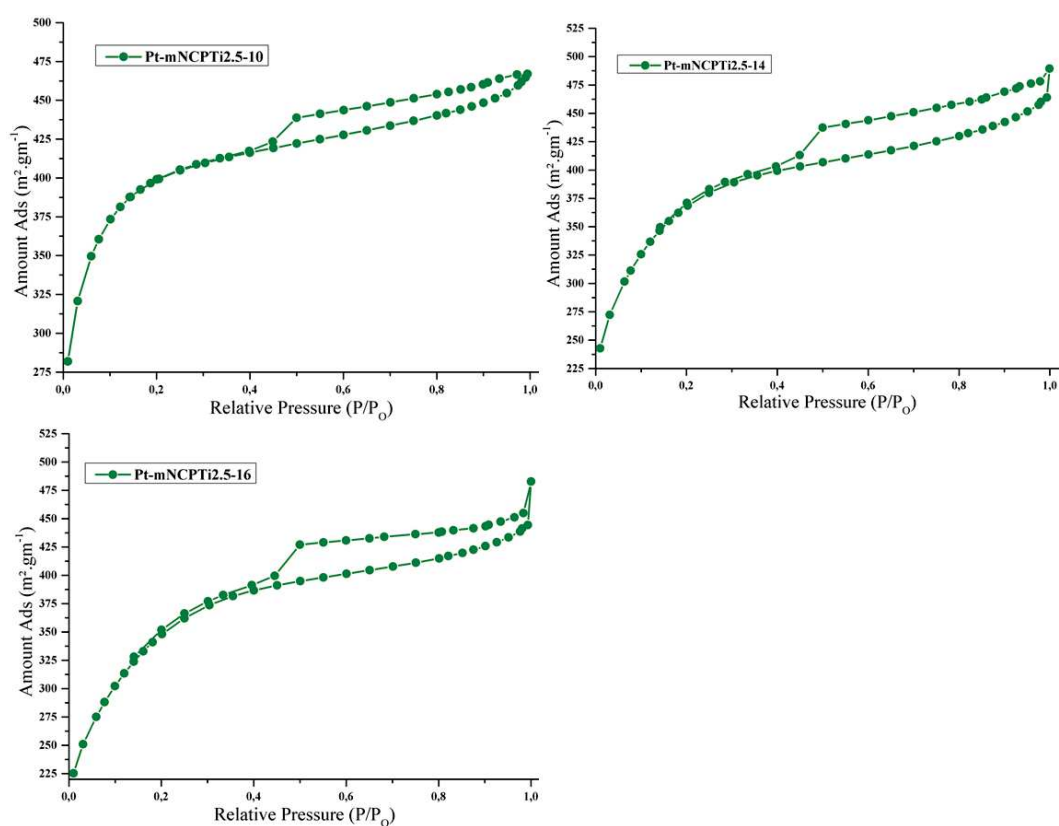


Figure 5. 23 BET isotherm of Pt-mNCPTi2.5-X samples with temperature

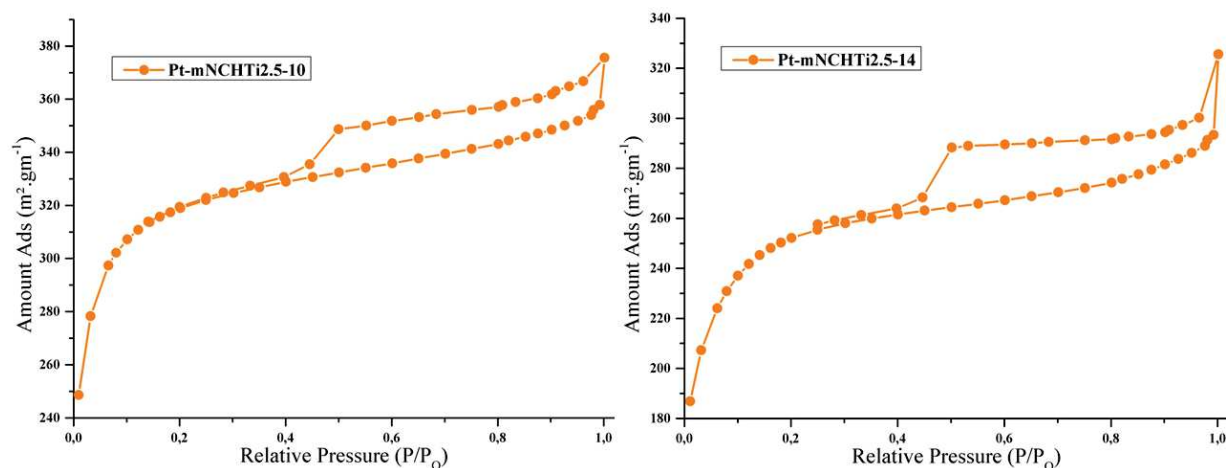


Figure 5.24 BET isotherm of Pt-mNCHTi2.5-X samples.

There is no clear trend for SSA values after Pt deposition. The amount of Platinum deposited on the monoliths was determined by performing area scan in EDX on the various regions both on the surface and the cross section and averaging out the values. The table shows the values obtained. For all cases the values obtained are close to the intended 1 wt% deposition.

Table 5. 4 SSA values of nanocomposite samples after Pt loading

Sample Name	Specific Surface Area (m ² /g) After Pt	Pt loading on monolith (wt %)
mNCPTi2.5-10	1098	1.07
mNCPTi2.5-14	1307	0.91
mNCPTi2.5-16	1247	1.2
mNCHTi2.5-10	1019	2.38
mNCHTi2.5-14	1169	2.73

3.2.2. Hydrolysis of NaBH₄

The hydrogen generation results are shown in Figure 5.25. The figure shows hydrolysis curve obtained for the Pt-supported Si-Ti-N materials prepared from NCPTi2.5 precursors (synthesized from PHPS) labelled Pt-mNCPTi2.5-X (X being the two first numbers of the temperature: 10 for 1000°C) and from NCHTi2.5 precursors (synthesized from HTT1800) labeled Pt-mNCHTi2.5-X (X being the two first numbers of the temperature: 10 for 1000°C).

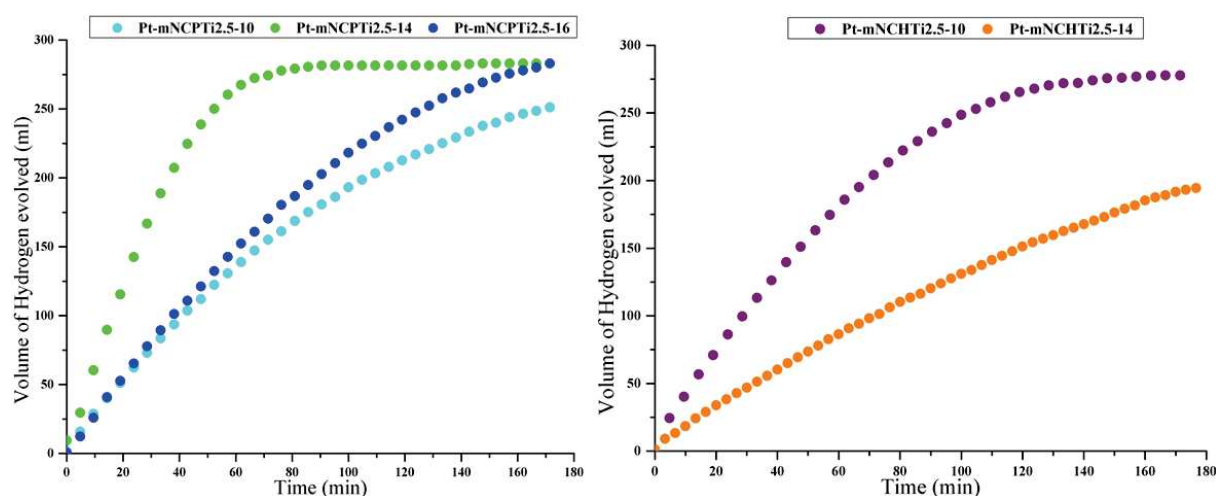


Figure 5.25 Volume of hydrogen measured after 180 min during hydrolysis of NaBH_4 using Pt-mNCPTi2.5-10, Pt-mNCPTi2.5-14, Pt-mNCPTi2.5-16, Pt-mNCHTi2.5-10 and Pt-mNCHTi2.5-14

Although the Si-Ti-N system is the same, the catalytic activity is different between Pt-mNCPTi2.5-X and Pt-mNCHTi2.5-X (X being the two first numbers of the temperature: 10 for 1000°C) samples. This proves that the chemistry of the precursor has a strong impact on the properties of the derived ceramics. In these cases, along with total amount of hydrogen released from the given fuel, the rate of hydrogen generation per gram of platinum used is also important. It is observed that the system labelled **Pt-mNCPTi2.5-14** has the highest rate with a value of $39.3 \text{ L}\cdot\text{min}^{-1}\cdot\text{g}_{\text{Pt}}^{-1}$. This reported rate is the highest for low noble metal content catalyst systems reported in the literature^{12,27}. Table 5.5 shows the hydrogen evolution rate calculated from other samples.

Table 5. 5 Rate of hydrolysis of NaBH₄ with different nanocomposite catalyst systems

Sample Name	Rate of H ₂ production (L.min ⁻¹ .g _{Pt} ⁻¹)
mNCPTi2.5-10	14.85
mNCPTi2.5-14	39.3
mNCPTi2.5-16	14.35
mNCHTi2.5-10	8.28
mNCHTi2.5-14	3.26

This **Pt-mNCPTi2.5-14** sample has a significantly better performance than the previously reported Pt supported-mesoporous Si₃N₄ monoliths studied in the previous section, *i.e.*, the **Pt-mSi₃N₄410** sample. In addition, the **Pt-mNCPTi2.5-14** sample solves the problem of structural integrity of the **Pt-mSi₃N₄410** sample which collapses during hydrolysis. This higher structural stability can be attributed to the presence of the activated carbon monolith. To understand the reasons for the different the catalytic behaviors between the Pt-mNCPTi2.5-X and Pt-mNCHTi2.5-X (X being the two first numbers of the temperature: 10 for 1000°C) samples, we compare their X-ray diffraction pattern. We already mentioned the effect of the chemistry of the precursor on the crystallization behavior of nanocomposites in chapter 3. Here, the figure 5.26 compares the **NCPTi2.5-10** and **NCPTi2.5-14** samples to **NCHTi2.5-10** and **NCHTi2.5-14** samples as mesoporous components.

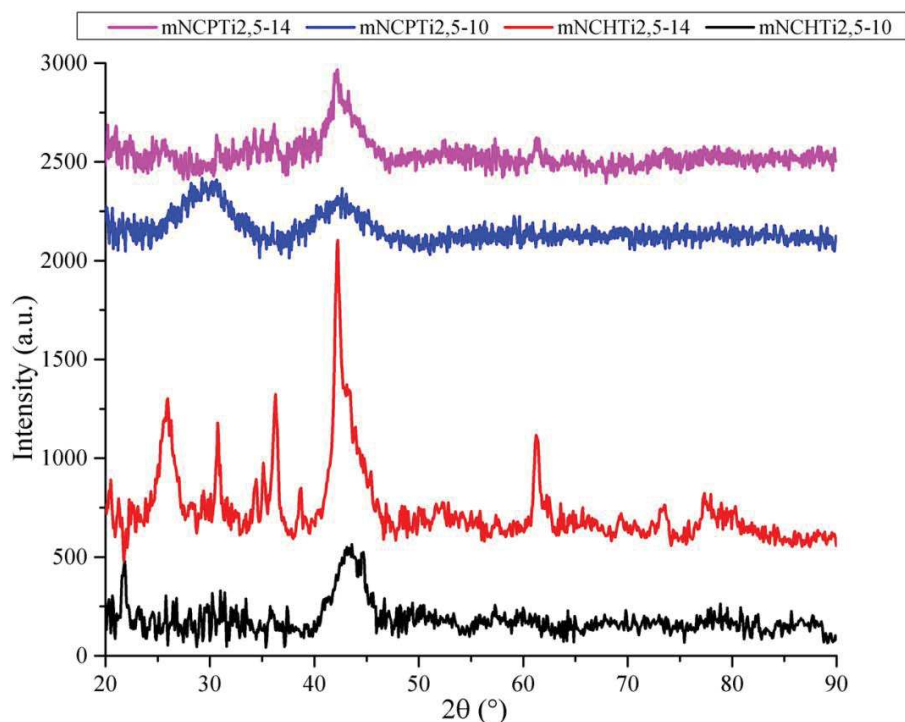


Figure 5. 26 X-ray diffractogram for mesoporous nanocomposite systems

The difference between both systems arises in the crystallization of the matrix phase. The Si_3N_4 matrix has started to crystallize along with TiN nanocrystals in the **NCHTi2.5-14** samples whereas it remains amorphous in the **NCPTi2.5-14** sample. Furthermore, the extent of crystallization of TiN nanocrystals is lower in the **NCPTi2.5-14** sample. The extent of crystallization of TiN in mesoporous monoliths is different from that in powders for the same system at the same temperature. This can be attributed to the porous nature of the system and the activated carbon template acting as a heat sink²⁸. The heat sink drains more heat from the nanocomposite layer thereby delaying the crystallization whereas the porous structure decreases the thermal conductivity of the overall system hence the heat transfer is lowered. Also this can be due to different pyrolysis procedure applied in both cases during the polymer to ceramic conversion. The amorphous structure formed in both cases can be different leading to different crystallization behavior.

To understand the catalytic behavior of the **Pt-NCPTi2.5-14** sample, we investigated the catalytic activity of mesoporous TiN samples prepared previously but after Pt deposition, *i.e.*, **Pt-mTiN10** (prepared at 1000°C) and **Pt-mTiN14** (prepared at 1400°C) and compared in the sample graph (Fig. 5.27), the volume of hydrogen evolved per gram of Pt for the **Pt-NCPTi2.5-14**, **Pt-mSi₃N₄410**, **Pt-mTiN10** and **Pt-mTiN14** samples.

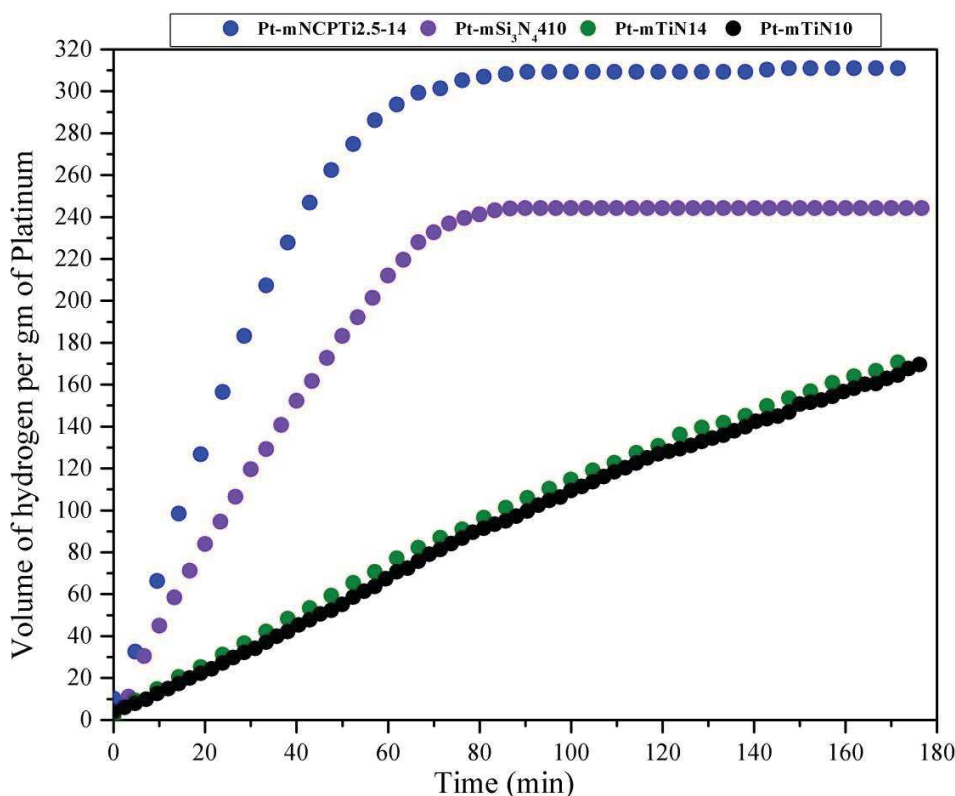


Figure 5.27 Comparison of hydrolysis behavior of Pt loaded mNCPTi2.5-14, mSi₃N₄410, mTiN14 and mTiN10

Upon comparing the hydrolysis behavior of all these systems we observe that both **Pt-mTiN10** and **Pt-mTiN14** have the lowest (and nearly similar) amount of hydrogen evolved per gram of platinum nanoparticles deposited. While the nanocomposite system has the highest value for the same and **Pt-mSi₃N₄410** lies between the two. In the two mesoporous TiN monoliths, the TiN crystals are not nanostructured (<10 nm) as in case of the nanocomposite system. The crystallite size differs by an order of magnitude in both cases. This Nano structuration of TiN in an amorphous Si₃N₄ matrix seems to be a crucial factor which leads to the nanocomposite acting as co-catalyst in the presence of Pt. For the synergistic effect between Pt and TiN to occur the particle size of both should be less than 10 nm²⁹⁻³¹. In case of the **Pt-mTiN14** sample the calculated average crystallite size using scherrer equation was 17 nm and for deposited Pt nanoparticles was 8 nm. While for **Pt-mNCPTi2.5-14** the TiN crystallite size was calculated to be around 3.8 nm and the Pt nanoparticles were calculated to be in the range of 6-8 nm.

Then, we investigated the same samples without Pt (Fig. 5.28).

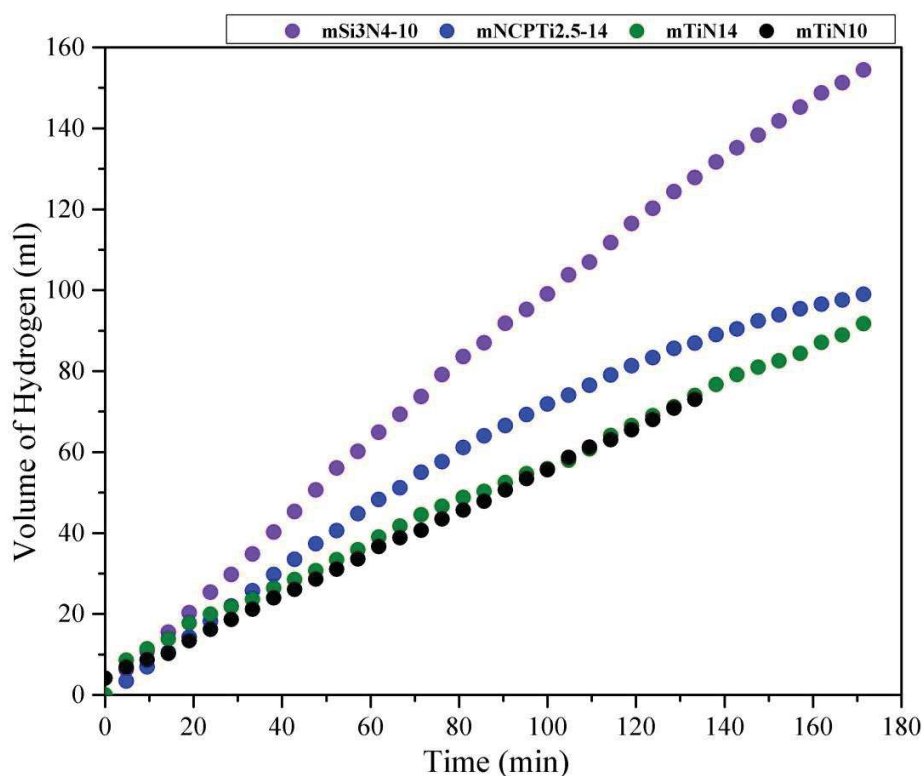


Figure 5. 28 Comparison of hydrolysis behavior of Pt free **mNCPTi_{2.5}-14**, **mSi₃N₄410**, **mTiN₁₄** and **mTiN₁₀**

For samples without Pt, **mSi₃N₄410** has the highest activity in hydrolyzing NaBH₄ among all investigated systems suggesting a catalytic nature to this nitride. Surprisingly **mNCPTi_{2.5}-14**, which has the highest rate of hydrolysis in presence of Pt, shows lower catalytic activity. This suggests that we need some amount of Pt in the Si-Ti-N system so that the nanocomposite can act as a co-catalyst. The catalytic activity of **mTiN₁₄** and **mTiN₁₀** alone is the lowest. The reason for this can be absence of nanoscale TiN in these monoliths. In case of the nanocomposite system, the secondary metal nitride phase is trapped inside an amorphous matrix which leads to its nanostructuration. Any such process is absent here; hence we do not obtain any nanoscale metal nitride leading to loss of catalytic properties associated with size. Although, all these systems alone can act as good supports due to sufficient strengths; they cannot act as efficient co-catalyst. The nanocomposite with a low loading of Pt shows drastic increase in its catalytic behavior as shown previously.

Leaching of active particles from such systems after successive cycles of hydrolysis is one of the biggest problems in such materials³². Hence a recyclability test was performed on this system. The same monolith was used for 5 successive cycles (sample name Pt-mNCPTi_{2.5}-

R1 to R5; last to symbols denoting the cycle number) and its hydrogen generation rate was studied (Figure 5.29). It was observed that there was no decrease in the activity even after 5 cycles. This observation suggests that there is no loss in catalytic activity due to leaching of Pt nanoparticles and/or poisoning by borate sorption.

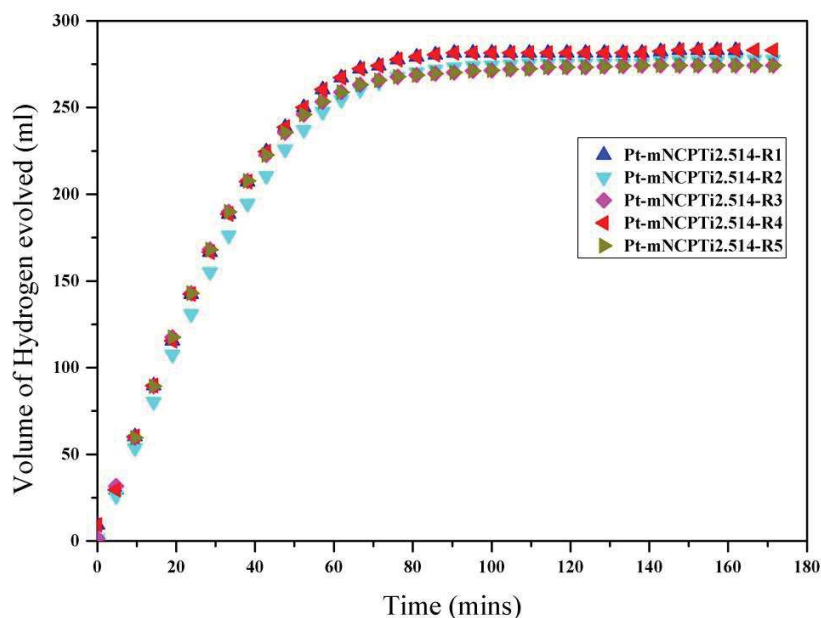


Figure 5. 29 Recyclability test for Pt-mNCPTi2.5-14 system

The apparent activation energy was calculated for the system. The rate was calculated at 4 different temperatures of 80°C, 65°C, 50°C and 35°C and the logarithmic reaction rate values were plotted against inverse of temperature and AAE was calculated by comparing the equation of the line to the Arrhenius rate equation.

$$\ln(k) = \ln(A) - (E_a)/RT$$

The AAE was found to be 62 kJ / mole. This value lies in intermediate range of AAE for such type of systems.

4. Conclusions:

In this chapter we focused on as the design of mesoporous monoliths in the systems investigated in chapters 3 and 4 using the nanocasting process based on activated carbon monoliths as templates. We were able to generate monoliths with very high specific surface area, significant pore volume and interconnected mesoporosity. This is particularly the case of Si-Ti-N ceramics for which it was impossible to remove the activated carbon template most probably because TiN acted as a thermal barrier coating against ammonia. As a consequence, SSA values above $1200 \text{ m}^2.\text{g}^{-1}$ have been generated. Such compounds have been used to support platinum nanoparticles (1 wt%) to be used in the hydrolysis of sodium borohydride at 80°C . Mesoporous Si_3N_4 -based ceramics including Si_3N_4 monoliths and TiN/ Si_3N_4 nanocomposites displayed the best performance in terms of volume of hydrogen released from sodium borohydride and structural stability. We achieved and reproduced hydrogen generation rate of up to $39000 \text{ L}.\text{min}^{-1}.\text{g}_{\text{Pt}}^{-1}$, which is one of the highest reported rates in the literature for the used conditions. This is most probably due to the catalytic activity of PHPS-derived amorphous Si_3N_4 combined with the presence of nanoscaled TiN and the synergetic effect between Pt with both TiN and Si_3N_4 .

References:

1. Han, Y., Yue, X., Jin, Y., Huang, X. & Shen, P. K. Hydrogen evolution reaction in acidic media on single-crystalline titanium nitride nanowires as an efficient non-noble metal electrocatalyst. *J. Mater. Chem. A* **4**, 3673–3677 (2016).
2. Molinari, V., Giordano, C., Antonietti, M. & Esposito, D. Titanium Nitride-Nickel Nanocomposite as Heterogeneous Catalyst for the Hydrogenolysis of Aryl Ethers. *J. Am. Chem. Soc.* **136**, 1758–1761 (2014).
3. Cui, Z., Yang, M. & Disalvo, F. J. Mesoporous Ti_{0.5}Cr_{0.5}N supported PdAg nanoalloy as highly active and stable catalysts for the electro-oxidation of formic acid and methanol. *ACS Nano* **8**, 6106–6113 (2014).
4. Kim, B. G. *et al.* Ordered Mesoporous Titanium Nitride as a Promising Carbon-Free Cathode for Aprotic Lithium-Oxygen Batteries. *ACS Nano* **11**, 1736–1746 (2017).
5. Shi, Y., Wan, Y. & Zhao, D. Ordered mesoporous non-oxide materials. *Chem. Soc. Rev.* **40**, 3854–78 (2011).
6. Borchardt, L. *et al.* Preparation and application of cellular and nanoporous carbides. *Chem. Soc. Rev.* **41**, 5053–67 (2012).
7. Schlienger, S. *et al.* Micro-, Mesoporous Boron Nitride-Based Materials Templated from Zeolites. *Chem. Mater.* **24**, 88–96 (2012).
8. Majoulet, O. *et al.* Silicon–boron–carbon–nitrogen monoliths with high, interconnected and hierarchical porosity. *J. Mater. Chem. A* **1**, 10991 (2013).
9. Bernard, S. & Miele, P. Ordered mesoporous polymer-derived ceramics and their processing into hierarchically porous boron nitride and silicoboron carbonitride monoliths. *New J. Chem.* **38**, 1923 (2014).
10. Whitmarsh, C. K. & Interrante, L. V. Carbosilane polymer precursors to silicon carbide ceramics. (1992).
11. Günthner, M. *et al.* High performance environmental barrier coatings, Part I: Passive filler loaded SiCN system for steel. *J. Eur. Ceram. Soc.* **31**, 3003–3010 (2011).
12. Salameh, C. *et al.* Monodisperse platinum nanoparticles supported on highly ordered

- mesoporous silicon nitride nanoblocks: superior catalytic activity for hydrogen generation from sodium borohydride. *RSC Adv.* **5**, 58943–58951 (2015).
13. Isoda, T. *et al.* Perhydropolysilazane precursors to silicon nitride ceramics. *J. Inorg. Organomet. Polym.* **2**, 151–160 (1992).
 14. Sing, K. S. W. *et al.* in *Handbook of Heterogeneous Catalysis* (Wiley-VCH Verlag GmbH & Co. KGaA, 2008). doi:10.1002/9783527610044.hetcacat0065
 15. Rouquerol, J. *et al.* in 1–9 (1994). doi:10.1016/S0167-2991(08)63059-1
 16. Mason, G. The effect of pore space connectivity on the hysteresis of capillary condensation in adsorption—desorption isotherms. *J. Colloid Interface Sci.* **88**, 36–46 (1982).
 17. Shi, Y. F. *et al.* Highly Ordered Mesoporous Silicon Carbide Ceramics with Large Surface Areas and High Stability. *Adv. Funct. Mater.* **16**, 561–567 (2006).
 18. Majoulet, O. *et al.* Ordered mesoporous silicoboron carbonitride ceramics from boron-modified polysilazanes: Polymer synthesis, processing and properties. *Microporous Mesoporous Mater.* **140**, 40–50 (2011).
 19. Shin, Y.-H. & Shimogaki, Y. Diffusion barrier property of TiN and TiN/Al/TiN films deposited with FMCVD for Cu interconnection in ULSI. *Sci. Technol. Adv. Mater.* **5**, 399–405 (2004).
 20. Gagnon, G., Currie, J. F., Brebner, J. L. & Darwall, T. Efficiency of TiN diffusion barrier between Al and Si prepared by reactive evaporation and rapid thermal annealing. *J. Appl. Phys.* **79**, 7612 (1996).
 21. Kwak, M. Y., Shin, D. H., Kang, T. W. & Kim, K. N. Characteristics of TiN barrier layer against Cu diffusion. *Thin Solid Films* **339**, 290–293 (1999).
 22. Wu, W.-F., Tsai, K.-C., Chao, C.-G., Chen, J.-C. & Ou, K.-L. Novel multilayered Ti/TiN diffusion barrier for Al metallization. *J. Electron. Mater.* **34**, 1150–1156 (2005).
 23. Ham, D. J. & Lee, J. S. Transition metal carbides and nitrides as electrode materials for low temperature fuel cells. *Energies* **2**, 873–899 (2009).

24. Novák, V., Kočí, P., Štěpánek, F. & Marek, M. Integrated Multiscale Methodology for Virtual Prototyping of Porous Catalysts. *Ind. Eng. Chem. Res.* **50**, 12904–12914 (2011).
25. Ortel, E. *et al.* Supported Mesoporous and Hierarchical Porous Pd/TiO₂ Catalytic Coatings with Controlled Particle Size and Pore Structure. *Chem. Mater.* **24**, 3828–3838 (2012).
26. Yan, J., Wang, A. & Kim, D.-P. Preparation of ordered mesoporous SiCN ceramics with large surface area and high thermal stability. *Microporous Mesoporous Mater.* **100**, 128–133 (2007).
27. Majoulet, O. *et al.* Preparation, characterization, and surface modification of periodic mesoporous silicon-aluminum-carbon-nitrogen frameworks. *Chem. Mater.* **25**, 3957–3970 (2013).
28. El-Sharkawy, I. I. *et al.* Experimental investigation on activated carbon–ethanol pair for solar powered adsorption cooling applications. *Int. J. Refrig.* **31**, 1407–1413 (2008).
29. Avasarala, B., Murray, T., Li, W. & Haldar, P. Titanium nitride nanoparticles based electrocatalysts for proton exchange membrane fuel cells. *J. Mater. Chem.* **19**, 1803 (2009).
30. Avasarala, B. & Haldar, P. Electrochemical oxidation behavior of titanium nitride based electrocatalysts under {PEM} fuel cell conditions. *Electrochim. Acta* **55**, 9024–9034 (2010).
31. Kakinuma, K. *et al.* Preparation of titanium nitride-supported platinum catalysts with well controlled morphology and their properties relevant to polymer electrolyte fuel cells. *Electrochim. Acta* **77**, 279–284 (2012).
32. Demirci, U. B. & Miele, P. Cobalt-based catalysts for the hydrolysis of NaBH₄ and NH₃BH₃. *Phys. Chem. Chem. Phys.* **16**, 6872 (2014).

CONCLUSION AND PERSPECTIVES



The work presented in this manuscript has dealt with investigation of the synthesis, processability into mesoporous components and pyrolytic conversion of “single source” precursors to generate mainly BN and Si₃N₄-based ceramics as single phase materials and nanocomposites with in-situ growth of MN (M= Ti, Zr, Hf) nanocrystals in the BN and Si₃N₄ matrix. The high temperature behavior of the final materials has been investigated whereas their use as catalyst support for the hydrolysis of sodium borohydride has been explored.

The **first chapter** proposes a bibliographic study on different **electrochemical power sources** and the issues which limit their commercialization. We provided a state of the art on the **synthesis of Si- and B- based carbide, carbonitride, nitride and their derived nanocomposites using the polymer derived ceramic (PDC) route**. We focused our attention on the PDC route in this thesis due to its advantages to control the ceramic composition precisely, its ability to synthesize complex shapes and the relatively low processing temperature.

The **second chapter** was focused on the **description of materials and experimental protocols** for synthesis, shaping and pyrolysis processes.

The **third chapter** was focused on **boron nitride (BN) and the derived B-M-N (M = Ti, Zr, Hf) ceramics**. We described the development of BN from two different precursors, *i.e.*, ammonia borane (AB) and polyborazylene (PB60), and detailed their pyrolytic conversion as well as the high temperature crystallization of BN to better understand the chemistry behind the process to elaborate B-M-N (M = Ti, Zr, Hf) ceramics in the second part of the chapter. Thus, we discussed on the synthesis and characterization of B-M-N (where M = Ti, Zr, Hf) ceramics through the reaction between BN precursors and MN precursors. The polymer synthesis was studied by FTIR and solid-state NMR spectroscopies which allowed us to identify the mechanisms that govern the polymer synthesis. Then, we focused on the polymer-to-ceramic conversion and we found that polymers containing Hf displayed the highest ceramic yield because of their high degree of crosslinking. Ammonia-treated samples are poorly crystallized and it was necessary to anneal samples at 1450°C to form nanocomposites in which MN nanocrystals are distributed in a BN matrix. Through the investigation of the microstructural evolution and the crystallization behavior at high temperature, we particularly demonstrated that the gradual increase of the transition metal nitride content in the B-M-N ceramics shifts the crystallization of the BN matrix to higher temperatures and can be even suppressed using hafnium as a metal. Thus, B-Ti-N ceramics with a B:Ti ratio of

1 and B-Hf-N ceramics with a B:Hf ratio below 2.5 form highly stable nanocomposite structures. However, such nc-MN/a-BN nanocomposites may have some potential disadvantages in some applications due to the low BN crystallinity which can involve a low oxidation resistance. To overcome this problem, we focused the last part of the present chapter on the investigation of the improvement of the BN crystallinity using AB and PB as BN precursors. We investigated two strategies using syntheses in solution and reactive ball-milling through the reaction of BN precursors with lithium amide (LiNH_2). We successfully demonstrated that a reactive ball-milling between AB and LiNH_2 according to a certain ratio allowed us to generate highly crystallized BN at 1450°C . The materials have been characterized at each step of their process.

The second solution to overcome the low oxidation resistance of the BN matrix in MN/BN nanocomposites is to change the nature of the matrix. Within this context, the **fourth chapter** was focused on **Si_3N_4 and Si-M-N(C) (M = Ti, Zr, Hf) ceramics**. We firstly sequenced a one-step synthetic method to obtain polymetallosilazanes. The synthesis consisted to perform the reaction between commercially available polysilazanes such as PHPS and HTT1800 and the low molecular weight metal-containing molecules (which have been already used in chapter 3) with controlled Si:M ratios. The role of the chemistry behind their synthesis was studied by FTIR, solid-state NMR and elemental analyses. Two mechanisms involving N-H and Si-H bonds in polysilazanes as well as $\text{N}(\text{CH}_3)_2$ groups in metal-containing precursors have been identified. It has been shown that PHPS is the most reactive polysilazane while Hf-based molecules were highly reactive with SiH groups of polysilazanes. Such a difference has an effect on the ceramic conversion and the high temperature behavior of ceramics. Thus, we provided a comprehensive mechanistic study of the polymetallosilazane to Si-M-N ceramic transformation under ammonia based on solid-state NMR coupled with TG experiments. Pyrolysis under ammonia generated X-ray amorphous ceramics

The subsequent annealing of ammonia-treated samples under nitrogen at 1400°C led to nanocomposites made of MN nanocrystals dispersed in an amorphous or crystallized matrix depending on the nature of the metal and the Si:M ratio fixed at molecular scale. After annealing to 1500°C , the effect of the chemistry of the polysilazane on the matrix crystallization was demonstrated. We found that the addition of Ti or Hf to PHPS in the correct Si/M molar ratio led to suppression of the matrix crystallization up to 1800°C . This generates a system where we have controlled growth of nanostructured metal nitride crystals

within an amorphous ceramic matrix. We also explored the effect of modification of a polysilazane with two different metallic precursors simultaneously. We obtain a new TiZr(C)N phase which crystallizes in an amorphous matrix.

Finally, in **chapter 5**, we focus on as the **design of mesoporous monoliths** in the systems investigated in chapters 3 and 4 using the nanocasting process based on activated carbon monoliths as templates. We were able to generate monoliths with very high specific surface area, significant pore volume and interconnected mesoporosity. This is particularly the case of Si-Ti-N ceramics for which it was impossible to remove the activated carbon template most probably because TiN acted as a thermal barrier coating against ammonia. As a consequence, SSA values above $1200 \text{ m}^2.\text{g}^{-1}$ have been generated. Such compounds have been used to support platinum nanoparticles (1 wt%) to be used in the hydrolysis of sodium borohydride at 80°C . Mesoporous Si_3N_4 -based ceramics including Si_3N_4 monoliths and TiN/ Si_3N_4 nanocomposites displayed the best performance in terms of volume of hydrogen released from sodium borohydride and structural stability. We achieved and reproduced hydrogen generation rate of up to $39000 \text{ L}.\text{min}^{-1}.\text{g}_{\text{Pt}}^{-1}$, which is one of the highest reported rates in the literature for the used conditions. This is most probably due to the catalytic activity of PHPS-derived amorphous Si_3N_4 combined with the presence of nanoscaled TiN and the synergetic effect between Pt with both TiN and Si_3N_4 .

These very interesting results demonstrated the functionality of the materials prepared in chapters 3 and 4. However, the development of novel solutions and system integration concepts constitutes the role of ceramics-based energy converters in future energy scenarios. The breakthrough in this field consists in providing and tuning specific properties by developing new formulations and structures/ morphologies (nanoparticles, mesoporous or 2D structures) from dedicated chemistry. Within this context, our perspectives are focused on the design of composites and nanocomposites, in particular those we present in this manuscript, to envision energy storage based on electrochemical reactions in fuel cells and supercapacitors, and conversion of renewable energy sources.

We firstly consider the **design and physico-chemical characterization of functional nanostructured ceramics as electrode materials**. Fuel cells and supercapacitors are important electrochemical energy storage/production devices but state-of-the-art supercapacitors and fuel cells are not able to meet the requirements for energy-efficient use in transportation,

grid, and commercial technologies. Both technologies seek new materials design concepts for higher energy densities, higher power densities, and longer cycle life.

For **fuel cells**, our perspectives are concerned by direct formic acid fuel cells (DFAFCs) and in particular on new fuel cell catalysts. FA is a liquid at room temperature with volumetric and gravimetric energy densities of 53 g/L and 4.3 wt%, respectively. However, there are still several challenges that hinder fuel cell commercialization, including insufficient durability/reliability of catalysts. The corrosion of carbon supports (cathodes and anodes) is identified to be the major contributor to the catalyst failure. To address the issue of carbon corrosion, alternative materials should be explored. Metal nitrides (MN) display noble-metal-like properties which result from their similar electronic structure¹. However, they need to be nanostructured and they suffer from wear and corrosion in highly acidic environments. Therefore, MN alone may not possess the necessary stability to replace carbon as supports. Confined in a Si-C-N matrix through the concept we applied in chapter 4, we expect a significant improvement of the chemical stability of the resulting materials in acid and alkaline media while proposing the electrocatalytic activity of nanostructured MN. **MN (M = Ti/Cr/Nb/Co)/Si-C-N electrodes for DFAFCs** obtained through the Polymer-derived ceramic route with an *in-situ* controlled growth of MN nanocrystals (~5 nm in diameter) during the formation of the Si-C-N matrix will be therefore considered in a close future. They will be prepared as capsules with hollow macroporous core/mesoporous shell structures, nanofibers and monoliths with tailored mesoporosity. The design of their porosity will be achieved using templating approaches as we planned in chapter 5 and additive manufacturing routes at the Research Institute of Ceramics in Limoges. Pt will be deposited as nanoparticles through impregnation of the support in a Pt salts then reduction in H₂ furnace in a controlled amount. A synergetic effect between Pt and MN is expected to optimize the electrocatalytic activity of the material investigated. We already started such experiments through the deposition of Pt NPs on mesoporous Si-Ti-N(C) supports (the carbon coming from the activated carbon template and/or free carbon present in the Si-C-N ceramics).

For **supercapacitors**, we already investigated the design of MXenes/Si-C-N composites as electrode materials and got interesting results. MXene are promising materials for use as electrodes in supercapacitors but are limited by oxidation/corrosion. It needs to be protected by a coating which will not decrease its electrical conductivity and also provide mechanical stability to the system. Under harsh condition of electrochemical cell most oxide based

coatings will fail, hence we need a non-oxide ceramic coating for this purpose. In the previous sections we discussed various ceramic non-oxides which can withstand harsh conditions. Out of those discussed earlier only HTT1800 derived Si-C-N system can provide electrical conductivity. Rest all are either semiconductors (SiC) or insulators (Si_3N_4). SiCN/MXene composites were synthesized as discussed in chapter 2 and tested as electrode materials in supercapacitors.

The CV (cyclic voltammogram) curve (Figure 1) of the 50 wt.% and 90 wt.% SiCN in MXenes is larger than that of the neat materials (Si-C-N and MXene). This indicates the 50 wt.% and 90 wt.% Si-C-N in MXene electrode has a higher capacitance which may be due to the modification of Si-C-N with MXene. In addition, the rectangular-shaped CV curve of the 50 wt.% and 90 wt.% Si-C-N in MXene electrode suggests the charge storage mechanisms of both materials is dominantly non-faradaic. According to Eqn. 1, the 90 wt.% Si-C-N in MXene displays the highest areal capacitance (137.17 mF/cm^2); which is comparable to the areal capacitance of similar 2D materials.

$$C_s = \frac{2 \int_{v_2}^{v_1} I(v) dv}{As\Delta v} \quad \text{Eqn. 1}$$

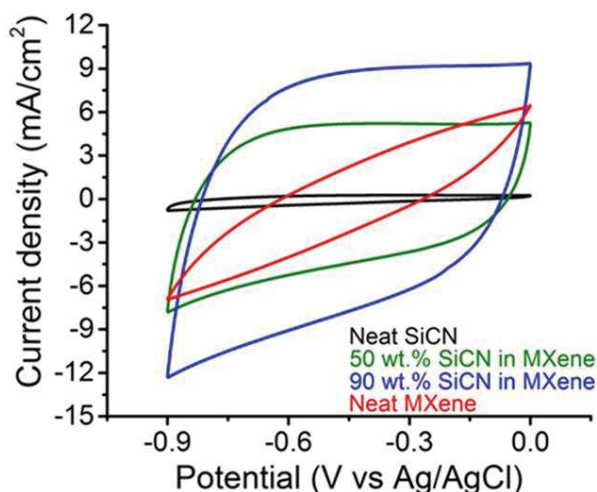


Figure 2 Cyclic voltammogram of MXene, neat SiCN, and SiCN in MXene electrodes at 200mV/s

More so, the CV displays a quasi-rectangular shape with no redox peaks which suggest the charge storage mechanism of the 90 wt.% Si-C-N in MXene is dominantly non-faradaic. Further work needs to be done to optimize the chemistry and properties of the composite. A

detailed study need to be performed to study the interaction between MXene and Si-C-N and to investigate the effect of the nature of the ceramic matrix.

Secondly, we will focus on **nanostructured ceramics as catalysts in the production of hydrogen**. The H₂-PEMFC is mainly limited by the high cost of miniaturised hydrogen containers. Liquid-phase **hydrogen carriers** are an interesting alternative. For the application of FA as a liquid organic hydrogen carrier or an energy source for fuel cells, its dehydrogenation is highly desired, and the catalytic selectivity for dehydrogenation depends on the catalytic surface, temperature, pH value in reaction system, FA concentration and so on [S. Moret, et al. *Nat. Commun.* (2014) 5, 4017]. The limitation of homogeneous catalysts involved the development of heterogeneous catalysts using various supports and metals. However, new materials investigations are required to propose highly efficient and effective for decomposition. Because of their co-catalytic property, the **MN/Si₃N₄ nanocomposites** will be evaluated as support of Pd and binary Ag/Pd nanoparticles for **the production of hydrogen from FA**. They would be also explored to recycle CO₂ into FA.

The key for successful applications as catalyst is the chemically inert support and the strong interactions between the metal nanoparticles and the support to allow for the stabilization of ultra-small metal nanoparticles. Our proposal consists in the synthesis of processable metal-containing polymer followed by their pyrolysis into nanocomposites during which an ***in-situ* growth of active metal sites occurs within the matrix**. This reduces the number of steps to prepare metal-supported ceramics and should increase the interaction with the fluid if the metal is accessible. We investigated such a route to prepare Co/Si₃N₄ nanocomposites in collaboration with Prof. Yuji Iwamoto (NITech, Japan) and Pt/Si-C-N nanocomposites in collaboration with the group of Rhett Kempe (University of Bayreuth) and as a proof of concept, we applied such materials for the hydrolysis of sodium borohydride.

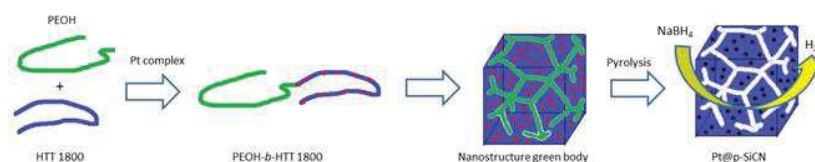


Figure 3 Hierarchically porous SiCN ceramics with surface Pt NPs were fabricated by the self-assembly and subsequent pyrolysis of an *in situ* generated block copolymer whose inorganic block (Si-N backbone) was modified with Pt (II) ions. The as-obtained catalysts

Such materials display great potential as nanocatalysts and also as electrocatalysts. The hydrolysis behavior of the such systems is demonstrated in the figure 3. Further work on these materials aims to reduce the platinum content in the system and shape these systems as monoliths thereby making them easier to use.

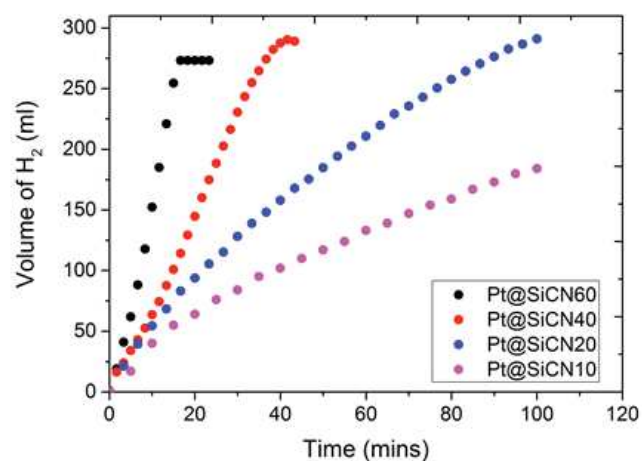


Figure 4 Volume of hydrogen (in mL) measured during the hydrolysis of sodium borohydride over the mass of nanocomposites containing the same amount of Pt. (0.35 mg) at 80°C. Under these conditions the amount (in mg) of nanocomposites used were different